Stepped-Frequency Radar Design and Signal Processing Enhances Ground Penetrating Radar Performance

David Andrew Noon
BE (Elec., Hons I)

Department of Electrical & Computer Engineering
The University of Queensland
and
Cooperative Research Centre for Sensor Signal and Information Processing

A thesis submitted for the degree of Doctor of Philosophy (PhD) of The University of Queensland

January 1996

Statement of Originality

The work contained in this PhD thesis is, to the best of my knowledge and belief, original and my own work, except as acknowledged in the text. This material has not been submitted, either in whole or in part, for a degree at this or any other university.

David A. Noon

Postscript Notice

Please note that this document does not contain Chapter 5, as it has not been released for publication.

Abstract

This thesis presents a theoretical analysis and applied evaluation of the stepped-frequency radar technique and shows that significant performance benefits can be achieved in ground penetrating radar (GPR) applications. These benefits are successfully demonstrated in field trials of a newly designed stepped-frequency GPR system.

An original contribution has been made in establishing a unified characterisation of the performance of GPR for constant Q materials. This enables the maximum penetration depth of a GPR system to be characterised as a fixed number of wavelengths which is constant for any frequency. Similarly, the resolution is expressed as a fixed number of wavelengths which is also constant with frequency. These expressions prove to be a useful design tool in characterising GPR performance independently of frequency, and in selecting the waveform parameters for a defined application.

A rigorous theoretical study of the stepped-frequency radar technique is undertaken, which demonstrates the "synthesis" of an impulse waveform using an IDFT-based matched filter with minimum-phase. It is concluded that a physically realisable stepped-frequency radar has far-reaching benefits in the form of higher processed mean energy than an impulse radar with the same frequency bandwidth.

A 1-2 GHz stepped-frequency GPR prototype has been completely designed and built to test the above theories. The primary application for this system design is the high-resolution mapping of thin coal seam structures in open-cut coal mines. The 1-2 GHz frequency band is selected to meet the performance requirements of one metre penetration and five centimetre resolution in coal.

A novel technique is presented which corrects the broadband quadrature receiver errors in the stepped-frequency radar prototype. It is shown that the technique suppresses the Hermitian images by more than 50 dB below the target responses.

The external loop gain of the system is measured to be 156 $\pm$ 6 dB for bow-tie antennas and 166 $\pm$ 6 dB for horn antennas. These figures represent the maximum power loss that the radiated signal, integrated over a defined ten millisecond interval, can tolerate between the transmit and receive antennas, for a defined signal-to-noise ratio of 10 dB. The performances of typical impulse GPR systems are noted in the literature to lie between 100-130 dB under similar conditions.

The system is successfully field tested at various sites, including two open-cut coal mines. The resulting images from these sites demonstrate a penetration depth of at least 80 centimetres and a resolving power of better than 8 centimetres.

List of Publications

Patent

Longstaff, I. D., **D. A. Noon** & G. F. Stickley, A System for Correcting Receiver Errors in Radar, Patent PCT/AU96/00217, The University of Queensland, Qld, Australia, Apr. 18, 1994.

Refereed Conference Papers

Noon, D. A. & I. D. Longstaff, Performances of GPR across a Broad Frequency Spectrum, 1995 Workshop on Applications of Radio Science (WARS '95), Canberra, ACT, Australia, June 25-27, 1995.

Noon, D. A., Management Skills in an Industry Collaborative Project Enhance a PhD Degree Program, 1994 Proc. Australian Association for Engineering Education (AaeE) - Inspiring Integration Conference, Sydney, NSW, Australia, 179-182, Dec. 11-14, 1994.

Noon, D. A., I. D. Longstaff & R. J. Yelf, Advances in the Development of Step Frequency Ground Penetrating Radar, Proc. of the Fifth Int. Conf. on Ground Penetrating Radar (GPR '94), Kitchener, Ont., Canada, 117-132, Jun. 12-16, 1994.

Noon, D. A., I. D. Longstaff & G. F. Stickley, Correction of I/Q Errors in Homodyne Step Frequency Radar Refocuses Range Profiles, 1994 Proc. IEEE Int. Conf. on Acoustics, Speech & Signal Processing (ICASSP '94), Adelaide, SA, Australia, 369-372, Apr. 19-22, 1994.

Workshop Paper

Noon, D. A. & I. D. Longstaff, A new ground penetration radar relevant to the Australian mining industry, Workshop in Pattern Analysis/Recognition, Townsville, Qld, Australia, 11-13, Oct. 2, 1992.

Contents

List of Figures

List of Tables

Preface

The majority of this doctoral thesis work was carried out as part of the Stepped-Frequency Ground Penetrating Radar Project at The University of Queensland. This project was funded by Generic Technology (GIRD) Grant Agreement 16040 between the Industry Research and Development Board (Commonwealth of Australia), The University of Queensland, MITEC Australia Ltd, Technological Resources Pty Ltd (CRA), Georadar Research Pty Ltd, and the Cooperative Research Centre for Sensor Signal and Information Processing (CSSIP).

The purpose of the GIRD project was to explore and exploit the theoretical and practical benefits of the stepped-frequency radar technique in ground penetrating radar applications. The primary application was the high-resolution mapping of thin coal seam structures, in order to assist continuous surface mining operations in open-cut coal mines. The performance requirements for this application are approximately one metre penetration and five centimetre resolution in coal. A high-resolution, stepped-frequency ground penetrating radar prototype was designed and built for this purpose. Part of this thesis describes the radar design and signal processing of this system. A second application introduced into the GIRD project was a system with deeper penetration for ore-body delineation and mine planning. Many of the concepts contained in this thesis are directly applicable to such a system, although that system and application are not discussed.

The outline of the thesis is as follows. Chapter 1 is an introduction to the radar principles of range and resolution, with a strong emphasis placed on high-resolution and ultra-wideband radar techniques. Chapter 2 contains an introduction to and a literature review of ground penetrating radar (GPR). The performance of GPR in terms of maximum penetration depth and resolving power are characterised in Chapter 3. This chapter develops a novel theoretical basis for GPR performance assessment throughout the remainder of the thesis. Chapter 4 focuses on the application of the stepped-frequency radar technique to ground penetration radar, although the principles developed are generic to any stepped-frequency radar. This chapter contains a comprehensive review of past and current achievements in stepped-frequency GPR, and a rigorous theoretical analysis of the stepped-frequency technique. Chapters 5 through to 7 are concerned with the complete design and testing of a high-resolution, stepped-frequency GPR prototype. The radar system is detailed in Chapter 5. Following this, Chapter 6 presents a novel technique for correcting the hardware receiver errors in the system. Chapter 7 contains the results of laboratory tests and field trials at various sites including two open-cut coal

mines. Chapter 8 concludes the thesis by addressing the contributions that have been made by this work in the areas of GPR performance characterisation (Chapter 3), stepped-frequency GPR development and testing (Chapters 4, 5 and 7), and broadband quadrature receiver error correction (Chapter 6).

Throughout the thesis, careful acknowledgements of contributions that are not original to the author are made using footnotes and references. All other material in the thesis is original to the author. However, the benefits of being part of a well-managed and active research team are immeasurable, and many ideas of co-researchers have been built upon in this thesis.

My foremost and complete respect is given to Professor Dennis Longstaff for his highest level of commitment during the supervision of my thesis work. Many initial ideas were contributed and nurtured by him throughout their development by the author. He also provided leadership as Principal Investigator to the GIRD project, without compromising his duties towards my supervision. Thank you for your dedication and support.

The GIRD project was well managed under the direction of Dr Ray Scott, who I thank for planning and organising the research tasks and responsibilities of the research team while respecting my thesis work. The full-time research team consisted of Glen Stickley, Stephen Nothdurft, Aruna Gunawardena and Pat Bellett. I thank each of these people for their contributions as noted in the thesis, and for their support during the project and my thesis work. I wish to thank Dr H Ashoka and Paul Van Wijk of MITEC for the lower level design and construction of the ruggedised prototype. I also express my gratitude to Rachael Skyring, Richard Yelf and Christina Yelf for their valuable assistance in proof-reading the text. The respective managements of Mt Thorley and Ebenezer Mines are sincerely acknowledged for accommodating the field trials.

To each of the collaborating parties who have supported the GIRD project, I express my gratitude for their contributions. In particular, I acknowledge the members of the Management Committee, Dr John Ness (MITEC), Prof Dennis Longstaff (UQ), Dr Robin Greenwood-Smith (CRA), Mr Richard Yelf (Georadar Research), and Prof Henry d'Assumpcao (CSSIP) for their guidance of the GIRD project and their support of my thesis work. I wish to especially thank Prof Henry d'Assumpcao and the partners to CSSIP for the working environment, and financial and travel assistance that the CRC provided throughout my thesis study.

I am grateful to my family who have encouraged and assisted my formal education which has now spanned twenty years. Finally, words are not adequate to express my love and thanks to my wife, Sarah, for her patience and understanding in many, many ways.

David A. Noon

Chapter 1

RADAR Principles of Range and Resolution

1.1 Introduction to RADAR

Radar is "a device for transmitting electromagnetic signals and receiving echoes from objects of interest (targets) within its volume of coverage" (IEEE Std 686-1990). In its original application, radar was used for revealing the presence of targets by detecting their reflected signals, and determining their ranges by measuring the elapsed times between transmission and reception. For this reason, *radar* was termed after the acronym for *ra*dio *d*etection *a*nd *r*anging.

Additional information about the targets can be extracted from their reflected radio signals; direction in azimuth and elevation can be determined using directive antenna patterns; velocity can be measured using the Doppler shift; and description and classification of the targets can be obtained by analysing their echo signals as they vary with time.

The principle of radar was discovered by Heinrich Hertz in the 1880's, who noticed that radio waves are reflected by objects in a similar fashion to light. Hülsmeyer obtained patents in 1904 throughout several countries (*e.g.* German Patent No. 165546) describing a system using *Continuous Wave* (CW) to detect the reflected radio waves from remote metallic objects. Further research into detecting the presence of ships and planes by CW radar was pursued separately in the early 1900's by Germany, the United Kingdom and the United States [*Skolnik*, 1962].

It was evident CW radars cannot measure the range to targets, because there are no timing marks in the CW radar waveform. By transmitting a pulsed CW signal, the *travel times* t_t between transmission and reception of the pulses can be related to target *ranges* R in equation 1.1 for a known *propagation velocity* v (usually taken as the speed of light c, in free space). (The "2" in the denominator is necessary because the travel time is for two-way propagation but range is expressed one-way only.)

$$R = \frac{v\, t_t}{2} \tag{1.1}$$

This *pulsed radar* technique was demonstrated by the US Naval Research Laboratories in 1935 [*Skolnik*, 1962]. A simple pulsed radar waveform (Figure 1.1) is a train of short bursts of CW with *pulsewidths* of τ seconds at a *pulse repetition frequency* of PRF Hertz (equal to the inverse of the *pulse repetition interval*, PRI). The pulsed waveform of Figure 1.1 has a *peak voltage* denoted V_p.

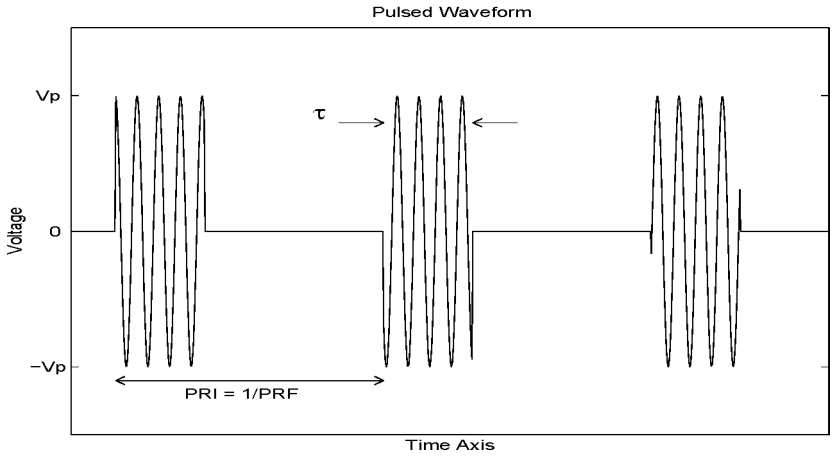

Figure 1.1: A simple pulsed radar waveform comprising of a carrier frequency pulsed at a repetition rate of PRF Hertz. The pulse repetition interval (PRI) is the inverse of the PRF. Each pulse has a width of τ seconds and a peak voltage of V_p.

The *peak power* of each CW pulse is defined as the output power averaged over its carrier cycle, or ${V_p}^2/2Z$, where Z is the *characteristic impedance* (usually taken as 50 Ω for transmission lines). The *mean* or *average* power of a pulsed waveform is less than the peak power because the signal is switched on for only a fraction of the total waveform time. The ratio of time for which the peak power is actually switched on is referred to as the *duty cycle*. For the waveform in Figure 1.1, the

duty cycle is equal to $\tau/(PRI)$ or $\tau(PRF)$, and the mean transmitted power P_T is given by equation 1.2.

$$P_T = \frac{V_p^2}{2Z}(duty\ cycle) = \frac{V_p^2}{2Z}\tau\,(PRF) \tag{1.2}$$

The pulsed waveform with a mean power of P_T is radiated into the propagating medium (*e.g.* free space) by a transmitting antenna, which has an *antenna gain* of G_{Tx} with respect to an isotropic radiator. The power density in Watts per square metre of the transmitted signal at a point target of range R is $\frac{P_T G_{Tx}}{4\pi R^2}$. Assuming the target has a *radar cross section area* of σ_T, the reflected power density at the radar receiver antenna is $P_T \frac{G_{Tx}}{4\pi R^2} \frac{\sigma_T}{4\pi R^2} \frac{1}{L}$. (Absorption of the signal during propagation to and from the target causes a reduction in power by a factor L.) The receiver antenna has an *effective aperture* of $G_{Rx}\frac{\lambda^2}{4\pi}$ square metres, where G_{Rx} is the *receiver antenna gain*, and λ is the *propagating wavelength* ($\lambda = c/f$ in free space, where f is the frequency). The *received signal power* P_R from the point target measured at the radar is given by equation 1.3. This equation is known as the *radar equation* [*Skolnik*, 1990].

$$P_R = \frac{P_T\ G_{Tx}\ G_{Rx}\ \lambda^2\ \sigma_T}{(4\pi)^3\ R^4\ L} \tag{1.3}$$

The *maximum range* R_{max} to a target can be calculated using the radar equation by defining the *minimum detectable signal* power P_{MDS} of the receiver (equation 1.4).

$$P_{MDS} = F\ kT_0B_N\ (SNR)_{in} \tag{1.4}$$

For a low probability of false alarm detection, P_{MDS} must be significantly larger (for example, an *input signal-to-noise ratio* or $(SNR)_{in}$ of 13 dB for single pulse detection) than the internally generated noise power at the receiver given by FkT_0B_N. F is the receiver *noise factor* which is multiplied by the thermal noise power, kT_0B_N, where k is *Boltzmann's constant* ($\approx 1.38\text{x}10^{-23}\ J\ K^{-1}$), T_0 is the *absolute ambient temperature standard* of $290K$ (ANSI/IEEE Std 161-1971), and B_N is the root-mean-squared (rms) *noise bandwidth* of the receiver in Hertz [*Skolnik*, 1990].

The input signal-to-noise ratio SNR_{in} can be made optimal for the type of transmitted waveform by using a *matched-filter* [*Wehner*, 1995]. For a matched-

filter receiver, the input signal-to-noise ratio SNR_{in} of the radar equation can be expressed as a ratio of the *average signal-to-noise ratio* SNR and the *time-bandwidth product* tB_N of the waveform (*i.e.* $SNR_{in} = SNR/tB_N$). The impulse response width t of the matched-filter is the *integration time* t_{int} for acquiring samples of the waveform. The minimum detectable signal power for a matched-filter receiver is then expressed by equation 1.5.

$$P_{MDS} = F\, kT_0(SNR)/t_{int} \tag{1.5}$$

Substituting P_{MDS} of equation 1.5 for P_R in equation 1.3 (as well as changing R to R_{max}) and rearranging the equation for R_{max}, the maximum range of the radar can be calculated using equation 1.6.

$$R_{max} = \left[\frac{P_T\, G_{Tx}\, G_{Rx}\, \lambda^2\, \sigma_T\, t_{int}}{(4\pi)^3\, F\, kT_0 B_N\, (SNR)\, L}\right]^{\frac{1}{4}} \tag{1.6}$$

Most of the parameters on the right hand side of equation 1.6 can be controlled by the radar designer, who is concerned with finding the most appropriate values of the parameters to suit the particular application. For example, the antenna gains can be increased by widening the antenna aperture, but this may be limited by the physical size of the antennas. The wavelength of propagation can be increased but this will reduce the resolving power of the system.

A more realistic improvement to the maximum range of the radar can be made by increasing the *processed mean energy*, which is defined in this thesis as the mean transmitter power multiplied by the integration time (*i.e.* $P_T t_{int}$). Several Watts of mean transmitter power are relatively easily obtained with simple solid-state amplifiers, although the delivery of kiloWatts can be prohibitive in cost and radiation safety aspects. However, the processed mean energy of the radar can be increased by acquiring the received power over longer integration times.

The solution to the radar equation is not the only restriction on the maximum range capability of a simple pulse radar. There is a range ambiguity for a uniform pulse train, which limits the system to having only one pulse propagating to and from the target at any time. Therefore, the *maximum unambiguous range* R_{max} is limited by the pulse rate (or PRF) of the waveform and the propagation velocity v by equation 1.7.

$$R_{max} = \frac{v}{2\,(PRF)} \tag{1.7}$$

Low PRF numbers are required to extend the maximum unambiguous range, but this is traded with a reduction in mean transmitter power P_T (for a constant peak power and pulsewidth) in equation 1.2. Magnetrons and high-power klystron amplifiers are used in pulsed transmitters to produce longer pulsewidths so that lower PRF numbers are generated without compromising the mean power. However, this is not a suitable solution for many radar applications that require high-range resolution.

An important characteristic of radar is its ability to separately detect and measure the ranges to multiple targets. The radar *range resolution* parameter is defined as "the ability to distinguish between two targets solely by the measurements of their ranges (distances from the radar); usually expressed in terms of the minimum distance by which two targets of equal strength at the same azimuth and elevation angles must be spaced to be separately distinguishable" (IEEE Std 686-1990). This definition refers to the *slant range* resolution which is along the radar's line-of-sight. It is distinguished from *cross-range* resolution, which is along the direction transverse to the radar's line-of-sight, determined by the beamwidth of a real or synthetically processed antenna. Unless otherwise specified in this thesis, the terms *resolution* and *resolving power* refer to the *slant range* case.

The quantitative definition of resolution for radar signals has been adapted from *Rayleigh's criterion* for optical resolution. For the radar case, this criterion states that "two point targets whose reflected signals are of equal amplitude are resolved when the peak response from one target falls on the first minimum of the second target's response" [*Wehner*, 1995]. Figure 1.2(a) displays a rectangular frequency spectrum of bandwidth B Hertz, with its corresponding $\sin \pi Bt / \pi Bt$ or $\mathrm{sinc}\,(Bt)$ envelope response in the time domain as Figure 1.2(b). The $\mathrm{sinc}\,(Bt)$ pulsewidth (defined as the width of the mainlobe at 4 dB's below the mainlobe peak) is equal to $1/B$ seconds. Similarly, the time difference between the peak and the first minimum of the $\mathrm{sinc}\,(Bt)$ pulse is equal to $1/B$ seconds.

The resolution in time of two of these $\mathrm{sinc}\,(Bt)$ signals with equal amplitudes is defined when the peak of the first pulse response is directly over the first minimum of the second pulse response. This occurs when the pulses cross at their -4 dB points, where both peaks are separated by $1/B$ seconds (Figure 1.3).

Using this quantitative definition, the range resolution ΔR is related to the signal bandwidth B and propagation velocity v by equation 1.8.

$$\Delta R = \frac{v}{2B} \tag{1.8}$$

The $v/2$ in this equation is necessary to convert two-way travel time in seconds to one-way range in metres. The resolving power is highly dependent on the bandwidth of the signals that are transmitted. Larger bandwidths are possible with high frequency signals, and alternatively smaller bandwidths are available with low frequencies. Therefore, it is desirable to classify signals in terms of their *fractional bandwidth.* This is defined as the ratio of the bandwidth B and the centre frequency of the band f_c, expressed as a percentage (*i.e.* B/f_c x 100%).

The -4 dB bandwidth of the simple pulsed waveform illustrated in Figure 1.1 is defined as the inverse of the pulsewidth (or $B = 1/\tau$). Therefore the range resolution of a simple pulsed radar can be calculated by equation 1.9.

$$\Delta R = \frac{v\tau}{2} \tag{1.9}$$

The fractional bandwidth B/f_c of a simple pulsed waveform can be expressed as $1/(\tau f_c)$, where the centre frequency f_c of the bandwidth is the carrier frequency

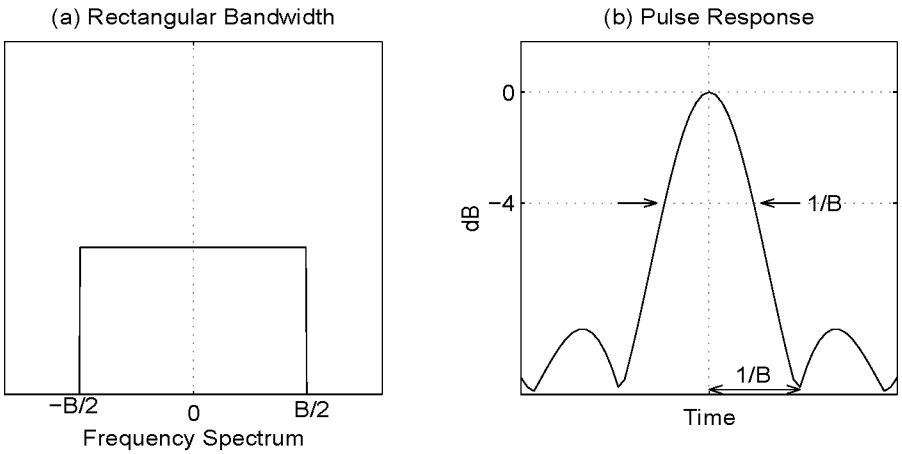

Figure 1.2: (a) A rectangular frequency spectrum of bandwidth B Hertz; (b) the corresponding sinc (Bt) time response with a -4 dB pulsewidth of $1/B$ seconds. The time difference between the peak and the first minimum of the pulse response is also equal to $1/B$ seconds.

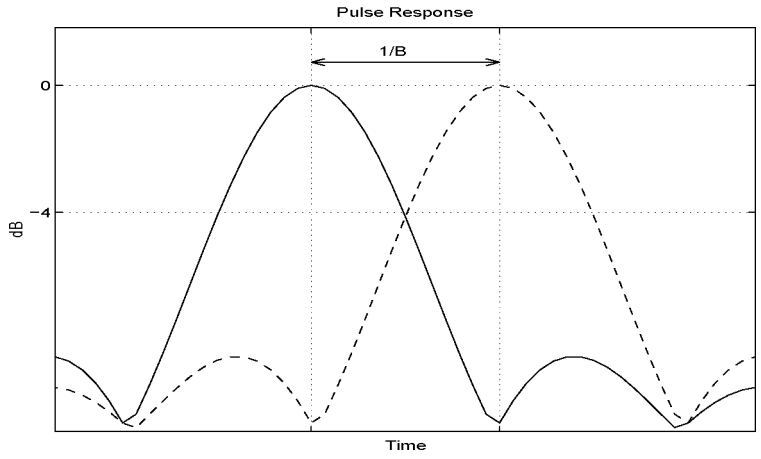

Figure 1.3: The resolution in time of two pulses with equal amplitudes and rectangular bandwidths of B Hertz is defined at the -4 dB cross-over point as $1/B$ seconds.

within the $1/B$ envelope width of the pulse. Pulsed signals with a low fractional bandwidth have wide envelopes which contain many cycles of the carrier frequency. Alternatively, signals with high fractional bandwidths have narrow envelopes which only contain a few cycles of the carrier frequency.

The CW and pulsed radar systems described in this section belong to the class of *narrowband* radars, whose bandwidths are small compared with their carrier frequency (*i.e.* small fractional bandwidths of the order of a percent). With the possible exception of millimetre-wave systems which have centre frequencies in excess of 40 GHz, narrowband pulsed radars are generally *low resolution*, and are only able to detect multiple targets that are well separated in range. In high-resolution radar applications at microwave and lower frequencies (for example, microwave radar imaging and GPR), it is necessary for the pulsed radars to have very narrow pulsewidths (which is equivalent to very large bandwidths) to achieve the required performance in resolution.

A dilemma eventuated soon after World War II in developing pulsed radar systems with both long range and high resolution capabilities [*Klauder et al.*, 1960]. For a fixed PRF, there is a compromise between transmitting high peak powers (which are required for long range) and short pulsewidths (necessary for high resolution). In addition, pulse transmitters with high peak powers approach fundamental limits of energy dissipation in components and voltage breakdown. It was evident that the simple pulsed radar was not suitable for higher resolution radar applications requiring ultimate performance in both range and resolution.

1.2 High-Resolution Radar (HRR)

In overcoming the power and bandwidth limitations of the simple pulsed radar, alternative waveforms were developed which allow high mean powers through the transmission of longer pulses for extending the range capability, yet retaining wide bandwidths for high resolution. Radar systems generating these waveforms are termed *wideband* (WB) or *high resolution*, where fractional bandwidths approach 20% [*Wehner*, 1995]. These systems are used in radar imaging, including synthetic and inverse synthetic aperture radar (SAR/ISAR) [*Curlander & McDonough*, 1991] and ground penetrating radar.

1.2.1 FMCW Radar

A simple waveform which simultaneously allows wide bandwidth and high mean power is the *Frequency-Modulated Continuous Wave* (FMCW). The FMCW radar transmits a CW signal with a frequency swept across a bandwidth B in either a sawtooth or triangular fashion, within a *dwell time* t_d (also known as the *Ramp Repetition Interval*, RRI [*Piper*, 1993]). The reflected CW signals from the targets are received and multiplied with a reference signal (replica of the transmitted signal) using a homodyne mixer (Figure 1.4).

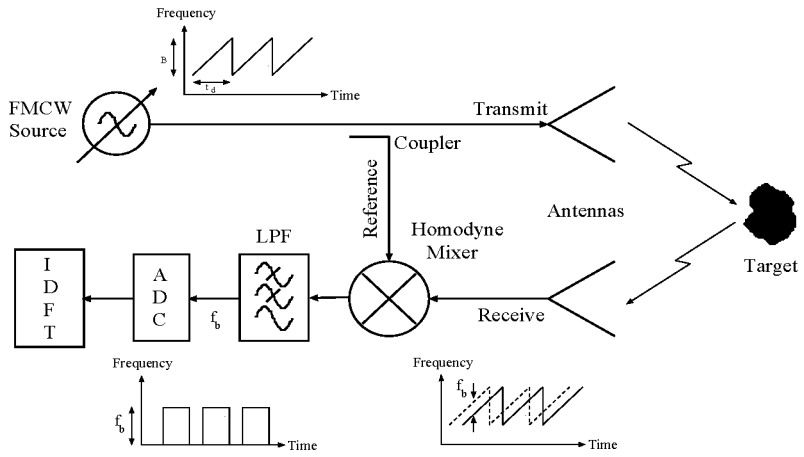

Figure 1.4: Block diagram of the FMCW radar hardware with waveform representations at each stage of the transmitter and receiver. Reflections with different travel times produce different beat frequencies which are sampled using an analog-to-digital converter (ADC), and transformed to a time profile using an IDFT.

The mixed signal is filtered to remove the additive frequencies and allow the difference or *beat* frequencies f_b to pass through to an analogue-to-digital converter (ADC). For a single targets, the beat frequency is related to the travel time t_t of the signal by equation 1.10.

$$f_b = \frac{B\ t_t}{t_d} \tag{1.10}$$

The beat frequencies of multiple reflections from multiple targets are separated using an inverse discrete Fourier transform (IDFT). The resulting sequence is a time profile of the targets with respect to their travel times. The time profile is analogous to one which would have been received using pulsed radar waveform with pulsewidths of $\tau = 1/B$.

Several advantages of the FMCW radar over the simple pulsed radar are attributed to the CW transmission and the homodyne mixing process. The FMCW radar can easily deliver several Watts of peak and mean power, because the duty cycle of the FMCW waveform is 100%. In addition, the wideband received signals are mixed down to baseband signals which have narrow bandwidths and can be sampled with inexpensive, high-precision digitisers.

There are, however, several hardware limitations with the FMCW technique [*Dennis & Gibbs*, 1974]. Conventional FMCW sources such as YIG-tuned and voltage-controlled oscillators are not perfectly linear across their frequency sweep. For short-range FMCW applications, the frequency linearity is not critical, because there is correlation between the non-linearities of the transmit and receive paths. However, longer range applications require stringent linearity specifications to maintain good range resolution [*Piper*, 1993; *Piper*, 1995]. There are also problems with phase noise on the transmitted and reference waveforms which reduce the detectability of targets.

Another critical area for an FMCW design is the high degree of isolation required between the receiver and transmitter because the FMCW transmits and receives simultaneously. For example, a major challenge is to reduce the leakage signal between the transmit and receive antennas sufficiently to enable weak reflections from targets to fall within the dynamic range of the receiver [*Saunders*, 1961]. One method of increasing the dynamic range is to subtract the leakage signal using an analog "reflected power cancellator" (RPC) in a closed-loop configuration before the homodyne mixer stage [*Stove*, 1992]. The preferred method of improving the isolation between the transmit and receive antennas is to pulse the FMCW waveform

and then switch off the receiver for a short blanking period to avoid the leakage pulse altogether. This type of waveform is known as FMICW (*frequency-modulated interrupted continuous-wave*) [*Nathanson*, 1991].

FMCW radar designs are simple and inexpensive to produce. They have been used fairly extensively in radar altimeters, short-range navigation systems [*Stove*, 1992] and non-destructive testing (NDT) which includes ground penetrating radar.

1.2.2 Pulse-Compression Radars

Pulse-compression waveforms are specially coded to allow the transmission of longer pulsewidths which allow higher mean powers, while retaining the bandwidth of a much shorter pulse [*Wehner*, 1995]. There are many types of pulse-compression radars which use frequency or phase coding techniques. This section outlines the techniques for three frequency-coded pulse compression methods; chirp, discrete-frequency coding, and stepped-frequency.

Chirp Radar

The principle of the chirp method is contained in patents dating back to the 1940's, as described by *Klauder et al.*, 1960. The chirp radar transmits a pulse train waveform where the carrier frequency of each pulse is rapidly increased (usually linearly) across the pulsewidth.

A pulsed waveform with a pulsewidth of τ (and bandwidth $B = 1/\tau$) is expanded in time (Figure 1.5) by a *surface acoustic wave* (SAW) expander. This "chirping" process increases the delay of each frequency component of the pulsed waveform in a linear fashion with frequency. For example, the lowest frequency of the SAW device is passed without delay while the highest frequency is delayed by the *chirp pulsewidth* T. The *chirp bandwidth* B is the difference between the highest and lowest frequency of the SAW device. The emerging pulses of the expander are spread in time with each pulse having a width T and a carrier frequency linearly changing across the bandwidth B. The *time-bandwidth product* of the linear chirp pulse is equal to TB, and represents the processing gain or improvement in the peak signal-to-noise ratio compared with the unprocessed pulse. Practical time-bandwidth products between 100 and 1000 are achievable with currently available SAW devices [*Kurtz*, 1993].

The radar receives the reflected chirp waveforms from targets which are then "dechirped" (Figure 1.6) using a SAW compressor. This device reverses the expansion

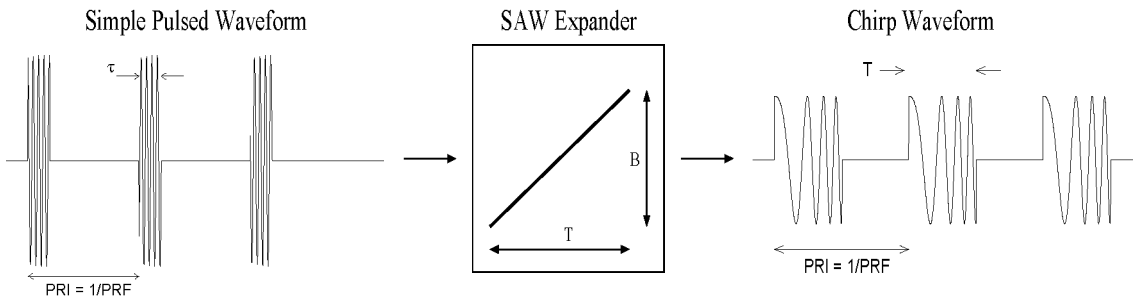

Figure 1.5: A pulsed waveform with a pulsewidth of τ seconds is expanded to produce a chirp waveform with a wider pulsewidth of T seconds and a bandwidth of B Hertz. The peak power of the chirp waveform is reduced, but the mean energy is equivalent to the simple pulsed waveform.

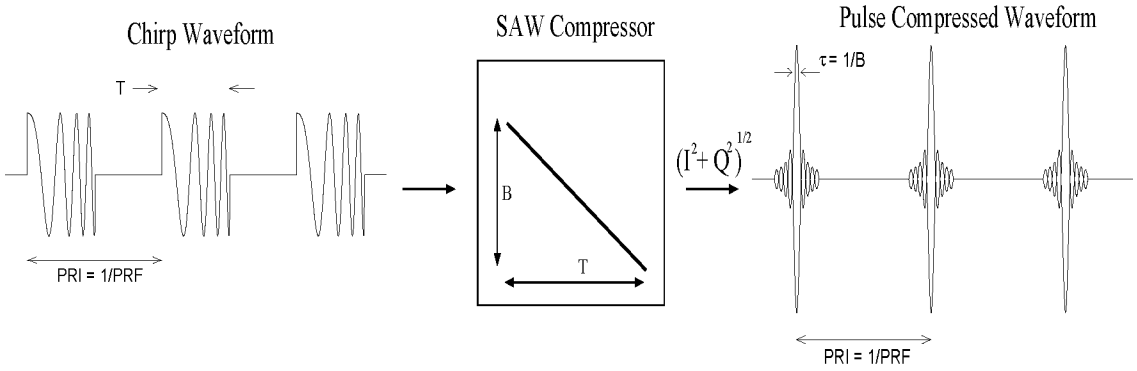

Figure 1.6: The received chirp waveforms are de-chirped by a pulse compressor and down-converted to I and Q components to produce $\mathrm{sinc}(Bt)$ envelope responses of width $\tau = 1/B$ seconds.

process by allowing high frequencies to pass and increasing the delay for the lower frequencies.

The de-chirped waveform is mixed with a reference carrier frequency of the transmitted waveform to down-convert to baseband. The baseband signal must comprise of two orthogonal components to preserve the magnitude and phase of the de-chirped waveform. These components, known as *in-phase* (I) and *quadrature* (Q) are produced using a *quadrature mixer* and sampled using a dual channel, analogue-to-digital converter. For the ideal matched-filter case, the magnitude of $I + jQ$ or $\sqrt{I^2 + Q^2}$ produces a $\mathrm{sinc}(Bt)$ envelope profile of the targets as a function of time. Each time response has a -4 dB pulsewidth equal to $1/B$.

The performance of chirp radars is generally limited by the SAW expander and compressor devices. In particular, the frequency linearity of the expander and compressor must be identical, otherwise the mainlobes of the compressed envelope response will broaden and degrade resolution due to an unmatched filter response [*Kurtz*, 1993].

Discrete Frequency-Coding Radar

Another pulse-compression technique is *discrete frequency-coding*, as described by *Darlington*, 1954 and *Ruttenberg & Chanzit*, 1968. This technique transmits a sequence of adjacent pulses of width T, each possessing a unique carrier frequency, discretely spaced by Δf Hertz across the bandwidth B (Figure 1.7). The transmitted waveform resembles a discrete frequency version of the chirp waveform, with an integer number of frequencies across the bandwidth [*Wehner*, 1995]. For this reason, an alternative name for discrete frequency-coding is *stepped-chirp* [*Nathanson*, 1991].

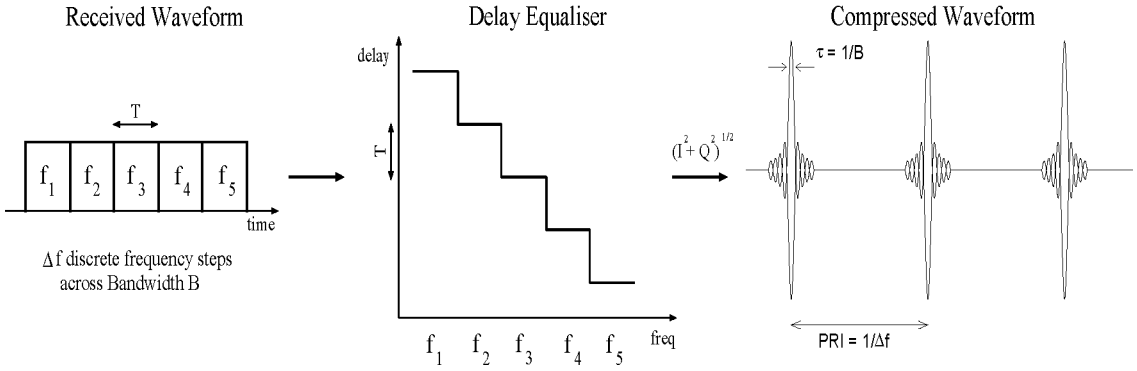

Figure 1.7: A discrete frequency-coded waveform with discrete frequency intervals of Δf Hertz and pulsewidths of T seconds is transmitted. The received waveform is compressed using a delay equaliser and down-converted to form the I and Q signals. The magnitude of $I + jQ$ produces $\text{sinc}\,(Bt)$ envelope responses of width $\tau = 1/B$ seconds, and with an effective pulse repetition frequency of Δf Hertz.

The receiver consists of a delay equaliser or tapped-delay line network which delays each received frequency-coded pulse by an amount such that all pulses sum simultaneously in time. This equalisation network is analogous to a discrete version of a de-chirp or SAW compressor device. In-phase I and quadrature Q baseband components are derived through down-conversion of the compressed signals, which are sampled with a dual-channel analogue-to-digital converter. For a perfectly matched filter, the magnitude of $I + jQ$ produces a $\text{sinc}\,(Bt)$ envelope response of

the targets with pulsewidths of $\tau = 1/B$. The effective pulse repetition frequency of the time responses are determined by the frequency interval Δf.

The advantage of discrete frequency-coding over the chirp method is that the delay equaliser in the receiver can be designed to accurately match the frequency linearity and delay of the transmitted discrete-frequency time waveforms.

Both the chirp and discrete-frequency coding techniques require sampling conversion rates of $2B$ (Nyquist's criterion, where B is the bandwidth of the transmitted signals) to adequately digitise the compressed reflected waveforms. For high-resolution radars, B is made large to improve the resolving capability. A stepped-frequency radar has a slight advantage over the discrete-frequency coding radar, which enables much slower analog-to-digital conversion rates [*Wehner*, 1995].

Stepped-frequency Radar

The *stepped-frequency* radar transmits a waveform comprising of single frequency tones or pulses stepped in frequency intervals of Δf Hertz across a bandwidth B. Each frequency step is received from the reflected targets and down-converted to I and Q narrow baseband signals using a quadrature mixer (Figure 1.8). Each I and Q signal is sampled with high precision, low frequency (audio) digitisers before the next frequency step is transmitted. Once the radar has completed the steps across the bandwidth, an IDFT is applied to the digitised I and Q frequency domain arrays to produce a *synthetic* $\mathrm{sinc}(Bt)$ envelope response [*Wehner*, 1995]. As is the case with the frequency-coding radar, the effective pulse repetition frequency of the synthesised envelope responses are determined by the frequency step interval Δf. The IDFT is the digital equivalent to the analog matched filter of the SAW compressor (chirp) and delay equaliser (discrete-frequency radar) which compress all the frequency steps to produce the *synthesised time profile* of the targets.

Stepped-frequency radars are quite often confused with FMCW or swept-FM radars because of their linear frequency transmission, down-conversion in the receiver, and the IDFT performed on the sampled data. There is, however, a technical distinction between these radar types. FMCW measures the travel time of a signal directly from the difference in frequency (*i.e.* the beat frequency, equation 1.10) between the receiver and reference paths. The IDFT is used to transform the different beat frequencies of the targets to a time profile where the travel times to the targets are well resolved according to the FMCW bandwidth. FMCW radars do not require the in-phase and quadrature components of the received signals to recon-

struct the time profile. On the other hand, the stepped-frequency radar measures the travel time of the reflected signals by measuring the phase difference between the receiver and reference paths at each frequency. In-phase and quadrature samples must be taken at each frequency step to measure the phase. An IDFT is then used as a matched-filter to properly construct the synthesised time profile.

The stepped-frequency radar can transmit each frequency step as a pulse which enables the receiver to be switched off for a short blanking period and avoid signals from close, unwanted targets (*e.g.* the antenna leakage signal). This type of waveform is called *interrupted continuous wave* ICW, and is frequently used in stepped-frequency ISAR systems [*Nathanson*, 1991; *Lane*, 1993; *Wehner*, 1995].

The stepped-frequency technique is not well suited to airborne and satellite-based radar systems, where the dwell time needed by the radar to transmit the frequency steps is limited by the platform velocity. Most airborne and satellite-based SAR systems use the chirp technique [*Curlander & McDonough*, 1991] which requires far shorter dwell times than the stepped-frequency method. Recent advances in fast switching frequency synthesisers and multiple frequency transmission techniques have enabled the use of airborne stepped-frequency SAR systems, for example, CARABAS [*Gustavsson et al.*, 1993; *Hellsten et al.*, 1994]. In general, stepped-frequency radars are more appropriate for inverse synthetic aperture radar and GPR applications [*Lane*, 1993; *Wehner*, 1995].

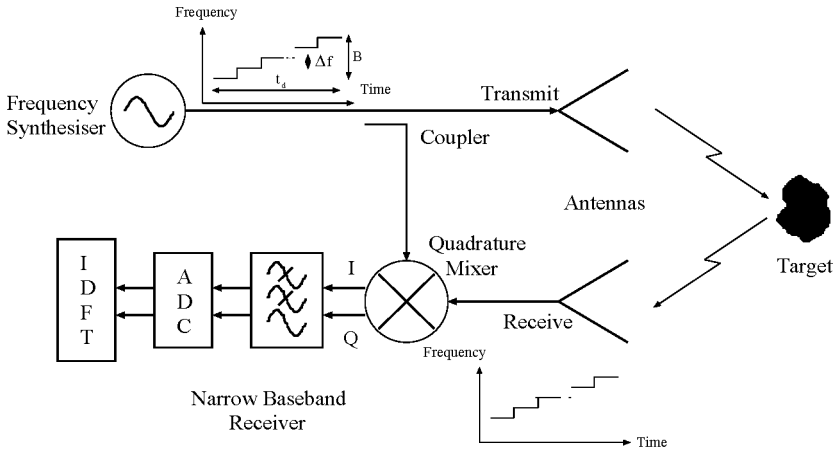

Figure 1.8: Block diagram of the stepped-frequency radar.

1.3 UWB and Impulse Radars

The term *Ultra-wideband* (UWB) describes a signal with a fractional bandwidth greater than 25%, corresponding to one-half to several cycles of the carrier frequency within the pulse envelope [*Wehner*, 1995]. The literature generally classifies UWB radars as *impulse* radars which transmit very short pulses or impulses. Technically, most FMCW and stepped-frequency GPR systems are UWB, having fractional bandwidths up to and exceeding 100%! In this thesis, UWB radars refer to systems with fractional bandwidths greater than 25%, and may include any of the other HRR techniques (*e.g.* impulse, FMCW, pulse-compression).

Impulse radars use very short-pulse transmitters (*e.g.* avalanche transistors) to generate impulse waveforms with high peak powers. Current impulse sources (for example, *Bulk Avalanche Semiconductor Switches* or BASS devices [*Oicles, Staskus & Brunemeier*, 1995]) are able to generate mega-Watts of peak power in impulses of sub-nanosecond widths. The received time signals can be coherently sampled using ultra-wideband digitisers.

The main disadvantage of the impulse radar compared with the pulse-compression techniques, is the low amount of processed mean energy for a signal for a given bandwidth. There are two reasons for this. Firstly, the deliverable mean power of an impulse transmitter is limited by the peak power (before component breakdown occurs) and low duty cycle (for a given component lifetime). State-of-the-art, optically-switched impulse generators (*e.g.* BASS devices) can deliver mega-Watts of peak power, but only several Watts of mean power [*Helava et al.*, 1993]. Secondly, the sampling of the received ultra-wideband signals can be conducted using efficient but very expensive flash-converters (several giga-samples per second conversion rates) which have a low number of bits (currently 8 bit). Alternatively, the received waveforms can be sampled with much slower and simpler higher-precision digitisers with a sliding window, but then require multiple pulses to be transmitted to reconstruct a single time profile [*Wright, Bradley & Grover*, 1994]. This sampling method reduces the efficiency of the available integration time, compared with the flash-converter method. The low mean transmitted power and the inefficient use of the integration time in the receiver limits the processed mean energy, and ultimately the maximum range performance for a given resolution.

Impulse radar systems are currently being used for airborne SAR applications [*Vickers, Gonzalez & Ficklin*, 1992] which have traditionally been chirp radars. The entire impulse waveform contains the amplitude and phase information required

for SAR processing. The in-phase I and quadrature Q components of the received impulse waveform can be computed digitally using a Hilbert transform [*McCorkle*, 1993], or by digitally transforming the sampled impulse waveform to the frequency domain, shifting it to baseband and inverse transforming [*Rutt*, 1993].

1.4 Summary

This chapter has outlined the fundamentals of radar, and the development of high-resolution and ultra-wideband radar techniques. Waveform modulation techniques (FMCW, chirp, discrete-frequency coding and step-frequency) have been described which give these radars the same bandwidth (and hence resolving power) as an impulse radar, but with higher processed mean energy.

The FMCW waveform allows wide transmission bandwidths at high mean powers, but is sensitive to non-linearities in the frequency sweep, resulting in a degradation of resolving power. Chirp, discrete frequency-coding and stepped-frequency are examples of pulse compression waveforms. Of these methods, the stepped-frequency technique achieves the highest frequency linearity in the transmitter (using frequency synthesisers) and in the receiver (digital matched-filter, IDFT). Higher transmitter mean powers than impulse radar are possible due to the transmission of longer waveforms of the stepped-frequency radar and using solid-state high power amplifiers. In addition, the stepped-frequency waveforms are easily sampled with audio frequency digitisers of high instantaneous dynamic range. These advantages combine to give the stepped-frequency radar more processed mean energy than impulse radar, and therefore superior performance in maximum range for a given resolution.

The next chapter introduces a practical application of high-resolution radar; that of *ground penetrating radar* (GPR). For GPR, the ground attenuates and scatters the penetrating radio signals far more than the free-space used in conventional radar systems. To penetrate the ground effectively, low frequency signals are required, but the underlying structures to be imaged can be relatively close together, and necessitate ultra-wide bandwidths for good resolving power. Therefore, GPR systems push the limits of high-resolution radar, with ultra-wide fractional bandwidths up to and exceeding 100%.

Chapter 2

Introduction to Ground Penetrating Radars

This chapter introduces the subject of *Ground Penetrating Radar* (GPR), and reviews its historical development (Section 2.1). Of particular importance to this thesis is the use of GPR in coal mining, which is discussed in Section 2.2.

2.1 Historical Development of GPR

The concept of using radio waves to penetrate the ground and detect buried objects was discovered in the early stages of radar research at the turn of the twentieth century. Leimbach and Löwy obtained a German patent (Nr. 237944) in 1910 describing a method of burying dipole antennas in an array of vertical boreholes and measuring the amplitude of CW signals transmitted between adjacent pairs of antennas. (A description is contained in the review articles by *Daniels, Gunton & Scott*, 1988 and *Thierbach*, 1994.) The patent claimed that changes in the material conductivities of the internal ground structure between the antennas could be imaged. A further German patent was awarded to the same inventors in 1911 (Nr. 246836) describing the use of a radar system with surface-coupled antennas to detect subsurface interfaces. However, the travel times (or distances) to the subsurface interfaces could not be measured with the techniques outlined in the patents, since the transmitted and received waveforms were continuous wave (CW). A 1926 German patent by Hülsenbeck *et al.*, (Nr. 489434) was the first to propose the use of a pulsed radar to detect and measure the depths to buried dielectric interfaces.

Cook, 1960 of the Southwest Research Institute (SwRI) proposed a VHF pulsed radar (125 MHz monocycle) for measuring ice thickness from an airplane. Although the proposed radar system was only tested in the laboratory, Cook's preliminary results indicated that interfaces separated by 60 centimetres could be resolved. In 1967, SwRI developed the first operational, man-portable GPR system to detect shallow man-made tunnels in soil [*SwRI*, 1978].

Other applications were proposed for GPR in the 1970's and 1980's. For example, there have been considerable efforts made in applying GPR to measure the roof thickness of coal in underground mines [*Cook*, 1975; *Ellerbruch & Belsher*, 1978; *Coon, Fowler & Schafers*, 1980; *Roe & Wittmann*, 1982; *Pittman et al.*, 1984; *Yelf & Turner*, 1990] (see Section 2.2), to detect pipes and cables [*Caldecott et al.*, 1988], and some military work including tunnel detection and non-metallic mine detection [*Iizuka & Freundorfer*, 1983]. In 1988, *Daniels, Gunton & Scott*, 1988 published their highly cited tutorial paper entitled "Introduction to subsurface radar", which comprehensively reviewed the history, applications and techniques of GPR at that time. This review article stimulated further developments and applications of GPR, which has now made GPR a well-established technology in many aspects of geotechnics and geophysics. In the early 1990's, GPR was used extensively for the detection of unexploded ordnance [*PRC*, 1995], environmental applications [*Peters, Daniels & Young*, 1994] including the detection of hazardous waste [*Lord & Koerner*, 1990], and non-destructive testing including the measurement of condition and thickness of pavements and roads [*Parry & Davis*, 1992; *Davis et al.*, 1994].

Table 2.1 illustrates the significant amount of interest that has been generated through attendances and participation in a series of bi-annual international meetings on GPR. In addition, there have been major US government workshops which have attracted over a hundred participants interested in the application of GPR to environmental problems, tunnel detection and unexploded ordnance (UXO) detection [*Daniels et al.*, 1993]. GPR topics are included in most of the major international meetings of the Society of Exploration Geophysics (*e.g.* SEG (US), EAEG (European), CSEG (Canadian) and ASEG (Australian)), Symposiums of Applied Geophysics to Engineering and Environmental Problems (SAGEEP), and relevant SPIE Proceedings series (*e.g.* Volumes 1631, 1875, 1942, 2217, 2235 and 2275).

Table 2.1: Attendances at international GPR conferences indicates the rapidly increasing awareness and use of GPR on an international scale

Meeting	**Papers**	**Attendances**
First Int. Symp. on Geotechnical Applications of GPR Tifton, Georgia, USA October 1986 (No proceedings)		26
Second Int. Symp. on Geotechnical Applications of GPR Gainesville, Florida, USA February 1988 (*Collins*, 1988)	34	90
Third Int. Conf. on GPR Lakewood, Colorado, USA May 1990 (*Lucius, Olhoeft & Duke*, 1990)	83	172
Fourth Int. Conf. on GPR Rovaniemi, Finland June 1992 (*Hänninen & Autio*, 1992)	45	196
Fifth Int. Conf. on GPR Kitchener, Ontario, Canada June 1994 (*Redman et al.*, 1994)	97	275
Sixth Int. Conf. on GPR Sendai, Japan September/October, 1996	?	?

2.1.1 Impulse GPR

Impulse radars have been used extensively since the earliest development stages of GPR. The impulse waveform generated by an impulse radar is similar to the simple pulsed waveform of Figure 1.1. Current impulse transmitters use avalanche transistors to switch hundreds or thousands of volts in short pulsewidths between 0.6 - 10 nanoseconds. The peak power of the impulses can typically be of the order of tens of kiloWatts. However, the mean power of transmission of GPR transmitters is generally a fraction of a Watt, due to the poor duty cycle performance of the impulse radar. The generated impulse is radiated into the ground using antennas designed for a particular bandwidth and centre frequency. GPR bow-tie antennas are usually designed with fractional bandwidths of 100% (*i.e.* the bandwidth of the antenna in Hertz is equal to the centre frequency in Hertz) [*Annan & Cosway*, 1994]. Other types of antenna such as horns and spirals have decade (or 163% fractional) bandwidths. Non-dispersive antennas (such as bowties and horns) are preferred for impulse GPR as the antennas do not significantly broaden the pulse upon transmission and reception. Once the impulse is transmitted through the antenna, the frequency response of the antenna causes the impulse to resonate at the antenna centre frequency, with a pulsewidth equal to the inverse of the antenna bandwidth. For improved isolation, most GPR systems use separate transmit and receive antennas (bistatic mode), rather than using a single transmit and receive antenna (monostatic mode) with a transmit-receive (T-R) switch.

The receiver circuitry of typical impulse GPR systems consist of a digitiser (analog-to-digital converter) which samples the reflected radio frequency signals in a "strobing" or "sliding window" mode. The ADC samples one point of the received waveform for each transmitted pulse. The sampling window is strobed by the transmitter to slide along adjacent points of the received waveform until the entire received signal is sampled. It is necessary to transmit the equivalent number of pulses as the number of samples per waveform to fully reconstruct the reflected signal.

A system parameter which is widely used to indicate GPR performance in penetration is *System Performance*, SP (the ratio of the mean transmitted power and the minimum detectable signal). For typical impulse radars, SP may range between 100-130 dB for a single recorded profile [*Wright, Bradley & Grover*, 1994].

The system performance SP of typical impulse GPR systems can be improved using more advanced designs and techniques. For example:

- High power impulse switches such as the *Bulk Avalanche Semiconductor Switch* (BASS) devices are being used for UWB military radar applications. These impulse switches can generate highly coherent pulses with pulsewidths down to 600 picoseconds ($\approx$ 50 picoseconds rise and fall times) and several Watts of mean power [*Helava et al.*, 1993; *Oicles, Staskus & Brunemeier*, 1995]. A laboratory-based UWB radar system has been built incorporating the BASS technology to collect data for FPR (*Foliage Penetrating Radar*) and GPR studies [*McCorkle*, 1993; *Ressler et al.*, 1995; *Ressler & McCorkle*, 1995]. More work is required to extend the lifetime of the BASS device (typical lifetime is one million pulses) before it can be applied in a commercially-viable system.

- "Flash" converters which digitise the entire RF waveform in one transmitter pulse interval are used to improve the sampling efficiency. The US Geological Survey has designed a *Digital Acquisition System* (DAS) for an experimental impulse GPR. This system directly samples the received impulse waveforms at 2 giga-samples per second with 8 bit resolution [*Wright, Bradley & Hodge*, 1989]. In the same time that the strobing ADC technique can reconstruct the reflected waveform, the DAS can integrate or "stack" the equivalent number of transmitted pulses using a high-speed *Digital Stacking Unit* (DSU). This effectively increases the processed mean energy of the GPR.

- The effective dynamic range of the DAS can be increased beyond the 8 bits of the flash converters by using a *Sensitivity Time Control* (STC) [*Wright et al.*, 1990]. This is a time-varying gain amplifier which is placed before the DSU to increase the gain in the receiver as a function of time. The gain of the amplifier is low when the signals from close reflections are being received, but is rapidly increased in time to receive the reflections from deeper targets. An example of an STC circuit used with an impulse GPR system is reported by *Wright et al.*, 1990, and can increase the gain of the receiver by 60 dB in a period of $2\mu s$. This task becomes increasingly more difficult over shorter periods. For example, a faster STC can increase the gain of the receiver by 30 dB in 10 ns [*Wright, Bradley & Grover*, 1994].

2.1.2 FMCW GPR

Frequency-Modulated Continuous Wave (FMCW) radars have been used in GPR applications, although not as widely as impulse radars. One of the first FMCW GPR systems was built in 1974 by the National Bureau of Standards for the US Department of Energy [*Ellerbruch & Adams*, 1974]. Using a 1-2 GHz FMCW radar design, the roof thickness of a layer of coal (up to 55 centimetres) was measured in three US underground coal mines [*Ellerbruch & Belsher*, 1978]. Further experimental work continued with this system until 1982, when it was decided that further efforts toward improving this FMCW GPR system were not worthwhile [*Roe & Wittmann*, 1982]. This decision was based on the fact that an alternative technique for determining the thickness of coal by measuring the intensity of the natural gamma background radiation from shales was acceptable for the application.

Around the same time of Ellerbruch's work, the Southwest Research Institute (SwRI) developed a prototype FMCW system operating between 2 and 6 GHz [*SwRI*, 1978] to measure the residual coal thickness in the roof and rib supports of highwall auger boreholes. A modified version of this system (30 MHz to 1 GHz frequency range) was used in 1986 to inspect brick and concrete subway tunnels for structural defects [*Hogan*, 1986].

Other developments in FMCW GPR were undertaken by the Queen Mary College of the University of London during the 1980's for detecting hidden objects in the ground and within construction walls [*Carr, Cuthbert & Olver*, 1981]. Three systems were built with frequency ranges of 1-2 GHz, 2-4 GHz and 9-11 GHz [*Botros & Olver*, 1986; *Olver & Cuthbert*, 1988]. The research focused heavily on the signal processing of the reflected signals. For example, digital filtering and non-linear optimisation techniques were applied to FMCW GPR data to improve the detection of buried objects amid other clutter [*Carr, Cuthbert & Olver*, 1981]. In addition, non-Fourier techniques based on autocorrelation and covariance methods were tested on the FMCW data to reduce the sidelobe levels and sharpen the responses of buried objects [*Liau, Carr & Cuthbert*, 1986]. There were also attempts to provide a means of distinguishing between different buried objects using template matching of target signatures [*Carr, Cuthbert & Olver*, 1981; *Farmer et al.*, 1984].

The ability of the FMCW radar to sweep across wide frequency bands and obtain high resolution is attractive for GPR applications. A major limitation of the FMCW radar is due to the CW transmission which reduces the dynamic range of the system. The FMCW radar is receiving signals at the same time as it is transmitting, and the

range sidelobes of the leakage signal between the antennas can "mask" the smaller signals reflected from deeper targets. Because of the CW nature of the waveform, it is not possible to use sensitivity time control which is often used in impulse radars. A method which actively cancels the leakage signal in the FMCW receiver [*Stove*, 1992] has been used in airborne altimeter systems, but the cancellation method is highly susceptible to vibrations in the leakage path length, and microphonisms in the receiver mixers [*Saunders*, 1961]. This method has also been used with an 8-12 GHz FMCW radar designed for probing dielectric materials to detect internal structural defects [*Tirkel, Osborne & Osborne*, 1990]. However, this cancellation technique does not offer a practical solution for GPR applications, where the leakage signal can change dramatically in amplitude and phase with small undulations in surface roughness. *Frequency-Modulated Interrupted Continuous Wave* (FMICW) techniques (refer back to Section 1.2.1) do offer a solution to the limited dynamic range of the FMCW radar. To the author's knowledge, there have been no reports of an FMICW system used in a GPR application.

2.1.3 Pulse-Compression GPR

There are many examples in the literature of the stepped-frequency technique being applied to GPR. Chapter 4 contains a comprehensive literature review of SFGPR developments and presents a novel description of the stepped-frequency waveform in relation to waveforms generated by impulse radars.

In addition to the stepped-frequency method, there have been other pulse compression techniques applied to GPR. For example, impulse waveforms transmitted through dispersive log-periodic or logarithmic spiral antennas are expanded in time to resemble a chirp waveform. At the receiver, the waveforms can be compressed in time using analog or digital matched filtering [*Chaudhuri & Chow*, 1981]. The advantage of this method is the extremely broad fractional bandwidth (decade) of the spiral antennas, which allows very high resolving capability. These antennas also possess a circular polarisation with the ability to detect long, thin objects (such as pipes and cables) independent of orientation [*Iwasaki, Freundorfer & Iizuka*, 1994].

Phase shift keying (PSK) pulse compression methods have been used to determine the ice thickness of glaciers [*Lukashenko et al.*, 1979; *Nicollin et al.*, 1992]. This technique involves the transmission of a carrier frequency which is phase modulated with coded sequences. A synchronous receiver determines the I and Q baseband signals from the reflected waveforms in an almost identical fashion to the discrete

frequency-coding radar described in Section 1.2.2. A matched filter correlates the I and Q signals with delayed versions of the transmitted signal to produce a time profile of targets.

Yet another type of pulse compression used for GPR has been *noise modulation* [*Walton*, 1993b]. In this system, ultra-wideband noise is transmitted and a matched receiver is used as a correlator to produce a time profile of the targets.

2.1.4 SAR Systems

Side-looking *synthetic aperture radar* (SAR) systems with antennas that are elevated off the ground have been designed for *foliage penetration radar* (FPR) and GPR applications (in particular, to detect buried ordnance [*Sargis et al.*, 1994]). For example :

- 40 MHz to 1 GHz impulse polarimetric SAR [*McCorkle*, 1993]
- 215 to 900 MHz chirp polarimetric SAR [*Goodman, Tummala & Carrara*, 1995].
- 400 MHz to 1300 MHz stepped-frequency polarimetric SAR [*Sheen et al.*, 1993b]
- 0.25 to 1 GHz stepped-frequency polarimetric SAR [*Blejer, Frost & Scarborough*, 1994]

The systems itemized above are fully polarimetric and can measure the full vector of the scattered electromagnetic field in co- and cross-polarisation components, to discriminate between planar and long thin objects (*e.g.* tree trunks for FPR) [*McCorkle*, 1993]. Other polarimetric GPR systems have been tested using impulse [*Arai & Suzuki*, 1993] and stepped-frequency [*Langman & Inggs*, 1994] techniques. A polarimetric borehole SFGPR system has also been reported by *Sato, Takashi & Hiroaki*, 1994, which is capable of discriminating between different geological structures.

Synthetic aperture radars have also been developed for a wide range of airborne and spaceborne applications [*Giglio, Ralston & Braunstein*, 1993]. The first spaceborne SAR system (L-band) was deployed on SEASAT and detected igneous dykes up to two metres depth below the Mojave desert [*Blom, Crippen & Elachi*, 1984].

Other results have been recorded using the L-band SAR shuttle imaging radars SIR-A [*McCauley et al.*, 1982; *Elachi, Roth & Schaber*, 1984; *Schaber et al.*, 1986] and SIR-B [*Farr et al.*, 1986], which have detected dry river beds under the Egyptian and Saudi sand [*McHugh et al.*, 1988]. Other cases of shallow penetration are expected with the latest shuttle SAR (SIR-C/X-SAR) [*Stuhr, Jordan & Werner*, 1995].

Several airborne radar systems with ground and foliage penetrating capabilities were trialed at the Yuma test site, Arizona USA to detect buried ordnance [*Mirkin et al.*, 1994; *Mirkin et al.*, 1995; *Binder et al.*, 1995]:

- CARABAS is an airborne 20-90 MHz stepped-frequency SAR designed by the Swedish National Defense Research Establishment to penetrate foliage and the ground [*Gustavsson et al.*, 1993; *Hellsten et al.*, 1994].
- The Stanford Research Institute's (SRI) FOLPEN II sensor is an airborne impulse SAR with selectable frequency bands of 100-300 MHz, 200-400 MHz or 300-500 MHz [*Rutt*, 1993; *Sargis et al.*, 1994; *Buseck, Kositsky & Vickers*, 1995].
- The EMS-20 radar designed by Airborne Environmental Systems (AES) is helicopter-based chirp radar with a bandwidth of 250-750 MHz [*Cameron et al.*, 1993; *Koppenjan & Martinez*, 1994].

It was concluded from the Yuma results that the systems with SAR capability (*i.e.* CARABAS and FOLPEN II) demonstrate superior performance in detecting buried objects and bunkers from the air in comparison with systems with no SAR capability (*i.e.* EMS-20) [*Mirkin et al.*, 1994].

2.2 GPR in Coal Mining Applications

Coal has a relatively low conductivity which makes it a suitable material for penetration of radar signals. In addition, it has a strong dielectric contrast with its host rock (*e.g.* shale) which results in a strong reflection at the interface. However, layered coal is strongly anisotropic which cause affect the propagation of signals at different polarisation [*Balanis et al.*, 1980].

Cook, 1970 measured the RF electrical properties of coal, and in 1975, first proposed the use of ground penetrating radar for coal applications [*Cook*, 1975]. Since then, many GPR systems have been tested in different coal mine situations.

Between 1977 and 1978, a series of impulse GPR tests were conducted to determine the potential reflection depths in coal [*Coon, Fowler & Schafers*, 1980]. It was reported that radar signals propagated across a 100 foot (30 metre) coal pillar, while reflections from air voids were detectable at 50 feet (15 metres). Other impulse GPR tests were conducted by *Fowler*, 1981. During 1979 to 1981, a stepped-frequency GPR system with a similar frequency band to the impulse GPR system (20-160 MHz) was built and reportedly transmitted radar signals through a 200 foot (60 metre) coal pillar [*Fowler, Hale & Houck*, 1981; *Pittman et al.*, 1984] (*i.e.* twice the distance as the impulse GPR tests by *Coon, Fowler & Schafers*, 1980 and *Fowler*, 1981). These tests and others by *Yelf*, 1995 had demonstrated the potential for GPR in coal mining applications.

For many of these applications, it is desirable for a GPR system to continually measure the coal thicknesses of thin coal seams (*i.e.* less than one metre thick). For example in underground coal mines, it is preferable to leave several centimetres of coal in the roof during mining to ensure better roof stability. The Southwest Research Institute (SwRI) built a 2-6 GHz FMCW GPR system capable of determining coal thicknesses up to 1.25 inches, with a resolution better than a quarter of an inch [*SwRI*, 1978]. A separate FMCW system was proposed around the same time by the US National Bureau of Standards [*Ellerbruch & Adams*, 1974], and a system operating between 1-2 GHz was built and tested in an experimental underground coal mine [*Ellerbruch & Belsher*, 1978]. Following on from this work, another FMCW system (1-4 GHz) was built to accurately measure the thickness of coal layers in centimetres (which also required the on-line measurement of the velocity of propagating signals in the material), but failed to deliver the required accuracy to warrant continued development [*Roe & Wittmann*, 1982].

High-resolution GPR tests in coal were obtained in the UK using a 1 GHz centre frequency impulse radar [*Daniels*, 1980]. A separate impulse GPR system was developed by the US Bureau of Mines (Tuscaloosa Research Centre) to recognise features which may cause instability in the coal roof structure [*Church, Webb & Boyle*, 1985]. Another system built by the US Bureau of Mines (Pittsburgh Research Centre) used stepped-frequency radar technology to accurately measuring coal layer thicknesses *in situ* up to six inches [*Chufo*, 1995].

Previous work in Australia has reported that the measurement of coal seam thickness using GPR may improve production in open-cut and underground coal mines [*Turner, Yelf & Hatherly*, 1989; *Yelf & Turner*, 1990; *Yelf et al.*, 1990; *Yelf*, 1995], as well as possibilities in other mining environments [*Baker & Cull*, 1990].

The primary application[1] for the stepped-frequency GPR system described in this thesis is the high-resolution mapping of thin coal seam structures in open-cut coal mines [*Noon & Longstaff*, 1992]. The design of a stepped-frequency GPR prototype and results from field trials at two open-cut coal mines are reported later in Chapters 5 through to 7.

[1]This application was initially chosen as the primary application for the GIRD project (see Preface).

Chapter 3

Performance Characteristics of GPR

3.1 Introduction

The operating performance of GPR is expressed in terms of two interdependent characteristics : *maximum penetration depth* and *depth resolution.* For GPR, maximum penetration depth relates to the maximum depth at which a buried target can be detected, and depth resolution (or *resolving power*) is the minimum separation in depth between two buried targets that can be detected. The main emphasis of this chapter is to evaluate these performance characteristics for a wide variety of materials.

In developing this idea, the *constant* Q (CQ) model for ground materials (which has been adopted from seismics and verified externally to this thesis and in other work referenced later) is described, whereby the attenuation of radar signals by ground materials has a linear dependence upon frequency, while at the same time the propagation velocities are constant. The constant Q model allows the development of expressions for maximum penetration depth and resolving power in wavelengths. It becomes evident that for a given Q value, the maximum penetration depth and resolution can be described as a fixed number of wavelengths. These expressions enable the simple evaluation of GPR performances for a variety of ground materials, and across a broad spectrum of frequencies. They can be used as a design tool for determining the bandwidth and centre frequency of the GPR waveform to achieve a required operating performance.

The ideas described in this chapter were presented at a national conference [*Noon & Longstaff*, 1995]. To the author's knowledge, there have been no other reports in the literature which describe this broad spectrum characterisation of GPR penetration and resolution performance.

3.2 Frequency Dependence of GPR Performance

The maximum range performance of any radar is well defined by the radar equation (Section 1.1). In addition, the range resolution of the radar waveforms is characterised by the ability to separately detect two or more sources of reflection (also Section 1.1). Most ground penetrating radars are high-resolution radars, with fractional bandwidths up to and exceeding 100% [*Annan & Cosway*, 1994]. For GPR, the performance is then based on two characteristics: *penetration* and *resolution* [*Davis & Annan*, 1989].

The main purpose of this section is to quantify the penetration and resolution performance of GPR, and describe the dependence of these characteristics on the operating frequency of the radar. The majority of the GPR systems considered in this thesis operate between 10 MHz and 2 GHz (defined here as the *GPR spectrum*). To quantify the penetration and resolution performance of GPR, it is first necessary to understand the relationships between electromagnetic wave propagation and ground material properties for frequencies within the GPR spectrum.

3.2.1 Relationships between Electromagnetic Propagation and Ground Material Properties

Propagation

The propagation of electromagnetic radiation (described by *Maxwell's equations*) through a material is strongly influenced by the attenuation and propagation velocity properties of the material. The *Helmholtz wave equation* can be derived from Maxwell's equations for plane waves propagating through a *general lossy medium* (characterised by *Ulaby, Moore & Fung*, 1981 as neither conducting nor only slightly lossy). A solution to the Helmholtz wave equation is the electric field $E(z)$, described by equation 3.1, of the plane wave propagating in the z direction. (Refer to Chapter

2 of *Ulaby, Moore & Fung*, 1981 for the complete derivation of equation 3.1 from Maxwell's equations).

$$E(z) = E_0 e^{-\gamma z} = E_0\, e^{-\alpha z}\, e^{-j\beta z} \tag{3.1}$$

E_0 is an electric field constant, e is the base exponential and γ is the *propagation constant*, which is made up of a real and an imaginary component : *attenuation constant* α (equation 3.2) and *phase constant* β (equation 3.3).

$$\alpha = \omega \left[\frac{\mu\epsilon}{2} \sqrt{1 + \tan^2 \delta} - 1 \right]^{1/2} \tag{3.2}$$

$$\beta = \omega \left[\frac{\mu\epsilon}{2} \sqrt{1 + \tan^2 \delta} + 1 \right]^{1/2} \tag{3.3}$$

For these equations, ω is the *radian frequency* ($\omega = 2\pi f$, where f is the electromagnetic frequency), μ is the *magnetic permeability* and ϵ the *electric permittivity* of the medium. The $\tan\delta$ term is the loss tangent defined in equation 3.4.

$$\tan\delta = \frac{\epsilon''}{\epsilon'} = \frac{\sigma}{\omega\epsilon} \tag{3.4}$$

Here, ϵ' is the real component and ϵ'' is the imaginary component of the permittivity ϵ, and σ is the *conductivity* of the medium. The attenuation constant α of equation 3.2 has the dimensions of Nepers per metre. Attenuation of the ground material is usually expressed in decibels per metre (dB/m). The conversion of α from Np/m to dB/m is obtained using equation 3.5.

$$\alpha\,[dB/m] = 20 \log_{10} e^{\alpha} = 20\alpha \log_{10} e = 8.686\alpha\,[Np/m] \tag{3.5}$$

The phase constant β (radians per metre) can be converted to *phase velocity* v using equation 3.6.

$$v = \lambda\, f = \frac{\omega}{\beta} = \left[\frac{\mu\epsilon}{2} \sqrt{1 + \tan^2 \delta} + 1 \right]^{-1/2} \tag{3.6}$$

Approximations of the constants α (in equation 3.7), β (in 3.8) and v (in 3.9) are derived for a low loss (where $\tan^2\delta << 1$), non-magnetic ($\mu = \mu_0$) medium. The low-loss, non-magnetic assumption is valid for a wide range of ground materials encountered in GPR applications [*Church, Webb & Salsman*, 1988].

$$\alpha \approx \frac{1}{2}\omega\sqrt{\mu\epsilon}\tan\delta = \frac{1}{2}\omega\sqrt{\mu\epsilon}\frac{\sigma}{\omega\epsilon} = \frac{1}{2}\sqrt{\frac{\mu_0}{\epsilon_0}}\frac{\sigma}{\sqrt{\epsilon_r}} = \frac{188.5\sigma}{\sqrt{\epsilon_r}} \tag{3.7}$$

$$\beta \approx \omega\sqrt{\mu\epsilon} \tag{3.8}$$

$$v \approx \frac{1}{\sqrt{\mu\epsilon}} = \frac{c}{\sqrt{\epsilon_r}} \tag{3.9}$$

For the above expressions, ϵ_r is the *relative electromagnetic permittivity* ($\epsilon_r = \epsilon/\epsilon_0$), ϵ_0 is the *electromagnetic permittivity in free space* (≈ 8.85 x 10^{-12} Fm^{-1}), μ_0 is the *electromagnetic permeability in free space* ($\approx 4\pi$ x 10^{-7} Hm^{-1}), and c is the *velocity of electromagnetic waves in free space* (≈ 3 x $10^8 ms^{-1}$).

The velocity and attenuation of the electromagnetic waves in a material are determined by first measuring the complex permittivity (*i.e.* ϵ' and ϵ'') of the ground material. The loss tangent $\tan\delta$ is then calculated using equation 3.4, which allows the attenuation α and velocity v terms to be determined using equations 3.2 and 3.6 respectively.

As an example, Figure 3.1 displays the relative permittivity ϵ_r, loss tangent $\tan\delta$, propagation velocity v and attenuation α of a coal sample measured using a coaxial probe[1] across the 1 to 2 GHz frequency range. The relative permittivity versus frequency graph indicates a constant permittivity ϵ_r, resulting in a constant propagation velocity v across the frequency range. In addition, the linear relationship in the attenuation versus frequency graph is because the loss tangent $\tan\delta$ is constant across all frequencies. The significance of these properties are explained later in Section 3.3.1.

[1]These measurements were taken by Stephen Nothdurft at The University of Queensland using a Hewlett-Packard HP-85070 Coaxial Probe.

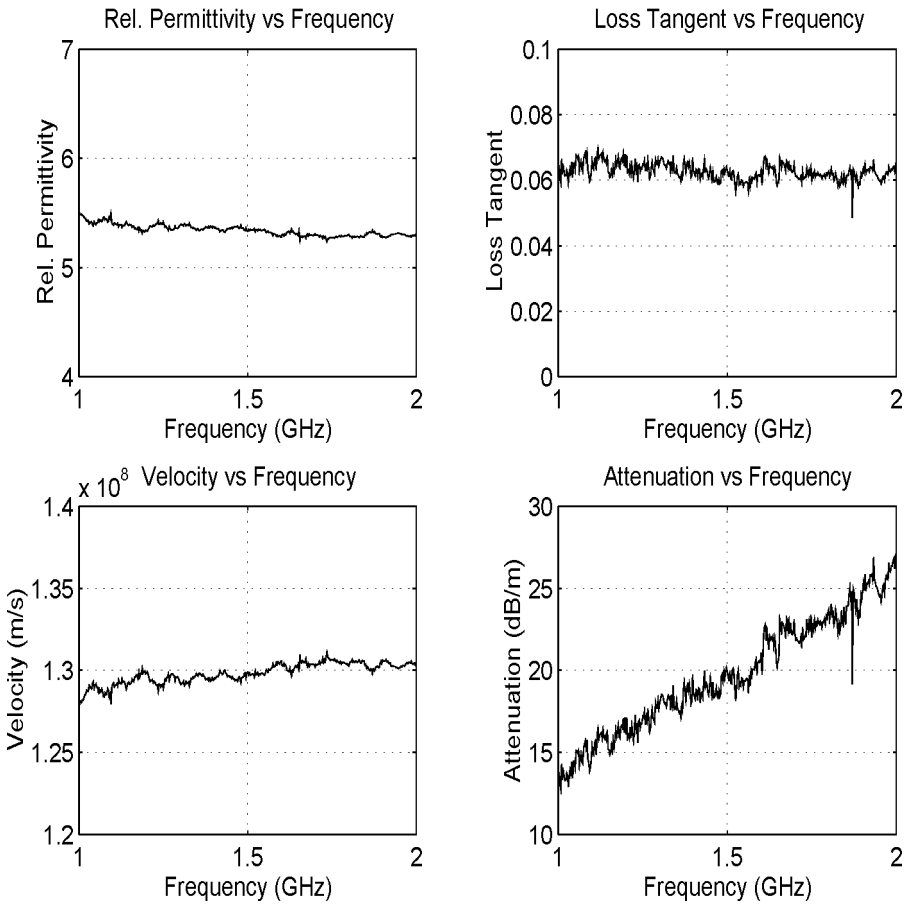

Figure 3.1: Dielectric measurements of a coal sample obtained with a coaxial probe

Reflection and RCS

The reflection and backscattering of electromagnetic energy from a target are described by its *radar cross section* (RCS) [*Skolnik*, 1990].

Part of the RCS parameter is associated with the reflection loss at the target's interface. A portion of the signal energy is reflected from a dielectric interface where there is a change in the permittivity ϵ between the target and its surroundings (*e.g.* host rock). For the case where the angle of incidence of the plane waves is perpendicular to the dielectric interface (with relative permittivities of ϵ_{r1} and ϵ_{r2} respectively), the *Fresnel Reflection Coefficient* Γ can be calculated using equation 3.10 [*Ulaby, Moore & Fung*, 1981].

$$\Gamma = \frac{\eta_2 - \eta_1}{\eta_2 + \eta_1} = \frac{\frac{1}{\sqrt{\epsilon_{r2}}} - \frac{1}{\sqrt{\epsilon_{r1}}}}{\frac{1}{\sqrt{\epsilon_{r2}}} + \frac{1}{\sqrt{\epsilon_{r1}}}} = \frac{\sqrt{\epsilon_{r1}} - \sqrt{\epsilon_{r2}}}{\sqrt{\epsilon_{r1}} + \sqrt{\epsilon_{r2}}} = |\Gamma|\, e^{j\phi} \tag{3.10}$$

In the above equation, $\eta_1 = \sqrt{\frac{\mu_1}{\epsilon_1}}$ and $\eta_2 = \sqrt{\frac{\mu_2}{\epsilon_2}}$ are the *intrinsic impedances* of media 1 and 2 (where $\mu_1 = \mu_2 = \mu_0$ for non-magnetic materials).

The reflection coefficient Γ is a vector quantity containing a *magnitude of reflection* $|\Gamma|$ and a *phase change upon reflection* ϕ. The *reflection power loss* at the interface is equal to $|\Gamma|^2$. For low loss materials, the *polarity* of the reflected signal in comparison with the incident signal is determined by the sign of the reflection coefficient Γ (*i.e.* $\phi = 0 \Rightarrow$ equal polarity; $\phi = \pi \Rightarrow$ opposite polarity). For example, interfaces between different materials with $\epsilon_{r1} > \epsilon_{r2}$ will reflect a signal with the same polarity as the incident signal. Alternatively, $\epsilon_{r1} < \epsilon_{r2}$ implies an opposite polarity of the reflected signal. For higher loss materials where the imaginary part of the dielectric constant is comparable to the real part (*i.e.* $\tan^2 \delta \sim 1$), the phase change upon reflection can be between 0 and 2π [*Turner*, 1993].

The *transmission coefficient* Υ describing the electromagnetic waves passing through a dielectric interface between two materials is expressed in equation 3.11 [*Ulaby, Moore & Fung*, 1981]. The *transmission power loss* is given by $|\Upsilon|^2$ and the *phase change upon transmission* is Φ.

$$\Upsilon = 1 + \Gamma = \frac{2\sqrt{\epsilon_{r1}}}{\sqrt{\epsilon_{r1}} + \sqrt{\epsilon_{r2}}} = |\Upsilon| \, e^{j\Phi} \tag{3.11}$$

Shape also has a bearing on the target's RCS (denoted σ_T). Buried targets can be considered as either spherical in shape (*e.g.* buried object) or planar interfaces (*e.g.* stratigraphic boundaries) [*Annan & Davis*, 1977]. A planar interface can be either smooth (which produces a specular scattering pattern) or rough (which produces a Lambertian scattering pattern). The radar cross sections σ_T corresponding to these three type of targets are defined below :

Spherical Target : The radar cross section of a spherical target or sphere is described by the plot in Figure 3.2 [*Stratton*, 1941]. Targets whose normalised circumference with respect to wavelength (*i.e.* $2\pi a/\lambda$) is larger than unity has a RCS asymptotically approaching the geometric optics approximation of $|\Gamma|^2 \pi a^2$. For a "candidate" sphere whose circumference is approximately equal to one wavelength (*i.e.* $2\pi a \approx \lambda$), the RCS can be approximated as $|\Gamma|^2 \lambda^2 / 4\pi$.

Rough Planar Target : A rough planar target is defined when the standard deviation of a plane's surface heights (denoted σ_s) relative to the wavelength is larger than $0.5/\pi$ [*Khanifar et al.*, 1994]. The radar cross for this target can be taken as the area of the "first Fresnel zone" on the surface [*Cook*, 1975], which

is equal to $|\Gamma|^2\pi\lambda R/2$ where R is the range or depth to the target [*Annan & Davis*, 1977].

Smooth Planar Target : A smooth planar target is defined when the standard deviation of a plane's surface height σ_s relative to the wavelength is less than $0.1/\pi$ [*Khanifar et al.*, 1994]. The radar cross section of this target can be derived using "image theory" (*i.e.* by assuming the receiver is placed symmetrically on the other side of the interface and taking into account the reflection coefficient). The result is an RCS equal to $|\Gamma|^2\pi R^2$ [*Annan & Davis*, 1977].

The RCS parameters can also take into account the polarisation losses for cylindrical and rough surfaces. Table 3.1 summarises the interactions which occur between electromagnetic propagation terms and ground material properties.

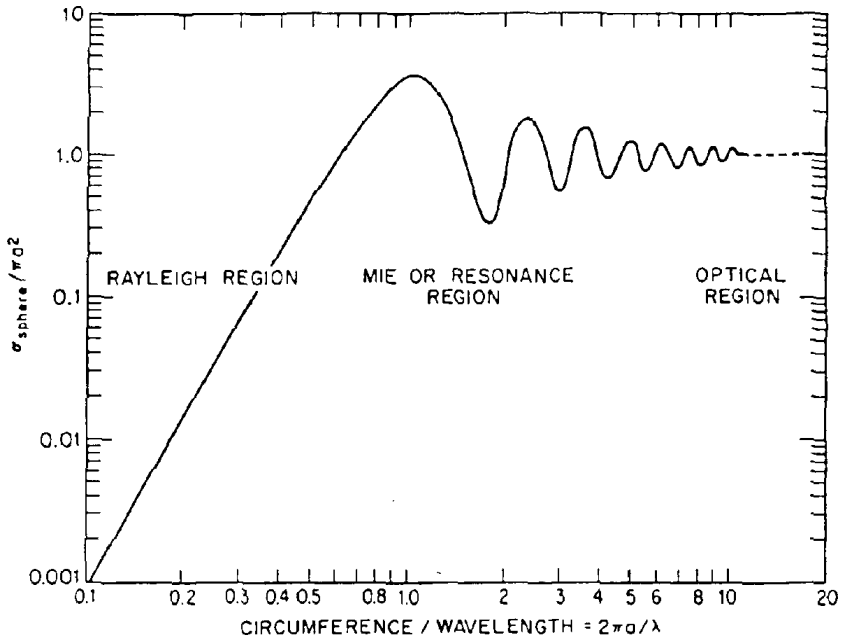

Figure 3.2: RCS of a metal spherical target as a function of electrical size (taken from *Stratton*, 1941). A "candidate" sphere is when the circumference is approximately equal to a wavelength (*i.e.* $2\pi a \approx \lambda$), and the RCS is approximated by $|\Gamma|^2\lambda^2/4\pi$.

Table 3.1: Summary of the relationships between electromagnetic propagation terms and ground material properties

Term	Symbol	Equation
Dielectric Permittivity	ϵ	$= \epsilon' + j\epsilon''$
Real part of Dielectric Constant	ϵ'	
Imaginary part of Dielectric Constant	ϵ''	
Permittivity of free space	ϵ_0	$\approx 8.85\text{x}10^{-12} Fm^{-1}$
Relative Permittivity	ϵ_r	$= \epsilon/\epsilon_0$
Magnetic Permeability	μ	$= \mu_0$ in nonmagnetic media
Permeability of free space	μ_0	$\approx 4\pi\text{x}10^{-7} Hm^{-1}$
Conductivity	σ	
Loss Tangent	$\tan\delta$	$= \frac{\epsilon''}{\epsilon'} = \frac{\sigma}{\omega\epsilon}$, ω is angular frequency
Propagation constant	γ	$= \alpha + j\beta$
Attenuation constant	α	$= \omega\left[\frac{\mu\epsilon}{2}\sqrt{1+\tan^2\delta} - 1\right]^{1/2}$
low loss ($\tan^2\delta << 1$, $\mu = \mu_0$)		$\approx 188.5\frac{\sigma}{\sqrt{\epsilon_r}}$
$[dB\ m^{-1}]$		$8.686\alpha[Np\ m^{-1}]$
Phase constant	β	$= \omega\left[\frac{\mu\epsilon}{2}\sqrt{1+\tan^2\delta} + 1\right]^{1/2}$
low loss ($\tan^2\delta << 1$, $\mu = \mu_0$)		$\approx \omega\sqrt{\mu\epsilon}$
Phase velocity	v	$= \lambda f = \frac{\omega}{\beta} = \left[\frac{\mu\epsilon}{2}\sqrt{1+\tan^2\delta} + 1\right]^{-1/2}$
low loss ($\tan^2\delta << 1$, $\mu = \mu_0$)		$\approx \frac{1}{\mu\epsilon} = \frac{c}{\sqrt{\epsilon_r}}$
Velocity in free space	c	$\frac{1}{\sqrt{\mu_0\epsilon_0}} \approx 3\text{x}10^8 ms^{-1}$
Intrinsic impedance	η	$= \sqrt{\frac{\mu}{\epsilon}}$
Reflection coefficient ($\mu_1 = \mu_2 = \mu_0$)	Γ	$= \lvert\Gamma\rvert\ e^{j\phi} = \frac{\sqrt{\epsilon_{r1}} - \sqrt{\epsilon_{r2}}}{\sqrt{\epsilon_{r1}} + \sqrt{\epsilon_{r2}}}$
Transmission coefficient	Υ	$= 1 + \Gamma = \frac{2\sqrt{\epsilon_{r1}}}{\sqrt{\epsilon_{r1}} + \sqrt{\epsilon_{r2}}}$
RCS	σ_T	
Sphere ($2\pi a/\lambda \approx 1$)		$\lvert\Gamma\rvert^2\lambda^2/4\pi\ [m^2]$
Rough Plane ($\sigma_s/\lambda > 0.5/\pi$)		$\lvert\Gamma\rvert^2\pi\lambda R/2\ [m^2]$
Smooth Plane ($\sigma_s/\lambda < 0.1/\pi$)		$\lvert\Gamma\rvert^2\pi R^2\ [m^2]$

3.2.2 Dependence of GPR Penetration on Frequency

GPR performance in terms of maximum penetration is governed, as other radars are, by the radar equation [*Skolnik*, 1990]. The standard radar equation for a point target (defined as equation 1.3) has to be modified to determine the penetration performance of GPR.

For instance, the radar equation assumes a point target (*i.e.* a very small target with respect to the resolution cell size) for the RCS term σ_T. For most GPR reflectors, the point target assumption is not valid because the resolution cell size is similar to the size of typical targets. Therefore, the RCS parameters for spherical, rough and smooth planar targets from Table 3.1 should be substituted for σ_T in the radar equation.

In addition, the antenna characteristics of GPR are typically separated into two terms : *directional gain* (G_{Tx} and G_{Rx}) and *coupling efficiency* (ζ_{Tx} and ζ_{Rx}) [*Annan & Davis*, 1977]. The reason is that the GPR antennas can have resistive loadings on their elements to reduce antenna ring (which is very important), but this also makes the antennas slightly inefficient. The coupling efficiency also takes into account the transmission loss associated with any mismatch between the antenna's impedance and the ground impedance.

Another modification to the standard radar equation is the substitution of the attenuation loss factor of the ground (given by $e^{4\alpha R}$ for the round trip) for the absorption power loss factor L. Incorporating these terms into the radar equation results in equation 3.12. In this thesis, the *depth* of a target buried in the ground is denoted by R (similar to *range* for conventional radar).

$$P_R = \frac{P_T\ G_{Tx}\ G_{Rx}\ \zeta_{Tx}\ \zeta_{Rx}\ \lambda^2\ \sigma_T\ e^{-4\alpha R}}{(4\pi)^3\ R^4} \tag{3.12}$$

The *maximum depth* R_{max} to a target of radar cross section σ_T can be calculated by substituting the minimum detectable signal power P_{MDS} (defined in equation 1.4) for the received power P_R in equation 3.12.

$$P_{MDS} = \frac{FkT_0(SNR)}{t_{int}} = \frac{P_T\ G_{Tx}\ G_{Rx}\ \zeta_{Tx}\ \zeta_{Rx}\ \lambda^2\ \sigma_T\ e^{-4\alpha R_{max}}}{(4\pi)^3\ {R_{max}}^4} \tag{3.13}$$

For GPR systems, a figure called the *System Performance SP* is defined in equation 3.14 [*Annan & Davis*, 1977].

$$SP = \frac{\text{mean transmitted power}}{\text{minimum detectable signal power}} = \frac{P_T}{P_{MDS}} = \frac{P_T t_{int}}{FkT_0(SNR)} \quad (3.14)$$

This system performance figure SP can be substituted into equation 3.13 for P_T/P_{MDS} to form equation 3.15.

$$SP = \left[\frac{G_{Tx}\, G_{Rx}\, \zeta_{Tx}\, \zeta_{Rx}\, \lambda^2\, \sigma_T\, e^{-4\alpha R_{max}}}{(4\pi)^3\, {R_{max}}^4}\right]^{-1} \quad (3.15)$$

This equation is a variation of the radar equation used to calculate the penetration capability of GPR [*Cook*, 1970; *Davis & Annan*, 1989; *Turner, Siggins & Hunt*, 1993]. For known values of the system parameters (*i.e.* SP, G_{Tx}, G_{Rx}, ζ_{Tx} and ζ_{Rx}) and the ground and target properties (*i.e.* σ_T, α and λ), the maximum penetration depth R_{max} in equation 3.15 can be computed numerically. (The equation is transcendental where R_{max} cannot be separated from the numerator and the denominator to solve the equation.)

Many GPR systems quote a SP figure (as determined from equation 3.14) as a basis for rating their maximum penetration capability. However, one must be careful when comparing these figures between different systems, because the quoted SP figures are often over-stated or not correctly defined. For instance, a System Performance figure should be quoted with reference to a defined *integration time* t_{int}. Instead, SP figures in GPR specification sheets often do not state the integration time or the number of times the received signal has been averaged or stacked to obtain the figure.

For example, *Davis & Annan*, 1989 states that typical GPR systems have system performances of 120-160 dB, but there is no mention of the amount of stacking (or the number of times the signal is oversampled). However, *Wright, Bradley & Grover*, 1994 are more specific in saying that typical impulse radar systems usually have system performances in the range of 100-130 dB with no stacking. Another problem with assessing GPR penetration performance using the system performance parameter is that it does not consider the antenna coupling efficiencies and the antenna directional gains. For example, a system performance of 110 dB is quoted for the GSSI SIR-8 impulse GPR system, but the antennas used have antenna coupling efficiencies ζ_{Tx} and ζ_{Rx} of -13 dB each (due to resistive loading), and directional

gains G_{Tx} and G_{Rx} of 2 dB each [*Annan & Davis*, 1977; *Turner, Siggins & Hunt*, 1993]. Therefore, there is a loss of 22 dB suffered by the signal before any of the ground absorption and spreading losses are considered.

A more descriptive performance parameter for evaluating the penetration capability of GPR is one which includes the antenna directional gains and coupling efficiencies with the system performance. Therefore, a new parameter called the *external loop gain* G_L (defined in equation 3.16) of the system is proposed, which contains all the terms that are system *dependent* or dependent on the system; that is, they are under the control of the system designer.

$$G_L = G_{Tx}\, G_{Rx}\, \zeta_{Tx}\, \zeta_{Rx}\, SP = G_{Tx}\, G_{Rx}\, \zeta_{Tx}\, \zeta_{Rx}\, \frac{P_T t_{int}}{FkT_0(SNR)} \tag{3.16}$$

The G_L parameter is equivalent to the maximum amount of loss that the radiated signal can tolerate before it is undetectable amongst the system noise (for a given t_{int} and SNR). For example, higher G_L parameters imply that the transmitted radio signals can sustain more loss during propagation in the ground. Therefore, it is truly indicative of the penetration capability of a GPR system.

The remaining terms in the GPR radar equation of 3.15 which are *independent* of the system are lumped together and called the *external loop loss* L_E (equation 3.17).

$$L_E = \left[\frac{e^{-4\alpha R_{max}}\, \sigma_T \lambda^2}{(4\pi)^3\, R_{max}^4} \right]^{-1} \tag{3.17}$$

The L_E parameter represents the maximum loss incurred by a radiated signal in propagating to and reflecting from a point target at a maximum depth of R_{max}. It consists of an absorption loss factor ($e^{4\alpha R_{max}}$), reflection and scattering loss factor at the target ($1/\sigma_T$) and the spherical spreading loss factor ($\propto R^4$).

Turner, Siggins & Hunt, 1993 derived similar equations to 3.16 and 3.17 which they called *system dependent* (same G_L) and *system independent* (same as L_E) parameters. However, there is confusion in their derivation concerning part of the effective aperture of the receiver antenna $G_{Rx}\lambda^2/4\pi$. Turner *et al.*, lumped the $\lambda^2/4\pi$ term in the system dependent or external loop gain parameter (G_L), which changes the dimensions of G_L from nil to square metres. Instead, the $\frac{\lambda^2}{4\pi}$ term should be placed with the system independent or external loop loss (L_E) parameter, which will then be dimensionless as well.

Table 3.2 summarises the L_E parameters for spherical, rough and smooth planar targets. The proportion of the spreading loss changes from R^4 for the spherical target, to R^3 for the rough planar target, to R^2 for the smooth planar target. This variation demonstrates the significance of the spreading loss for spherical targets, as compared with the planar targets.

Table 3.2: External Loop Loss L_E for spherical, and rough and smooth planar targets.

Type of Target	**Condition**	σ_T	L_E
spherical	$2\pi a/\lambda \approx 1$	$\lvert\Gamma\rvert^2\lambda^2/4\pi$	$\left[\frac{\lvert\Gamma\rvert^2 e^{-4\alpha R_{max}}\lambda^4}{256\pi^4 R_{max}^4}\right]^{-1}$
rough planar	$\sigma_s/\lambda > 0.5/\pi$	$\lvert\Gamma\rvert^2\pi\lambda R_{max}/2$	$\left[\frac{\lvert\Gamma\rvert^2 e^{-4\alpha R_{max}}\lambda^3}{128\pi^2 R_{max}^3}\right]^{-1}$
smooth planar	$\sigma_s/\lambda < 0.1/\pi$	$\lvert\Gamma\rvert^2\pi R_{max}^2$	$\left[\frac{\lvert\Gamma\rvert^2 e^{-4\alpha R_{max}}\lambda^2}{64\pi^2 R_{max}^2}\right]^{-1}$

Maximum penetration depth R_{max} is the range at which the external loop loss L_E is equal to the external loop gain G_L (*i.e.* $L_E = G_L$). As stated previously, the equation $L_E = G_L$ (which forms the same equation as 3.15) is transcendental, and R_{max} cannot be solved for algebraically. *Turner, Siggins & Hunt*, 1993 suggested the use of nomograms to graphically determine R_{max} (although the published nomograms are incorrect because of the misplacement of the $\frac{\lambda^2}{4\pi}$ term as discussed above). Figures 3.3, 3.4 and 3.5 are the correct nomograms for spherical, and rough and smooth planar targets (for $\lambda = 1\,m$), based on the L_E equations in Table 3.2.

To determine the maximum penetration depth, *Turner, Siggins & Hunt*, 1993 suggested the following procedure :

1. Determine the system's external loop gain G_L (dB) of the GPR system using equation 3.16.

2. Calculate the reflection loss $|\Gamma|^2$ (dB) at the dielectric interface from dielectric measurements and using equation 3.10. Add this value to G_L from step 1. The resulting number is equivalent to the maximum spreading and attenuation losses that the radar signal can tolerate before it is lost in the system noise (for a given integration time t_{int} and SNR).

3. The intersection of the spreading/attenuation losses (from the vertical axis of Figures 3.3, 3.4 and 3.5) calculated in step 2 with the relevant attenuation curve of the material in dB/m, allows the maximum penetration depth R_{max} to be determined from the horizontal axis.

The nomograms illustrate how significantly the spreading loss affects the GPR penetration for a spherical target in a medium with low attenuation (*e.g.* 0.1 dB/m), as opposed to targets which are planar. For highly attenuating media (*e.g.* 50 dB/m), the spreading loss has very little effect on GPR penetration for any target type.

It is also evident from the graphs that the GPR penetration is highly dependent on frequency (*i.e.* both wavelength λ and attenuation α are highly dependent on frequency). The significance of this will be discussed later in Section 3.3.2.

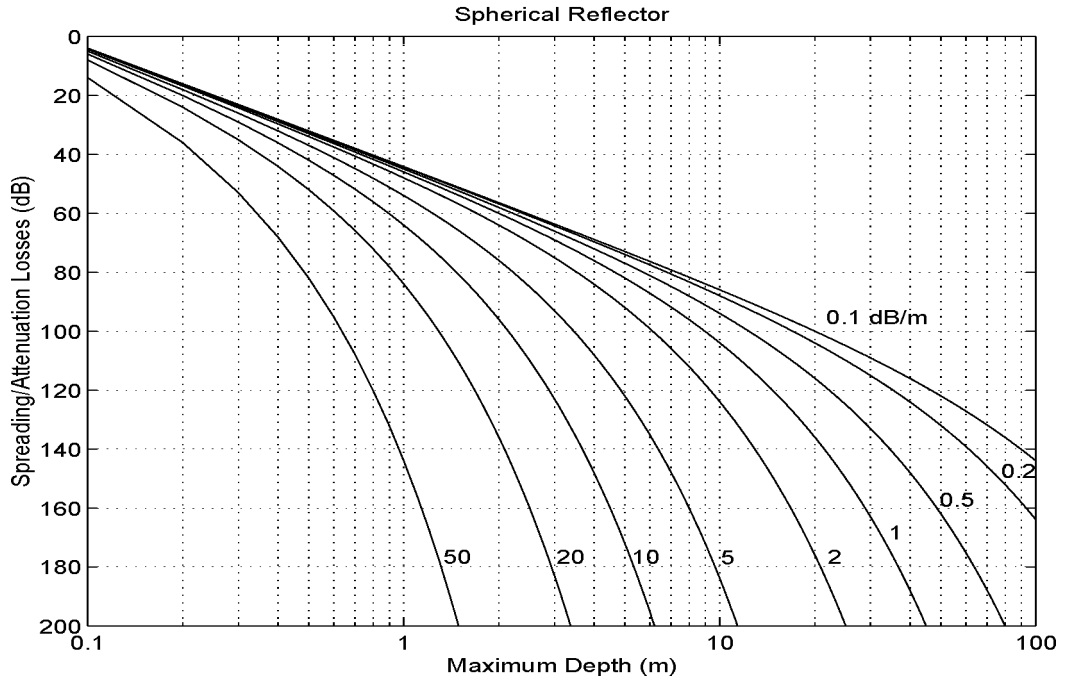

Figure 3.3: Nomogram for determining GPR penetration for a spherical target (where $2\pi a \sim \lambda$, and $\lambda = 1\,m$).

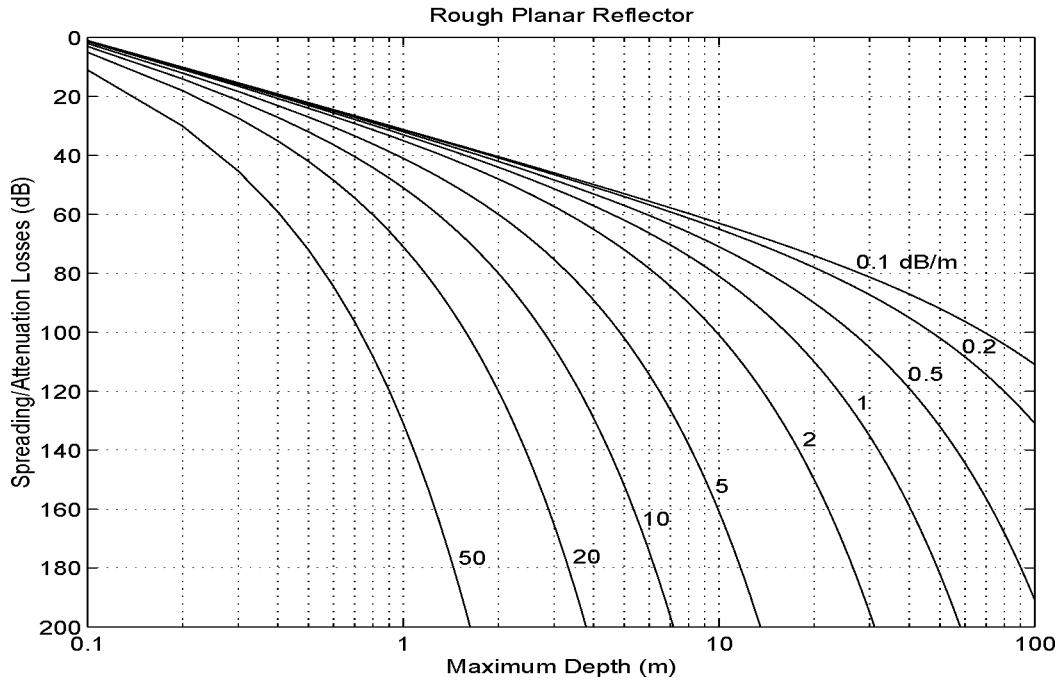

Figure 3.4: Nomogram for determining GPR penetration for a rough planar target (where $\sigma_s/\lambda > 0.5/\pi$, and $\lambda = 1\,m$).

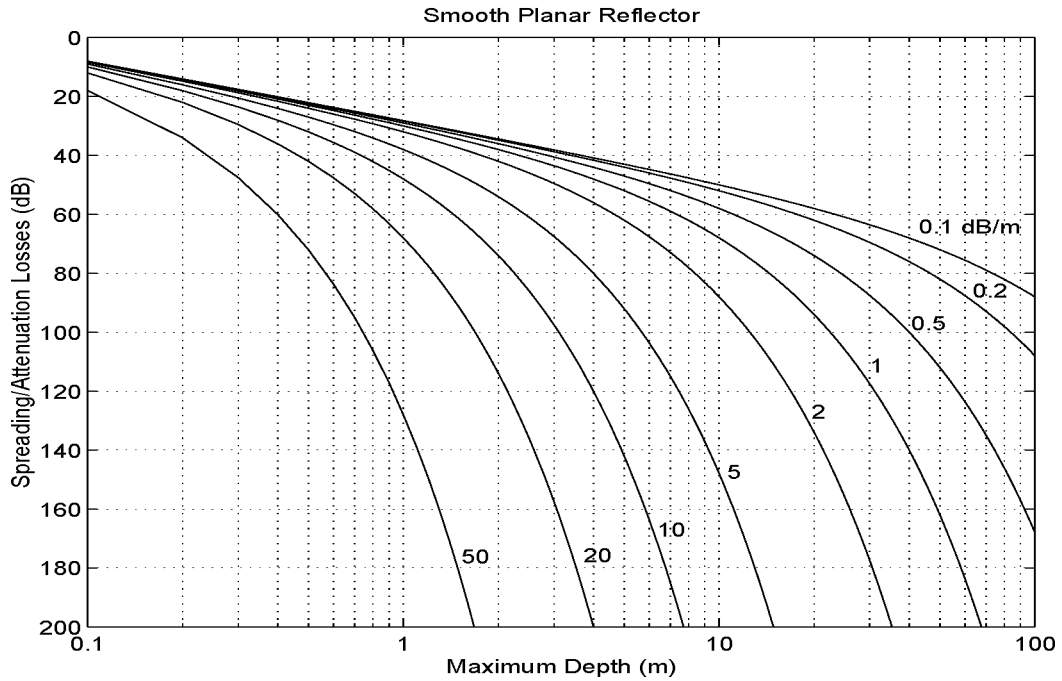

Figure 3.5: Nomogram for determining GPR penetration for a smooth planar target ($\sigma_s/\lambda < 0.1/\pi$, and $\lambda = 1\,m$).

3.2.3 Resolving Power of GPR

The techniques described above are relevant for determining the maximum penetration depth of a single target buried in the ground. For the detection of multiple targets, the resolution of the GPR system is an important parameter.

Chapter 1 introduced the concept of radar range resolution which was defined in equation 1.8 and repeated here as equation 3.18.

$$\Delta R = \frac{v}{2B} \tag{3.18}$$

For GPR applications, ΔR is the *depth resolution* in ground material for a propagation velocity of v ($v = c/\sqrt{\epsilon_r}$ where ϵ_r is the relative dielectric permittivity of the ground material). In this thesis, the term *resolution* or *resolving power* of GPR system refers to the depth resolution.

A GPR system with a transmitter bandwidth of B is capable of resolving two buried targets which are separated by ΔR metres (from equation 3.18) in depth. Systems with wider bandwidths have finer resolving powers or smaller ΔR values (for materials with the same ϵ values) as compared with systems with narrower bandwidths. Figure 3.6 is a graph which calculates the theoretical resolution (from the horizontal axis of the graph) of a GPR system with a transmitter bandwidth B (vertical axis) and for a material with a relative permittivity of ϵ.

Many impulse GPR systems are designed with fractional bandwidths of 100% (*i.e.* the bandwidth in Hertz is equal to the centre frequency of the bandwidth in Hertz) [*Annan & Cosway*, 1994]. Therefore, higher centre frequency antennas are used to improve the resolving power. However, increasing the frequency has the detrimental effect of reducing the GPR penetration capability. There is normally a compromise between penetration and resolution in GPR due to the conflicting dependence on frequency [*Jol*, 1995].

3.3 GPR Performance in Constant Q Materials

The previous Section 3.2 has described how GPR penetration and resolution are dependent on the electromagnetic properties of the ground material and the frequencies of the waveform generated by the GPR system. For example, penetration depths of several tens of metres can be achieved with radar waveforms centred at 10

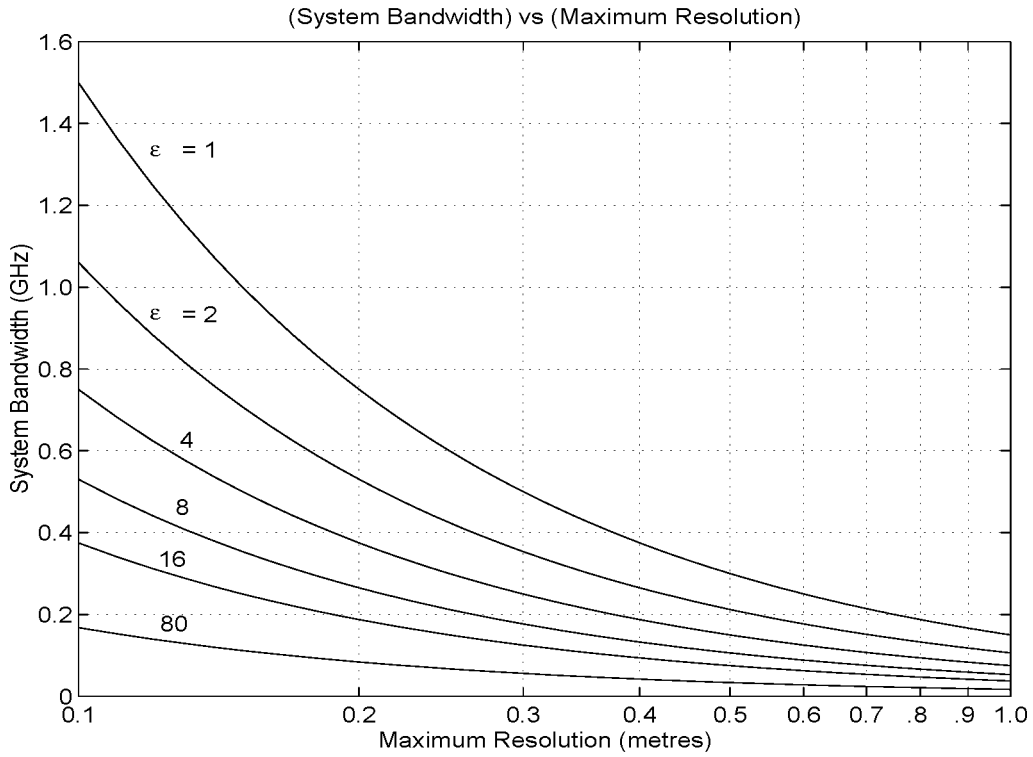

Figure 3.6: Transmitter bandwidth verses resolution for various relative permittivities ϵ.

MHz. However, the bandwidth of these signals (which will be 10 MHz for a 100% fractional bandwidth) is narrow in absolute terms and they have poor resolving power. Wider bandwidth signals obtained with radar waveforms centred at say 2 GHz enable resolving powers of centimetre resolution, but the high frequencies reduce the depth of penetration. With such a wide frequency range available and the high dependence of penetration and resolution on frequency, it is generally difficult to evaluate these performance characteristics of GPR for a wide variety of materials and applications.

This section describes a novel approach for evaluating the penetration (Section 3.3.2) and resolution (Section 3.3.3) performances of GPR across a broad frequency spectrum. In developing this method, it is first necessary to outline the *constant Q* model for ground materials. The validity of this model has been confirmed within the GPR spectrum by experimental dielectric measurements conducted elsewhere [*Siggins & Turner*, 1992; *Turner & Siggins*, 1994; *Nothdurft & Longstaff*, 1995].

3.3.1 Constant Q Model for Ground Materials

Attenuation

Q or *Quality Factor* is a well-known mechanical and electrical measurement "of the ratio of 2π times the energy stored to the energy radiated and dissipated in one cycle" (ANSI/IEEE Std 145-1983). In seismics, it is commonly used to describe mechanical wave propagation through the ground [*Kjartansson*, 1979]. For these seismic waves, Q is related to the ground attenuation constant α and propagation velocity v using equation 3.19, where λ is the seismic wavelength, and ω is the angular frequency [*Strick*, 1967].

$$Q = \frac{\omega}{2v\alpha} = \frac{\pi}{\lambda\alpha} \tag{3.19}$$

It has been found experimentally that the Q for ground materials are relatively constant over a wide range of seismic wavelengths [*Stacey et al.*, 1975]. This implies that the attenuation α is linear with the wavelength λ (*i.e.* $\alpha \propto 1/\lambda$ for a constant Q in equation 3.19). For a constant propagation velocity v, the attenuation α will also be linear with frequency f (*i.e.* $\alpha \propto f$ for constant v in equation 3.19). *Kjartansson*, 1979 offered a practical explanation for this observation; that there are a number of competing attenuation mechanisms each having their own frequency dependence, but when brought together produces a bulk attenuation effect which is approximately linear with frequency. This observation is known as the *constant Q* (CQ) model for seismic waves, where Q is constant for most frequencies associated with stress wave propagation.

Jonscher, 1977 held that the constant Q model can be extended to a universal criterion for dielectric, mechanical and magnetic relaxations in solids. For the case of dielectrics, *Jonscher*, 1977 suggested a "universal" behaviour where the electrical conductivity σ of a wide variety of materials is directly proportional to ω^n, where n is close to one across a wide frequency spectrum (part of which is the GPR spectrum). This implies that the attenuation due to conduction loss (for electromagnetic propagation) is roughly proportional to frequency ($\omega = 2\pi f$).

Siggins & Turner, 1992 and *Turner & Siggins*, 1994 proposed a similar constant Q propagation model for describing radar propagation in the ground. For low loss media (where $\tan^2\delta << 1$), the attenuation constant α is approximately equal to $\frac{1}{2}\omega\sqrt{\mu\epsilon}\tan\delta$ (equation 3.7) and when substituted into the Q definition of

equation 3.19, forms equation 3.20. Q values which are less than 3 are generally not considered as low-loss (*e.g.* some clay materials with moisture contents higher than 10% volume), and the approximation in equation 3.20 is less valid.

$$Q \approx \frac{\omega 2}{2v\omega\sqrt{\mu\epsilon}\tan\delta} = \frac{\omega 2v}{2v\omega\tan\delta} = \frac{1}{\tan\delta} \tag{3.20}$$

For low loss ground materials which conform to the constant Q model, the loss tangent $\tan\delta$ is approximately (or near) constant for all GPR frequencies. It follows then that the attenuation due to absorption loss in the material will be relatively linear for these frequencies. The attenuation measurement of the coal sample in Figure 3.1 illustrates this linear relationship with frequency.

Q values for ground materials are generally in the range of 2 to 30 [*Turner & Siggins*, 1994]. Figure 3.7 contains a graph by *Turner & Siggins*, 1994 of attenuation verses radio frequency for a variety of ground materials within the upper and lower Q^* bounds of 8 and 30. (Q^* describes the gradient of the best-fit line for each attenuation curve, where the attenuation at zero Hertz can be a non-zero value.)

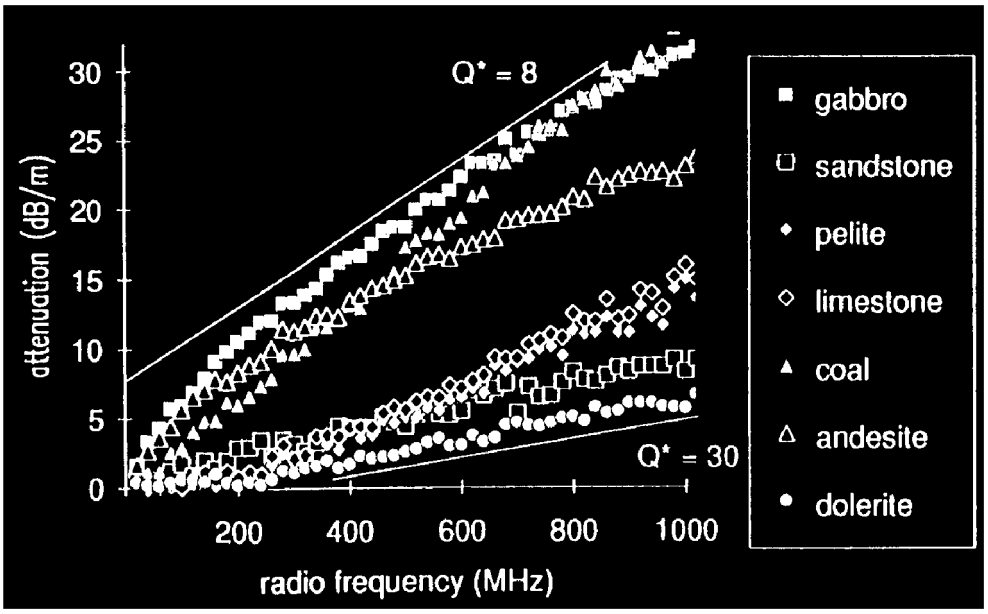

Figure 3.7: Attenuation versus radio frequency for a variety of materials and their Q^* values (taken from *Turner & Siggins*, 1994).

Other independent measurements[2] have strongly supported the validity of the constant Q model for electromagnetic propagation. In some materials, the measured Q value (for frequencies below 100 MHz) has a slight dependence upon frequency (as noted in Figure 3.7). For these materials and frequencies, the *near constant* Q model (also borrowed from seismics [*Liu, Anderson & Kanamori*, 1976]) may apply. Whether the material holds to a constant or near constant Q model, the close linear relationship between electromagnetic attenuation of ground materials and frequency has been confirmed with many measurements over the past twenty-five years (see Table 3.3). In this thesis, the constant Q model is assumed for ground materials across the 10 MHz to 2 GHz GPR spectrum. Based on this assumption, the attenuation of these materials has an approximate linear relationship with frequency, with a Q value defined by the gradient.

Table 3.3: Constant Q ground materials based on experimental data as referenced

Ground Material	**Reference**
sandstones	*Siggins & Turner*, 1992
dolerite	"
pelite	"
limestone	"
coal	*Cook*, 1970; *Houck*, 1985; *Siggins & Turner*, 1992 and
clay	*Turner, Siggins & Hunt*, 1993
sand	*Turner & Siggins*, 1994
loam	"
most soils and clays	*Hipp*, 1974; *Scott & Smith*, 1992;
clays	*Turner, Siggins & Hunt*, 1993
river water	"
gabbro	*Turner*, 1992
basalt	"
andesite	"
shale	*Turner*, 1993
siltstone	"

[2]Dielectric measurements across 10 MHz to 2 GHz (using techniques such as capacitive bridge, coaxial cell and coaxial probe) have been conducted on a wide variety of materials by Stephen Nothdurft of The University of Queensland.

Relative Permittivity

Figure 3.8 displays the real (connected line) and imaginary (dashed line) components of the dielectric constant for a sandstone sample measured with a coaxial cell[3]. An interesting observation to be made from this data is that the real part is relatively constant with frequency. This observation is supported by the experimental measurements reported in the references of Table 3.3. *Davis & Annan*, 1989 reported this phenomena for materials with conductivities less than 100 mS/m and for frequencies between 10 and 1000 MHz. Much higher frequencies are affected by the relaxation of water molecules, and do not exhibit such a constant permittivity behaviour.

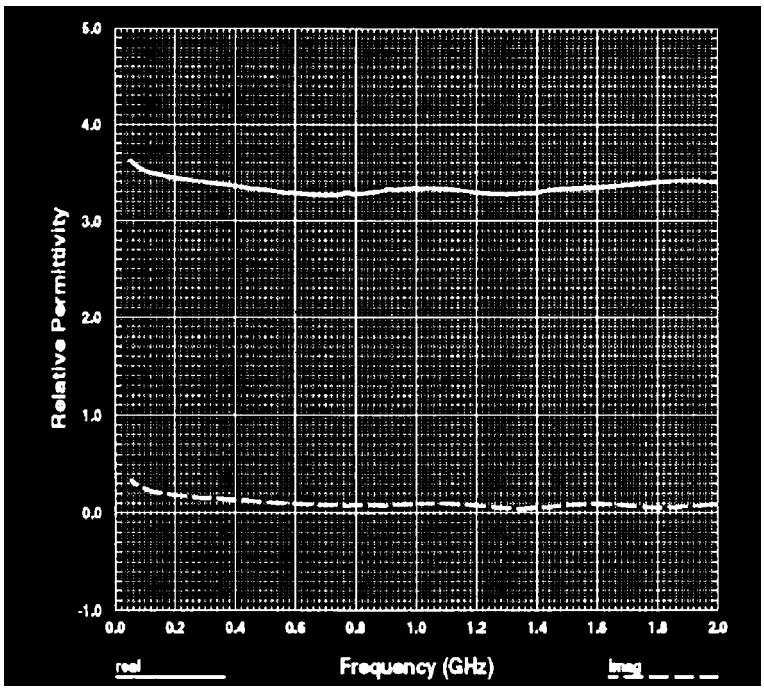

Figure 3.8: Real (line) and imaginary (dash) components of the complex permittivity for a sandstone sample measured with a coaxial cell (conducted by Stephen Nothdurft).

3.3.2 Maximum Penetration Depth in Constant Q Materials

In Section 3.2.2, the radar equation for GPR was separated into the system dependent or external loop gain parameters G_L (equation 3.16), and system independent or

[3]The sandstone sample was prepared by Stephen Nothdurft and measured by Damaskos Inc. using a coaxial cell.

external loop loss parameters L_E (equation 3.17). The GPR penetration capability was then determined at a single frequency by solving for R_{max} when $L_E = G_L$.

By assuming a constant Q model for ground materials, GPR penetration can be quantified across many frequencies within the broad GPR spectrum. The following approach sets out to remove the frequency dependence from the radar equation parameters, and to simply characterise the GPR penetration capability for all frequencies within the GPR spectrum. The outcome will be the characterisation of maximum penetration depth as a fixed number of wavelengths. For a given resolution, the shortest wavelength corresponding to the upper frequency bound of the GPR bandwidth should be used for predicting the maximum penetration depth. This is because the attenuation of the ground is largest for the highest frequency, and the available bandwidth is dependent on the detectability of the upper frequency bound. If resolution is not as critical as the maximum penetration capability, then a longer wavelength corresponding to a lower frequency within the bandwidth may be a more suitable choice.

The external loop gain parameter G_L for a single frequency can be assumed constant across the GPR spectrum using the following assumptions:

- The directional gains (G_{Tx}, G_{Rx}) of electrically large antennas can be made relatively constant at a single resonant frequency by scaling the antenna dimensions. For example, a bow-tie antenna has a fixed directional gain if the length of the bow-tie elements are always designed to be $\lambda/2$ metres [*Brown & Woodward*, 1952].

- The coupling efficiencies (ζ_{Tx}, ζ_{Rx}) of the antennas are partly determined by the resistive loadings of the bow-tie elements which reduce antenna ring. To be effective, the Q of the antenna due to the resistive loadings should be lower than the Q of the ground material so that the antenna ring is more heavily attenuated than the signals through the ground. The impedance mismatch between the antennas and ground are also a component of the coupling efficiency. Both components can be treated as independent of frequency.

- The system performance figure SP of a GPR system is generally independent of frequency. Slightly higher SP figures (variation of perhaps 10 dB) can be obtained at lower frequencies (*e.g.* 10 MHz) where higher mean powers are easier to generate than at higher frequencies (*e.g.* 2 GHz).

When these assumptions are valid, the external loop gain parameter ($G_L = G_{Tx}G_{Rx}\zeta_{Tx}\zeta_{Rx}SP$) can be assumed constant for any frequency within the GPR spectrum. For example, a GPR system designed at a frequency of 10 MHz can be redesigned at 2 GHz without a significant change in the G_L parameter.

Unlike G_L, the external loss L_E parameter is highly dependent on frequency. For instance, the attenuation term α has a strong relationship with frequency, even more so the λ^2 term. The L_E parameter can be expressed in an alternative way which is independent of frequency, by using the following procedure :

1. Letting $\alpha = \pi/Q\lambda$ where Q is constant for frequencies within the GPR spectrum. In addition, the relative permittivity ϵ_r of the ground material is constant with frequency, which implies that the propagation velocity v and reflection loss $|\Gamma|^2$ at the dielectric boundary of the target are constant. Measurements have shown that these assumptions are justified for most materials (see Section 3.3.1).

2. Normalising the radar cross section area σ_T of the relevant target (in Table 3.1) with respect to λ^2 to form a dimensionless RCS term (*i.e.* $\sigma_{\lambda^2} = \sigma_T/\lambda^2$). Therefore, σ_T can be rewritten as $\lambda^2\sigma_{\lambda^2}$.

3. Normalising the maximum penetration depth R_{max} with λ to form a dimensionless term (*i.e.* $R_{max_\lambda} = R_{max}/\lambda$). This enables R_{max} to be expressed as $R_{max} = \lambda R_{max_\lambda}$, where R_{max_λ} is the maximum penetration depth expressed as a number of wavelengths.

Carrying out the above procedure on L_E of equation 3.17 results in the expression of the *external loop loss for constant Q materials* L_{E_Q} in equation 3.21. The frequency dependent terms α and λ that were part of the previous L_E parameter (equation 3.17) have been cancelled in this L_{E_Q} equation, and the maximum penetration depth R_{max_λ} is now expressed as a number of wavelengths in the ground.

$$L_{E_Q} = \left[\frac{e^{-4\frac{\pi}{Q\lambda}\lambda R_{max_\lambda}}\lambda^2\sigma_{\lambda^2}\lambda^2}{(4\pi)^3\lambda^4 R_{max_\lambda}^4}\right]^{-1} = \left[\frac{e^{-4\frac{\pi}{Q}R_{max_\lambda}}\sigma_{\lambda^2}}{(4\pi)^3 R_{max_\lambda}^4}\right]^{-1} \tag{3.21}$$

For the three type of targets considered before (*i.e.* spherical, rough and smooth planar targets), the corresponding normalised radar cross section terms σ_{λ^2} are redefined as the following :

- For a spherical target whose circumference $2\pi a_\lambda$ in wavelengths (a_λ is the radius in terms of wavelengths) is approximately one (*i.e.* $2\pi a_\lambda \sim 1$), then $\sigma_{\lambda^2} \approx |\Gamma|^2/4\pi$.
- For a rough planar target where $\sigma_{s_\lambda} > 0.5/\pi$, ($\sigma_{s_\lambda}$ is the standard deviation of the surface heights in wavelengths), then $\sigma_{\lambda^2} \approx |\Gamma|^2 \pi R_{max_\lambda}/2$.
- For a smooth planar target where $\sigma_{s_\lambda} < 0.1/\pi$, then $\sigma_{\lambda^2} \approx |\Gamma|^2 \pi R^2_{max_\lambda}$.

The L_{E_Q} parameters for each of these targets are recorded in Table 3.4.

Table 3.4: External Loop Loss L_{E_Q} for spherical, rough and smooth planar targets in constant Q materials

Type of Target	**Condition**	σ_{λ^2}	$\mathbf{L_{E_Q}}$
spherical	$2\pi a_\lambda \sim 1$	$\|\Gamma\|^2/4\pi$	$\left[\frac{\|\Gamma\|^2 e^{-4\frac{\pi}{Q}R_{max_\lambda}}}{256\pi^4 R^4_{max_\lambda}}\right]^{-1}$
rough planar	$\sigma_{s_\lambda} > 0.5/\pi$	$\|\Gamma\|^2 \pi R_{max_\lambda}/2$	$\left[\frac{\|\Gamma\|^2 e^{-4\frac{\pi}{Q}R_{max_\lambda}}}{128\pi^2 R^3_{max_\lambda}}\right]^{-1}$
smooth planar	$\sigma_{s_\lambda} < 0.1/\pi$	$\|\Gamma\|^2 \pi R^2_{max_\lambda}$	$\left[\frac{\|\Gamma\|^2 e^{-4\frac{\pi}{Q}R_{max_\lambda}}}{64\pi^2 R^2_{max_\lambda}}\right]^{-1}$

The maximum penetration depth in wavelengths R_{max_λ} for a target can be determined by solving the equation $L_{E_Q} = G_L$. This equation is transcendental (similar to equation 3.15), where R_{max_λ} cannot be solved algebraically. The nomogram technique described in Section 3.2.2 can be used again to solve this equation.

Figures 3.9, 3.10 and 3.11 are the constant Q nomograms based on the L_{E_Q} equations of Table 3.4 for spherical, and rough and smooth planar targets.

An advantage of using these constant Q nomograms over the nomograms in Section 3.2.2 is that a specified frequency or wavelength is not required to quantify the maximum penetration depth. That is, the number of wavelengths calculated from these nomograms is constant for any frequency within the GPR spectrum. It is now possible to compare the maximum penetration performances of different GPR systems independently of frequency. A hypothetical example will illustrate this process.

GPR System 1 has an external loop gain G_L of 100 dB, while GPR System 2 has a G_L equal to 165 dB (both G_L parameters are referenced to a common

integration time and signal-to-noise ratio). For this example, the "candidate" target is a metal sphere (reflection loss $|\Gamma|^2$ is equal to 0 dB) with a circumference size approximately equal to a wavelength (*i.e.* $2\pi a \approx \lambda$). The relative performances of the two systems can now be compared using the constant Q nomogram for a spherical target (Figure 3.9). For materials with a low constant Q (*i.e.* high loss, say $Q = 1$), GPR System 1 is capable of penetrating to a maximum depth of one wavelength. Using a similar process, GPR System 2 is capable of penetrating a depth of two wavelengths. Hence, GPR System 2 has the capability to penetrate twice as far in this material to the target as GPR System 1, no matter what frequency is selected (assuming both systems are operating at the same frequency within the GPR spectrum). Now consider the same systems applied to a ground material with a higher constant Q value of 64 (*i.e.* very low loss). GPR System 1 is capable of penetrating to a maximum depth of 15 wavelengths, while GPR System 2 is capable of penetrating to 60 wavelengths. Hence, in this material, GPR System 2 has the capability of penetrating to four times the depth of GPR System 1, no matter what centre frequency is selected (again, assuming both systems are operating at the same frequency within the GPR spectrum).

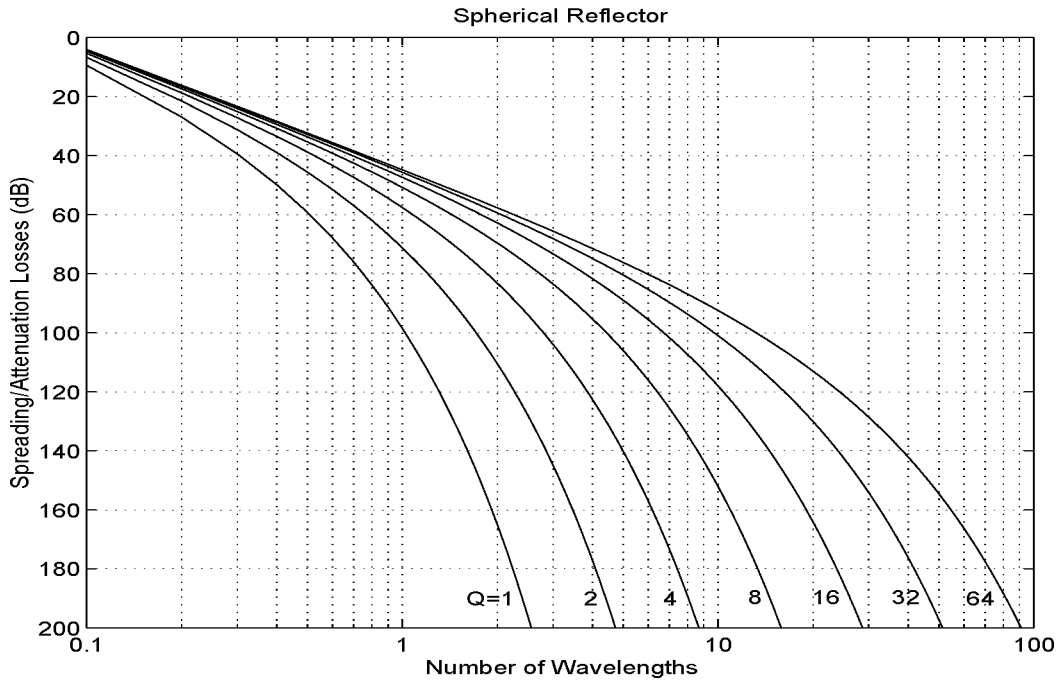

Figure 3.9: Constant Q Nomogram for determining GPR penetration in wavelengths for a spherical target ($2\pi a_\lambda \sim 1$).

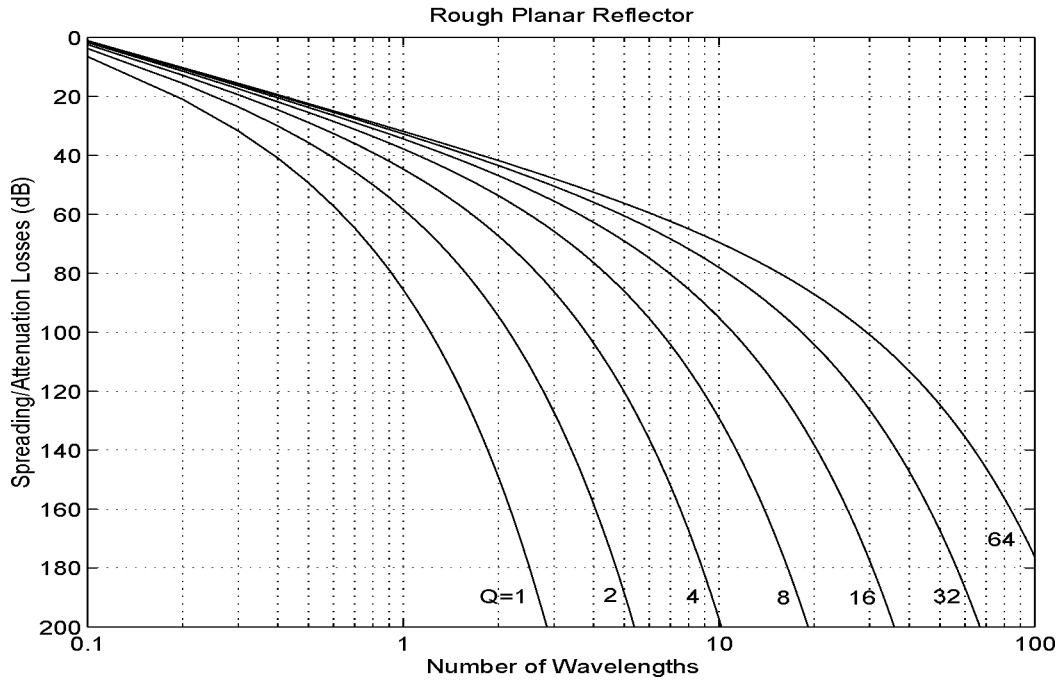

Figure 3.10: Constant Q Nomogram for determining GPR penetration in wavelengths for a rough planar target ($\sigma_{s_\lambda} > 0.5/\pi$).

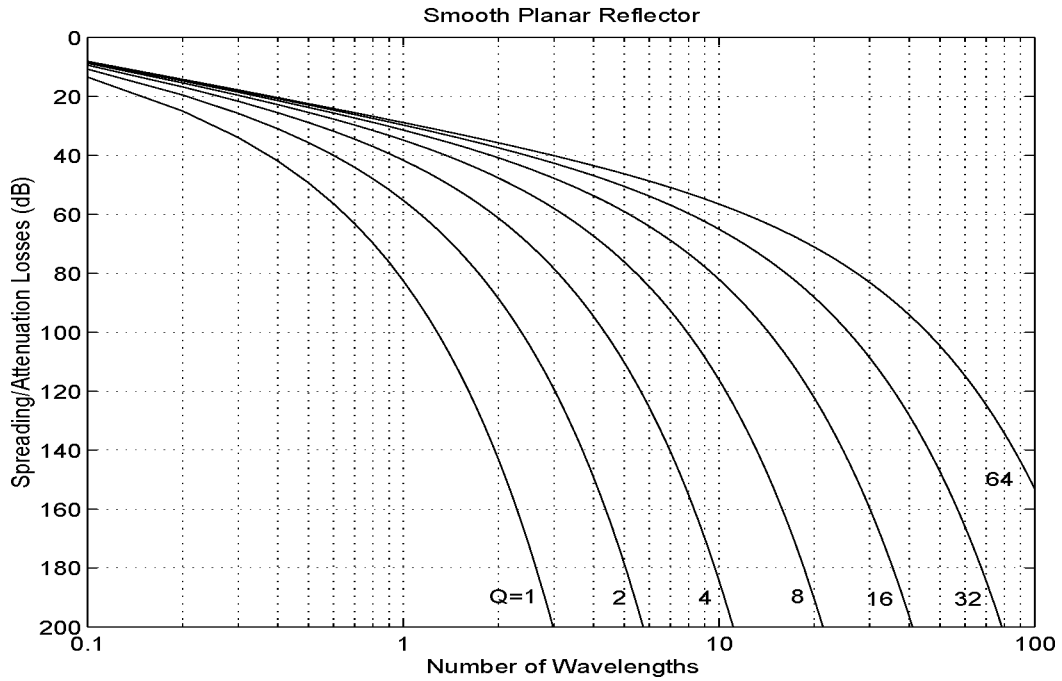

Figure 3.11: Constant Q Nomogram for determining GPR penetration in wavelengths for a smooth planar target ($\sigma_{s_\lambda} < 0.1/\pi$).

3.3.3 GPR Resolution for a Constant Fractional Bandwidth

In Section 3.2.3, the resolving power ΔR of a GPR system was defined as a function of the transmitter bandwidth B and the relative permittivity ϵ_r of the ground material. It was shown that for a fixed fractional bandwidth B/f_c, the available bandwidth B is proportional to the centre frequency of the band f_c. The conclusion was that there is a compromise between GPR penetration (which requires low centre frequencies) and resolution (with requires wide bandwidths). This section describes how the resolving power of GPR can be expressed in an alternative form which is independent of the centre frequency. The method outlined here assumes a broadband system with a constant fractional bandwidth, which is valid for most antennas (*e.g.* octave for bow-tie, decade for horns).

Figure 3.12(a) illustrates the frequency spectrum of a pulsed radar signal with a bandwidth B and a centre frequency f_c, and defined lower and upper frequency bounds of f_L and f_U respectively ($B = f_U - f_L$). The corresponding pulse in the time domain (Figure 3.12(b)) is a bandpass signal with a -4 dB envelope width of $1/B$ seconds, and a carrier frequency of f_c Hertz.

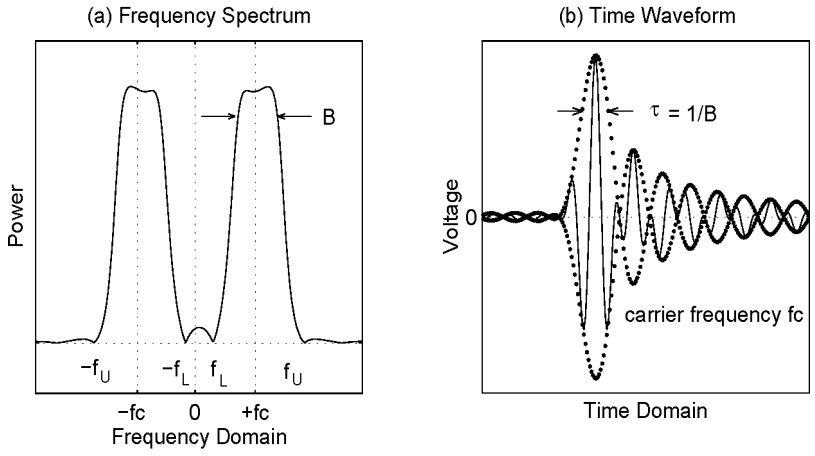

Figure 3.12: (a) Frequency bandwidth $B = f_U - f_L$ Hertz centred at $\pm f_c$ Hertz of a pulsed radar waveform; (b) the corresponding time waveform and envelope of a pulse of width $1/B$ seconds and with a carrier frequency of f_c Hertz.

Let the *upper bound fractional bandwidth* be defined as the percentage ratio of the bandwidth B and the upper frequency bound f_U (*i.e.* B/f_U x 100%). The fractional bandwidth B/f_c of a GPR system can be converted to the upper bound fractional

bandwidth B/f_U by using equation 3.22.

$$B/f_U = \frac{1}{f_c/B + 0.5} \tag{3.22}$$

The GPR resolving power ΔR is equal to $v/2B$ where v is the propagation velocity which is equal to the upper frequency bound f_U multiplied with the shortest wavelength λ_s (*i.e.* $v = f_U\lambda_s$). The resolution can be expressed in λ_s and B/f_U terms (equation 3.23).

$$\Delta R = \frac{v}{2B} = \frac{f_U\lambda_s}{2B} = \frac{\lambda_s}{2(B/f_U)} \tag{3.23}$$

λ_s is the *shortest wavelength* in the ground medium corresponding to the upper frequency bound f_U. Normalising ΔR with respect to λ_s (*i.e.* $\Delta R_{\lambda_s} = \Delta R/\lambda_s$) enables the expression of resolution as a number of wavelengths, ΔR_{λ_s} (equation 3.24). The expression for the resolving capability of GPR is now in terms of the fractional bandwidth B/f_c and independent of centre frequency.

$$\Delta R_{\lambda_s} = \frac{1}{2(B/f_U)} = \frac{\frac{1}{B/f_c} + 0.5}{2} \tag{3.24}$$

Figure 3.13 is a graph of the GPR fractional bandwidth B/f_c plotted with respect to the number of wavelengths, ΔR_{λ_s}. Because this expression is normalised with wavelength, it is not necessary to specify the relative permittivity constant ϵ_r as was the case with Figure 3.6.

The resolving power of two GPR systems can now be compared independently of their centre frequency. For example, GPR System 1 may have a fractional bandwidth of 100%, which relates to a resolution of 0.75 wavelengths using Figure 3.13. Using a similar argument, GPR System 2 may have a fractional bandwidth of 150%, which has a resolution of 0.58 wavelengths. Therefore, GPR System 2 has a resolving power that is a factor of 1.3 better than GPR System 1, no matter what frequency is selected (assuming both have identical centre frequencies).

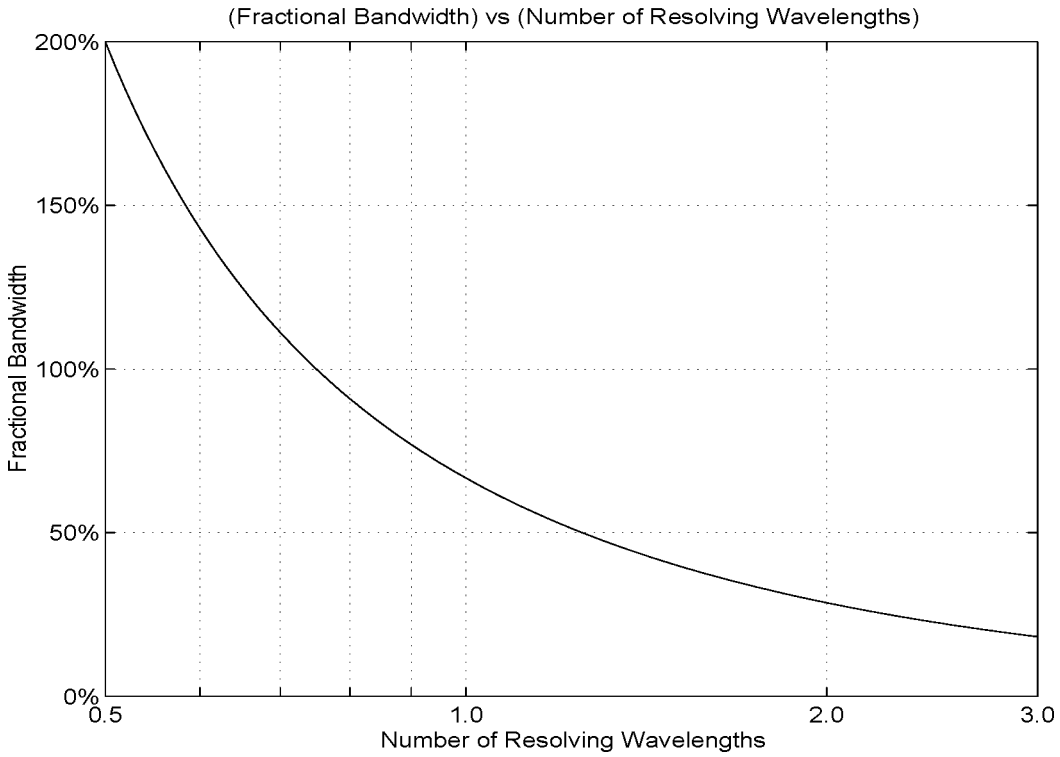

Figure 3.13: Resolution in λ_s wavelengths versus system fractional bandwidth

3.4 Waveform Design

An important part of the design process for GPR is determining the optimal bandwidth and centre frequency of the waveform to achieve the required penetration and resolution. Using the concepts developed in Section 3.3, the following procedure outlines a design tool for selecting these two waveform parameters. A running example is included with this outline.

1. Predict the external loop gain parameter G_L :

For example, $G_L = 130$ dB.

2. Calculate the spreading/attenuation losses that can be tolerated :

Add the reflection loss of the target to G_L. This determines the spreading/attenuation losses that the radar signal can tolerate. For example, a metallic target has $|\Gamma|^2$ equal to 0 dB. Therefore, the spreading/attenuation losses that can be tolerated by the radiated signal for this target are equal to 130 dB.

3. Determine the maximum penetration depth in wavelengths :

GPR penetration in number of wavelengths is determined using the appropriate constant Q nomogram (Figures 3.9, 3.10 or 3.11) for the target type, Q of the material, and the spreading/attenuation losses that can be tolerated. For example, a "candidate" metal spherical target (whose circumference is approximately equal to a wavelength) in a material with Q equal to 16, can be detected up to a maximum depth of 15 wavelengths for 130 dB of spherical/attenuation losses (using Figure 3.9).

4. Calculate the upper frequency bound f_U of the band :

For example, a required maximum depth of 10 metres corresponds to the shortest wavelength λ_s of 0.66 metres. The upper frequency bound f_U is then equal to 200 MHz, assuming a relative permittivity of the ground material of 5.

5. Express the required resolution as a number of wavelengths :

Based on the shortest wavelength calculated in step 4, the required resolution in wavelengths can be determined. For example, a required resolution of 0.5 metres is equivalent to 0.75 wavelengths, where λ_s is equal to 0.66 metres (from step 4).

6. Determine the fractional bandwidth B/f_c of the system :

Using the result of step 5, the fractional bandwidth B/f_c of the system can be determined using Figure 3.13. For example, 0.75 wavelengths is equal to a fractional bandwidth of 100%.

7. Calculate the bandwidth B and centre frequency f_c :

The bandwidth B and centre frequency f_c can be calculated from the upper frequency bound f_U (step 4) and the fractional bandwidth B/f_c (step 6) using equation 3.22. For example, f_U of 200 MHz and a 100% fractional bandwidth implies that the bandwidth B and centre frequency f_c should be both equal to 130 MHz.

Table 3.5 summarises this example design of the waveform parameters.

Table 3.5: Design example of the waveform parameters

Required Performance :	Maximum Depth = 10 m Resolution = 0.5 m
Target Description :	metal sphere $\|\Gamma\|^2 = 0$ dB
Ground Material Properties :	$\epsilon_r = 5$ $Q = 16$
System External Loop Gain :	130 dB
Waveform Parameters :	$B/f_c = 100\%$ $B = 130$ MHz $f_c = 130$ MHz

3.5 Summary

This chapter has discussed the performance characteristics of ground penetrating radar in terms of *penetration* and *resolution*. Starting from the radar equation, it was shown that the *external loop gain* (G_L) parameter properly describes the penetration capability of GPR, and several valid assumptions can be made to ensure that this parameter is virtually independent of frequency. The *external loop loss* (L_E) parameter describes the loss mechanisms that are involved in signal propagation through the ground material and reflection from a target. To determine the maximum penetration depth R_{max}, the equation $L_E = G_L$ is solved for R_{max} using the nomogram technique. This method is complicated by the strong frequency dependence of L_E. It was also shown that there is a compromise between penetration and resolution for GPR, due to their conflicting dependence upon frequency.

To overcome the complications in analysing these two performance characteristics, the *constant Q model* was introduced into the L_E parameter, and the frequency dependent terms contained in L_E were normalised with respect to wavelength. A new parameter L_{E_Q} evolved which is valid for a wide variety of ground materials, and across a broad frequency spectrum. This allows characterisation of the maximum penetration depth in terms of a fixed number of wavelengths, which is constant for any frequency within the GPR spectrum. Using a similar procedure, the *fractional bandwidth* of the transmitter was related to the GPR resolution, and expressed as a fixed number of wavelengths which is also constant with frequency.

It was shown how a comparison of penetration and resolution between different GPR systems can be made, no matter what centre frequency is chosen for each. In addition, these processes provide a design tool whereby the GPR waveform parameters of *bandwidth* and *centre frequency* can be obtained to achieve an operating requirement in penetration and resolution.

The following chapters will utilise the principles developed here and focus on the theme of *Stepped-Frequency GPR* (SFGPR). In particular, the next chapter will review the developments and describe the stepped-frequency technique as it applies to GPR.

Chapter 4

The Stepped-Frequency Radar Technique

4.1 Introduction

In Chapter 1, it was described how *high-resolution radar* (HRR) or *ultra-wideband radar* (UWB) techniques enable the transmission of signals with wide fractional bandwidths and high mean powers. Of these techniques, the stepped-frequency method has distinct advantages. For example, each frequency tone generated by a stepped-frequency synthesiser is highly stable and uniformly spaced across a wide fractional bandwidth. In addition, the sampling of the received frequency signal is efficiently performed using low speed, high precision digitisers. A matched filter is then digitally applied (usually in the form of an inverse discrete Fourier transform) to transform the sampled frequency domain data to form high-resolution time domain profiles. From this, the two-way travel times and reflectivities of targets can be extracted. This chapter now focuses on the application of the stepped-frequency radar technique to ground penetrating radar, although the principles developed here are generic to any stepped-frequency radar.

In the past, *Stepped-Frequency Ground Penetrating Radar* (SFGPR) has found many successful applications. For example in 1983, it was reported that an experimental SFGPR system penetrated twice as far as impulse GPR [*Fowler*, 1983]. It is well documented that stepped-frequency radar has significant advantages over impulse radar systems in terms of processed mean energy and available bandwidth [*Ralston*, 1993; *Gill*, 1994; *Hamran et al.*, 1995]. These advantages are very relevant

to extending the performances of GPR in terms of penetration depth and resolving power (as defined in Chapter 3).

Section 4.2 of this chapter contains an comprehensive review of the past and current achievements in stepped-frequency GPR. The information contained in this review was obtained from the literature and also gathered during an overseas visit[1] to a conference (GPR'94) and organisations actively developing SFGPR where the most recent developments in the field and other historic information were revealed.

Sections 4.3 and 4.4 describe the stepped-frequency technique based on the frequency domain synthesis of short time-domain pulses and the processing to form synthesised range profiles. This description illustrates the resemblance that exists between the waveforms generated by an impulse radar and synthesised by a stepped-frequency radar. This material has been presented as a paper at the Fifth International Conference on Ground Penetrating Radar (GPR'94) in Kitchener, Canada on June 12-16, 1994 [*Noon, Longstaff & Yelf*, 1994].

Section 4.5 contains a simulation of a synthesised profile containing several buried targets. The simulation illustrates how the sidelobes of a strong reflector can mask the mainlobe of weaker targets which are received shortly afterwards in time. Section 4.6 describes a method to overcome this frequently occurring situation by processing the synthesised profile as maximum-phase waveforms.

4.2 A Review of Stepped-Frequency GPR

This review of SFGPR is divided into two sections. Section 4.2.1 contains a review of the work considered by the author to be the foundation of stepped-frequency GPR. Section 4.2.2 is a review of the current SFGPR developments known to the author. Often "stepped-frequency" has been referred in the literature as "stepped-chirp", "stepped-FM", "stepped FM-CW" and "synthesised pulse". This thesis uses the terms "stepped-frequency" and "synthesised pulse".

4.2.1 Foundation of Stepped-Frequency GPR

The original concept of using the synthesised pulse technique to locate dielectric reflections was tested in 1972 at the **Stanford Research Institute** [*Robinson,*

[1] In June 1994, the author visited several companies and universities developing stepped-frequency GPR in the USA and Canada.

Weir & Young, 1972; *Robinson, Weir & Young*, 1974]. The experimental system was based on a Network Analyser operating over selected frequency bands between 400-3560 MHz. Broadband TEM horn antennas were used to measure reflections from metal targets, paraffin and plastic foam in free space, and buried objects (*e.g.* brick, rock pile and paraffin block) in soil. It was reported that these objects were successfully detected in sandy-loam soil to depths of ten centimetres. These results were the first obtained to demonstrate the high-resolution capability of the stepped-frequency technique in discriminating between buried objects.

After this initial work, two major contracts were sponsored by the US Bureau of Mines to **ENSCO Inc.** from 1979 to 1981 [*Fowler, Hale & Houck*, 1981] and later **XADAR Corp.** between 1981-1983 [*Fowler*, 1983]. These contracts were to demonstrate the synthesised pulse radar in underground coal mining applications. A prototype system operating between 20-160 MHz measured reflections within the first 50 feet (15 metres) of a coal seam. In another reported experiment, the prototype received signals that were transmitted across a 200 foot (60 metre) coal pillar. This performance was claimed to be better (by a factor of two in penetration) than other GPR systems [*Pittman et al.*, 1984]. Two separate US patents were issued to ENSCO [*Fowler, Rubin & Still*, 1980] and XADAR [*Fowler, Wheatley & Davis*, 1985] as a result of these contracts. The system was also used to measure the permittivity and attenuation of underground coal *in situ* across the 20-160 MHz frequency band [*Houck*, 1985]. The US Bureau of Mines in Denver has used the XADAR synthesised pulse system for delay-time tomography to detect seam anomalies in coal pillars [*Foss & Leckenby*, 1987; *Dennen & Stroud*, 1991].

Independent research into stepped-frequency GPR was initiated at the **University of Toronto**, Canada around 1978. Several masters theses [*Wu*, 1979; *Freundorfer*, 1983], a doctoral thesis [*Freundorfer*, 1989], and numerous papers [*Iizuka & Freundorfer*, 1983; *Iizuka et al.*, 1984] have since been produced. The main applications for the GPR system were the detection of non-metallic buried objects and ordnance, and the measurement of lake ice thickness. (An almost identical radar system based around an unsolicited proposal by *Iizuka*, 1978 was built in Japan to measure the thickness of sea ice [*Uratsuka et al.*, 1988b; *Uratsuka et al.*, 1988a].) The radar operated at frequencies between 300-800 MHz, and could detect a buried metallic object (66 mm long) at a depth of 55 centimetres in soil with attenuation of 95 dB/m. The high resolving power of the system could differentiate between a 40 and a 66 millimetre long projectile, and also resolve the orientation of the target. Non-metallic objects were detected at shallower depths. A hardware modification

was later made to the system in an attempt to cancel the analogue RF leakage signal between the transmit and receive antennas [*Iizuka, Freundorfer & Iwasaki*, 1989]. In addition to these developments, there were other reported spin-offs from this research. For example, the system was used with monopole antennas to determine the electrical properties of the ground [*Freundorfer, Iizuka & Ramseier*, 1984]. As well, unidirectional semi-circular spiral antennas were later developed for use in both stepped-frequency and impulse GPR systems [*Iwasaki, Freundorfer & Iizuka*, 1994]. Recently, an experiment using the stepped-frequency radar system was conducted to investigate the scattering of radio waves from buried targets [*Freundorfer & Iizuka*, 1993].

The outcomes of these initial projects clearly demonstrate the feasibility of using stepped-frequency radar in GPR applications. Recent technological advances in wideband frequency synthesisers and digital signal processing hardware has now stimulated further interest in stepped-frequency GPR. There are now numerous groups around the world actively involved to some degree in the research and development, testing and commercialisation of SFGPR technology.

4.2.2 Current Developments in Stepped-Frequency GPR

The US Department of Energy (USDOE) **Special Technologies Laboratory** in California, USA have designed a "stepped FM-CW" or stepped-frequency GPR which operates between 196-708 MHz [*Koppenjan & Bashforth*, 1993b]. Several claims associated with the system hardware have been patented [*Vadnais et al.*, 1994]. Currently, the system is being marketed by **GeoRadar Inc.**, as the first commercially available stepped-frequency GPR. Performance results based on field trials have been published [*Koppenjan & Bashforth*, 1993a; *Bashforth & Koppenjan*, 1993; *Koppenjan & Martinez*, 1994; *PRC*, 1995]. Reportedly, a feature of the system is the narrow antenna beamwidth produced by logarithmic spiral antennas. This feature is claimed to reduce the characteristic hyperbolic response that is recorded as the radar passes over a buried spherical or cylindrical reflector. In addition, ground clutter is said to be reduced due to the focussed radar beam[2].

Coleman Research Corporation in Orlando, Florida have developed two stepped-frequency GPR systems. The "Earth Penetrating Radar Imaging System" (EPRIS) operates between 100 MHz and 1000 MHz [*Steinway & Barrett*, 1993; *Bar-*

[2]Recent results of the work by Aruna Gunawardena at The University of Queensland have shown that broad antenna beamwidths can be focussed using SAR processing [*Gunawardena & Longstaff*, 1995b; *Gunawardena & Longstaff*, 1996].

rett et al., 1993]. The principal application of EPRIS is the detection and location of unexploded ordnance and buried drums containing waste and contaminants. A US patent has been awarded for the radar design and its application in detecting buried containers holding hazardous waste [*Steinway et al.*, 1994b]. The EPRIS system coherently processes the radar data and produces synthetic aperture images of targets that are well resolved in two and three dimensions [*Steinway et al.*, 1994a]. Results obtained with a multiple sensor system based on radar (EPRIS) and magnetometer (EM61) sensors have been independently evaluated for unexploded ordnance detection and identification [*PRC*, 1995].

The second SFGPR system designed and built by Coleman Research Corporation is a "Mine Detection Radar". This design is similar to EPRIS, but has a frequency range of 1-3 GHz. The radar is fully portable and can offer real-time detection of twelve inch diameter targets buried six inches, and three inch diameter targets buried at a one inch depth.

The **Environmental Surveillance Technology Programme** (PFM) of Norway has used a stepped-frequency GPR (built in-house) since 1985 to measure glacier thicknesses of several hundred metres [*Ødegård et al.*, 1992]. Three frequency bands have been used: 5-30 MHz for mapping glacier thickness; 320-370 MHz for cold and temperate regimes; and 1-3 GHz for snow thickness [*Hamran*, 1992; *Hamran & Aarholt*, 1993]. The stepped-frequency radar waveform can be *range-gated* to suppress the antenna leakage signal and improve the dynamic range [*Hamran et al.*, 1995]. Considerable advances have been made by this group in the development of synthetic aperture [*Hamran & Aarholt*, 1993] and tomography inversion algorithms [*Hamran & LeComte*, 1993; *LeComte & Hamran*, 1993]. These algorithms are processed in the frequency-wavenumber domain (similar to migration), rather than in the time-space domain [*Cafforio, Prati & Rocca*, 1991].

The **Radar Systems and Remote Sensing Laboratory** at the University of Kansas (Centre for Research Inc.) has developed a stepped-frequency radar (called "KTRAN") for the Kansas Department of Transportation [*Pippert, Soroushian & Plumb*, 1993; *Pippert, Plumb & Soroushian*, 1994]. This radar has a bandwidth of 600 to 1112 MHz, and is used to detect moisture in the subgrade pavements of roads. Other research has involved *in situ* dielectric measurements using a short monopole antenna and a stepped-frequency reflectometer [*Plumb & Ma*, 1993].

A project at the **ElectroScience Laboratory** (ESL) of the Ohio State University (OSU) set out to design a pulsed stepped-frequency GPR [*Poirier*, 1993]. The pulsed-waveform is apparently used for range-gating, however, no further details

have been published. Work has also been carried out in developing spectral estimators using autoregressive techniques, and target classification using time-frequency distributions [*Walton*, 1993a]. *Poirier*, 1993 briefly mentioned the possibility of tuning the antennas at each frequency step to improve the coupling over a broad bandwidth. This idea was earlier proposed by *Fowler, Hale & Houck*, 1981. Variable frequency antennas have been fabricated at low frequencies for impulse GPR (22 to 47 MHz) [*Fenner*, 1992] and stepped-frequency GPR (1-3 MHz) [*Etten & Brown*, 1993], but appear to be unsuccessful at higher frequencies.

There are many examples in the literature of using a Network Analyser as a stepped-frequency GPR. **C.E.T.E.** together with the French Ministry of Transportation and two other French companies have taken part in the feasibility study of a synthetic pulse GPR [*Cariou*, 1992]. A radar system was built using a Network Analyser and a log periodic antenna and rough comparisons were made with a typical impulse radar.

The **Bureau for Geology and Mine Research** (BRGM) in France has also based a synthetic pulse GPR around a Network Analyser [*Pottecher*, 1990; *Pottecher*, 1992]. Several frequency bands have been used with loaded loop antennas (5-50 MHz), loaded bow-ties (15-150 MHz), bowties (200-1500 MHz) and a zig-zag spiral antenna (500-3000 MHz). *Pottecher*, 1992 very briefly described how the penetration performance of this system was enhanced using hardware range-gating (see Appendix E for a discussion on hardware range-gating).

The **Norwegian Geotechnical Institute** (NGI) has developed a stepped-frequency "Geo-radar", based on an HP 8753A Network Analyser [*Kong & By*, 1990; *By, Kong & Westerdahl*, 1992; *Kong & By*, 1995]. The novelty of the Geo-radar system is its ability to electronically switch between different frequency bands across a 10 MHz to 3 GHz bandwidth. Many field trials have been conducted with this system [*Westerdahl, Austvik & Kong*, 1992; *Kong, Kristiansen & By*, 1992]. Current activities are being concentrated towards radar tomography [*Kong et al.*, 1994] and asphalt profiling [*Kong & By*, 1995].

At **Tohoku Univeristy** in Japan, a network analyser based system operating between 0.3 MHz and 3 GHz has been used as a directional borehole radar [*Sato, Satoshi & Hiroaki*, 1994]. Data collected using this radar at an experimental mine has been processed using a time-frequency distribution to discriminate between different propagation modes in reflection waves.

The **US Bureau of Mines** has developed a "Radar Coal Thickness Sensor" using the stepped-frequency technique [*Chufo*, 1993; *Chufo & Johnson*, 1993]. This sensor automatically measures the roof or pillar thicknesses of underground coal mines. The system consists of a Network Analyser operating between 0.6-1.4 GHz, and uses a monostatic air-launched antenna which is retracted vertically (for roof measurement) or horizontally (for pillar measurement) from the coal surface. Radar measurements are taken at several positions, and using an appropriate model, the dielectric constant of the surface material and a true measurement of coal thickness are determined. Accurate *in situ* measurements have been made of coal thicknesses up to six inches. Work is continuing towards the development of a sensor array which includes this GPR system to support an automated continuous mining machine [*Chufo*, 1995].

Research began at the **University of Cape Town** in 1990 to investigate stepped-frequency and synthetic aperture radar (SAR) techniques for GPR [*Garvin*, 1991; *Garvin & Inggs*, 1991]. A Network Analyser was used to generate a wide range of frequencies from UHF to X-band. Polarimetric measurements of buried objects have been taken in an attempt to discriminate between different objects [*Langman & Inggs*, 1994]. In addition, high-resolution spectral estimators (based on Prony's method) have been trialed on SFGPR data [*Langman, Inggs & Flores*, 1994]. Current research is now directed towards developing an inexpensive system operating between 300-1000 MHz [*Kabutz*, 1995]. The current system employs a hardware cancellator which aims to suppress the leakage signal between the transmit and receive antennas [*Kabutz, Langman & Inggs*, 1994].

The **Lincoln Laboratory** at MIT uses a ground-based rail SAR (stepped-frequency) system to image objects buried in the ground, or objects obscured in foliage [*Blejer, Frost & Scarborough*, 1994]. The system is built around an HP Network Analyser and collects data over a 0.25 to 1 GHz frequency band. The transmitter is pulsed and the receiver is range-gated to suppress the antenna leakage signal. The receiver is fully polarimetric to assist in the identification of buried targets.

Another ground-based rail SAR (stepped-frequency) system has been developed by **The Environmental Research Institute of Michigan** (ERIM) [*Sheen et al.*, 1993a; *Sheen et al.*, 1993b]. This system is based on an HP Network Analyser operating between 400-1300 MHz and produces full polarimetric images of objects obscured in foliage and buried in the ground.

At the **University of Illinois**, a Network Analyser is used to obtain data between 2 and 12 GHz for non-destructive evaluation of pipes and rods [*Weedon, Chew & Ruwe*, 1994; *Chew, Weedon & Moghaddam*, 1995]. A switchable array of 11 antennas is used to image the interior of these objects.

In 1987, the **Swedish National Defense Research Establishment** (FOA) initiated the development of an airborne SAR system called *CARABAS* (acronym for *Coherent All Radio Band Sensing*) [*Gustavsson et al.*, 1993; *Hellsten et al.*, 1994]. This system is a stepped-frequency radar operating between 20-90 MHz. The motivation for the airborne SAR system was foliage and ground penetration applications. In order to collect the data within the coherent processing interval (which is limited by the aircraft speed), several bursts in frequency sub-bands are transmitted, which together cover the 20-90 MHz range in quick succession. SAR processing is carried out in ground-based equipment after the data is collected. The CARABAS system as well as other airborne systems (such as SRI FOLPEN II and EMS-20 systems mentioned in Section 2.1.4) were trialed at the Yuma Proving Ground, Arizona in 1993 [*Mirkin et al.*, 1994; *Mirkin et al.*, 1995].

The **Metratek** Model 200 GPR is a stepped-frequency SAR system (frequency range selectable between 100-2000 MHz) which can operate as a ground-based (portable) or airborne (from a helicopter) sensor [*Metratek*, 1994]. The purpose of the system is primarily the detection buried landmines and culverts [*PRC*, 1995].

Finally, it is worth mentioning a US patent owned by **Earth Sounding International** describing a stepped-frequency radar system for probing the earth using frequencies between 1 and 3 MHz [*Etten & Brown*, 1993]. At these frequencies, the ground attenuation is of the order of 0.01 dB/m and penetration depths of the order of kilometres are possible. The invention consists of a 1 kW peak power transmitter with a bandwidth of 500 kHz within the 1-3 MHz frequency band. The antennas are resonant loop designs which are 8 feet (2.4 metres) square and 2 feet (0.6 metres) high. To obtain maximum performance in penetration, the integration time is approximately 5 minutes. A novelty of the invention is the ability to tune the antennas at each frequency step by switching certain reactive elements in and out. This enables matching of the resonant frequency of narrowband antennas with each transmitted frequency step. Another novel idea contained in the patent is the use of two receiving antennas; one as the main receiver and the other as a reference placed at a distance away from the main receiving antenna. This setup provides a means of compensating for the frequency dependent antenna gain and phase characteristics, and by using a spatial notching technique, of suppressing the direct antenna signal.

4.3 Impulse Synthesis using Stepped-Frequency

Many texts, reports and papers describe stepped-frequency radar (for example, *Robinson, Weir & Young*, 1974; *Fowler, Hale & Houck*, 1981; *Iizuka et al.*, 1984; *Nathanson*, 1991; *Lane*, 1993; *Wehner*, 1995). Appendix A contains a rigorous mathematical description of the stepped-frequency technique. This section presents an alternative description of the stepped-frequency technique, and illustrates the resemblance that exists between waveforms generated by the impulse radar, and the waveforms synthesised by the stepped-frequency radar.

The ideal time waveform generated by an impulse radar can be represented by Figure 4.1(a). The pulse rises to a *peak voltage* V_p almost instantaneously and is held for a short duration (*pulsewidth* τ is usually between 0.6-10 nanoseconds for most GPR applications) before returning to zero volts. Figure 4.1(b) represents the corresponding frequency spectrum of the impulse. The -4 dB bandwidth (denoted BW) of the impulse spectrum is equal to $1/\tau$ Hertz. The majority of the impulse energy is concentrated around the baseband frequencies near zero Hertz. Clearly, much shorter pulsewidths (with ultra-fast risetimes) are necessary to generate higher frequency impulses.

The *range resolution* ΔR of the impulse signal (defined in Chapter 1) is equal to $v/2BW$ or $v\tau/2$ metres, where v is the propagation velocity. The *two-way travel time resolution* Δt is equal to $1/B$ seconds.

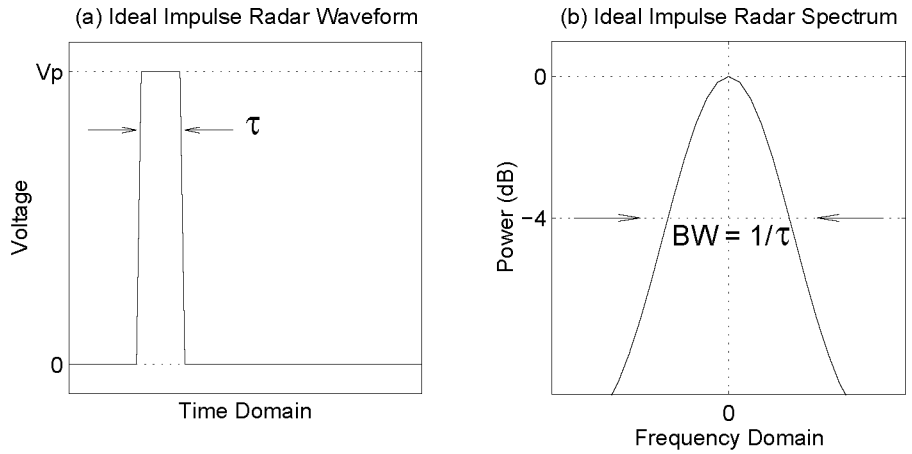

Figure 4.1: (a) An ideal impulse radar waveform with a peak voltage of V_p and a pulsewidth of τ seconds; (b) the corresponding spectrum with a -4 dB bandwidth (BW) equal to $1/\tau$ Hertz.

The impulse is transmitted through a wideband antenna with a frequency response resembling a bandpass filter with a -4 dB *bandwidth* of B Hertz and a *centre frequency* of f_c Hertz. It is desirable that the spectrum of the impulse BW is larger than or equal to the frequency bandwidth of the antenna, so that the full antenna bandwidth is used to transmit the impulse. Figure 4.2(a) illustrates an antenna bandwidth B (segmented line) centred at $\pm f_c$ Hertz and the impulse spectrum (connected line - same as Figure 4.1(b)) centred at zero Hertz.

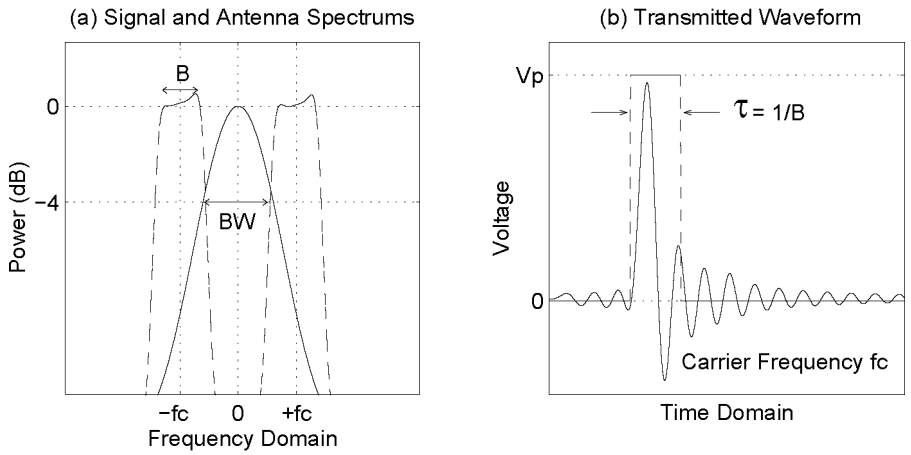

Figure 4.2: (a) The impulse radar spectrum (connected line - same as Figure 4.1(b)) with antenna bandwidth (segmented line) B centred at $\pm f_c$ Hertz; (b) the transmitted waveform with a pulsewidth $\tau = 1/B$ seconds and a carrier frequency equal to f_c Hertz.

The resulting spectrum of the transmitted signal through the antenna is the product of the impulse spectrum with the frequency response of the antenna. The transmitted impulse (Figure 4.2(b)) has a pulsewidth determined by the antenna bandwidth (*i.e.* $\tau = 1/B$), and a *carrier frequency* equal to the antenna centre frequency f_c. This waveform can be interpreted as an envelope modulation of a carrier frequency. The energy in the impulse waveform near zero Hertz is not radiated by the antenna, which reduces the bandwidth and limits the mean energy of the transmitted impulse. This effect combined with the difficulty of generating high mean powers in short-time pulses (as discussed in Chapter 1), places a practical limit on the penetration and resolving capability of the impulse technique.

A more appropriate waveform with a high antenna transmission efficiency has its entire spectrum and energy contained within the antenna passband. One such waveform is a *pulse-modulated carrier* or *monocycle* as illustrated in Figure 4.3(a).

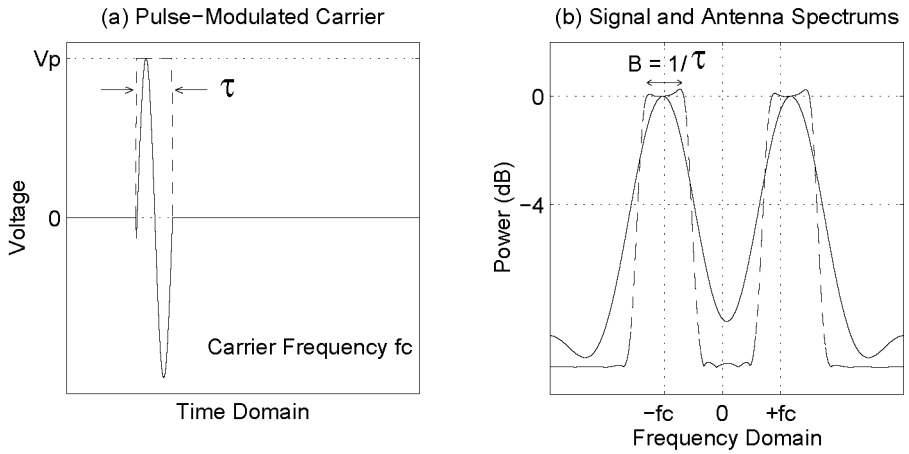

Figure 4.3: (a) Pulse-modulated carrier signal with a pulsewidth of τ seconds and a carrier frequency of f_c Hertz; (b) the corresponding spectrum with a -4 dB bandwidth $B = 1/\tau$ and centred at $\pm f_c$ Hertz. Much higher transmission efficiencies are possible with this signal as compared with the impulse signal of Figure 4.2.

This waveform is similar to the waveform introduced as Figure 1.1. A continuous wave (CW) signal with a frequency equal to the antenna centre frequency f_c is modulated in amplitude by the impulse waveform of Figure 4.1(a). This modulation process shifts the centre of the impulse spectrum from zero Hertz (Figure 4.1(b)) to $\pm f_c$ Hertz (Figure 4.3(b)). Most of the signal energy is now contained within the antenna passband. This enables much higher efficiencies in energy transmission of the waveform through the antennas.

Figure 4.4 is the block diagram of the pulse-modulated carrier radar system (or simple pulsed radar system as was referred in Chapter 1). A fixed CW source with the carrier frequency of f_c Hertz is switched on and off with an impulse envelope of width τ seconds to give a peak voltage of V_p. The reflected signals are received and down-converted to baseband through mixing with a reference signal of the CW frequency and low pass filtering. In Section 1.2, the necessity of deriving *in-phase* (I) and *quadrature* (Q) components when down-converting a bandpass signal to baseband was explained, and is applicable here.

The bandwidth of the baseband receiver is broad to enable sampling of the impulse envelope. As a result, high-speed digitisers (with low precision) are necessary for efficient sampling. To reduce the sampling frequency constraints on the digitisers, a narrower-band receiver matched to a wider pulse could be used, but this reduces the resolving power (as discussed in Chapter 1). This problem is common to both the monocycle and impulse radar.

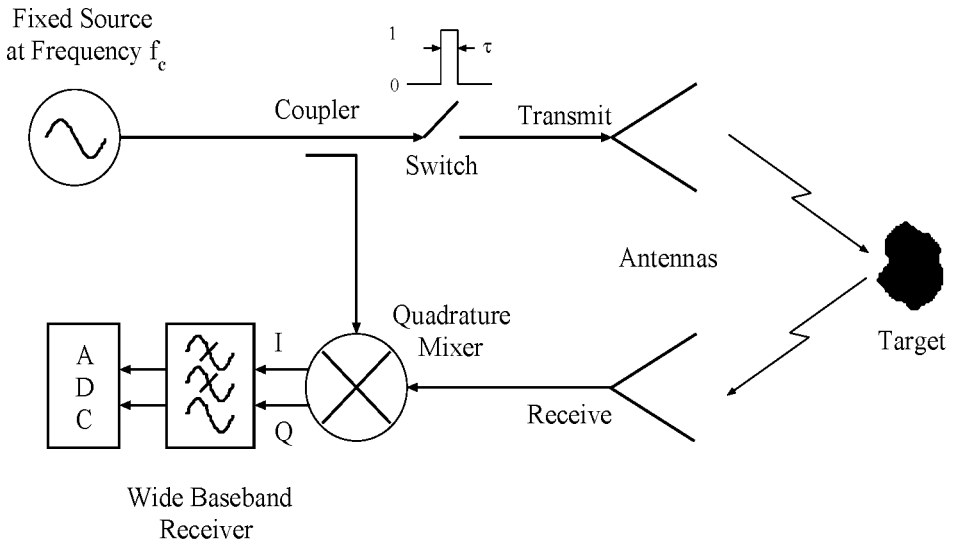

Figure 4.4: Block diagram of a pulse-modulated carrier radar system

Another problem which is common to both radars is the limited mean power that can be generated in short-time impulses (as described in Chapter 1). Once again, longer pulsed-waveforms with higher duty cycles can be generated to improve the mean power, but the resolving power is compromised.

Instead of transmitting a single pulse waveform with a continuous spectrum, a pulse train can be *synthesised* by transmitting discrete frequency components of the spectrum (Figure 4.3(b)) as CW waveforms. This type of radar is called a *multiple discrete-frequency radar.* The block diagram for this system is contained in Figure 4.5.

This radar system simultaneously transmits a discrete number of n multiple-frequencies from a lower frequency bound f_L to an upper frequency bound f_U Hertz, all linearly spaced in frequency by Δf Hertz across the antenna bandwidth B ($= f_U - f_L$). The centre of the bandwidth is set to coincide with the centre frequency of the antenna f_c. Figure 4.6(a) displays the frequency spectrum as a line spectrum containing these multiple frequencies.

All frequencies are simultaneously detected using a wideband receiver. The resulting time waveform of this line frequency spectrum is called a *synthesised pulse-modulated carrier* (Figure 4.6(b)). The pulsewidth τ of each synthesised pulse is

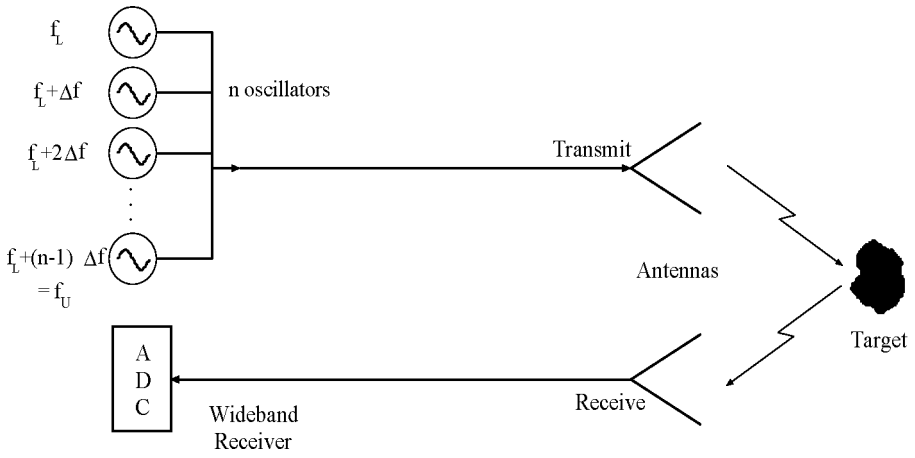

Figure 4.5: Block diagram of a discrete multiple-frequency radar which uses a bank of CW oscillators to simultaneously transmit n discrete frequencies spaced by Δf Hertz between f_L and f_U Hertz, across a bandwidth B.

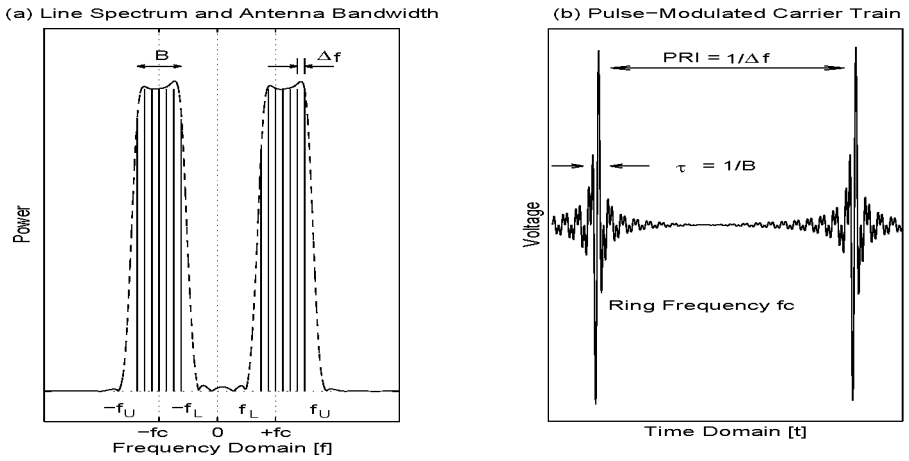

Figure 4.6: (a) The discrete multiple-frequency spectrum which contains n discrete frequencies from f_L to f_U Hertz and spaced by Δf Hertz across the antenna bandwidth B, and centred at the antenna centre frequency f_c; (b) the resulting synthesised pulse-modulated carrier waveform with pulsewidth τ equal to $1/B$ seconds and a carrier frequency of f_c Hertz. The pulse repetition frequency PRF $(= 1/(PRI))$ is equal to Δf Hertz.

equal to $1/B$ seconds and has a carrier frequency equal to the centre frequency of the antenna f_c. The range resolution ΔR of these synthesised pulses is equal to $v/2B$ or $v\tau/2$ metres. The two-way travel time resolution Δt is equal to $1/B$ seconds.

Because the frequency spectrum is a line spectrum, the synthesised pulses form a pulse train which is periodic in time with a synthesised *pulse repetition interval*

PRI equal to $1/\Delta f$ seconds. This repetition interval is equivalent to an impulse waveform with a *pulse repetition frequency* ($PRF = 1/PRI$) equal to Δf Hertz. From Chapter 1, the PRF was related to the *maximum unambiguous range* R_{max} to a target by equation 4.1 (compare with equation 1.7).

$$R_{max} = \frac{v}{2(PRF)} = \frac{v(PRI)}{2} = \frac{v}{2\Delta f} \tag{4.1}$$

Due to the transmission of CW signals, the mean power is equal to the peak power. However, the wideband nature of the receiver bandwidth still requires high-speed digitisers to efficiently sample the received waveform.

Rather than transmitting all the spectral lines of the synthesised pulse simultaneously, the CW frequencies can be transmitted separately. Each received frequency is in turn down-converted to I and Q narrow baseband signals using a quadrature mixer. These signals can now be sampled efficiently using high precision, low speed digitisers. The narrow bandwidth of the receiver also has a higher immunity to *radio frequency interference* (RFI). This system is called the *stepped-frequency radar* and is shown schematically in Figure 4.7.

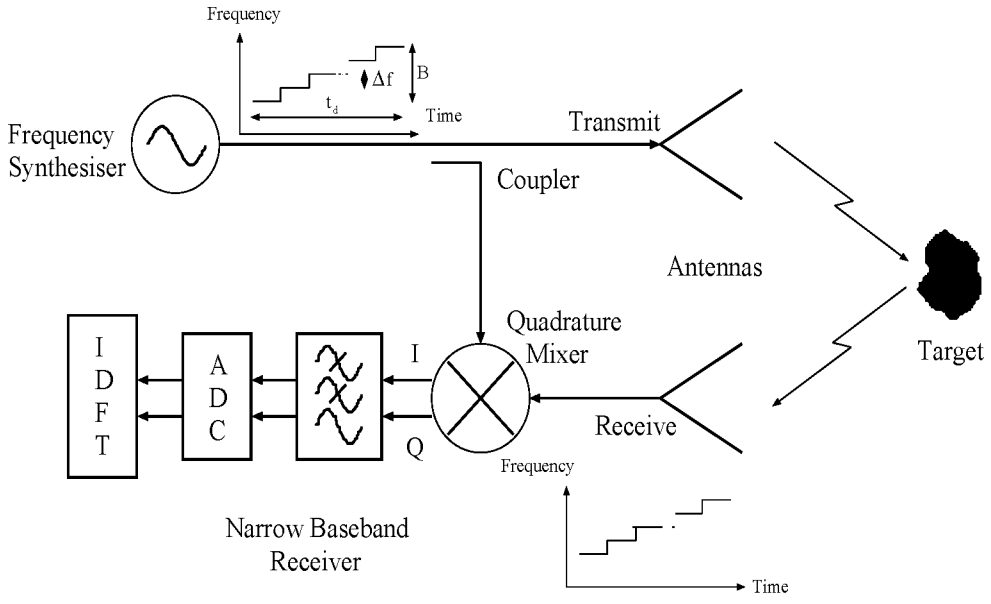

Figure 4.7: Block diagram of a stepped-frequency radar (same diagram as Figure 1.8)

The stepped-frequency radar uses a frequency synthesiser to individually step (n times) a CW frequency tone in Δf Hertz intervals across the bandwidth B. Figure 4.8 illustrates the stepping procedure from f_L to f_U (with a centre frequency

f_c and bandwidth $B = f_U - f_L = (n-1)\Delta f$). The total time in seconds to complete all the frequency steps is called the *ramp repetition interval* (RRI). This time must be less than or equal to the *coherent processing interval* (CPI) as determined by the maximum radar platform velocity which allows the synthesis of an undistorted range profile [*Lane*, 1993]. Table 4.1 summarises the stepped-frequency radar parameters and their relationships.

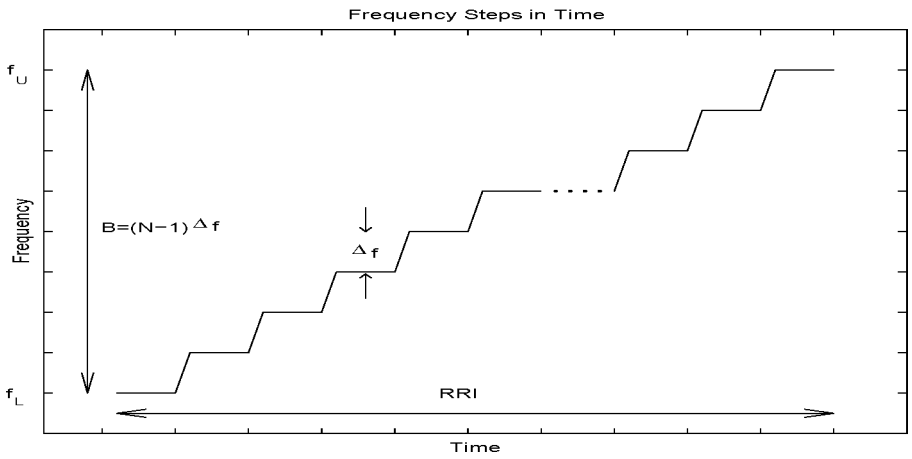

Figure 4.8: The n narrowband frequencies are progressively transmitted from f_L to f_U in Δf Hertz steps across the bandwidth B. The time to transmit all frequency steps is RRI seconds ($\leq CPI$).

Table 4.1: Stepped-frequency radar parameters

Parameter	**Symbol**	**Formula**
lower frequency	f_L	
upper frequency	f_U	
bandwidth	B	$= f_U - f_L$
centre frequency	f_c	$= f_L + B/2$
fractional bandwidth	B/f_c	$= B/f_c$
number of steps	n	
frequency step interval	Δf	$= B/(n-1)$
range resolution	ΔR	$= v/(2B)$
time resolution (two-way)	Δt	$= 1/B$
maximum unambiguous range	R_{MAX}	$= v/(2\Delta f)$
pulse repetition frequency	PRF	$= \Delta f$
pulse repetition interval	PRI	$= 1/PRF$
coherent processing interval	CPI	
ramp repetition interval	RRI	$\leq CPI$

4.4 Minimum-phase Processing

The I and Q data samples taken at each of the frequency steps are placed into a complex frequency domain array $(I + jQ)$ of length n. This frequency data is transformed to the time domain to form a synthesised pulse using the following procedure [*Walton*, 1994] :

1. Begin with a frequency domain array of length n containing the complex frequency data $I + jQ$.

2. Insert the frequency domain array into an N element array (where $N > n$) so that zero Hertz corresponds to element zero (where the data point increment is equal to the frequency step size of Δf Hertz). The complex conjugate values of the frequency domain array are inserted into the negative frequency portion (or second half) of the N element array. All the remaining elements in the array are padded with zeros.

3. Perform an N point IDFT on the array.

4. The result is an N point time domain array.

Figure 4.6(a) above illustrates the frequency domain array of the $I + jQ$ data after step 2 of the procedure. The frequency domain array resembles the frequency spectrum of the multiple discrete-frequency radar. An IDFT of the frequency data results in the synthesised pulse of Figure 4.6(b), containing the carrier waveform (of frequency f_c) within the envelope (of width $1/B$ or $1/(f_U - f_L)$).

Transforming the frequency domain array using the above procedure suggested by *Walton*, 1994 results in the time waveform appearing only in the real component of the time domain array. The imaginary component of the time domain array is zero. Hence, it is not possible to derive the envelope of the synthesised pulse by taking the magnitude of the time domain array in step 4, nor can the phase be determined. The benefit of viewing the envelope is that it truly represents the resolution of the data (see Figure 1.3) and does not clutter the profile with multiple cycles of the carrier waveform [*Annan*, 1993]. However, the information concerning the phase of the carrier waveform is lost. The phase of the carrier is useful information which indicates the phase-change associated with the sense-of-reflection of Γ for buried targets (see Section 3.2.1).

The magnitude and phase of the time domain array of step 4 can be determined using the *Hilbert transform* [*Oppenheim & Schafer*, 1989]. The Hilbert transform inserts a $\pi/2$ phase-delayed version (an orthogonal component) of the real data into the imaginary component of the array. The result is a complex time domain array which enables the magnitude (or envelope) and phase to be obtained. This method involves extra digital signal processing of the stepped-frequency radar data.

An alternative method can be used to achieve the same result, but does not involve extra digital signal processing. Rather than transforming the frequency domain data to the time domain using the above procedure (as suggested by *Walton*, 1994), a modified procedure can be used which preserves the magnitude (envelope) and carrier phase information of the synthesised waveform.

The modification is in step 2 of the above procedure by *Walton*, 1994. The frequency domain array of step 1 is inserted into an N element array (where $N > n$) in the same way so that zero Hertz corresponds to element zero (where the data point increment is equal to Δf). However, the complex conjugate values are not inserted into the negative frequency portion of the array. Instead, the negative frequencies are padded with zeros. Only the positive frequency elements corresponding to the $I + jQ$ frequency domain array are non-zero. An N point complex IDFT on this frequency domain array will produce a *complex* time domain array. The frequency and time domain arrays of this modified procedure are illustrated in Figure 4.9.

The real and imaginary components of the time domain array are now orthogonal. Therefore, the magnitude of the complex time domain array produces the envelope of the synthesised waveform, and the angle corresponds to the phase of the reflection coefficient.

Figure 4.9(a) illustrates the frequency spectrum of the stepped-frequency radar with the envelope and carrier phase preserved. Note that the spectrum contains only positive frequency values. This spectrum is mathematically represented as the discrete frequency function $X[f]$ in equation 4.2.

$$X[f] = \text{rect}\left[\frac{f - f_c}{B}\right] \tag{4.2}$$

The $X[f]$ spectrum is a rectangular function of width B Hertz, and centred at $+f_c$ Hertz to preserve the carrier phase. The envelope information is preserved by omitting the complex conjugate from the negative frequencies (at $-f_c$ Hertz).

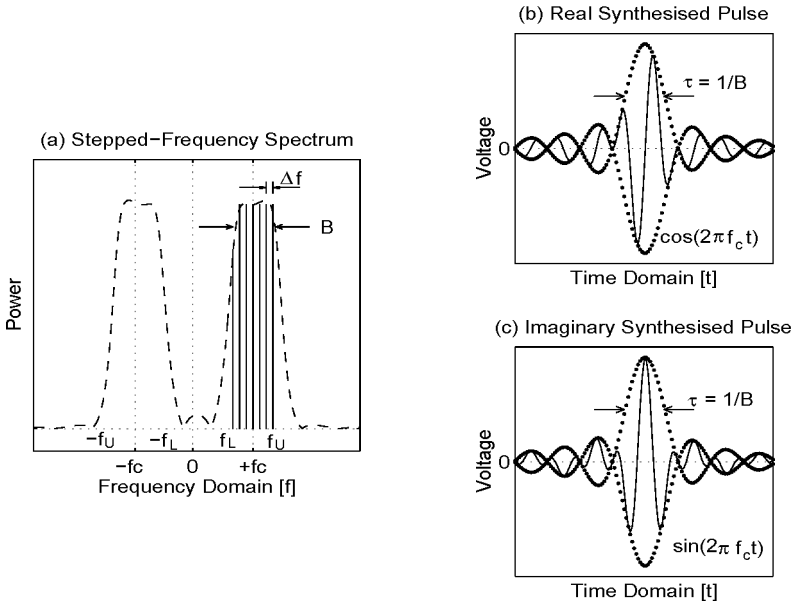

Figure 4.9: (a) The stepped-frequency spectrum consisting only of positive frequencies; (b) the corresponding real and (c) imaginary synthesised pulses with envelope widths of $\tau = 1/B$ seconds and carrier frequencies of f_c Hertz. The dotted lines are the envelopes of the synthesised pulse. The phase of the pulse is obtained by calculating the angle of the complex time domain array. The pulse repetition frequency PRF is equal to Δf Hertz.

A complex IDFT applied to $X[f]$ results in a *complex* or *analytic* signal which contains two orthogonal waveforms. Figures 4.9(b) and (c) display the real and imaginary components of the synthesised pulses. These discrete waveforms are represented as $x[t]$ in equation 4.3.

$$x[t] = \frac{B \sin(\pi B t)}{\pi B t} e^{j2\pi f_c t} = B\text{sinc}(Bt)\left[\cos(2\pi f_c t) + j \sin(2\pi f_c t)\right] \tag{4.3}$$

The sinc(Bt) envelope (dotted waveforms in Figures 4.9(b) and (c)) of $x[t]$ has a -4 dB envelope width equal to $1/B$ or $1/(f_U - f_L)$ seconds. The carrier waveform of $x[t]$ is a complex sinusoid of frequency f_c Hertz, represented as a cosine function in the real domain (Figure 4.9(b)), and as a sine function in the imaginary (Figure 4.9(c)). The number of carrier cycles within the envelope is related by the fractional bandwidth (B/f_c). The time-domain waveform described by $x[t]$ is the equivalent time-domain pulse that is synthetically transmitted by the stepped-frequency radar after processing. The stepped-frequency technique is often called the *synthesised pulse* technique because a time-domain impulse waveform is synthesised in the frequency domain.

The synthesised pulse consists of a *mainlobe* of width $1/B$, and *sidelobes* which roll-off on both sides of the mainlobe. (In this thesis, *sidelobes* are referred to the time or range sidelobes of the synthesised pulse, not the spatial sidelobes of antennas.)

The sidelobes of the sinc(Bt) envelope are the result of the IDFT on the rect$(f - f_c)/B$ spectrum. The symmetry of the sidelobes about the mainlobe of the synthesised pulse is the characteristic of a *zero-phase cepstrum* [*Oppenheim & Schafer*, 1989]. A zero-phase signal is produced by a *noncausal* system which has the poles and zeros of $X(z)$ ($\mathcal{Z}$ transform of $x[t]$) on the unit circle. Up to this point, the stepped-frequency radar can be thought of as a noncausal system which processes the $I + jQ$ data as zero-phase signals.

The transmitted waveform of an impulse radar (Figure 4.2(b)) has its sidelobes falling on the right side or behind in time of the mainlobe. This is a *minimum-phase* signal, and is produced by a *causal* system which has the poles and zeros of $X(z)$ inside the unit circle. It is *nonanticipative* in time and includes all stable signals generated in real time (*e.g.* an impulse radar).

It is now shown how the zero-phase synthesised pulse of a stepped-frequency radar can be processed to resemble a causal impulse radar waveform.

The *causality theorem* states that a zero-phase signal can be changed to minimum-phase by switching the causality of the *complex cepstrum* from non-causal to causal [*Oppenheim & Schafer*, 1989]. Equation 4.4 is the relationship between $X[f]$ and its complex cepstrum $\hat{X}[f]$ ($\log_c$ is a complex logarithm).

$$\hat{X}[f] = \log_c(X[f]) = \log(|X[f]|) + j \arg(X[f]) \tag{4.4}$$

To change the complex cepstrum $\hat{X}[f]$ to minimum-phase (*i.e.* causal), equation 4.5 is used. The real part of $\hat{X}_{MIN}[f]$ is identical to the real part of $\hat{X}[f]$, and the imaginary part of $\hat{X}_{MIN}[f]$ is equal to the the negative value of the $\pi/2$ phase-delayed version (*i.e.* the Hilbert transform $\mathcal{H}[f]$) of the real part of $\hat{X}[f]$.

$$\hat{X}_{MIN}[f] = \log(|X[f]|) - j\,\mathcal{H}[f] \log(|X[f]|) \tag{4.5}$$

The Hilbert transform relationship between the real and imaginary parts of the complex cepstrum is the requirement for causality [*Oppenheim & Schafer*, 1989]. Because $\hat{X}_{MIN}[f]$ is causal, it follows by the causality theorem that $X_{MIN}[f]$ (and hence $x_{MIN}[t]$) will be causal or minimum-phase. The spectrum $X_{MIN}[f]$ is calculated using equation 4.6, and the minimum-phase signal is deduced using equation 4.7 ($\exp_c$ is a complex exponential function and $\mathcal{F}^{-1}$ is the IDFT).

$$X_{MIN}[f] = \exp_c(\hat{X}_{MIN}[f]) \tag{4.6}$$

$$x_{MIN}[t] = \mathcal{F}^{-1}\{X_{MIN}[f]\} = \mathcal{F}^{-1}\left\{\exp_c(\hat{X}_{MIN}[f])\right\} \tag{4.7}$$

$X_{MIN}[f]$ is a *minimum-phase complex window function* which has a unity magnitude response and a phase response which converts zero-phase signals to minimum-phase signals. This complex window function can be multiplied with the $I + jQ$ frequency data prior to the IDFT, in the same way as a standard window function (*e.g.* Hanning). Figure 4.10(a) displays the unchanged magnitude of the stepped-frequency spectrum when the complex window is applied. However, the phases of each frequency step are altered by the complex window function to produce *minimum-phase synthesised pulses* (Figures 4.10(b) and (c)).

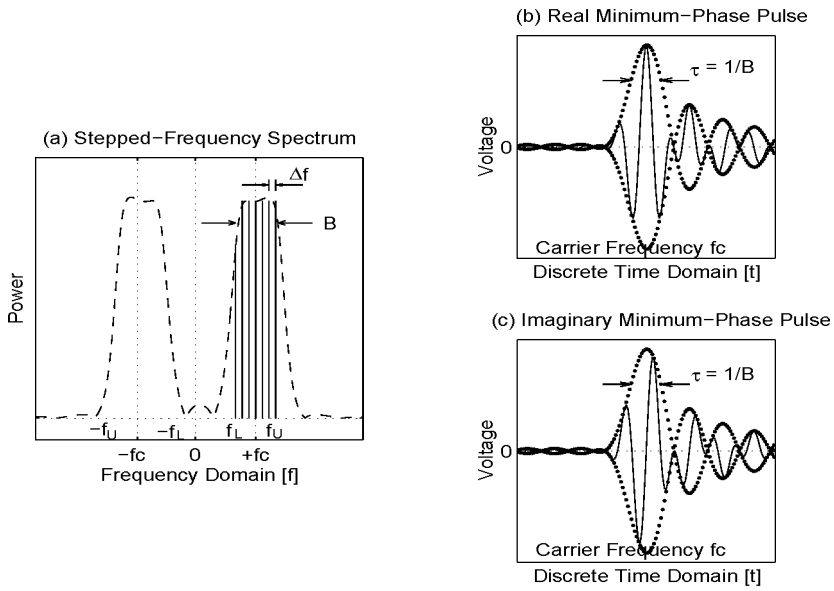

Figure 4.10: (a) Stepped-frequency spectrum with a minimum-phase complex window applied. The magnitude spectrum is unchanged, but the phase spectrum is altered to produce minimum-phase synthesised pulses after the IDFT; (b) the corresponding real and (c) imaginary minimum-phase synthesised pulses.

The sidelobes of the synthesised pulse now fall to the right side or behind in time of the mainlobe. This waveform can be considered as the equivalent time-domain pulse that is synthetically transmitted by the stepped-frequency radar after minimum-phase processing. The minimum-phase sidelobes of this synthesised pulse now resemble the sidelobes of the waveform generated by an impulse radar (compare with Figure 4.2(b)). The small amount of signal aliased to the left side of the mainlobe exists because the complex cepstrum cannot be completely formulated with discrete data, since the cepstrum of a real signal is infinite [*Turner*, 1993]. These are equivalent to the tails of the earlier pulses.

This section has detailed the synthesis of a causal synthesised pulse by a stepped-frequency radar using minimum-phase processing. The following section contains a simulation of the synthesised time profiles corresponding to several buried targets.

4.5 A Simulation of Synthesised Profiles

Consider a number $p = 1, 2, \ldots m$ smooth interface targets, each with a reflection coefficient of $\Gamma_p = |\Gamma_p| \exp(j\phi_p)$ and located at depths of R_p metres in a lossless ground material. Assuming a constant propagation velocity of v for the ground material, the two-way travel time t_p to each target is equal to $2R_p/v$ seconds.

A stepped-frequency GPR transmits the frequency spectrum $X[f]$ (equation 4.2) which is effectively a synthesised impulse $x[t]$ in the time domain (equation 4.3). The spectrum of the reflected signal $Y[f]$ from the smooth interface targets are described by equation 4.8.

$$Y[f] = \sum_{p=1}^{m} |\Gamma_p| e^{j\phi_p} \operatorname{rect}\left(\frac{f - f_c}{B}\right) e^{-j(2\pi \frac{2R_p}{v} f)} \tag{4.8}$$

The inverse Fourier transform of $Y[f]$ results in the zero-phase *synthesised profile* of the targets, which is described by $y[t]$ (equation 4.9). The synthesised profile is an amplitude versus time function which contains the relative amplitudes $|\Gamma_p|$, two-way travel times t_p and phase changes ϕ_p of the reflections as recorded by the radar.

$$y[t] = \sum_{p=1}^{m} \left\{ |\Gamma_p| e^{j\phi_p} B \operatorname{sinc}[B(t - \frac{2R_p}{v})] \, e^{j[2\pi f_c (t - \frac{2R_p}{v})]} \right\} \tag{4.9}$$

For convenience, equations 4.8 and 4.9 can be expressed more generally in terms of these dimensionless quantities: *fractional frequency* $[\frac{f}{B}]$ (in equation 4.10) and *resolution bin* $[tB]$ (in equation 4.11). There are n resolution bins (n is equal to the number of frequency steps) in the synthesised profile, and each bin corresponds to a two-way travel time resolution of $1/B$ seconds (B is the transmitted bandwidth).

$$Y[\frac{f}{B}] = \sum_{p=1}^{m} |\Gamma_p| e^{j\phi_p} \operatorname{rect}\left([\frac{f}{B}] - \frac{f_c}{B}\right) e^{-j(2\pi t_p B [\frac{f}{B}])} \tag{4.10}$$

$$y[tB] = \sum_{p=1}^{m} \left\{ |\Gamma_p| e^{j\phi_p} B \operatorname{sinc}[([tB] - t_p B)] \, e^{j\{2\pi \frac{f_c}{B} ([tB] - t_p B)\}} \right\} \tag{4.11}$$

The expressions for $Y[\frac{f}{B}]$ and $y[tB]$ are now in a general form for the simulation. Assume there are three interface targets ($p = 3$) at depths expressed as a number of resolution bins $t_p B$, and with reflection coefficients $|\Gamma_p| e^{j\phi}$ as recorded in Table 4.2.

For this simulation, the fractional bandwidth B/f_c of the radar is assumed to be unity, with the bandwidth centred at a fractional frequency $\frac{f}{B}$ of unity also (*i.e.* $0.5 \leq \frac{f}{B} \leq 1.5$).

Table 4.2: Simulation of three dielectric interface targets

Reflector p	**Resolution Bin** t_pB	**Reflection Coefficient** $\lvert\Gamma_p\rvert\, e^{j\phi_p}$
1	5	$1.0\, e^{j0}$
2	10	$0.5\, e^{j\pi}$
3	20	$0.2\, e^{j0}$

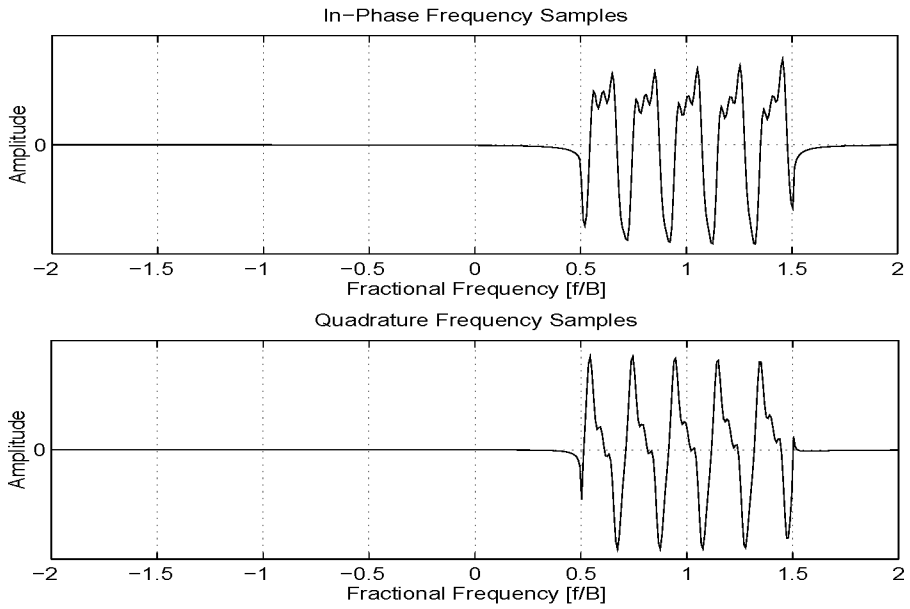

Figure 4.11: In-phase (I) and quadrature (Q) frequency domain arrays ($N = 1024$) of the simulation example of Table 4.2. Note that there are no negative frequency values. The radar has a fractional frequency range $\frac{f}{B}$ of $0.5 \leq \frac{f}{B} \leq 1.5$ with $n = 128$ frequency steps.

The stepped-frequency radar in the simulation transmits $n = 128$ frequency steps between $0.5 \leq \frac{f}{B} \leq 1.5$. The I and Q data for each frequency step is placed in an $I + jQ$ frequency domain array of length $n = 128$. To transform the frequency domain data to time domain data, the modified procedure of *Walton*, 1994 (outlined in the previous section) which preserves the envelope and carrier phase information is used. The $n = 128$ point frequency domain array is placed in an $N = 1024$ point array at the corresponding positive frequency elements, with the remaining elements padded with zeros. Figures 4.11(a) and (b) are the $N = 1024$ point I and Q arrays

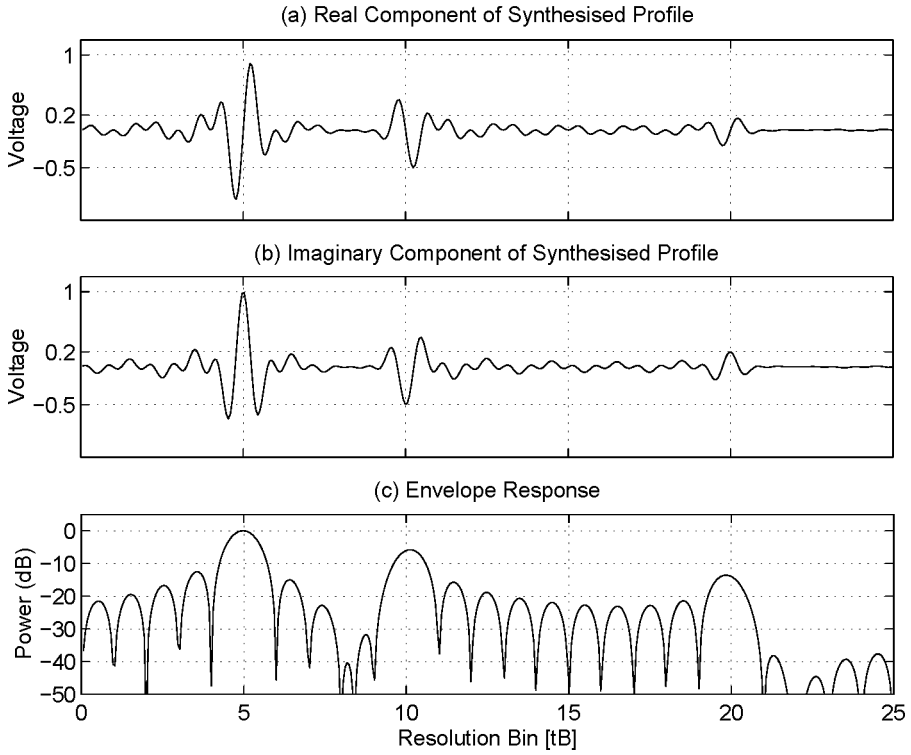

Figure 4.12: (a) Real and (b) imaginary components of the zero-phase synthesised profile and (c) envelope response of the simulation of Table 4.2.

for the simulation of Table 4.2. This complex signal is represented by the $Y[\frac{f}{B}]$ expression in equation 4.10.

By applying an $N = 1024$ point complex IDFT to the $I + jQ$ frequency domain array, a complex zero-phase synthesised profile is formed. Figure 4.12(a) displays the real component and (b) the imaginary component of the zero-phase synthesised profile. These signals are represented analytically by equation 4.11.

The three reflecting interfaces contained in resolution bins 5, 10 and 20 tB are evident with their relative amplitudes $|\Gamma_p|$ of 1, 0.5 and 0.2. The polarity of the second target at 10 tB is reversed with respect to the first and third targets, a result of the π radian phase change in the reflection coefficient of target number 2.

The envelope of the synthesised profile is plotted by taking the magnitude of the real and imaginary components. The envelope response is displayed using a dB scale in Figure 4.12(c). As described before, the envelope response truly represents the resolution of the data, but ignores the phase information concerning the reflection coefficient.

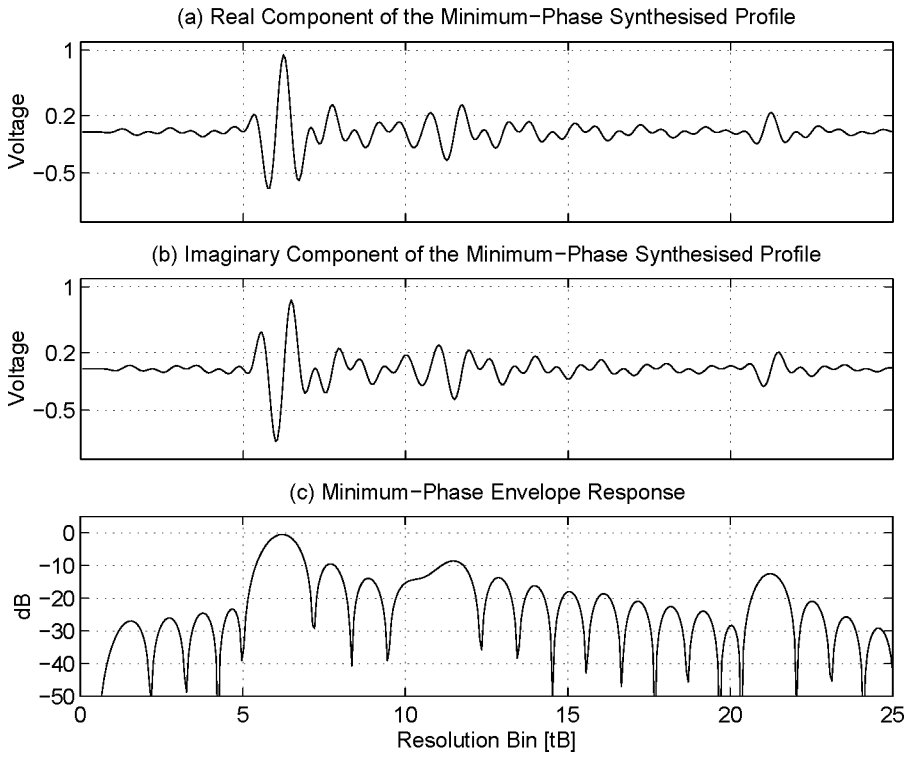

Figure 4.13: (a) Real and (b) imaginary minimum-phase synthesised profile and (c) the envelope response of the simulation of Table 4.2. The sidelobes of the reflections fall to the right side or temporally behind the mainlobes. These sidelobes mask the mainlobes of weak reflections that are received slightly after in time.

The sidelobes of each target (emphasised with the dB scale of Figure 4.12(c)) exhibit the zero-phase cepstrum property. An $n = 128$ point minimum-phase complex window $X_{MIN}[f]$ (equation 4.6) can be multiplied with the n point $I + jQ$ frequency domain array prior to the padding and IDFT to produce a minimum-phase synthesised profile (Figure 4.13). The minimum-phase profile resembles the type of profile that would be received by an impulse radar in the same simulation.

The mainlobes of the minimum-phase reflections of Figure 4.13 are in slightly different resolution bins than in the zero-phase plot of Figure 4.12. This is because the two-way travel time is now referenced to the leading edge of the minimum-phase pulse, as opposed to the centre of the zero-phase pulse.

In Figure 4.13(c), it is evident that the minimum-phase sidelobes of stronger reflections mask the weaker reflections that are received slightly after in time. The scenario is often encountered in GPR applications, where the sidelobes of the leakage signal between the transmit and receive antennas often mask the weak reflected

signals from buried targets received slightly after in time. A discussion on this point will be carried out later in Chapter 7.

4.6 Maximum-phase Processing

The data recorded by a stepped-frequency GPR can be processed in such a way that the sidelobes of the targets fall to the left side or temporally ahead of the mainlobes. This prevents the sidelobes of stronger reflections masking the responses of weaker reflections which are received slightly later in time. This type of processing is called *maximum-phase*. *Pottecher*, 1992 briefly mentioned the potential of this technique in stepped-frequency GPR, but did not elaborate further on its implementation or provide results.

Maximum-phase signals are produced by an *anticausal* or *anticipative* system, which has the poles and zeros of $X(z)$ outside the unit circle. Like the non-causal system (which produces zero-phase signals), an anticausal system cannot exist in reality, only in the signal processing domain.

To change the synthesised pulse from noncausal to anticausal, the causality theorem requires the complex cepstrum $X[f]$ to be anticausal (equation 4.12 defines this relationship) [*Oppenheim & Schafer*, 1989]. The conversion between $\hat{X}_{MIN}$ and $\hat{X}_{MAX}$ is by the complex conjugate operator *.

$$\hat{X}_{MAX}[f] = \hat{X}_{MIN}[f]^* = \log\left(|X[f]|\right) + j\,\mathcal{H}[f]\,\log\left(|X[f]|\right) \tag{4.12}$$

The *maximum-phase complex window function* $X_{MAX}[f]$ is then determined by equation 4.13.

$$X_{MAX}[f] = \exp_c\left(\hat{X}_{MAX}[f]\right) \tag{4.13}$$

The maximum-phase synthesised pulse x_{MAX} is derived from $\hat{X}_{MAX}$ using equation 4.14, and displayed in Figure 4.14. This waveform can be considered as the equivalent time-domain pulse that is synthetically transmitted by the stepped-frequency radar after maximum-phase processing.

$$x_{MAX}[t] = \mathcal{F}^{-1}\{X_{MAX}[f]\} = \mathcal{F}^{-1}\left\{\exp_c(\hat{X}_{MAX}[f])\right\} \tag{4.14}$$

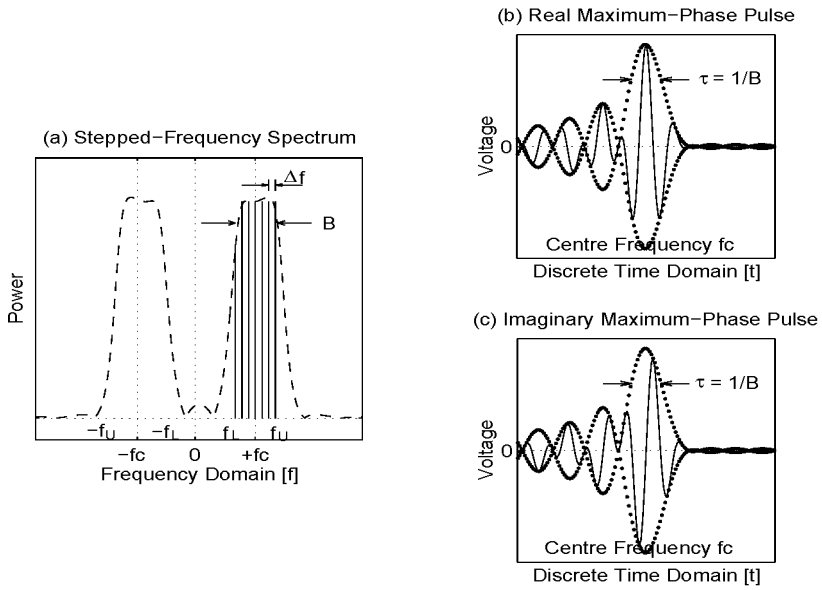

Figure 4.14: (a) Stepped-frequency spectrum with a maximum-phase complex window applied. The magnitude spectrum is unchanged, but the phase spectrum is altered to produce maximum-phase synthesised pulses; (b) the corresponding real and (c) imaginary maximum-phase synthesised pulses.

Figure 4.15 displays the maximum-phase synthesised profile of the simulation in Table 4.2. This was formed by applying an n point maximum-phase complex window to the n point $I + jQ$ frequency data prior to the padding and IDFT. The mainlobe of the weaker reflections are now easier to distinguish for the maximum-phase case as compared with the zero-phase (Figure 4.12) and minimum-phase (Figure 4.13) cases.

The resolution bins containing the maximum-phase mainlobes of the targets are slightly different to the resolution bins of the zero-phase mainlobes. For the maximum-phase pulses, the lagging edge is the reference for the two-way travel time of a target.

A summary of the complex window functions for zero, minimum and maximum-phase signals is contained in Table 4.3.

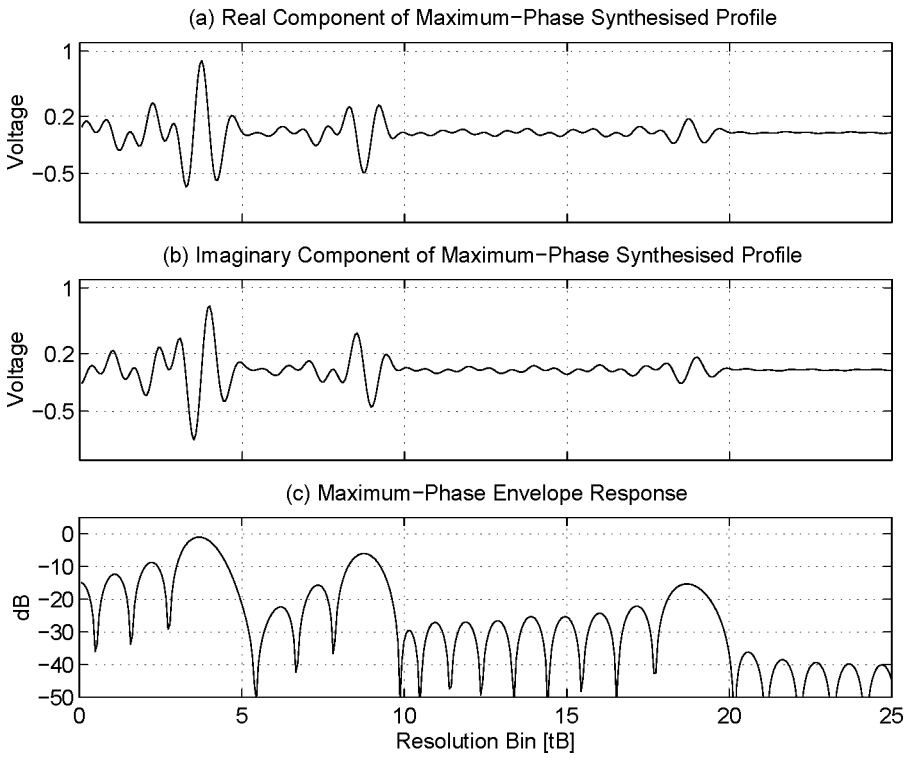

Figure 4.15: (a) Real and (b) imaginary components of the maximum-phase synthesised profile and (c) the envelope response of the simulation of Table 4.2. The sidelobes of the reflection signals fall to the left side or temporally before the mainlobes. This reduces the chance of weak reflections being masked by the sidelobes from strong reflections received slightly before in time.

Table 4.3: Summary of the zero, minimum and maximum-phase complex window functions (where $X[f]$ is defined in equation 4.2)

Complex Window	**Definition**	**Complex Window Function**
Zero-Phase	poles and zeros of $X(z)$ on the unit circle	1
Minimum-Phase	poles and zeros of $X(z)$ inside the unit circle	$\exp_c\left[\log\left(\lvert X[f]\rvert\right) - j\mathcal{H}[f]\log\left(\lvert X[f]\rvert\right)\right]$
Maximum-Phase	poles and zeros of $X(z)$ outside the unit circle	$\exp_c\left[\log\left(\lvert X[f]\rvert\right) + j\mathcal{H}[f]\log\left(\lvert X[f]\rvert\right)\right]$

4.7 Summary

The main objective of this chapter was to illustrate the resemblance that exists between waveforms generated by an impulse radar, and synthesised by a stepped-frequency radar after minimum-phase processing.

There are benefits in synthesising an impulse over generating one using an impulse radar. Impulse radars have these inherent limitations:

1. High mean powers are difficult to obtain in short-time impulses.

2. A substantial part of the available impulse energy at low frequencies is not radiated by the transmitting antenna.

3. The received waveforms are typically sampled using inefficient (sliding window) digitisers to overcome the ultra-fast sampling requirements.

It was shown how the pulse-modulated carrier radar overcame the second limitation by shifting the bulk of the impulse energy to the middle of the antenna bandwidth. In theory, the same waveform can be generated by simultaneously generating and combining a discrete number of narrowband frequencies across the antenna bandwidth. Finally, the bandwidth of the radar receiver was reduced by stepping a single narrowband frequency signal across the bandwidth. This resulted in much simpler sampling and also increased immunity to radio frequency interference. These progressive conceptual changes in the radar hardware resulted in the stepped-frequency radar design.

A simulation of a stepped-frequency GPR's response to several smooth interface targets was conducted. The in-phase (I) and quadrature (Q) frequency samples produced by the simulation were transformed to the time domain while preserving the magnitude (envelope) and carrier phase information. This resulted in a complex synthesised profile with two orthogonal components. The magnitude of the complex data resulted in the envelope response of the targets, and the phase determined the phase changes associated with the reflection coefficients of the targets.

The simulation illustrated how sidelobes of the leakage signal (or other strong reflections) can mask the weaker reflections of buried targets. This situation was avoided by processing the synthesised profile as maximum-phase, which had the sidelobes of reflections falling ahead of the mainlobes.

The following chapter will now describe the design of a stepped-frequency GPR prototype and investigate the limiting factors of its performance. Later chapters will then illustrate how improvements can be made in hardware and signal processing.

Figure 5.4: Photograph image of the 1-2 GHz SFGPR ruggedised prototype with the horn antenna trolley towed behind a 4WD

Chapter 6

Correction of Quadrature Receiver Errors

6.1 Introduction

Chapter 4 contains a description of how the stepped-frequency radar transmits ultra-wide bandwidth signals, and receives them using a narrow instantaneous bandwidth receiver. This allows efficient sampling of the received signals using low sampling speed, high precision digitisers. The narrow instantaneous bandwidth of the stepped-frequency receiver is achieved by the down-conversion of the received RF signals to baseband using either superheterodyne, heterodyne with direct quadrature sampling or homodyne techniques as described in Chapter 5. To fully retain the magnitude and phase information of the received RF signal, the baseband signal must consist of two orthogonal components. These are the *in-phase* (I) and *quadrature* (Q) components (refer to Chapter 1). In the superheterodyne and homodyne receivers, the I and Q components are generated using a *quadrature mixer*. However, the I and Q channels may not be perfectly orthogonal due to hardware gain and phase errors in the quadrature mixer. These *quadrature* or *I/Q errors* introduce false targets (called *Hermitian images*) into the synthesised profile, which reduces the number of real targets that may lie within the maximum unambiguous range of the stepped-frequency radar. Thus, it is desirable to correct these quadrature errors to obtain the true synthesised profile and fully utilise the processed mean energy available within the maximum unambiguous range of the stepped-frequency radar.

Section 6.2 of this chapter describes how the quadrature or I/Q errors affect the synthesised profile of a stepped-frequency radar. A portion of this analysis

was presented at the 1994 IEEE International Conference on Acoustics, Speech and Signal Processing (ICASSP'94) [*Noon, Longstaff & Stickley*, 1994]. Section 6.2.1 describes the quadrature errors of a superheterodyne receiver, and discusses how conventional quadrature correction techniques can be applied to reduce the effects of these errors. Section 6.2.2 expands this analysis to cover the homodyne receiver, where the quadrature errors are frequency dependent.

Section 6.3 presents a patented method of correcting the quadrature errors of a homodyne receiver [*Longstaff, Noon & Stickley*, 1994]. This method was successfully tested on the SFGPR prototype described in Chapter 5. Although the emphasis of this chapter is on the stepped-frequency radar, the content is also relevant to other types of coherent radar systems, network analysers and wideband communication systems employing single-sideband modulators or quadrature detectors.

6.2 Quadrature Errors of Stepped-frequency Radar

Chapter 4 described the stepped-frequency radar as transmitting a waveform consisting of n narrowband pulses. Each pulse is stepped in frequency by a fixed interval Δf Hertz, across a broad bandwidth B. These narrowband pulses can be individually represented by the expression $\cos(\omega_f t)$, where $\omega_f = 2\pi f$ and f is the frequency of each narrowband pulse. Assuming that each frequency signal is reflected by a single target, the received signal will have a time delay of Δt seconds with an amplitude A and a phase ϕ. This received signal is expressed as $A\cos[\omega_f(t-\Delta t)+\phi]$.

The received signal can be directly down-converted to baseband using a homodyne quadrature mixer, or via an *intermediate frequency* IF using either superheterodyne (heterodyne to an IF and homodyne to baseband) or heterodyne (heterodyne to an IF and digital down-conversion to baseband) configurations (see Section 5.3.1). The homodyne and superheterodyne configurations use a hardware quadrature mixer to derive the in-phase (I) and quadrature (Q) components of the baseband signal. (Appendix F describes the digital down-conversion of the IF signal into the I and Q components.) The block diagram of an ideal quadrature mixer is displayed in Figure 6.1.

The RF signal $A\cos(\omega t - \omega_f \Delta t + \phi)$ sent to the quadrature mixer is the received signal at the angular frequency ω (where $\omega = \omega_f$ for homodyne, or $\omega = \omega_{IF}$ for superheterodyne). The LO (local oscillator) signal is the reference signal from the transmitter, which is split into two quadrature components I_{LO} and Q_{LO} using a

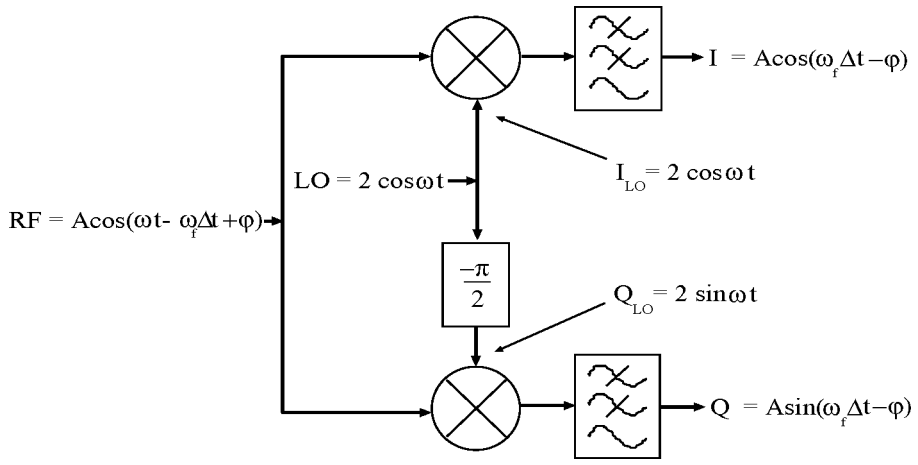

Figure 6.1: Block diagram of an ideal quadrature mixer. The reference signal LO is split into its two quadrature components I_{LO} and Q_{LO} using a $-\pi/2$ quadrature hybrid, and separately mixed with the received signal RF and filtered to produce the I and Q baseband signals.

$-\pi/2$ quadrature hybrid. By mixing the RF signal separately with the I_{LO} and Q_{LO} components and low-pass filtering, the baseband I and Q signals corresponding to the transmitted frequency f emerge.

For the ideal quadrature mixer, the gains of the I and Q channels are equal and the phase difference between the channels is 90 degrees (or $\pi/2$ radians). The I and Q signals of the ideal quadrature mixer are represented by equations 6.1 to 6.4.

$$I = A\cos(\omega_f \Delta t - \phi) \tag{6.1}$$

$$= \frac{A}{2}e^{j(\omega_f \Delta t-\phi)} + \frac{A}{2}e^{-j(\omega_f \Delta t-\phi)} \tag{6.2}$$

$$Q = A\sin(\omega_f \Delta t - \phi) \tag{6.3}$$

$$= \frac{A}{2j}e^{j(\omega_f \Delta t-\phi)} - \frac{A}{2j}e^{-j(\omega_f \Delta t-\phi)} \tag{6.4}$$

These I and Q expressions can be vectorially combined as a complex exponential to yield the analytic signal $I + jQ$ of equation 6.5.

$$I + jQ = Ae^{j(\omega_f \Delta t-\phi)} \tag{6.5}$$

For a single target with a delay of Δt seconds, the time domain representing the $I + jQ$ signal is one-sided, with a sinc (Bt) function positioned at $+\omega_f \Delta t$. Figure 6.2(a) displays the Q versus I representation of the ideal signal (equation 6.5).

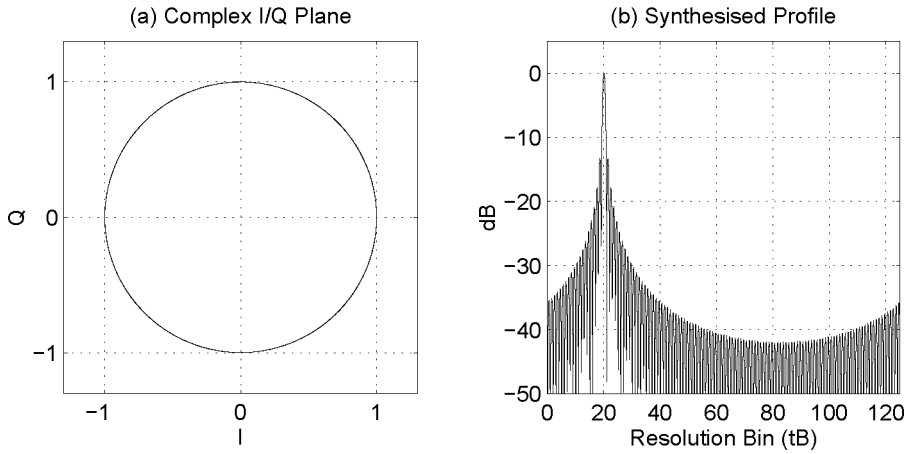

Figure 6.2: (a) An ideal I/Q phasor rotating twenty ($\Delta tB = 20$) times; (b) the corresponding synthesised profile with the peak located in the twentieth resolution bin. $AB = 1$ and $n = 128$ for this and following examples.

For this example, the I/Q phasor rotates twenty times in a perfectly circular fashion, as the frequency of the transmitter is stepped across the bandwidth B. Figure 6.2(b) is the ideal synthesised profile as a function of resolution bin tB. The peak associated with the time delay of the target is located in the twentieth ($\Delta tB = 20$) resolution bin. The ideal synthesised profile begins to alias after the nth resolution bin (where n is the number of frequency steps of the stepped-frequency waveform). Therefore, a maximum of n targets can be unambiguously resolved within the ideal synthesised profile.

In practice, there are *differential gain errors* and *differential phase errors* between the I and Q channels of the quadrature mixer. (In addition, there are DC offset errors in the I and Q channels, but these can be measured and subtracted [*Noon & Bialkowski*, 1993].) The effect of the quadrature errors in a stepped-frequency radar varies slightly between receiver types. Section 6.2.1 describes the effects of the quadrature errors in a superheterodyne receiver. These concepts are then extended in Section 6.2.2 for the homodyne receiver.

6.2.1 Quadrature Errors of a Superheterodyne Receiver

For the ideal superheterodyne receiver (described in Figure 6.3), the received RF signal of a single target ($A\cos[\omega_f(t-\Delta t)+\phi]$) is down-converted to an intermediate frequency ω_{IF} by mixing it with the signal $2\cos[(\omega_f-\omega_{IF})t]$. This results in the intermediate frequency IF being $A\cos(\omega_{IF}t-\omega_f\Delta t+\phi)$. A quadrature mixer is then used to separately mix the IF signal with $I_{LO}=2\cos(\omega_{IF}t)$ and $Q_{LO}=2\sin(\omega_{IF}t)$. After filtering, the I and Q signals described by equations 6.1 and 6.3 emerge. However, practical quadrature mixers introduce a differential gain error and a differential phase error in the I and Q channels.

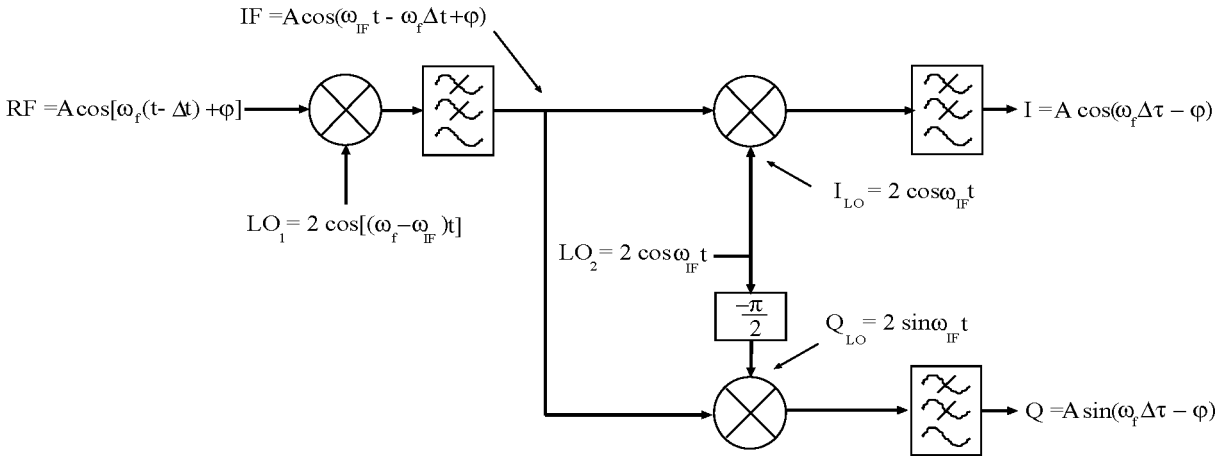

Figure 6.3: Block diagram of an ideal superheterodyne receiver

Figure 6.4 is a block diagram of a superheterodyne receiver with a differential gain error of $1+\epsilon$ (ϵ is the fractional gain imbalance) and a differential phase error of α radians between the I and Q channels of the quadrature mixer. It is convenient to arbitrarily include both quadrature errors in the Q channel, and leave the I channel equal to the ideal case. (There is no loss of in generality in making this assumption.) Both of the quadrature error terms are present at the IF stage in the superheterodyne receiver (*i.e.* ω_{IF}), and are therefore independent of the transmitted frequency ω_f.

Equations 6.6 through 6.9 are the i and q signals (based on equations 6.1 to 6.4) including the superheterodyne quadrature error terms $1+\epsilon$ and α for the superheterodyne receiver.

$$i = A\cos(\omega_f\Delta t-\phi) \tag{6.6}$$

$$= \frac{A}{2}e^{j(\omega_f\Delta t-\phi)}+\frac{A}{2}e^{-j(\omega_f\Delta t-\phi)} \tag{6.7}$$

$$q = A(1+\epsilon)\sin(\omega_f \Delta t - \phi + \alpha) \quad (6.8)$$

$$= \frac{A}{2j}(1+\epsilon)e^{j(\omega_f \Delta t - \phi)}e^{j\alpha} - \frac{A}{2j}(1+\epsilon)e^{-j(\omega_f \Delta t - \phi)}e^{-j\alpha} \quad (6.9)$$

Once again, these equations can be vectorially combined to form the following complex exponential :

$$i + jq = \frac{A}{2}[1 + (1+\epsilon)e^{j\alpha}]e^{j(\omega_f \Delta t - \phi)} + \frac{A}{2}[1 - (1+\epsilon)e^{-j\alpha}]e^{-j(\omega_f \Delta t - \phi)} \quad (6.10)$$

For a single target with an associated delay of Δt seconds, the $i + jq$ frequency domain signal has two time-domain components. The signal representing the target at $+\omega_f \Delta t$ has an amplitude and phase response of $0.5A[1 + (1+\epsilon)e^{j\alpha}]$. The other component is the *Hermitian image* of this signal at $-\omega_f \Delta t$, with an amplitude and phase response of $0.5A[1 - (1+\epsilon)e^{-j\alpha}]$.

The Hermitian images of the real target responses are false targets in the synthesised profile. Their positions are in the conjugate resolution bins of the real targets. Therefore, the maximum number of targets that can be unambiguously resolved is halved (*i.e.* $n/2$), compared with the ideal synthesised profile (Section 6.2). The conjugate half of the synthesised profile containing the Hermitian images is redund-

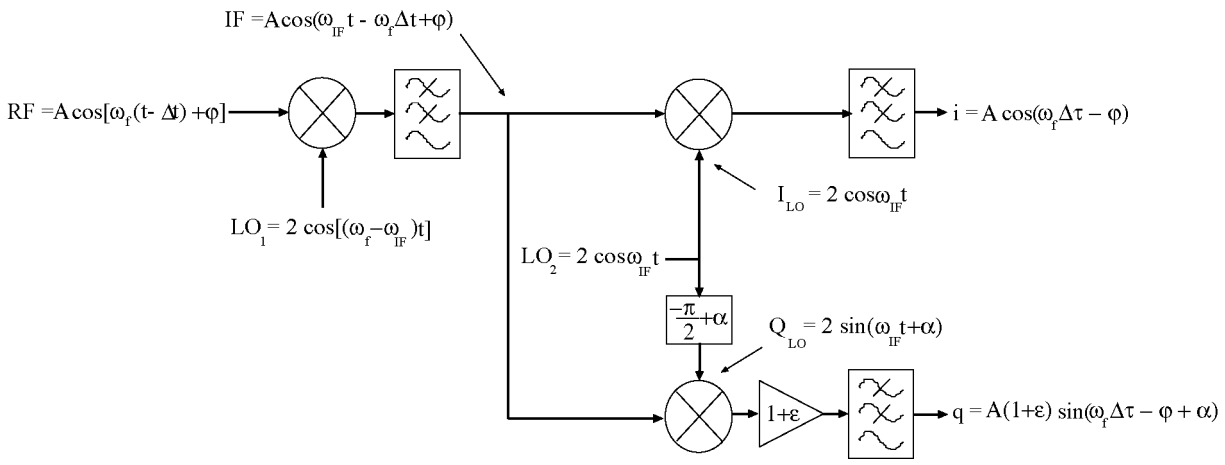

Figure 6.4: Block diagram of a superheterodyne receiver with a differential gain error $1 + \epsilon$ and a differential phase error α at the intermediate frequency.

ant, causing a 3 dB inefficiency of the processed mean energy in a given integration time.

The relative amplitudes of the real signal and the Hermitian image are characterised by both the differential gain error $(1+\epsilon)$ and the differential phase error α. The *image-to-signal* power ratio (equation 6.11) is derived from equation 6.10.

$$\begin{aligned} ISR &= \left|\frac{1-(1+\epsilon)e^{-j\alpha}}{1+(1+\epsilon)e^{j\alpha}}\right|^2 = \left|\frac{1-(1+\epsilon)(\cos\alpha - j\sin\alpha)}{1+(1+\epsilon)(\cos\alpha + j\sin\alpha)}\right|^2 \\ &= \left|\frac{1-(1+\epsilon)\cos\alpha + j(1+\epsilon)\sin\alpha}{1+(1+\epsilon)\cos\alpha + j(1+\epsilon)\sin\alpha}\right|^2 \\ &= \frac{(1-(1+\epsilon)\cos\alpha)^2 + (1+\epsilon)^2\sin^2\alpha}{(1+(1+\epsilon)\cos\alpha)^2 + (1+\epsilon)^2\sin^2\alpha} \\ &= \frac{1-2(1+\epsilon)\cos\alpha + (1+\epsilon)^2}{1+2(1+\epsilon)\cos\alpha + (1+\epsilon)^2} \end{aligned} \tag{6.11}$$

This equation is identical to the equations obtained in the separate analyses carried out by *Sinsky & Wang*, 1974 and *Monzingo & Au*, 1987. *Monzingo & Au*, 1987 further showed that contours of constant ISR (using equation 6.11) resemble ellipses in a plot of differential phase error α versus differential gain error $1+\epsilon$. Figure 6.5 illustrates the constant contours for selected ISR values. (A similar plot can be found in the text by *Kurtz & Pauley*, 1993).

As an example, the Figure 6.5 shows that a 0.1 dB differential gain error and a 0.5 degree differential phase error will cause a Hermitian image which is approximately 50 dB below the signal power.

The contribution of the differential gain error $(1+\epsilon)$ to the ISR can be determined by setting the differential phase error term α in equation 6.11 to zero. (The approximation in equation 6.12 is valid for small ϵ values.)

$$ISR_\epsilon = \frac{1-2(1+\epsilon)+(1+\epsilon)^2}{1+2(1+\epsilon)+(1+\epsilon)^2} = \frac{\epsilon^2}{4+4\epsilon+\epsilon^2} \approx \frac{\epsilon^2}{4} \tag{6.12}$$

Figure 6.6(a) illustrates the complex I/Q plane of the $i+jq$ phasor with $\epsilon = 0.2$ (1.6 dB differential gain error) and a zero differential phase error.

The resulting ellipse has a major axis of length $(1+\epsilon)$ along the Q axis and a minor axis of unity length along the I axis. The synthesised profile contained in Figure 6.6(b) displays the peak of the reflection signal in the twentieth ($\Delta tB =$

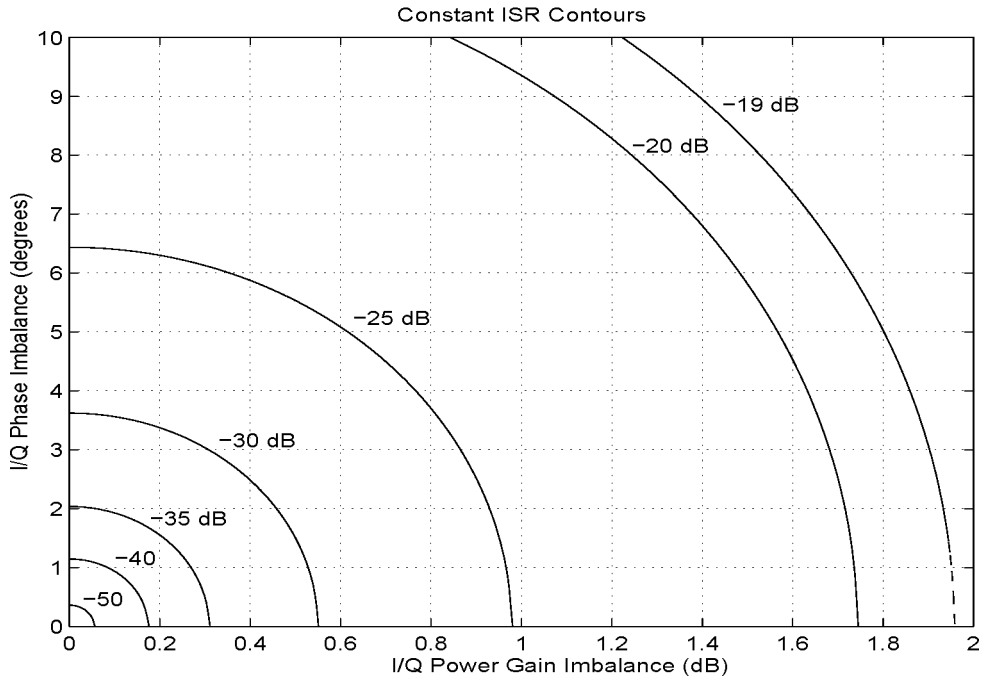

Figure 6.5: Constant ISR contours as a function of the differential gain error $(1+\epsilon)$ and the differential phase error (α).

20) resolution bin, and its Hermitian image in the conjugate resolution bin 106. Using equation 6.12, the ISR_ϵ for $\epsilon = 0.2$ is approximately -20 dB, as is evident in Figure 6.6(b).

Similarly, the contribution of the differential phase error α to the ISR can be determined by setting the differential gain error ϵ to zero. (The approximation in equation 6.13 is valid for small α radian values where $\cos\alpha \approx 1 - \frac{\alpha^2}{2}$.)

$$ISR_\alpha = \frac{1-\cos\alpha}{1+\cos\alpha} \approx \frac{1-(1-\frac{\alpha^2}{2})}{1+(1-\frac{\alpha^2}{2})} \approx \frac{\alpha^2}{4} \tag{6.13}$$

(The approximations for ISR_ϵ and ISR_α in equation 6.12 and equation 6.13 agree with the results reported separately by *Churchill, Ogar & Thompson*, 1981.)

Figure 6.7(a) illustrates the complex I/Q plane of the $i + jq$ phasor with an 8^o phase imbalance (and with a zero differential gain error). The major and minor axes of the ellipse are rotated and misaligned with the I and Q axes. The I and Q channels are partially *correlated*, as there is a component of the I signal in the Q channel, and information of the Q signal in the I channel. The synthesised profile in Figure 6.7(b) shows the reflection peak in resolution bin 20, and its Hermitian

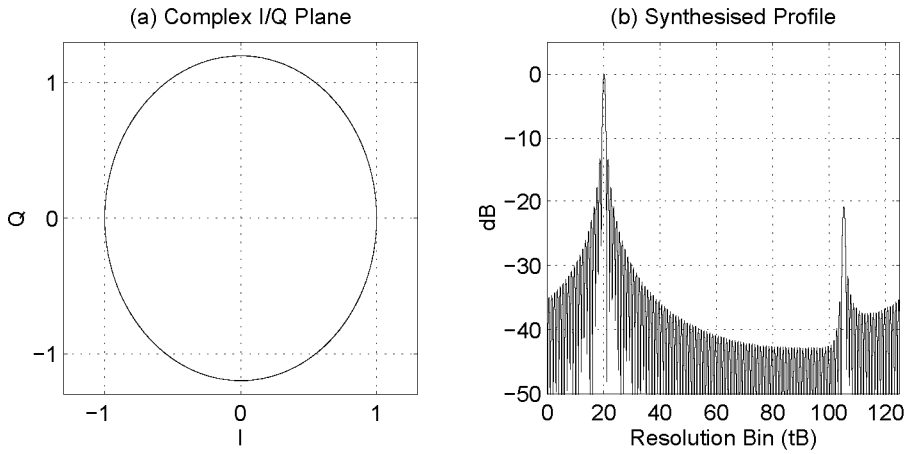

Figure 6.6: (a) An I/Q phasor rotating twenty ($\Delta tB = 20$) times with a differential gain imbalance of 20% or 1.6 dB ($\epsilon = 0.2$, $\alpha = 0$); (b) the corresponding synthesised profile containing the main peak located in the twentieth resolution bin and the Hermitian image in bin 106 ($n = 128$). The ISR_ϵ is approximately -20 dB.

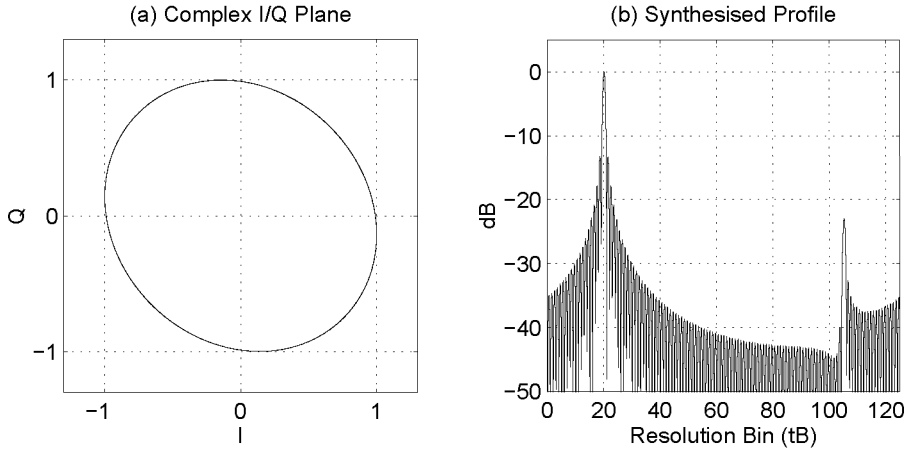

Figure 6.7: (a) An I/Q phasor rotating twenty ($\Delta tB = 20$) times with a differential phase imbalance of 8° ($\alpha = 0.14$ rad, $\epsilon = 0$); (b) the corresponding synthesised profile with the main peak located in the twentieth resolution bin and the Hermitian image in bin 106 ($n = 128$). The ISR_α is approximately -23 dB.

image in the conjugate bin 106. The 0.14 radian phase error corresponds to an ISR_α of approximately -23 dB (using equation 6.13), which agrees with the result in Figure 6.7(b).

The quadrature errors of a superheterodyne receiver can be measured by processing the I and Q components of a known test signal [*Churchill, Ogar & Thompson*, 1981; *Harris*, 1987]. A suitable test signal is a sinusoid CW signal with a frequency

slightly offset from the IF (but still within the instantaneous bandwidth of the receiver). The I and Q signals of this test signal will be time-varying sinusoids with a frequency equal to the offset frequency. By taking enough I and Q samples of the test signal, *correlation functions* can be used to determine the quadrature error terms [*Harris*, 1987].

The *autocorrelation functions* (with zero lag) $R_{II}(0)$ and $R_{QQ}(0)$, and the *crosscorrelation function* (with zero lag) $R_{IQ}(0)$ between the I and Q channels can be derived from the expressions for i and q in equations 6.6 and 6.8 [*Kitchen*, 1991] ($\mathcal{E}$ is the *expected value* or *mean square value.*)

$$R_{II}(0) = \mathcal{E}\{ii\} = \frac{A^2}{2} \tag{6.14}$$

$$R_{QQ}(0) = \mathcal{E}\{qq\} = \frac{A^2(1+\epsilon)^2}{2} \tag{6.15}$$

$$R_{IQ}(0) = \mathcal{E}\{iq\} = \frac{A^2(1+\epsilon)}{2}\sin\alpha \tag{6.16}$$

The values of $R_{II}(0)$, $R_{QQ}(0)$ and $R_{IQ}(0)$ can be determined from the I and Q samples of the test signal. Equation 6.14, 6.15 and 6.16 can be simultaneously solved with these values to determine the quadrature error terms $1+\epsilon$ and α of the quadrature mixer. *Harris*, 1987 presents an alternative technique to determine the quadrature error terms using a set of adaptive, one-tap, cancelling filters.

Once the quadrature error terms are known, an appropriate linear transform can be found to correct the I and Q imbalances of the quadrature mixer [*Kitchen*, 1991]. The desired I and Q signals in equations 6.1 and 6.3 can be rewritten in matrix form as equation 6.17.

$$\begin{bmatrix} I \\ Q \end{bmatrix} = \begin{bmatrix} A\cos(\omega_f \Delta t - \phi) \\ A\sin(\omega_f \Delta t - \phi) \end{bmatrix} \tag{6.17}$$

Similarly, equations 6.6 and 6.8 describing the i and q signals with the quadrature errors of a superheterodyne receiver can be rewritten as equation 6.18.

$$\begin{bmatrix} i \\ q \end{bmatrix} = \begin{bmatrix} A\cos(\omega_f \Delta t - \phi) \\ A(1+\epsilon)\sin(\omega_f \Delta t - \phi + \alpha) \end{bmatrix} \tag{6.18}$$

Expanding the q component of equation 6.18 and substituting the I and Q components from equation 6.17 results in the derivation of equation 6.19.

$$\begin{aligned}\begin{bmatrix} i \\ q \end{bmatrix} &= \begin{bmatrix} A\cos(\omega_f \Delta t - \phi) \\ A(1+\epsilon)\sin(\omega_f \Delta t - \phi)\cos\alpha + A(1+\epsilon)\cos(\omega_f \Delta t - \phi)\sin\alpha \end{bmatrix} \\ &= \begin{bmatrix} I \\ (1+\epsilon)Q\cos\alpha + (1+\epsilon)I\sin\alpha \end{bmatrix} \\ &= \begin{bmatrix} 1 \\ (1+\epsilon)\cos\alpha + (1+\epsilon)\sin\alpha \end{bmatrix} \begin{bmatrix} I \\ Q \end{bmatrix} \end{aligned} \tag{6.19}$$

Therefore, the corrected I and Q signals can be determined by applying the linear transform of equation 6.20 to the i and q signals of the non-ideal quadrature mixer.

$$\begin{bmatrix} I \\ Q \end{bmatrix} = \frac{1}{(1+\epsilon)\cos\alpha} \begin{bmatrix} (1+\epsilon)\cos\alpha & 0 \\ -(1+\epsilon)\sin\alpha & 1 \end{bmatrix} \begin{bmatrix} i \\ q \end{bmatrix} \tag{6.20}$$

Effectively, the above transformation is a rotation and scaling of the I/Q ellipses in Figures 6.6(a) and 6.7(a) to form the circle in Figure 6.2(a).

Other quadrature correction methods use digital filters to measure the quadrature error terms from an offset sinusoidal test signal. A similar correction transform to equation 6.20 can be formed using the *Gram-Schmidt Orthogonalisation Procedure* [*Churchill, Ogar & Thompson*, 1976; *Kurtz & Pauley*, 1993]. Variations of this method have been reported elsewhere [*Goldstone*, 1977; *Taylor*, 1986].

6.2.2 Quadrature Errors of a Homodyne Receiver

The correction techniques reviewed in the previous section were devised for superheterodyne receivers which have a fixed intermediate frequency and therefore constant quadrature errors across the broad transmitted bandwidth.

For the homodyne receiver, the I and Q signals are derived directly from the received RF signals without an intermediate frequency stage. Therefore, the homodyne quadrature mixer is a broadband device with quadrature errors that are frequency dependent. Figure 6.8 shows the block diagram of a homodyne receiver with frequency dependent quadrature errors. The differential gain error and the

differential phase errors are now a function of transmitter frequency f and denoted as ϵ_f and α_f respectively.

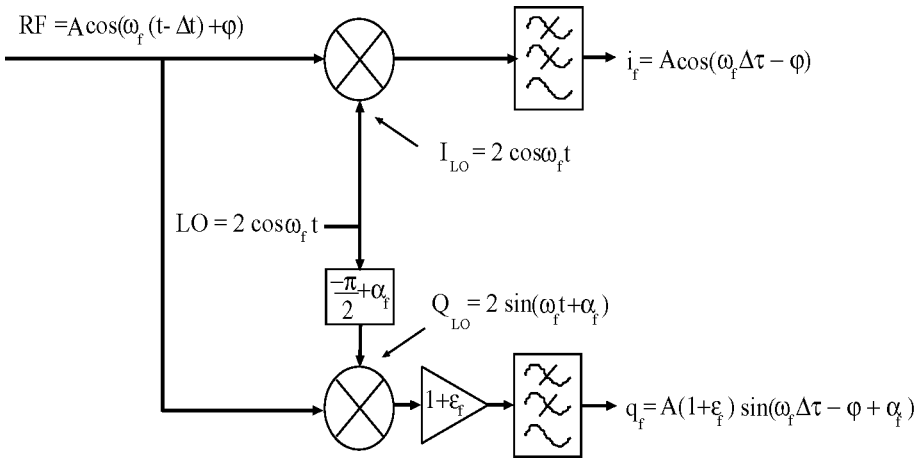

Figure 6.8: Block diagram of a homodyne quadrature receiver with a frequency dependent differential gain error $(1 + \epsilon_f)$ and a frequency dependent differential phase error α_f.

Without loss of generality, the homodyne receiver in Figure 6.8 arbitrarily includes both errors in the Q channel, leaving the I channel as the reference. Equations 6.21, 6.22 and 6.23 are the i_f and q_f signals (based on equations 6.6, 6.8 and 6.10) for the homodyne receiver.

$$\begin{aligned} i_f &= A\cos(\omega_f \Delta t - \phi) \\ &= \frac{A}{2}e^{j(\omega_f \Delta t - \phi)} + \frac{A}{2}e^{-j(\omega_f \Delta t - \phi)} \end{aligned} \tag{6.21}$$

$$\begin{aligned} q_f &= A(1+\epsilon_f)\sin(\omega_f \Delta t - \phi + \alpha_f) \\ &= \frac{A}{2j}(1+\epsilon_f)e^{j(\omega_f \Delta t - \phi)}e^{j\alpha_f} - \frac{A}{2j}(1+\epsilon_f)e^{-j(\omega_f \Delta t - \phi)}e^{-j\alpha_f} \end{aligned} \tag{6.22}$$

$$\begin{aligned} i_f + jq_f &= \frac{A}{2}[1 + (1+\epsilon_f)e^{j\alpha_f}]e^{j(-\omega_f \Delta t - \phi)} \\ &\quad + \frac{A}{2}[1 - (1+\epsilon_f)e^{-j\alpha_f}]e^{-j(\omega_f \Delta t - \phi)} \end{aligned} \tag{6.23}$$

Figure 6.9(a) illustrates the complex I/Q plane of the $i_f + jq_f$ phasor with a differential gain error ϵ_f randomly distributed (uniformly) between 0.1 and 0.3 for each transmitted frequency f (with a zero differential phase error).

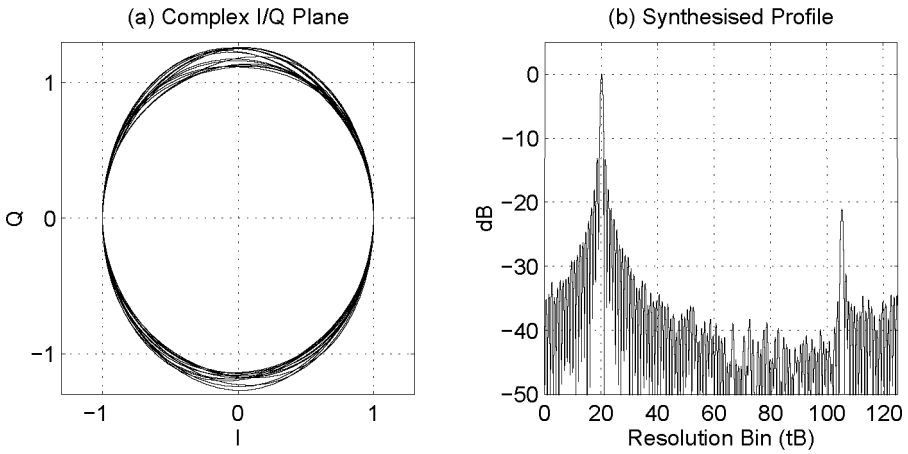

Figure 6.9: (a) A distorted I/Q phasor rotating twenty ($\Delta tB = 20$) times with a differential gain imbalance of $0.1 \leq \epsilon_f \leq 0.3$ ($\alpha_f = 0$); (b) the corresponding synthesised profile with the main peak located in the twentieth resolution bin and the Hermitian image in bin 106 ($n = 128$). Compare with Figure 6.6. The ISR_ϵ is approximately -20 dB.

The frequency variation of ϵ_f in the Q channel defocuses the ellipses in the I/Q plane (compare with Figure 6.6(a)). This produces a noisy synthesised profile as shown in Figure 6.9(b). The ISR_ϵ of this example is -20 dB, which agrees with the calculated value based on the mean of ϵ_f (0.2 or 1.6 dB).

Figure 6.10(a) illustrates the complex I/Q plane of the $i_f + jq_f$ phasor with a differential phase error α_f randomly distributed (uniformly) between 0^o and 16^o (with a zero differential gain error).

The frequency variation of α_f in the Q channel defocuses the tilted ellipses in the I/Q plane, and also produces a noisy synthesised profile (Figure 6.10(b)). The Hermitian image in resolution bin 106 is 23 dB below the main peak. This result agrees with the ISR_α calculated using equation 6.13, with a mean value α_f of 8^o (or 0.14 radians).

The effects of quadrature errors on an actual homodyne radar system are illustrated in Figure 6.11. The 1-2 GHz SFGPR prototype described in Chapter 5 was used to obtain the synthesised profile of the closed loop connected between the transmitter and receiver.

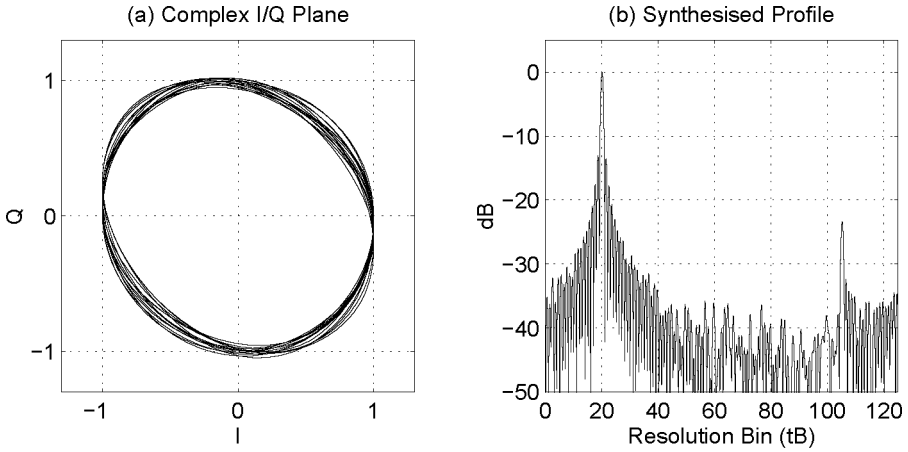

Figure 6.10: (a) A distorted I/Q phasor rotating twenty ($\Delta tB = 20$) times with a differential phase imbalance $0 \leq \alpha_f \leq 16^o$ ($\epsilon_f = 0$); (b) the corresponding synthesised profile with the main peak located in the twentieth resolution bin and the Hermitian image in bin 106 ($n = 128$). Compare with Figure 6.7. The ISR_α is approximately -23 dB.

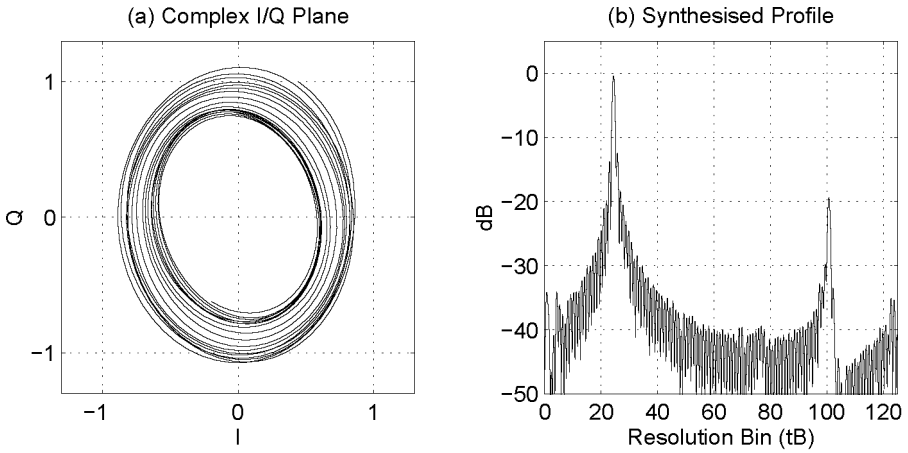

Figure 6.11: (a) I/Q phasor of the closed loop connected to the SFGPR ($\Delta tB = 25$); (b) the synthesised profile of the closed loop data with the main peak located in the twenty-fifth resolution bin and the Hermitian image in bin 101 ($n = 128$). The measured ISR is approximately -19 dB.

The main peak in Figure 6.11 corresponds to the time delay (*i.e.* 25 resolution bins = 25 ns for $B = 1$ GHz), and the Hermitian image due to the quadrature errors is present in resolution bin 101. The ISR value measured is approximately -19 dB, which indicates that the mean gain and mean phase imbalances lie close to

the constant -19 dB contour of Figure 6.5. The quadrature mixer used in the system has a specified minimum image rejection of 15 dB.

The differential gain and differential phase error terms of a homodyne receiver were measured using the technique described in Section 6.2.1 for the superheterodyne receiver. A second frequency synthesiser (with a slight frequency offset from the master transmitter synthesiser frequency) was used to inject a sinusoidal test signal into the homodyne quadrature mixer at each of the transmitted frequency steps. The autocorrelations $R_{II}(0)$ and $R_{QQ}(0)$, and crosscorrelation $R_{IQ}(0)$ measurements were performed, and the gain and phase errors determined at each frequency step.

Figure 6.12 plots the measured differential gain (a) and differential phase (b) errors as a function of transmitter frequency for the 1-2 GHz SFGPR.

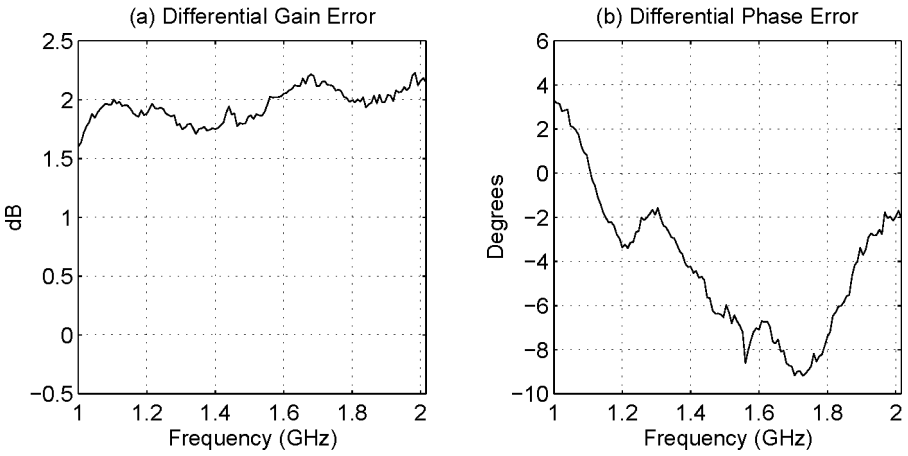

Figure 6.12: (a) Differential gain and (b) differential phase errors measured of the 1-2 GHz SFGPR prototype.

The mean differential gain error is approximately 1.9 dB and mean differential phase error is approximately -4 degrees. These mean imbalances lie close to the constant -19 dB contour of Figure 6.5. The frequency variation of these errors contribute to the noise in the synthesised profile of Figure 6.11(b).

6.3 Homodyne Quadrature Error Correction

A new correction procedure is proposed which uses a transform to decorrelate and match the I and Q channels of a homodyne receiver [*Longstaff, Noon & Stickley*, 1994]. The coefficients of the transform are derived from a test signal at each of the

transmitter frequency steps. Each transform is stored and subsequently applied to the raw radar frequency domain data.

To determine the transform for a single transmitter frequency, the I and Q values of an offset sinusoidal test signal are measured. It is necessary to ensure that several cycles of the I and Q signals are contained within the N samples. The matrix $\mathbf{X}$ (N by 2) is formed with I values in the first column and Q values in the second column (equation 6.24).

$$\mathbf{X} = \begin{bmatrix} I_1 & Q_1 \\ I_2 & Q_2 \\ . & . \\ . & . \\ I_N & Q_N \end{bmatrix} \tag{6.24}$$

Figure 6.13(a) displays the I and Q samples of the test signal injected into the SFGPR receiver at a single transmitter frequency. Figure 6.13(b) contains the complex I/Q plane representation of the I and Q phasor. The differential gain and phase errors of the homodyne quadrature mixer at this frequency step are represented in the inclined ellipse of the I/Q phasor.

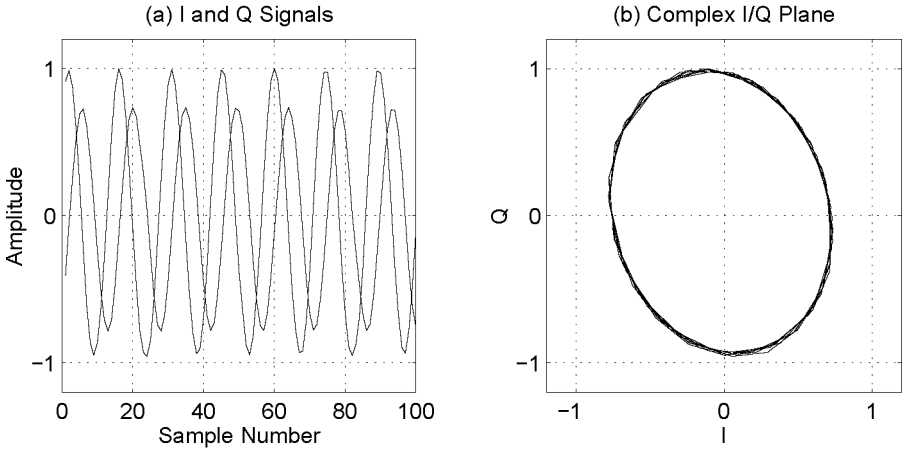

Figure 6.13: (a) I and Q samples of an offset sinusoidal test signal at a single transmitter frequency; (b) the complex I/Q plane representation of the I and Q phasor ($N = 100$).

Statistically, the effects of the quadrature errors in the I and Q samples can be represented in a *covariance matrix*. Equation 6.25 defines the covariance matrix $\mathbf{C}$ for the two data sets, I and Q. The expected values $\mathcal{E}\{\}$ become the mean values

over a large number of data samples. The matrix is symmetric (*i.e.* $\mathbf{C} = \mathbf{C}^T$) because $\overline{QI} = \overline{IQ}$.

$$\mathbf{C} = \begin{bmatrix} \mathcal{E}\{II\} & \mathcal{E}\{IQ\} \\ \mathcal{E}\{QI\} & \mathcal{E}\{QQ\} \end{bmatrix} \approx \begin{bmatrix} \overline{II} & \overline{IQ} \\ \overline{QI} & \overline{QQ} \end{bmatrix} \tag{6.25}$$

The covariance matrix for the data in $\mathbf{X}$ can be calculated using the following derivation.

$$\mathbf{C}_X = \mathbf{X}^T\mathbf{X} \tag{6.26}$$

A perfectly uncorrelated data set of I and Q would have the $\overline{QI}$ and $\overline{IQ}$ values of $\mathbf{C}_X$ equal to zero (*i.e.* no correlation between the I and Q channels). For perfectly matched gains in the I and Q data set, $\overline{II}$ would equal $\overline{QQ}$. Differential phase errors produce non-zero values of $\overline{QI}$ and $\overline{IQ}$ in $\mathbf{C}_X$, while differential gain errors cause $\overline{II} \neq \overline{QQ}$. For example, $\mathbf{C}_X$ for the data used in Figure 6.13 is the following matrix (normalised with respect to $\overline{II}$).

$$\mathbf{C}_X = \begin{bmatrix} 1.0000 & -0.1548 \\ -0.1548 & 1.6941 \end{bmatrix} \tag{6.27}$$

The algorithm which transforms this covariance matrix to the identity matrix $\mathbf{I}$ will correct the quadrature errors at this frequency step. It is important that the transform does not introduce a phase error which may disturb the alignment of the $I + jQ$ phasors across all frequency steps.

Singular value decomposition (SVD) is a suitable method for obtaining the transform which diagonalises a 2 by 2 covariance matrix of an N by 2 data matrix. This is because the SVD of an N by 2 matrix results in a 2 by 2 diagonal matrix $\mathbf{S}$ and a 2 by 2 orthogonal matrix $\mathbf{V}^T$, which are both used in the diagonalisation procedure as described below. (The N by N orthogonal matrix $\mathbf{U}$ from the SVD is not used).

The covariance matrix $\mathbf{C}_X$ of the data set $\mathbf{X}$ can be decomposed into $\mathbf{S}$ and $\mathbf{V}$ terms of equation 6.28 using SVD (note that $(\mathbf{USV}^T)^T = \mathbf{VS}^T\mathbf{U}^T$ and $\mathbf{U}^T\mathbf{U} = \mathbf{I}$).

$$\begin{aligned} \mathbf{C}_X &= \mathbf{X}^T\mathbf{X} = (\mathbf{USV}^T)^T(\mathbf{USV}^T) = \mathbf{VS}^T(\mathbf{U}^T\mathbf{U})\mathbf{SV}^T \\ &= \mathbf{VS}^T\mathbf{SV}^T \end{aligned} \tag{6.28}$$

To correct the quadrature errors in $\mathbf{X}$, a linear transformation $\mathbf{T}$ can be applied to $\mathbf{X}$ which results in a matrix $\mathbf{Y}$ whose covariance matrix is equal to the identity matrix $\mathbf{I}$ (*i.e.* $\mathbf{Y} = \mathbf{XT}$ where $\mathbf{C}_Y = \mathbf{I}$).

The covariance matrix of $\mathbf{Y}$ is equal to $\mathbf{C}_Y$ in equation 6.29, where $\mathbf{Y} = \mathbf{XT}$.

$$\mathbf{C}_Y = \mathbf{Y}^T\mathbf{Y} = \mathbf{T}^T\mathbf{X}^T\,\mathbf{XT} \tag{6.29}$$

Substituting $\mathbf{X}^T\mathbf{X}$ from equation 6.28 into 6.29 produces the following expression:

$$\mathbf{C}_Y = \mathbf{Y}^T\mathbf{Y} = (\mathbf{T}^T\mathbf{V}\mathbf{S}^T)(\mathbf{S}\mathbf{V}^T\mathbf{T}) \tag{6.30}$$

The transform $\mathbf{T}$ which causes the covariance matrix $\mathbf{C}_Y$ to become an identity matrix is given by :

$$\mathbf{T} = \mathbf{V}\mathbf{S}^{-1}\mathbf{V}^T \tag{6.31}$$

$\mathbf{T}$ is composed of three transformations. $\mathbf{V}$ performs a rotation of the data $\mathbf{X}$ so that the major and minor axes of the ellipse in Figure 6.13(b) are aligned with the I and Q axes. $\mathbf{S}^{-1}$ then scales the major and minor axes of the ellipse to form a circle. The final transformation $\mathbf{V}^T$ rotates the data back to the original position so that the $I + jQ$ phasors remain aligned across all frequency steps.

Substituting $\mathbf{T}$ from equation 6.31 into equation 6.30 produces the identity matrix $\mathbf{I}$. This result verifies that the I and Q channels are now corrected.

$$\mathbf{C}_Y = \mathbf{Y}^T\mathbf{Y} = (\mathbf{T}^T\mathbf{V}\mathbf{S}^T)(\mathbf{S}\mathbf{V}^T\mathbf{T}) = \mathbf{V}\mathbf{S}^{-1^T}(\mathbf{V}^T\mathbf{V})\mathbf{S}^T\mathbf{S}(\mathbf{V}^T\mathbf{V})\mathbf{S}^{-1}\mathbf{V}^T = \mathbf{I} \tag{6.32}$$

The transformation $\mathbf{T}$ for each transmitted frequency step can be simplified to two unique coefficients in a 2 by 2 matrix. Because $\mathbf{V}$ is orthogonal (*i.e.* $\mathbf{V}^{-1} = \mathbf{V}^T$ and $|\det\mathbf{V}| = 1$), it can be expressed in the following way :

$$\mathbf{V} = \begin{bmatrix} x & y \\ y & -x \end{bmatrix} \tag{6.33}$$

The matrix $\mathbf{S}^{-1}$ (and $\mathbf{S}$) is diagonal and can be written :

$$\mathbf{S}^{-1} = \begin{bmatrix} c & 0 \\ 0 & d \end{bmatrix} \tag{6.34}$$

Therefore, the transformation $\mathbf{T}$ can be expressed as :

$$\mathbf{T} = \mathbf{V}\mathbf{S}^{-1}\mathbf{V}^T = \begin{bmatrix} xa & yb \\ ya & -xb \end{bmatrix} \begin{bmatrix} x & y \\ y & -x \end{bmatrix} = \begin{bmatrix} x^2a + y^2b & xay - ybx \\ xay - ybx & x^2b + y^2a \end{bmatrix} \tag{6.35}$$

This transform can be normalised with respect to the first element $(x^2a + y^2b)$ so that the transform has unity gain. Equation 6.36 contains the transform $\mathbf{T}$ used to correct the I and Q samples of Figure 6.13 to produce Figure 6.14. The circle in the I/Q plane shows that the I and Q channels are decorrelated and gain matched. The transform for this particular frequency step consists of the two unique numbers $\gamma = 0.0662$ and $\delta = 0.7902$ (equation 6.36).

$$\mathbf{T} = \begin{bmatrix} 1 & \frac{xay-ybx}{x^2a+y^2b} \\ \frac{xay-ybx}{x^2a+y^2b} & \frac{x^2b+y^2a}{x^2a+y^2b} \end{bmatrix} = \begin{bmatrix} 1 & \gamma \\ \gamma & \delta \end{bmatrix} = \begin{bmatrix} 1.0000 & 0.0662 \\ 0.0662 & 0.7902 \end{bmatrix} \tag{6.36}$$

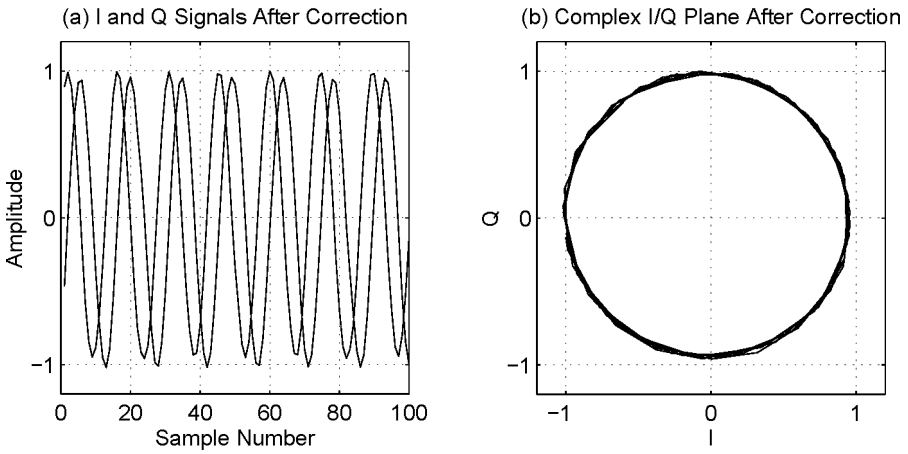

Figure 6.14: (a) The corrected I and Q samples at a single transmitted frequency; (b) the complex I/Q plane representation of the corrected I/Q phasor.

The correction transforms **T** have been obtained for all the transmitted frequencies of the 1-2 GHz SFGPR prototype. Figure 6.15 displays the measured differential gain (a) and differential phase (b) errors of the corrected homodyne quadrature receiver.

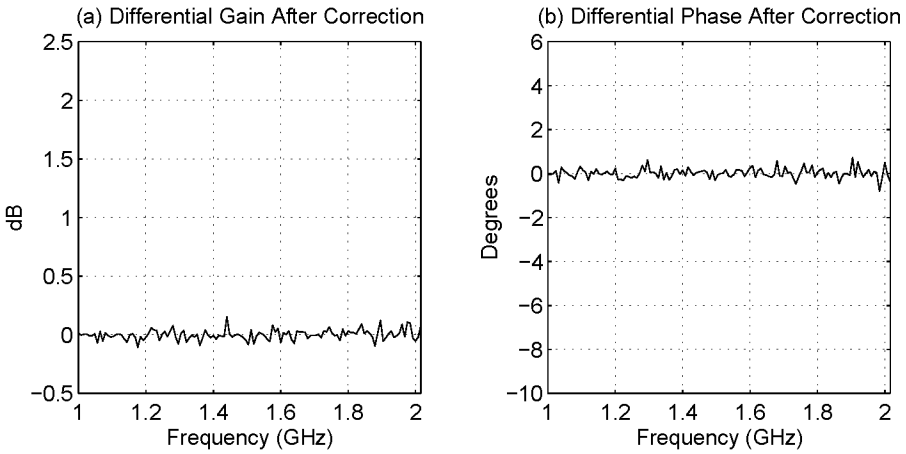

Figure 6.15: (a) Differential gain and (b) differential phase error measured after the correction. Compare with Figure 6.12. The transform decorrelates and matches the I and Q channels so that they are orthogonal and matched.

These errors were measured using the correlation technique described in Section 6.2.1. It is evident from these diagrams that the I and Q channels are decorrelated (*i.e.* very close to 0 degree differential phase error) and matched (*i.e.* very close to 0 dB differential gain error) across all frequencies of the 1-2 GHz SFGPR prototype.

Figure 6.16 contains the plots of the corrected closed loop data of Figure 6.11. The concentric circles in the I/Q complex plane are due to the frequency dependent (1-2 GHz) losses of the closed loop, which is common to both I and Q channels. The synthesised profile has a peak associated with the delay in resolution bin 25, and no Hermitian image in bin 101 (compare with Figure 6.11).

The plots in Figure 6.17 are before (a) and after (b) correction of the closed loop data with a strong window function applied (Dolph-Chebyshev with a -70 dB constant sidelobe level). It is evident that Hermitian image has been suppressed to more than 50 dB below the main peak response.

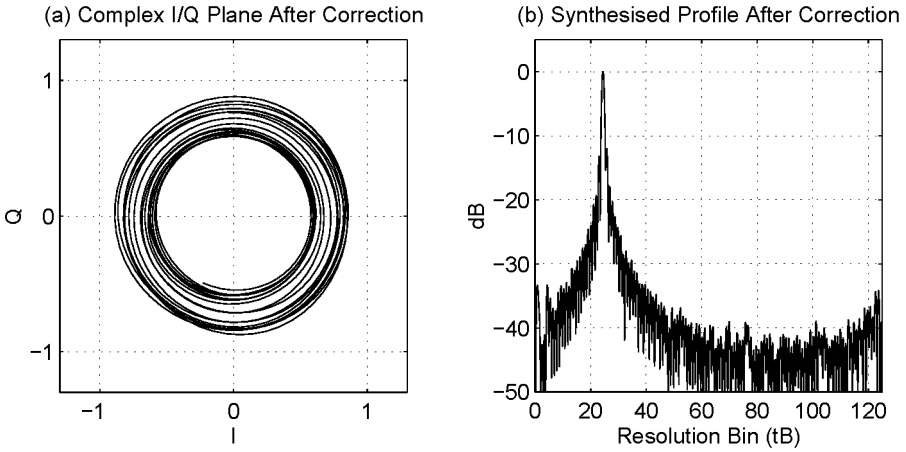

Figure 6.16: (a) Corrected I/Q phasor of the closed loop connected to the SFGPR ($\Delta tB = 25$); (b) the corrected synthesised profile with the main peak located at the $\Delta tB = 25$ bin, and the Hermitian image suppressed in bin 101 (compare with Figure 6.11).

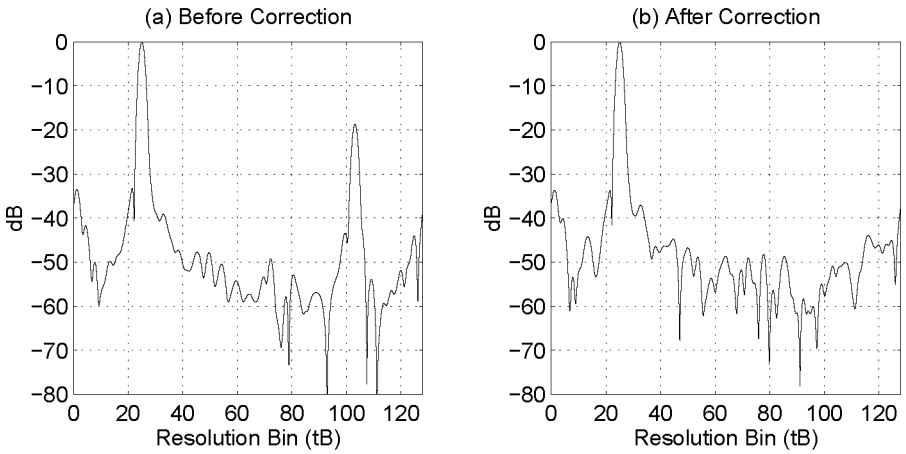

Figure 6.17: (a) Before and (b) after correction of the closed loop data with heavy windowing (Dolph-Chebyshev with a -70 dB constant sidelobe level).

Chapter 7

1-2 GHz SFGPR Results and Discussion

7.1 Introduction

Laboratory measurements on the 1-2 GHz SFGPR prototype to determine its external loop gain G_L are reported in Section 7.2 of this chapter. Although G_L is treated as a performance indicator of maximum penetration, in practice it is the sidelobe level of the direct leakage signal between the antennas which limits the maximum penetration depth of the system. Section 7.3 then discusses the field trial results of the system at various sites, including two open-cut coal mines. This section also presents the results of using synthetic aperture radar processing, high-resolution spectral estimation and range-gain control to improve the subjective quality and interpretation of the data.

7.2 Laboratory Measurements

In Section 5.2, a predicted external loop gain G_L of 150 dB, based on a 10 millisecond integration time and a 10 dB signal-to-noise ratio, was used to derive the waveform parameters of the SFGPR prototype. Actual measurements of G_L were conducted in the laboratory.

The G_L parameter (defined in equation 7.1) consists of a number of measurable quantities. Table 5.5 records the gain and coupling efficiency parameters

($G_{Tx}, G_{Rx}, \zeta_{Tx}$ and ζ_{Rx}) of the bow-tie and horn antennas. The remaining terms in equation 7.1 make up the system performance parameter SP.

$$G_L = G_{Tx}\, G_{Rx}\, \zeta_{Tx}\, \zeta_{Rx}\, SP = G_{Tx}\, G_{Rx}\, \zeta_{Tx}\, \zeta_{Rx}\, \frac{P_T t_{aq}}{FkT_0(SNR)} \tag{7.1}$$

Two measurable quantities in the SP definition are the mean transmitter power P_T and the receiver noise figure F. The integration time t_{int} and the signal-to-noise ratio SNR are defined in this thesis as 10 milliseconds and 10 dB respectively. The mean transmitter power P_T of the SFGPR system was measured as +15 dBm $\pm$ 1 dB across the 1-2 GHz bandwidth. The receiver noise figure F was measured by injecting a broadband noise signal into the low noise pre-amplifier of the receiver. The injected noise level was increased until the noise floor of the receiver rose by 3 dB. This indicated that the noise temperature of the noise source was equal to the noise temperature of the radar receiver. Using this technique, the noise figure F of the receiver was measured as 4 $\pm$ 1 dB (within the specifications of the low noise amplifier). Based on these measurements, the maximum system performance SP of the 1-2 GHz SFGPR system was at 155 $\pm$ 2 dB.

An independent measurement of the SP parameter was conducted using a sequence of attenuators connected in a coaxial closed loop between the transmitter and receiver ports of the antennas (antennas were disconnected). The radar frequency was stepped across the 1-2 GHz band and the data was collected to form the synthesised profile of this closed loop. Multiple profiles were stacked (incoherent averaging) in real-time to increase the integration time to one second. The attenuation of the closed loop was increased until the time domain signal fell below the 10 dB SNR threshold. This occurred for an attenuation level of 170 $\pm$ 1 dB. Scaling the SP parameter to a 10 milliseconds integration time results in 150 $\pm$ 1 dB. This figure is slightly less than the maximum 155 $\pm$ 2 dB previously measured. The difference is attributable to the loss in integration time (of around 2.4 dB), due to delays in frequency switching, DSP computation and the real-time display of the system.

Summing the nett antenna gain from Table 5.5 with the measured system performance figure SP yields the external loop gain parameter G_L of the system. The results are 156 $\pm$ 6 dB using bow-tie antennas, and 166 $\pm$ 6 dB using horns antennas.

The threshold set by the G_L parameter assumes that a target is detected if the received signal is stronger in power than the receiver's minimum detectable signal. In

practice, there is another factor which can limit the maximum penetration capability of the SFGPR system.

The sidelobes of the direct leakage signal between the transmit and receive antennas often mask weak reflected signals from buried targets which are received slightly after in time. This limitation, described previously in Chapter 4, is illustrated by Figure 7.1.

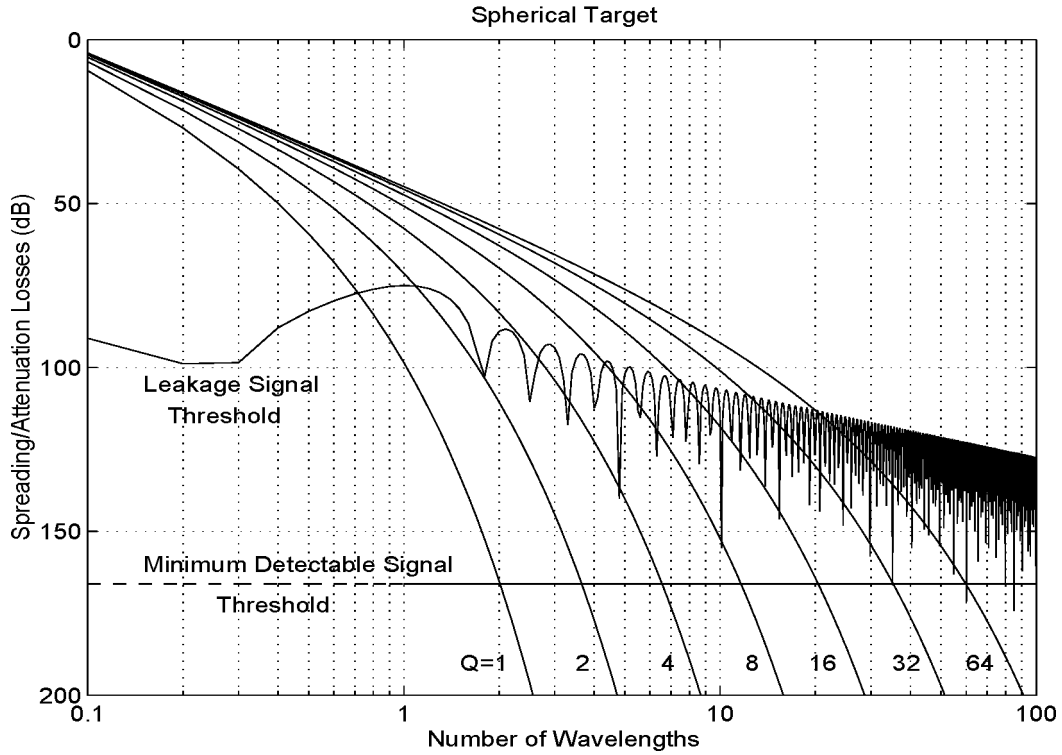

Figure 7.1: Constant Q nomogram of a spherical target with minimum detectable signal and leakage signal thresholds superimposed.

The figure is based on the constant Q nomogram for a spherical target of Figure 3.9. Superimposed on the nomogram are two thresholds; the minimum detectable signal at 166 dB below the transmitted power; and the sidelobes of the direct leakage signal between the transmit and receive antennas. It is evident from this figure that the sidelobe threshold is the practical limit for maximum penetration depth. Until the sidelobes of the leakage signal (or any other strong received signal) are suppressed significantly, the full external loop gain of the system can not be utilised in the field.

Various hardware and software solutions to reduce the sidelobe threshold have been proposed. For example, *Iizuka, Freundorfer & Iwasaki*, 1989 and *Kabutz, Lang-*

man & Inggs, 1994 have both built hardware cancellators to suppress the leakage signal before it is sampled by the analogue-to-digital converter. However, changes in the surface roughness and ground material properties can adversely effect the reliability of hardware cancellators.

The $I+jQ$ frequency domain data can be windowed with a more suitable function than rectangular prior to the IDFT [*Harris*, 1978]. However, these window functions remove energy concentrated at the lower frequency data points, resulting in a greater loss in resolution of the data. A signal processing technique called *FIR range-gain control* is described in Appendix D, and results in Section 7.3.4 have shown that the leakage signal threshold can be reduced using this technique.

7.3 Results from Field Trials

The 1-2 GHz SFGPR ruggedised prototype was tested at various sites[1]. The following subsections contain a selection of GPR images obtained during these field trials and discusses the results.

The GPR images consist of multiple synthesised profiles that were collected as the antennas were moved along the ground. The odometer was used to ensure a constant distance interval between consecutive profiles. The intensity of the gray-scale images represent the loss (in dB) associated with the return.

7.3.1 Experimental Pit

An experimental pit (360 cm long, 160 cm wide and 80 cm deep) was built by the research team in The University of Queensland grounds. It was constructed from blocks (40 cm by 20 cm by 20 cm) made of crushed coal and shale materials[2] with 5% cement. The measured Q of the block materials was approximately 18, with ϵ_r around 4. The pit consisted of four layers of blocks (total thickness of 80 cm) on a sheet metal base. Aluminium foil strips (30 cm wide) were placed along the width of the pit under the second (40 cm deep) and third layer (60 cm deep) of blocks.

[1]These trials were conducted by the author and co-researchers. The collected data was processed and interpreted by the author.

[2]The coal and shale materials were supplied by CRA from Tarong mine.

Figure 7.2 is the GPR image of the experimental pit, obtained with the SFGPR system using bow-tie antennas separated by 400 millimetres. The horizontal axis of the image is the cross-range dimension corresponding to the length of the pit. The vertical axis corresponds to the depth measured by the GPR. The gray scale intensity indicates the power loss in dB's relative to the transmitter power.

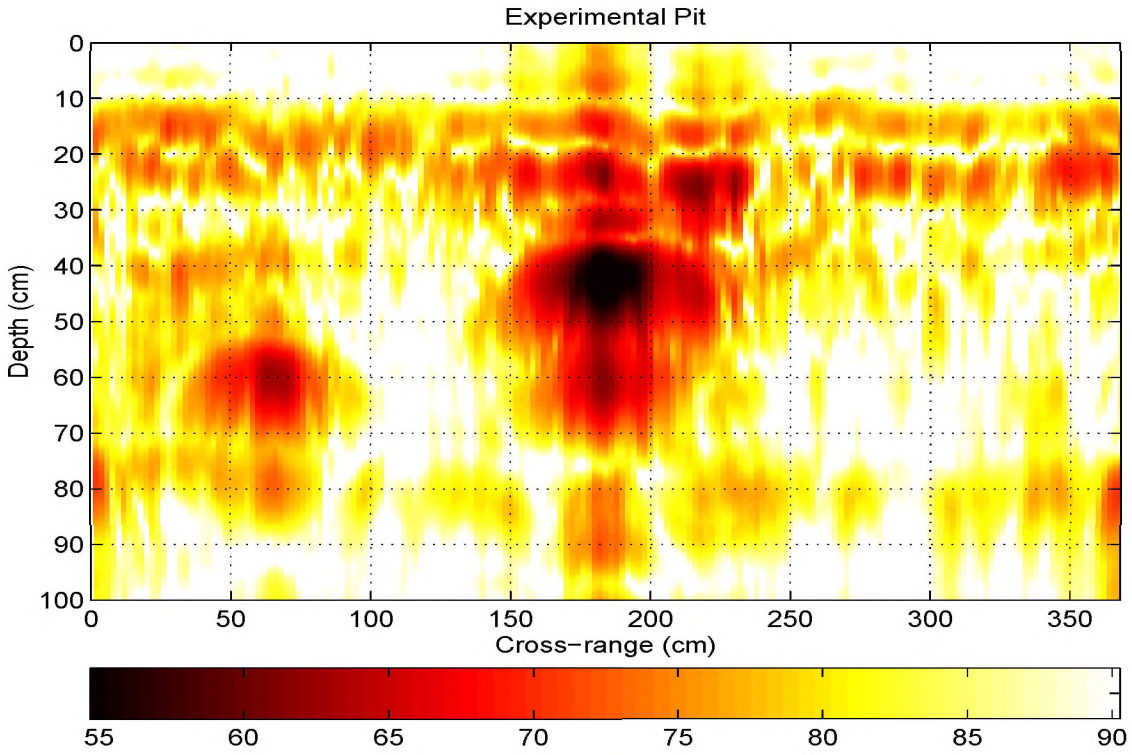

Figure 7.2: SFGPR image of the experimental pit containing two metallic targets buried at 40 and 60 centimetres, and a metallic base at 80 centimetres.

Both aluminium targets were easily detected by the SFGPR at the correct depths of 40 and 60 centimetres. The aluminium target located at a cross-range of 185 centimetres has an associated power loss of approximately 55 dB. The other aluminium target at a cross-range of 60 centimetres has a weaker signal with a power loss around 65 dB. The metal base of the pit is fairly well detected at 80 centimetres deep (with associated losses of around 80 dB). The first apparent layer in the image positioned slightly below 10 centimetres is the direct leakage signal between the bow-tie antennas. The next apparent layer around 20 centimetres deep corresponds to the first interface between the top and second layer of blocks. The interfaces between the remaining block layers are not detectable amid the clutter associated with the inhomogeneities of the blocks.

7.3.2 Concrete Pavement

The detection of reinforcing bars in concrete pavement gives a good illustration of the resolving power of the SFGPR system. The image in Figure 7.3 was obtained along a concrete pavement (ϵ_r is approximately 5 for dry concrete [*Bungey et al.*, 1994]) using bow-tie antennas separated by 200 millimetres.

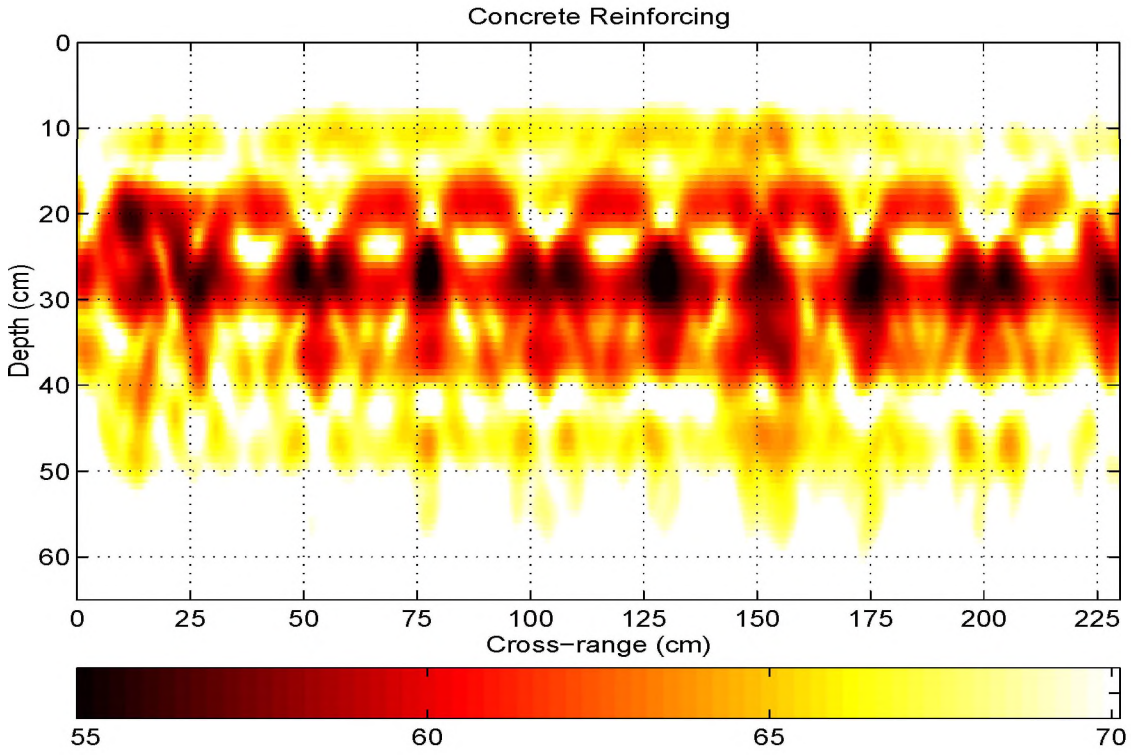

Figure 7.3: SFGPR image of reinforcing bars in concrete pavement.

The series of bright spherical targets around the 28 centimetre depth are equally spaced in the horizontal dimension by 25 centimetres. At first it seemed that these targets were the metal bars of the reinforcing mesh buried 28 centimetres below the surface of the concrete pavement, but this interpretation proved to be incorrect for the following reason.

Consider the two scenarios, illustrated in Figure 7.4 of antenna position relative to the concrete reinforcing bars. Scenario 1 represents the situation where the midpoint between the antennas is directly above a reinforcing bar. The target is between the beamwidths of the transmit and receive antennas. This situation describes the weaker series of targets at 20 centimetres deep, between the bright targets in the image. As the midpoint of the antennas moves away from the reinforcing bar, the

apparent depth of the target increases in a hyperbolic fashion until both antennas are almost directly over adjacent reinforcing bars. This is the second scenario in Figure 7.4. Two different reflection paths are now possible. The signal along the first path (indicated as 1) travels along the boresight of the transmit (Tx) antenna, and reflects diagonally towards the receive (Rx) antenna. The signal along the second path (indicated as 2) travels diagonally from the Tx antenna, and reflects towards the boresight of the Rx antenna. Because the antenna spacing of 20 centimetres is slightly less than the 25 centimetre spacing of the reinforcing bars, the two paths will occur at slightly different cross-range positions. This situation explains the series of strong target pairs in the image around 28 centimetres deep. The reason these reflections are stronger than those of scenario 1 is because the targets are in the centre beamwidth of one antenna, as opposed to being between the antenna beamwidths.

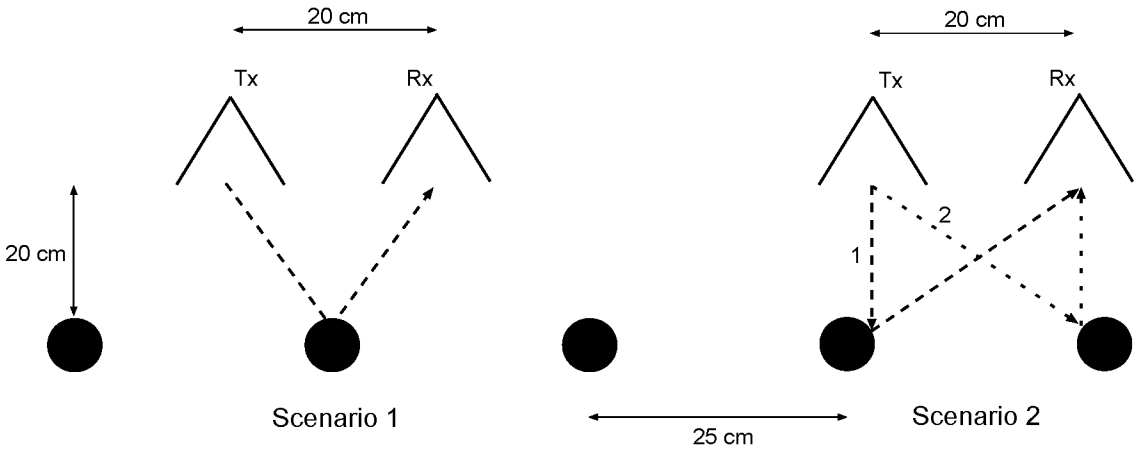

Figure 7.4: Two scenarios of antenna positions relative to the concrete reinforcing bars. The first scenario is where the midpoint between antennas is directly over the target. The reflections for this scenario correspond to the weaker returns in the image at 20 cm deep. The second scenario is where the midpoint of the antennas is between two reinforcing bars. The reflections of this scenario are the strong returns around 28 cm deep.

The image of the reinforcing bars is a good demonstration of the system's ability to resolve slightly different path lengths to within 8 centimetres. The geometrical aberration described in this image can be corrected using a SAR algorithm[3].

Figure 7.5 is the SAR processed image of the raw data in Figure 7.3. The reinforcing bars at 20 centimetres deep are now well resolved in both depth and cross-range dimension after the SAR processing. The processing gain due to the

[3]The SAR algorithm was written by Aruna Gunawardena of The University of Queensland. Refer to Appendix B.

increased aperture length is evident in the stronger reflections of the reinforcing bars relative to the leakage signal and clutter.

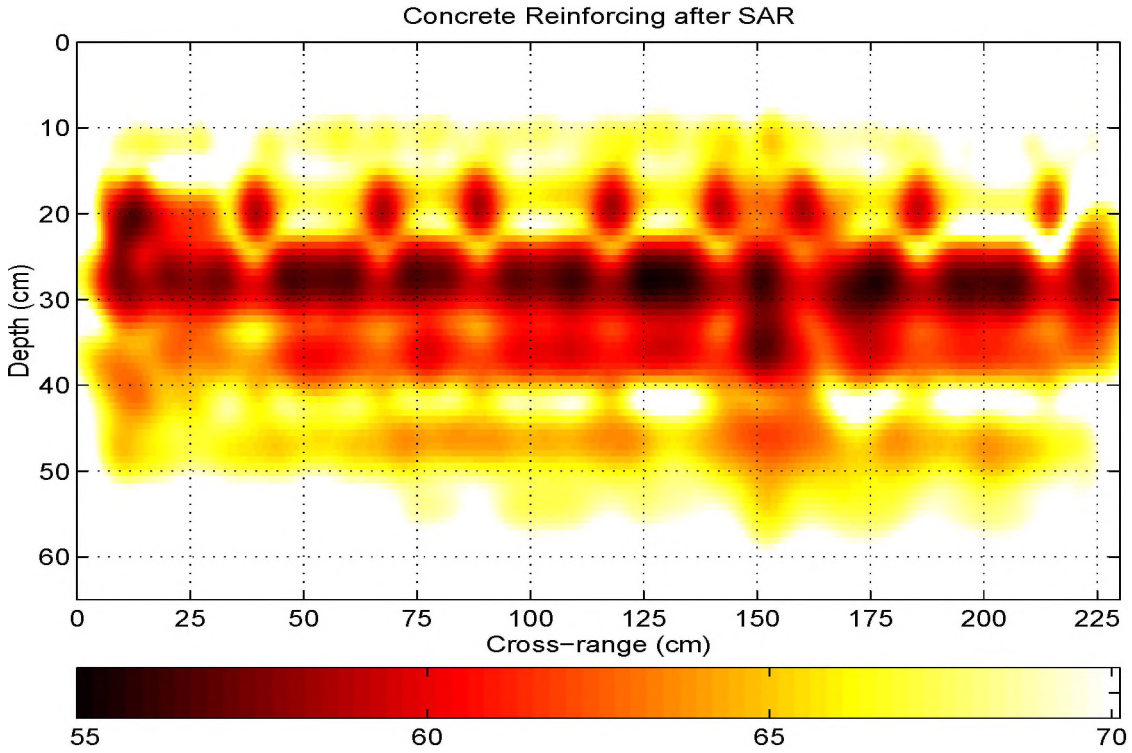

Figure 7.5: SAR processed image of the reinforcing bars in concrete pavement.

The strong reflection signals around 28 centimetres are those described by scenario 2 in Figure 7.4. Because the SAR algorithm has not yet taken into account the antenna beam patterns[4], these reflections are still present, but have been slightly defocused along the cross-range dimension.

7.3.3 Mt Thorley Mine, Hunter Valley NSW

The 1-2 GHz SFGPR system was first tested in an open-cut coal mine at Mt Thorley. A large slab of coal (185 cm long, 100 cm wide and 22 cm thick) was dislodged from a thin coal seam and orientated so that the top and bottom surfaces were clear of obstructions. The SFGPR system was used on the top surface to image the coal/air interface at the bottom surface.

[4]Further work by Aruna Gunawardena is concentrating on including the effect of antenna beam patterns into the SAR algorithm to properly focus all energy of the reinforcing bars to their correct range and cross-range bins.

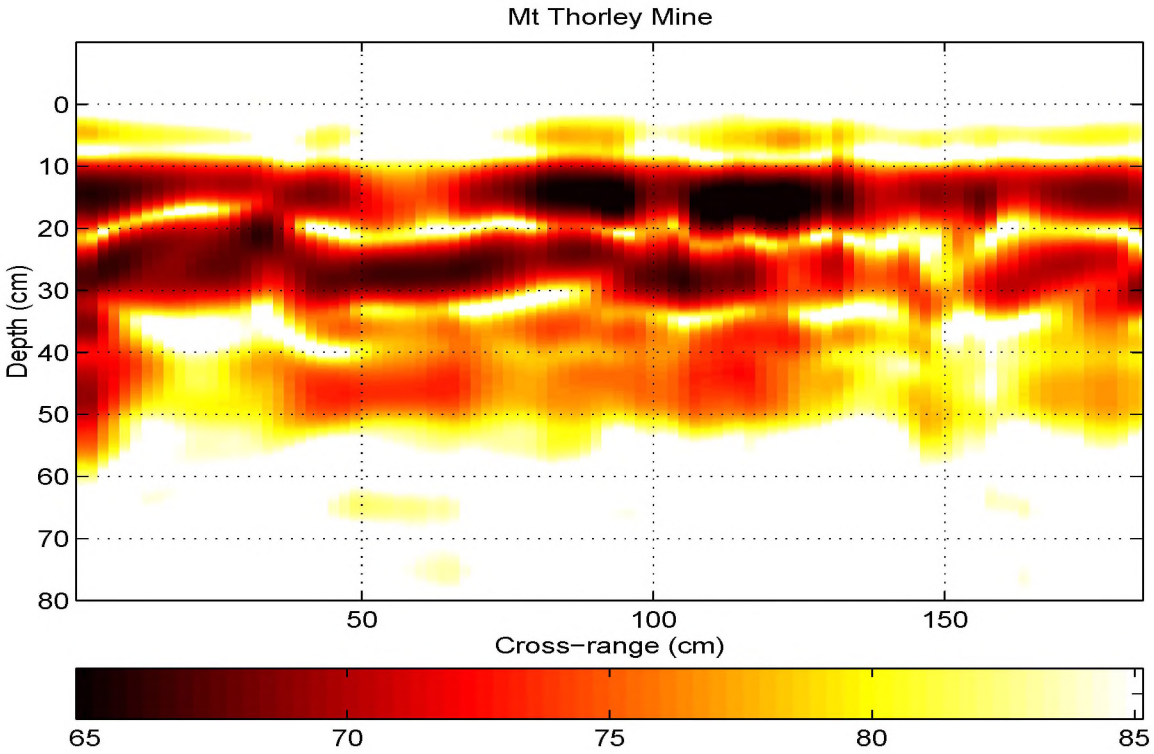

Figure 7.6: SFGPR image of a 22 centimetre thick coal slab at Mt Thorley mine. The Q of the coal is approximately 16, and ϵ_r is approximately 7.

The GPR image in Figure 7.6 was obtained using bow-tie antennas with a separation of 200 millimetres. The first layer between 10 and 20 centimetres is the direct leakage signal between the bow-tie antennas. The second layer corresponds to the 22 centimetre thickness of the coal slab. This image illustrates the high-resolution capability of the SFGPR system for mapping closely spaced coal interfaces.

It is unclear from this image whether the targets around 40 centimetres were multiple reflections within the coal slab, or other artifacts such as sidelobes. The correct interpretation of these reflections became clearer when a high-resolution spectral estimator (see Appendix C) was applied to the raw data.

Figure 7.7 is the processed image using the MUSIC algorithm. An AR model number p of 20 was chosen, with a k value of 6 representing the number of sinusoids estimated. This gave the best result in accurately estimating the target positions without introducing spurious peaks.

The direct leakage signal and the underside reflection of the coal slab in the MUSIC image are better resolved than the unprocessed image using the IDFT. In addition, the deeper reflection at around 48 centimetres can be identified as a

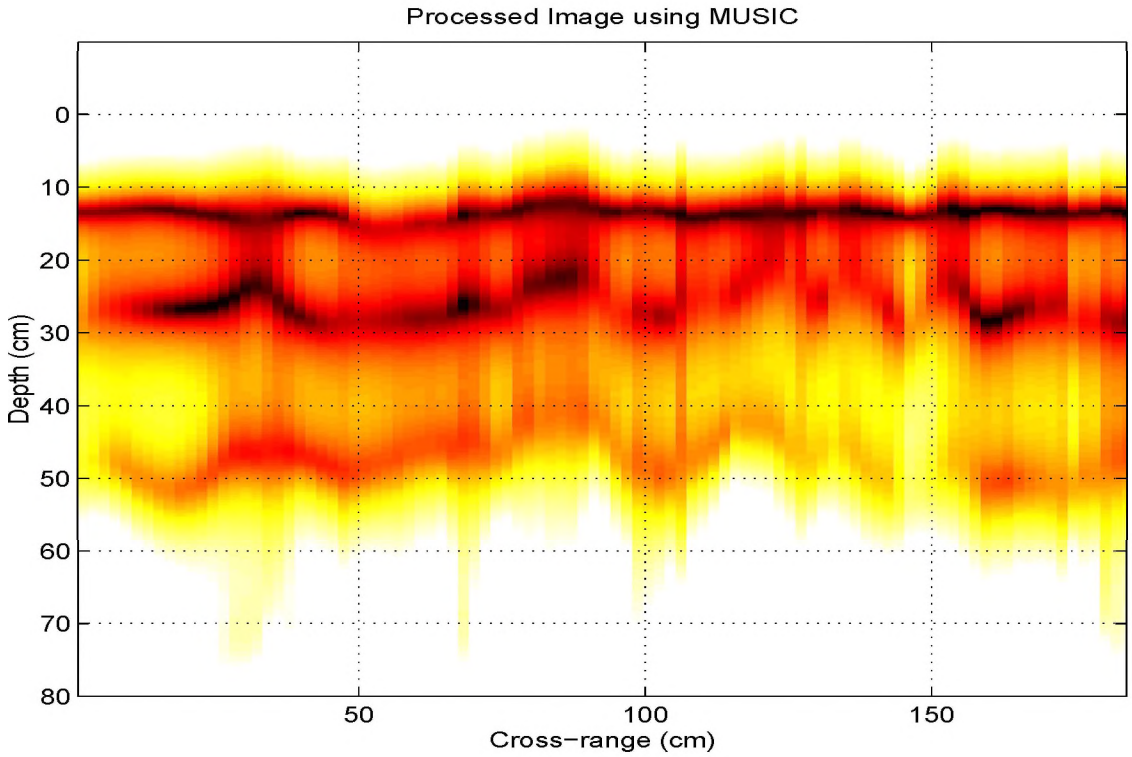

Figure 7.7: Processed image using the MUSIC algorithm of the 22 centimetre thick coal slab at Mt Thorley.

multiple reflection between the top and bottom surfaces of the coal slab. This interpretation was not clear from the image of the data processed using the IDFT.

Figure 7.8 is an example of single synthesised profiles of the same data processed using the IDFT (a) and MUSIC (b) algorithms. (The data was collected prior to the development of the quadrature error correction process of Chapter 6. As a result, the Hermitian images of the targets are present in the conjugate resolution bins.) The MUSIC spectral estimator produced sharp peaks, in comparison with the broad mainlobes and sidelobes of the targets which are characteristic of the IDFT algorithm.

In other cases, it was found that the modern spectral estimates were useful for providing higher resolution images of simple planar interfaces. However, the robustness of the spectral estimates in relation to tolerable SNR's and the sensitivity of the p and k parameters between different data sets pose a problem for reliability. As a general rule, modern spectral estimation techniques should be used for further processing when the initial IDFT processing suggests that improvements in resolution may be possible.

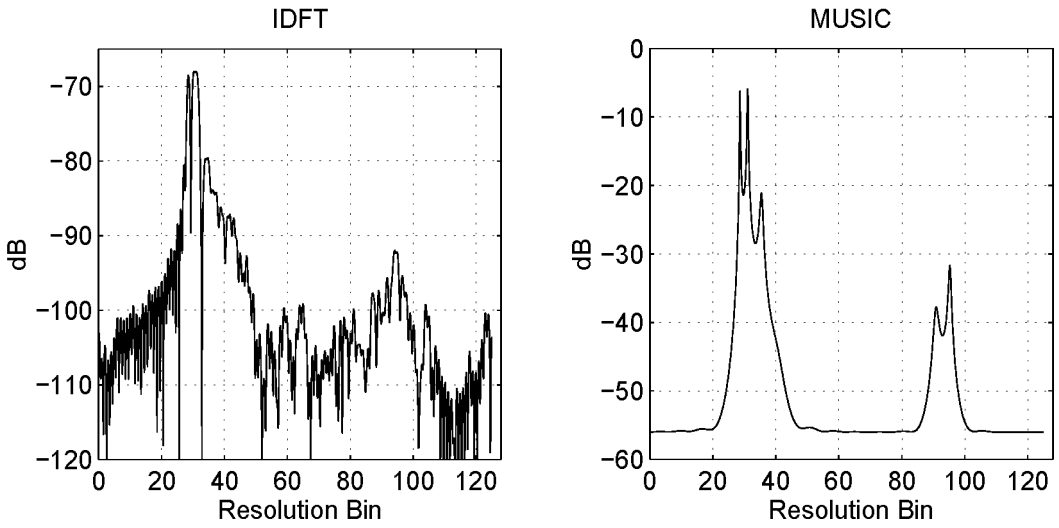

Figure 7.8: Single synthesised profiles of coal slab image using (a) IDFT and (b) MUSIC.

7.3.4 Ebenezer Mine, South-East Queensland

At Ebenezer mine, the SFGPR system was tested on top of a thin coal seam *in situ*. Beneath the coal at a depth of 70 centimetres was a shale interface. Horn antennas were used on the trolley to image the coal/shale interface through the coal seam.

The image recorded at this site is displayed in Figure 7.9. The bottom layer around the 70 centimetre depth corresponds to the coal/shale interface at the site. The cause of the reflections above the interface were not confirmed but are most likely due to fracturing within the coal seam. Results consistent with this image were obtained during multiple parallel passes along the coal seam. The strength of the coal/shale interface can be increased relative to the leakage signal and other reflections within the coal seam using a range-gain control (see Appendix D).

Figure 7.10 is the image of the thin coal seam at Ebenezer mine processed with the complex FIR range-gain function of Figure D.2. In comparison with the unprocessed image of Figure 7.9, the strength of the coal/shale interface at 70 centimetres deep has been increased by 15 dB relative to the direct leakage signal. The sidelobes

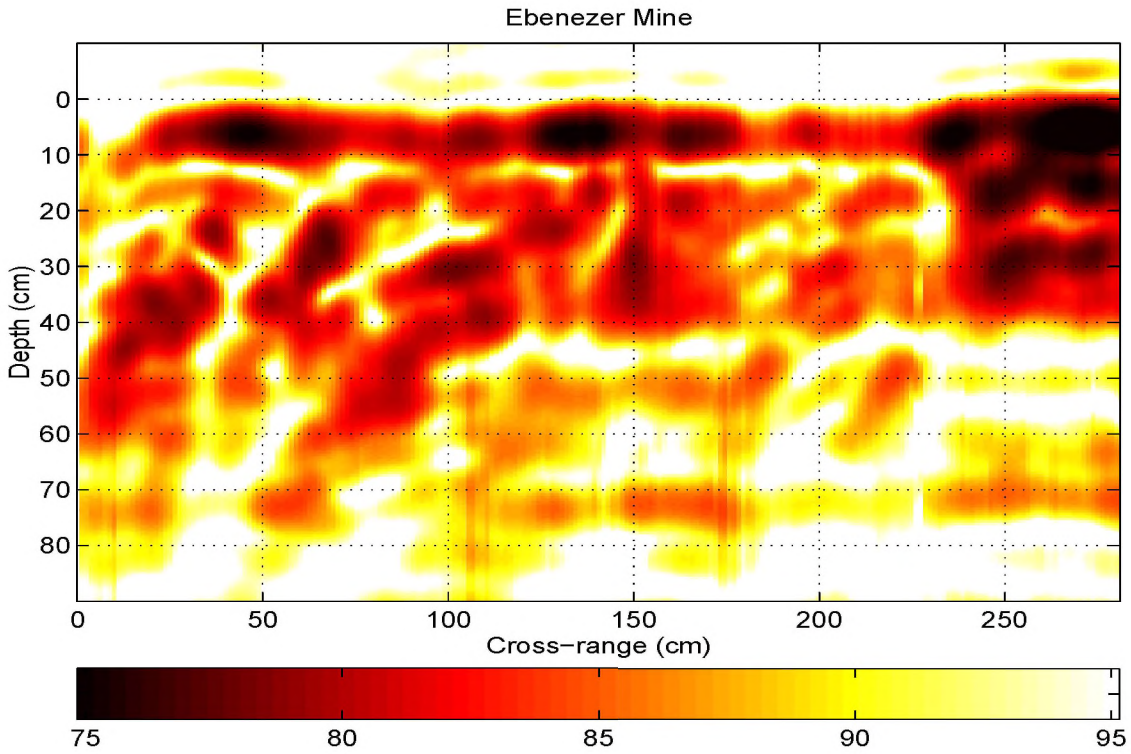

Figure 7.9: SFGPR image of a fractured coal seam at Ebenezer mine with a shale interface at 70 centimetres depth. The measured Q of coal was approximately 10, and ϵ_r was around 4.5.

of the leakage signal remain at their correct dB levels. Other targets within the coal seam are also enhanced relative to the leakage signal.

Other types of range-gain function such as "range-gates" can be designed using complex FIR functions. For example, measurements of radar cross sections of targets in a RCS test facility often use software range-gating to suppress spurious scatter and clutter from outside the test zone [*Walton & Young*, 1984; *Walton*, 1994].

7.4 Summary

In this Chapter, the laboratory measurement of the external loop gain G_L was described for the 1-2 GHz SFGPR system. The measured result was 156 $\pm$ 6 dB for bow-tie antennas and 166 $\pm$ 6 dB for horn antennas. These measurements are slightly better than the prediction made in Chapter 5.

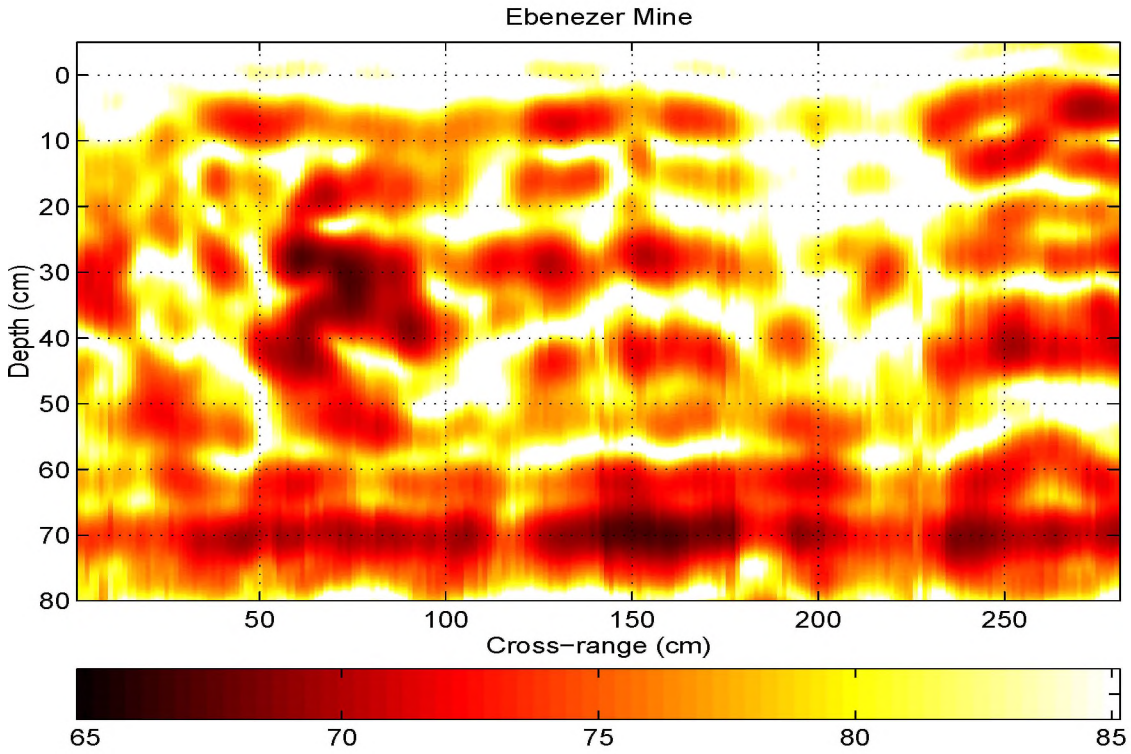

Figure 7.10: Processed image of the Ebenezer coal seam with the complex FIR range-gain function of Figure D.2. Compared with the unprocessed image of Figure 7.9, the strength of the coal/shale interface at 70 centimetres is increased relative to the direct leakage signal.

It is shown that the sidelobes of the direct leakage signal between the transmit and receive antennas may set the threshold which limits the maximum penetration depth, rather than the external loop gain of the system.

The field results obtained from these tests at several sites showed that the penetration depth was at least 80 centimetres and a resolving power was better than 8 centimetres. The subjective quality of the field results were improved using several signal processing algorithms which included synthetic aperture processing, high-resolution spectral estimation and range-gain control.

Chapter 8

Conclusions and Future Work

8.1 Conclusions

This work has demonstrated the practical benefits of the stepped-frequency radar technique in high-resolution, ground penetrating radar applications. Results obtained at several sites including two open-cut coal mines have shown a penetration depth of at least 80 centimetres and a resolving power of better than 8 centimetres. Three main contributions have been made in association with this work :

1. GPR performance characterisation
2. Stepped-frequency GPR development and testing
3. Broadband quadrature error correction

1. GPR Performance Characterisation

The analysis of GPR performance characteristics was greatly simplified by using the constant Q model for ground materials. This provided a novel and useful method for characterising the maximum penetration depth of a GPR system as a fixed number of wavelengths which is constant for any single frequency of the constant Q model. Similarly, the resolving power was expressed as a fixed number of wavelengths which is also constant with frequency. These expressions enabled a comparison of performances between different GPR systems, irrespective of the frequency chosen for each. In addition, they provided a useful design tool for selecting the waveform parameters required by a GPR system to achieve the necessary operating performance for a defined application.

2. Stepped-Frequency GPR Development and Testing

A review of high-resolution and ultra-wideband radar techniques concluded that impulse radars have the following inherent disadvantages when compared with pulse-compression radars:

- High mean powers are difficult to obtain in short-time impulses.
- A substantial part of the available impulse energy at low frequencies is not radiated by the transmitting antenna.
- The received waveforms are typically sampled using inefficient (sliding window) digitisers to overcome the ultra-fast sampling requirement.

In view of this, it was decided to conduct an extensive literature review and rigorous theoretical study of an alternative radar technique. The stepped-frequency radar was chosen because it had potential advantages over impulse radar. It was demonstrated that the stepped-frequency radar can "synthesise" an impulse-like waveform using an IDFT-based matched filter with minimum-phase. However, the practical benefits of impulse synthesis over impulse generation were found to be:

- Ultra-wideband signals with high mean powers are easily obtained with the transmission of longer, stepped-frequency pulses.
- All the energy of these signals is contained within the antenna bandwidth and is therefore radiated efficiently.
- Stepped-frequency waveforms are easily sampled with audio-frequency digitisers of high instantaneous dynamic range.

These advantages combine to give the stepped-frequency radar more processed mean energy than impulse radar for the same bandwidth, and therefore should give superior performance in maximum penetration depth and resolving power in GPR applications.

The complete design (excluding antennas) of a stepped-frequency GPR prototype for the high-resolution mapping of thin coal seam structures in open-cut coal mines was described. The external loop gain of the system was estimated at 150 dB. This figure implied that the radiated signal, integrated over a ten millisecond interval, could tolerate a maximum power loss of 150 dB between the transmit and receive

antennas and maintain a signal-to-noise ratio of 10 dB. Based on this prediction and from dielectric measurements of coal conducted elsewhere, the 1-2 GHz frequency bandwidth was chosen for the performance requirements of one metre penetration depth and five centimetre resolution in coal.

A working prototype was designed around a simple yet sensitive homodyne system. Laboratory measurements of the system's external loop gain were obtained for a 10 millisecond integration time interval and a 10 dB signal-to-noise ratio :

Table 8.1: External Loop Gain measured of the 1-2 GHz SFGPR system

Antenna Used	**External Loop Gain**
Bow-tie	156 $\pm$ 6 dB
Horn	166 $\pm$ 6 dB

These measurements were better than the 150 dB design prediction. The performances of typical impulse GPR systems were noted in the literature to lie between 100-130 dB under similar conditions [*Wright, Bradley & Grover*, 1994].

A ruggedised version of the SFGPR system was built by MITEC based on the working prototype. The ruggedised system was used for the field trials and was successfully tested at various sites, including two open-cut coal mines. The resulting images demonstrated a penetration depth of at least 80 centimetres and a resolving power of better than 8 centimetres. Signal processing techniques including a SAR algorithm, high-resolution MUSIC spectral estimator and range-gain control were successful in improving the subjective quality and interpretation of the raw images.

3. Broadband Quadrature Error Correction

A new and novel technique was presented which corrects broadband quadrature errors of the stepped-frequency radar receiver. The correction algorithm was obtained from a transform which diagonalised and scaled the covariance matrix of a test signal, and aligned the $I + jQ$ phasors across all frequency steps.

Using this technique, the quadrature receiver errors of the 1-2 GHz SFGPR prototype were corrected to within a 0.1 dB gain imbalance, and to within a 0.5 degree phase imbalance. The Hermitian images of the radar reflections were shown to be suppressed by more than 50 dB below the main reflection peaks.

8.2 Future Work

This thesis has characterised and tested the performance of a stepped-frequency radar system operating in the 1-2 GHz frequency range for the purpose of high-resolution GPR applications. Most of the hardware designs and signal processing techniques proposed in this thesis are relevant to any stepped-frequency radar system (including GPR) across different frequency bandwidths. For instance, the author and co-researchers are currently developing a 10-620 MHz SFGPR system for deeper penetration applications which do not require such high-resolution.

There are three separate areas where the author believes future work may be directed to implement an improved stepped-frequency GPR system. The author and co-researchers are currently working in these areas.

Hardware Range-Gating

The transmission of continuous waveforms by a stepped-frequency GPR has two problems which limit its maximum penetration capability. The first problem was described in Section 7.2 as the sidelobe threshold of the leakage signal which can mask weaker reflections. The FIR range-gain control described in Appendix D goes a long way to remedy this problem. The second problem is the limited dynamic range of the receiver. The radar receiver can only simultaneously detect strong and weak reflected signals that are within the hardware dynamic range. The upper bound of the dynamic range is usually set by the strongest expected return signal. In many situations, the leakage signal between the antennas constitute the strongest signal. It follows then that the weakest signal that will be detected must be stronger than the lower bound of the dynamic range. FIR range-gain control does not improve the limited dynamic range of the hardware, which is usually determined by the analogue-to-digital converter.

Hardware range-gating (see Appendix E) can be used to "blank" unwanted strong signals in the receiver prior to sampling. This technique enables the upper bound of the system's dynamic range to be positioned at a lower power level without being saturated. The range-gate position can be shifted along the unambiguous range during consecutive transmissions, during which a *sensitivity range control* amplifier can increase the gain of signals in range-gates further along in range. This method is the hardware analogy to the software range-gating technique briefly described at the end of Appendix D.

It is proposed to couple the hardware range-gating technique and the FIR software range-gain control into one system. Hardware range-gating with sensitivity range control could be used for "coarse" adjustments of the received signal strength along the unambiguous range, while the FIR range-gain control in software could be a "fine" adjustment within each range-gate.

Digital Quadrature Sampling

Although the DC offset and quadrature errors of the homodyne receiver can be suppressed using the techniques described in Chapter 6, these errors are subject to long-term drifting. The correction procedures can be repeated periodically, which has proven to be an acceptable solution for the 1-2 GHz SFGPR prototype.

A more robust solution would be the implementation of a digital quadrature receiver. This technique, described further in Appendix F, uses a heterodyne mixer to obtain a fixed intermediate frequency of the received signals. A band-pass filter is used to remove the DC offset and higher-frequency mixing components. The resulting signal is sampled at twice the Nyquist rate using a single analogue-to-digital converter. These samples are digitally down-converted into their baseband quadrature components (see Appendix F). The digital down-conversion technique is not vulnerable to quadrature gain and phase errors, and also suppresses the DC component added by the analogue-to-digital converter.

Optimal Matched Filtering

The IDFT is not an optimal matched filter for the received stepped-frequency GPR signals. The external losses associated with attenuation and spherical spreading were shown to be strongly frequency dependent in Section 3.2.2. These frequency variations cause *frequency dispersion*, where the resulting target responses are broadened by an amount which is a function of depth. Therefore, the resolving power of targets deteriorate with increasing depth [*Siggins & Turner*, 1992]. The effects of frequency dispersion can be analysed using time-frequency distributions of the received radar data [*Sato, Satoshi & Hiroaki*, 1994; *Ling et al.*, 1995].

Turner, 1992 approached this problem with impulse GPR using a deconvolution technique in the time-domain (refer also to *Turner*, 1993). This work assumed that the frequency variation of the received signals is described by the Q-factor (*i.e.* attenuation dispersion) of the ground material. However, it does not take into

account the frequency variation of the radar cross section for spherical and rough planar targets.

For stepped-frequency GPR, the amplitudes of the received frequency domain signals $I + jQ$ from a target will be exponentially-damped with a damping constant related to the Q-factor of the ground and the scattering mechanisms of the target.

An optimal matched filter for the received exponentially-damped frequency signals of a known target and material Q-factor is proposed. Two approaches are recommended, following the work by *Walton & Gerry*, 1995. Firstly, a *chirp* $\mathcal{Z}$-*transform* [*Rabiner, Schafer & Rader*, 1969] could be used as a matched filter with a tunable parameter relating to the Q-factor of the ground and the scattering (*i.e.* spherical, rough or smooth planar) process. Secondly, a high-resolution spectral estimator [*Kumaresan*, 1982] could be designed to estimate the exponentially-damped frequency data samples outside the transmitter bandwidth.

Appendix A

Mathematical Description of Stepped-frequency

Figure A.1 is a simple block diagram of a stepped-frequency radar system. The transmitted waveform $x(t)$, received waveform $y(t)$ and the complex baseband waveform $I(t) + jQ(t)$ are represented in Figure A.2. A mathematical description of these waveforms associated with the stepped-frequency technique will now be conducted.

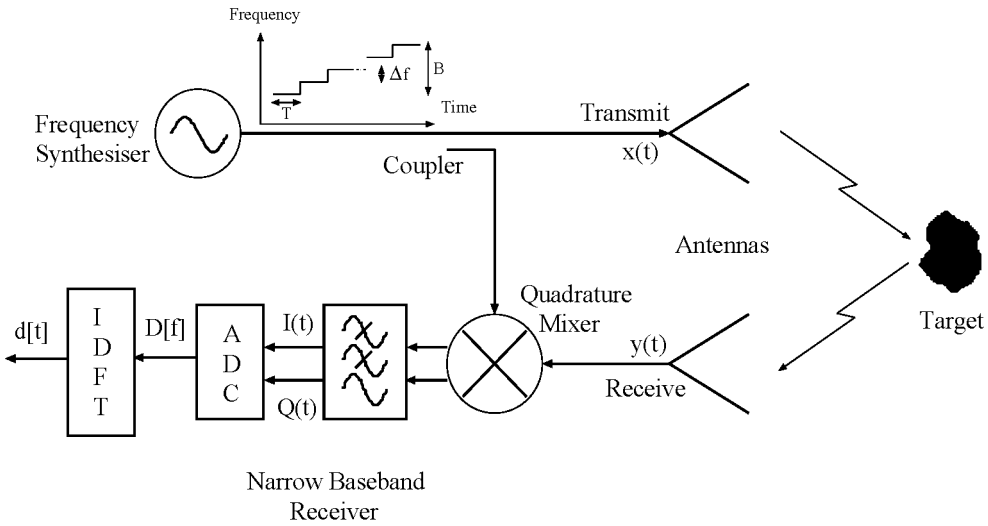

Figure A.1: Simple block diagram of a stepped-frequency radar.

The expanded time waveform of the transmitted stepped-frequency signal $x(t)$ can be represented as a continuous train of n stepped-frequency pulses (see top waveform in Figure A.2). Each pulse in the train has a width of T seconds and a carrier frequency which is stepped from pulse to pulse in Δf steps starting from the

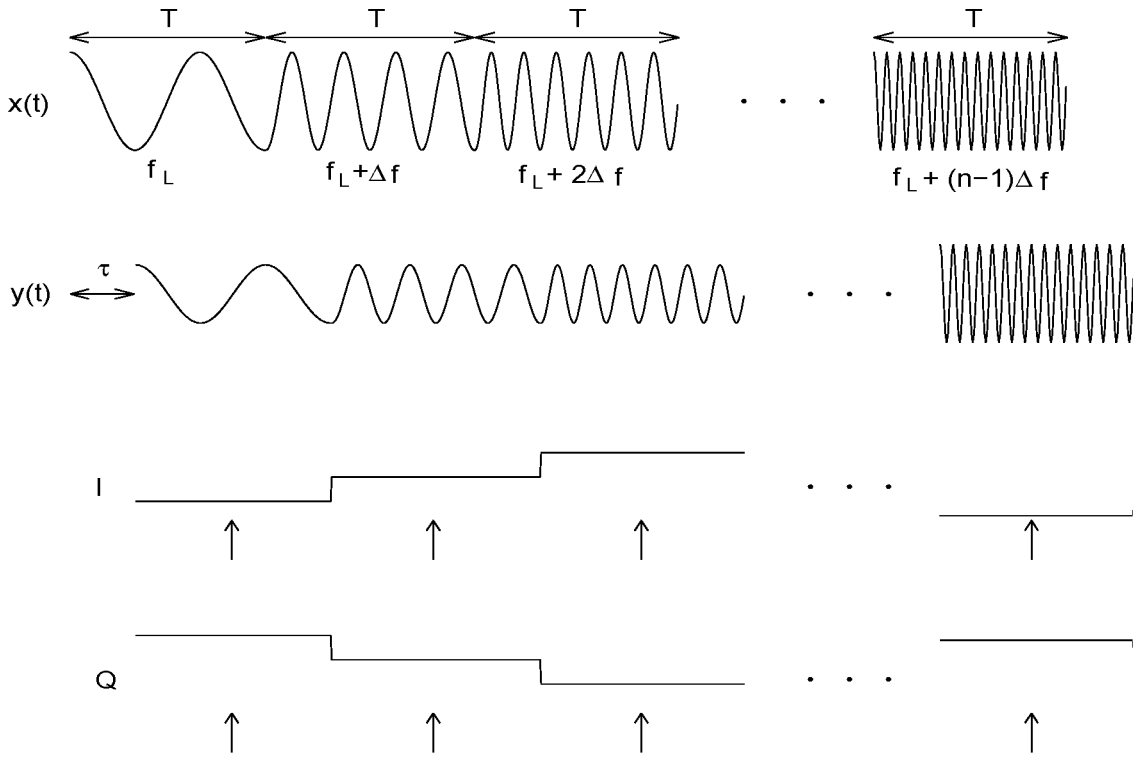

Figure A.2: Waveform representation of the stepped-frequency technique. $x(t)$ is the transmitted waveform, $y(t)$ is the received waveform with a delay τ, and I and Q are the complex baseband components of the received waveform.

lower frequency bound f_L. Generally, there are many cycles of the carrier frequency within each pulse envelope. (It is assumed for a coherent system that the amplitude and phase of each stepped-frequency pulse in the train is constant for all frequency steps. The switching delay between frequency steps is assumed negligible.)

The stepped-frequency pulse train $x(t)$ is mathematically represented by :

$$x(t) = \sum_{i=0}^{n-1} \mathbf{Re}\left\{\exp\left(j2\pi(f_L + i\Delta f)t\right)\right\} \text{ rect}\left(\frac{t - iT - T/2}{T}\right) \qquad \text{(A.1)}$$

Consider a single point target with a reflection coefficient of $\Gamma = |\Gamma|e^{j\phi}$ and an associated delay τ in a lossless medium. (It is assumed that the permittivities of the target and medium are constant with frequency so that Γ and τ can be treated constant as well.)

The reflected signal $y(t)$ from this single point target is represented by :

$$y(t) = \sum_{i=0}^{n-1} \mathbf{Re}\left\{|\Gamma|e^{j\phi}\exp\left(j2\pi(f_L + i\Delta f)(t-\tau)\right)\right\} \text{ rect}\left(\frac{t-\tau-iT-T/2}{T}\right) \quad \text{(A.2)}$$

A reference version of the transmitted signal is coupled to the receiver and the complex signal $I_{ref}(t) + jQ_{ref}(t)$ is formed using a quadrature mixer:

$$I_{ref}(t) + jQ_{ref}(t) = 2\sum_{i=0}^{n-1} \exp\left(-j2\pi(f_L + i\Delta f)t\right) \text{rect}\left(\frac{t-iT-T/2}{T}\right) \quad \text{(A.3)}$$

The received signal is down-converted to a complex baseband signal $I(t) + jQ(t)$ through mixing with the reference signal components and low-pass filtering (it is assumed that $T >> \tau$) :

$$I(t) + jQ(t) = \sum_{i=0}^{n-1} |\Gamma|e^{j\phi}\exp\left(-j2\pi(f_L + i\Delta f)\tau\right) \text{rect}\left(\frac{t-iT-T/2}{T}\right) \quad \text{(A.4)}$$

A sampling waveform $s(t)$ which samples a single point in the middle of each pulse of the complex baseband pulse train $c(t)$ can be described by:

$$s(t) = \sum_{i=0}^{n-1} \delta(t - iT - T/2) \quad \text{(A.5)}$$

Multipling $s(t)$ with $I(t) + jQ(t)$ results in this sampled complex array :

$$C[k] = |\Gamma|e^{j\phi}\ \exp\left(-j2\pi(f_L + k\Delta f)\tau\right) \qquad k = 0, 1, 2, \ldots n-1 \quad \text{(A.6)}$$

Each element in the above array is a frequency sample of the complex baseband signal for each pulse in the train. Hence, it can be expressed as a discrete frequency domain array $C[f]$:

$$C[f] = |\Gamma|e^{j\phi}\ \exp\left(-j2\pi(f_L + f)\tau\right) \qquad f = 0, \Delta f, 2\Delta f, \ldots (n-1)\Delta f \quad \text{(A.7)}$$

The analogue down-conversion process by the quadrature mixer can be reversed after sampling by up-converting the complex baseband frequency data to the band-pass equivalent of the transmitter bandwidth. This is carried out by inserting the

n-element $C[f]$ array into an N element array $D[f]$ (where $N > n$) so that the lower frequency bound f_L begins at element $f_L/\Delta f$, and so on to the upper frequency bound in increments of the frequency step Δf. The remaining elements in the array including the negative frequency half are padded with zeros. The resulting N-element array is :

$$\begin{aligned} D[f] &= 0 && f = 0, \Delta f, 2\Delta f, \ldots f_L - \Delta f \\ &= |\Gamma| e^{j\phi} \exp(-j2\pi f\tau) && f = f_L, f_L + \Delta f, \ldots f_L + (n-1)\Delta f \\ &= 0 && f = f_L + n\Delta f, f_L + (n+1)\Delta f, \ldots N \end{aligned} \quad \text{(A.8)}$$

A discrete frequency function of the above array can be written as equation A.9, where f_c is the centre frequency of the transmitter bandwidth :

$$D[f] = |\Gamma| e^{j\phi} \text{ rect}\left[\frac{f - f_c}{B}\right] e^{-j2\pi f\tau} \quad \text{(A.9)}$$

An inverse discrete Fourier transform (IDFT) is used to transform the frequency domain function $D[f]$ to the time domain $d[t]$:

$$d[t] = \text{IDFT}\{D[f]\} = |\Gamma| e^{j\phi} B\text{sinc}(B(t-\tau)) e^{(j2\pi f_c(t-\tau)} \quad \text{(A.10)}$$

The result is a synthesised time profile containing the target's reflection coefficient and delay time. The IDFT algorithm is a pulse compression filter which compresses the received time waveform y(t) in equation A.2 to form the high-resolution synthesised time waveform d[t] of equation A.10. For multiple targets, the IDFT compresses the reflected time waveforms by coherently summing the voltages of each target into their respective time bin in the synthesised profile. For threshold detection of a point target amid white noise, the IDFT is a matched filter for optimising the peak signal to rms noise.

Appendix B

SAR Processing

Unprocessed images of buried targets obtained using GPR have a cross-range (or azimuthal) resolution dependent on the physical aperture of the antennas. Because the aperture of low-gain, broad beamwidth antennas is narrow, the cross-range resolution is rather poor in comparison with the range or depth resolution. Therefore, spherical targets such as pipes and cables are defocused along the azimuthal dimension of images, generally following the trajectory of a hyperbola [*Gunawardena & Longstaff*, 1995a].

Migration is a well-known technique in geophysical processing which is used to focus the hyperbolic response of targets in seismograms [*Stolt & Benson*, 1986; *Robinson & Durrani*, 1986]. The same type of algorithm is also used to focus targets in GPR images [*Stolte & Klaus-Peter*, 1994]. (The similarities and differences between the migration and SAR algorithms are discussed by *Rocca*, 1987, *Ottolini*, 1987 and *Gunawardena & Longstaff*, 1996.)

A *matched filter-based* SAR algorithm[1] was tested on data obtained with the 1-2 GHz SFGPR system. The algorithm coherently sums the data points along the curved hyperbolic path of a target's response using a matched filter. This process synthetically widens the aperture length of the data to focus hyperbolic target responses into a point, thereby increasing the cross-range resolution. Slanting interfaces are also focussed to their correct geometry by the algorithm. In addition to the increased cross-range resolution, there is a processing gain relative to incoherent noise and clutter signals associated with the coherent summing of the target's energy along the synthesised aperture length.

[1]The SAR algorithm was written and processed by Aruna Gunawardena of The University of Queensland [*Gunawardena & Longstaff*, 1995b].

Appendix C

High-Resolution Spectral Estimation

The bandwidth of the stepped-frequency radar defines the resolution limit for an IDFT-based matched filter. This is because the IDFT assumes that the frequency domain data points outside the bandwidth have zero values, and estimates the synthesised profile based on this band-limited condition. Broader bandwidths effectively synthesise narrower pulses which are more highly resolved in the synthesised profile. However, it is difficult to broaden the bandwidth of a stepped-frequency radar beyond the fractional bandwidth limit of the antennas.

Types of spectral estimators other than the IDFT (or *periodogram*) can be used to form a higher-resolution synthesised profile from the same bandlimited frequency domain data. These modern spectral estimators use parametric functions to model the data and predict data points outside the frequency range of the collected data samples. By estimating over a broader bandwidth than the sampled data, higher-resolution synthesised profiles can be obtained.

The theory and application of modern spectral estimation can be found in textbooks by *Marple*, 1987 and *Kay*, 1988, and in a special journal issue edited by *Haykin & Cadzow*, 1982. Many applications of spectral estimation have been made in the areas of radar and geophysics [*Robinson*, 1982]. Some work has been reported applying modern spectral estimators to GPR data. *Liau, Carr & Cuthbert*, 1986, *Olver & Cuthbert*, 1988 and *Agbinya*, 1993 have reported results using *maximum entropy methods* (MEM) to improve the time-domain representation of data obtained with FMCW GPR systems. *Walton*, 1993a proposed using autoregressive models with least square solutions on frequency domain data of a stepped-frequency

GPR. So too did *Langman, Inggs & Flores*, 1994, who conducted some preliminary work on applying extended Prony's method to SFGPR simulation and laboratory measurements. However, none of these reports have presented high quality results of spectral estimation on real GPR data.

A suitable parametric model for spectral estimation of frequency domain data sampled by a SFGPR system is the *autoregressive* (AR) function, because the data can be represented as a finite sum of sinusoids (each with a frequency relating to the range or depth of the target). AR is also a well-tested model for high-resolution estimation of frequency.

The *power spectral density* PSD for the AR model is defined in equation C.1.

$$\mathrm{PSD}_{AR}(f) = \frac{\sigma^2}{|1 + \sum_{k=1}^{p} a[k] e^{-j2\pi fk}|^2} \tag{C.1}$$

σ^2 is the PSD of a white noise sequence of zero mean and variance σ^2, and $a[k]$ are the AR coefficients for a parametric model order of p. This model is known as an *infinite impulse response* (IIR) all-pole model, and enables the PSD to have sharp peaks at the estimated frequencies and therefore high resolution.

Several methods can be used to estimate the AR coefficients $a[k]$ of the frequency domain data sequence. Some of these are *autocorrelation*, *covariance*, *modified covariance* and *recursive maximum likelihood estimate* [*Kay*, 1988].

Covariance methods were tested on the frequency domain data obtained with the 1-2 GHz SFGPR system to test whether high-resolution spectral estimates of the synthesised profile could be achieved. The best results were obtained with the MUSIC (*MUltiple SIgnal Classification*) algorithm. The MUSIC algorithm estimates the sinusoidal frequencies as the peaks of the PSD estimate of equation C.2.

$$\mathrm{PSD}_{MUSIC}(f) = \frac{1}{\sum_{i=k+1}^{p} |\mathbf{e}^H \mathbf{v}_i|^2} \tag{C.2}$$

$\mathbf{e}$ is a *steering vector* defined as $[1\ e^{j2\pi f}\ e^{j4\pi f}\ \ldots\ e^{j2\pi f(p-1)}]^T$, $\mathbf{v}_i$ are the *eigenvectors* of the data, p is the order number of the AR parametric model and k is the number of sinusoids for the estimate. The eigenvectors can be determined by *eigendecomposition* of the covariance matrix of the data, or by *singular value decomposition* (SVD) of the data. (The SVD method was used to avoid the numerical instability associated with the inversion of the covariance matrix in the eigendecom-

position algorithm.) The $i = k+1 \ldots p$ eigenvectors correspond to the noise subspace of the data, which is assumed to be orthogonal to the signal subspace eigenvectors $i = 1 \ldots k$.

It is evident that when the frequency estimate is perfect (*i.e.* $\mathbf{e} = \mathbf{e}_i$), the PSD of MUSIC approaches infinity. Therefore, the magnitude of the MUSIC PSD is not a good estimate of the true PSD magnitude of the data. However, the sharp peaks of the PSD produce highly resolved frequency estimates if an appropriate AR order number p is chosen. In practice, higher order estimators cause sharper peaks and higher resolvability, however orders which are too high cause spurious peaks to appear in the estimate. As a rule of thumb, the order number p should be chosen to conform with $n/3 < p < n/2$ where n is the number of data samples [*Ulrych & Bishop*, 1975]. However for a small number of estimates, p may be chosen to be less than $n/3$. As with most spectral estimators, the SNR of the data must be high enough for acceptable performance. For the MUSIC algorithm, the SNR should be above 16 dB [*Kay*, 1988].

The following listing is the MUSIC algorithm written for MATLAB.

```
% MUSIC.m Matlab script
% Processes SFGPR data using the MUSIC spectral estimator
% Written by David Noon, 1/12/1994
% iq is a (n x nrp) matrix containing the I+jQ complex samples
% n is the number of frequency steps in each range profile
% nrp is the number of range profiles recorded.

N = 1024;      % DFT size
 p = 20;        % order of AR model
 k = 6;         % number of sinusoids
 n=size(iq,1);
nrp=size(iq,2);

for t=1:nrp

% Conduct SVD for eigendecomposition of iq matrix.
  X = zeros(p,n-p);
  for i=1:p,
    X(i,:) = iq(1,i:n-p+i-1);
  end;
  [U,S,V] = svd(X);
  dg = diag(S).^2/(n-p);
```

```
% Sort eigenvalues (d) and eigenvectors (v) in ascending order.
  [ds,I] = sort(dg);
  d = diag(ds);
  v = conj(U(1:p,I)/(n-p));

% Calculate MUSIC PSD
  den = zeros(1,N);
  for i=1:p-k,
    den = den + abs(fft(v(:,i)',N)).^2;
  end;
  PSD = 1./den;
  PSD_db(:,t) = 10*log10(PSD).';

end;

% Plot the image of PSD_db.
xax=(0:nrp); % x-axis dimension of image
yax=(0:N-1)/N*n; % y-axis dimension of image
PSD_db_norm = -PSD_db+max(max(PSD_db));
imagesc(xax,yax,PSD_db_norm,[0 20])
colormap(gray(64));
xlabel('cross-range')
ylabel('two way travel time (ns)')
title('MUSIC Processed Image')
```

Appendix D

Range-Gain Control

Most GPR systems can digitally process their data in such a way that the reflected signal strength is relatively independent of depth. For impulse GPR, this is achieved by multiplying the amplitudes of the received digitised signals in time with a range-gain function. This process does not improve the dynamic range or the detectability of targets in noise, but can enable the threshold detection of deeper targets. For example, range-gain control can increase the amplitudes of the received signals of buried targets relative to the direct leakage signal of the antennas. This then allows the setting of a threshold level to permit only the deeper targets to be detected by the GPR.

For stepped-frequency GPR, the direct application of a range-gain control to the data of the synthesised profile does not achieve the same result as for the impulse GPR. Figure D.1(a) illustrates a simulation of a synthesised profile containing three targets. The two weak reflections are barely detectable amid the sidelobes of the strong reflection. Figure D.1(b) is a range-gain function which is intended to increase the magnitudes of the weak reflections relative to the strong reflection. The result of summing the magnitudes (in dB's) of (a) and (b) is Figure D.1(c). The weak reflections have been amplified, but so too have the sidelobes of the strong reflection. Obviously, this process has not achieved the desired result.

Instead, the range-gain function can be expressed as a w point complex *Finite Impulse Response* (FIR) function and convolved with the $I + jQ$ frequency domain data of length n prior to the IDFT. The result is a frequency domain array of length $w + n - 1$. The first and last $w - 1$ data points of the array are removed, reducing the length of the frequency domain array to $n - w + 1$. This array is then padded with zeros to a length of N and transformed to the time domain using an

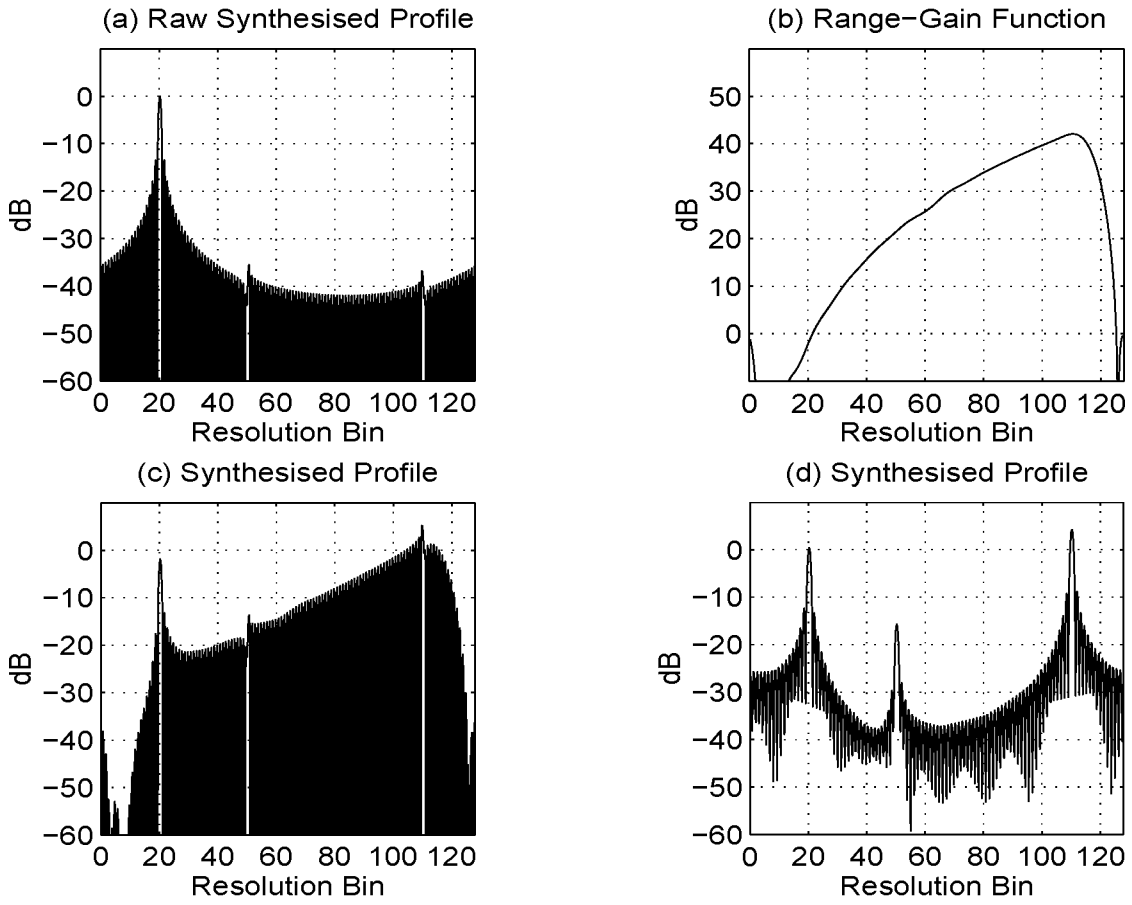

Figure D.1: (a) Simulation of three targets in the synthesised profile; (b) range-gain function; (c) the summation of (a) and (b) in dB's. The weak reflections are still masked by the sidelobes of the strong reflection; (d) IDFT after the frequency domain data of (a) is convolved with the impulse response of (b). The weak reflections are now amplified according to the range-gain function, without being masked by the sidelobes of the strong reflection.

N point IDFT. The result is the synthesised profile in Figure D.1(d) showing the amplification of the weaker reflections, without being masked by the sidelobes of the strong reflection. The relevance of this technique for SFGPR was briefly mentioned in an extended conference abstract by *Pottecher*, 1992, but no further work or results on its application to SFGPR data has appeared in the literature.

The FIR range-gain function can be designed as a complex *discrete-time differentiator* with linear phase [*Oppenheim & Schafer*, 1989]. The *differentiation in frequency* theorem states that the inverse discrete Fourier transform of j times the derivative of a frequency domain array is equal to t times the time domain array (*i.e.* $\mathcal{F}^{-1}\{j\frac{d}{d\omega}X[w]\} = tx[t]$). According to this theorem, a complex FIR differentiator

applied to the $I + jQ$ frequency domain data will add a linear range-gain function to the synthesised profile. Higher order derivatives (*i.e.* $d^k/d\omega^k$) will produce a range-gain function which is proportional to R^k. Therefore, the spherical spreading losses associated with say a rough planar target ($\propto R^3$) can be compensated for by applying a 3rd order complex FIR differentiator which has an 18 dB/octave slope.

Figure D.2(a) is a 12 point complex FIR impulse response of a 5th order complex differentiator, and Figure D.2(b) is the associated range-gain function in the synthesised profile. The curve of the range-gain function along most of the synthesised profile varies by 30 dB/octave.

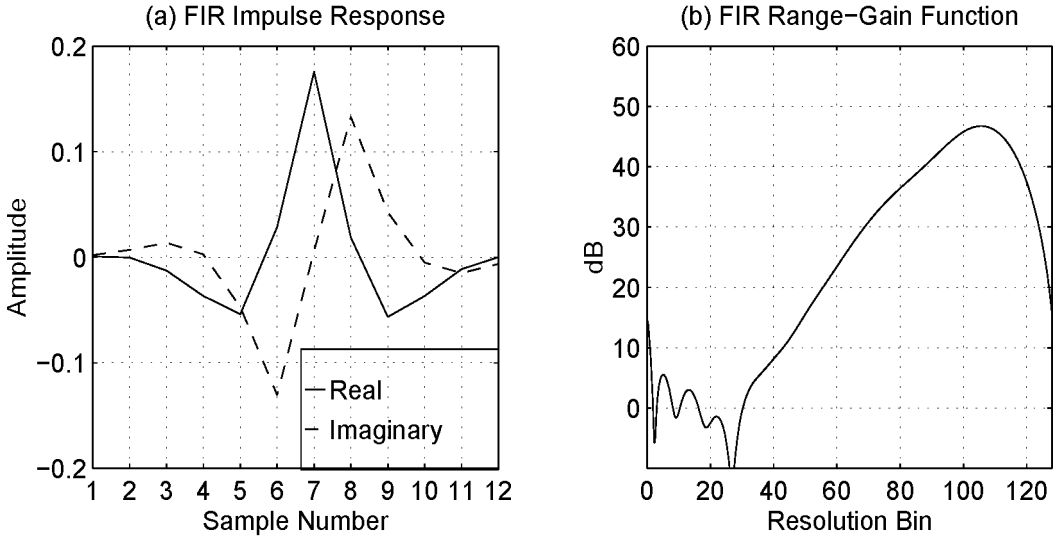

Figure D.2: (a) Real (connected line) and imaginary (dashed line) components of the 12 point complex FIR impulse response of a 5th order differentiator; (b) the corresponding range-gain function in the synthesised profile with a 30 dB/octave slope. A larger number of FIR points in (a) will produce a more consistent range-gain curve in (b), but at the expense of reduced resolving power.

A large number of points in the complex FIR function produce a very smooth range-gain curve in the synthesised profile. However, the resolution of the synthesised profile is reduced due to the removal of the first and last $w - 1$ data points of the frequency domain array prior to zero padding. In most cases, a small w value compared with n is best for range-gain control without a major reduction in resolution.

Appendix E

Hardware Range-gating

Hardware range-gating is a technique used to suppress the leakage signal between the antennas (or other unwanted reflections) in a stepped-frequency radar. By pulsing the stepped-frequency transmission, a receiver "gate" can be opened at a delayed time to pass the reflections of targets at desirable ranges and "blank" the unwanted signals. This technique is also called *Interrupted Continuous Wave* (ICW) by *Nathanson*, 1991 and is described elsewhere by *Einstein*, 1984, *Lane*, 1993 and *Wehner*, 1995. *Pottecher*, 1992 and *Poirier*, 1993 have briefly mentioned (in passing) the use of hardware range-gating for SFGPR. *Hamran et al.*, 1995 has described a 320-370 MHz SFGPR system which utilises hardware range-gating.

The block diagram of a stepped-frequency radar employing hardware range-gating is in Figure E.1. A pulse modulator in the transmitter is used to form a pulse train of the stepped-frequency signals with pulsewidth and pulse repetition intervals of t and T respectively. The transmitter pulsewidth is not associated with the resolving power and thus can be much longer. (The carrier frequencies of the pulses are stepped across a broad bandwidth which defines the resolving power.) The maximum unambiguous range of the pulse train is equal to $vT/2$ (using equation 1.7).

A second pulse modulator is used in the receiver to perform the range-gating. The receiver gate is closed while the transmitter pulse is on to blank the direct leakage signal between the antennas. The first range-gate is then opened to allow the reflected signals within the effective range extent of the transmitted pulse to pass through to the receiver. The receiver sensitivity can then be increased without being saturated by the strong leakage signal using a *sensitivity range control* (SRC) amplifier. The second range-gate is opened after the first range-gate has closed,

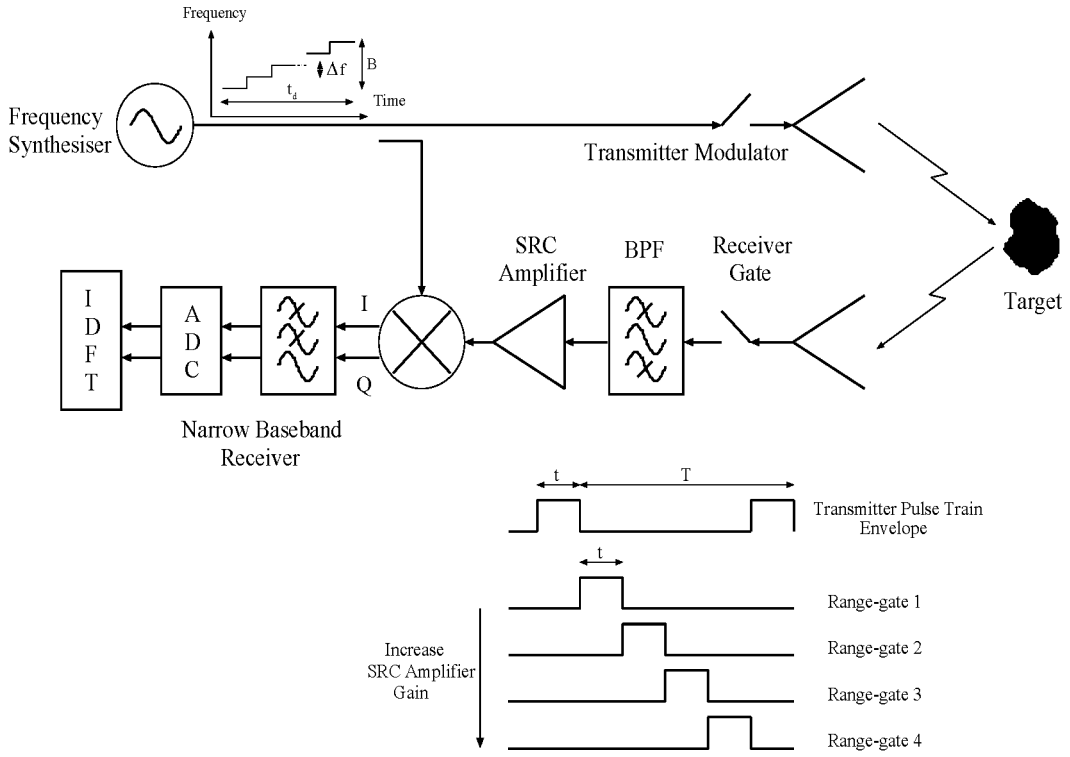

Figure E.1: Block diagram of a stepped-frequency radar with hardware range-gating and sensitivity range control (SRC)

and so on along the maximum unambiguous range. The sensitivity of the receiver is increased as a function of range-gate position, hence termed sensitivity range control.

The band-pass filter following the receiver gate in Figure E.1 selects a single frequency component of the pulsed waveform to pass through to the down-conversion and narrow baseband receiver. The energy loss associated with the spectral lines of the pulse train outside the band-pass filter is equal to the duty cycle T/t factor.

The effective range extent over which scatterers contribute to the received signal is given by the convolution of the transmitter pulse train and the receiver gate train functions. For a receiver gatewidth which is equal to the transmitter pulsewidth, a triangular shape extent of $2t$ or length vt in range results (v is the propagation velocity). Figure E.2 illustrates the effective range extent due to the range-gating process. The effective range extent vt is shorter than the maximum unambiguous range $vT/2$ which enables multiple receiver positions with sensitivity range control.

Figure E.3 illustrates the hardware range-gating and sensitivity range control principles using the minimum-phase waveforms of the simulation in Table 4.2. The

real component and the envelope response of the synthesised profile in Figure 4.13 are displayed in the top row of Figure E.3. The middle rows are four consecutive range-gates with the sensitivity increased for each range-gate position. The result of combining the responses of all the range-gates is contained in the bottom row. The peaks of the two weaker reflections have been increased relative to the strong reflection.

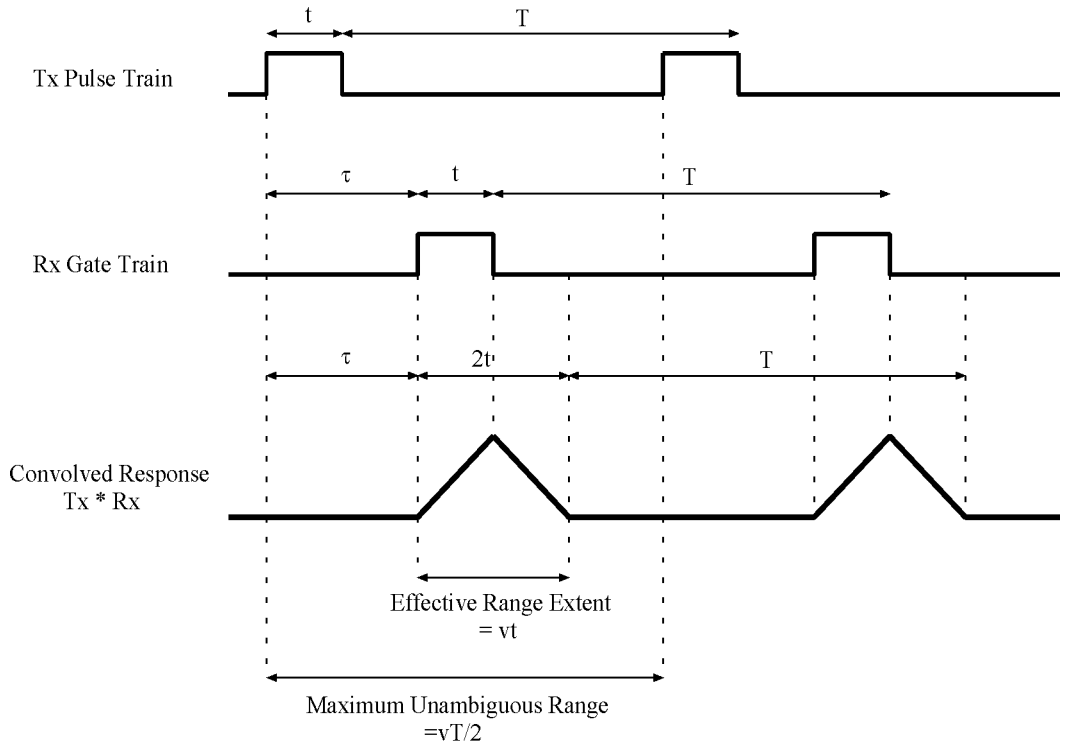

Figure E.2: Transmitter pulse train (Tx), receiver gate train (Rx) and their convolved response (Tx*Rx).

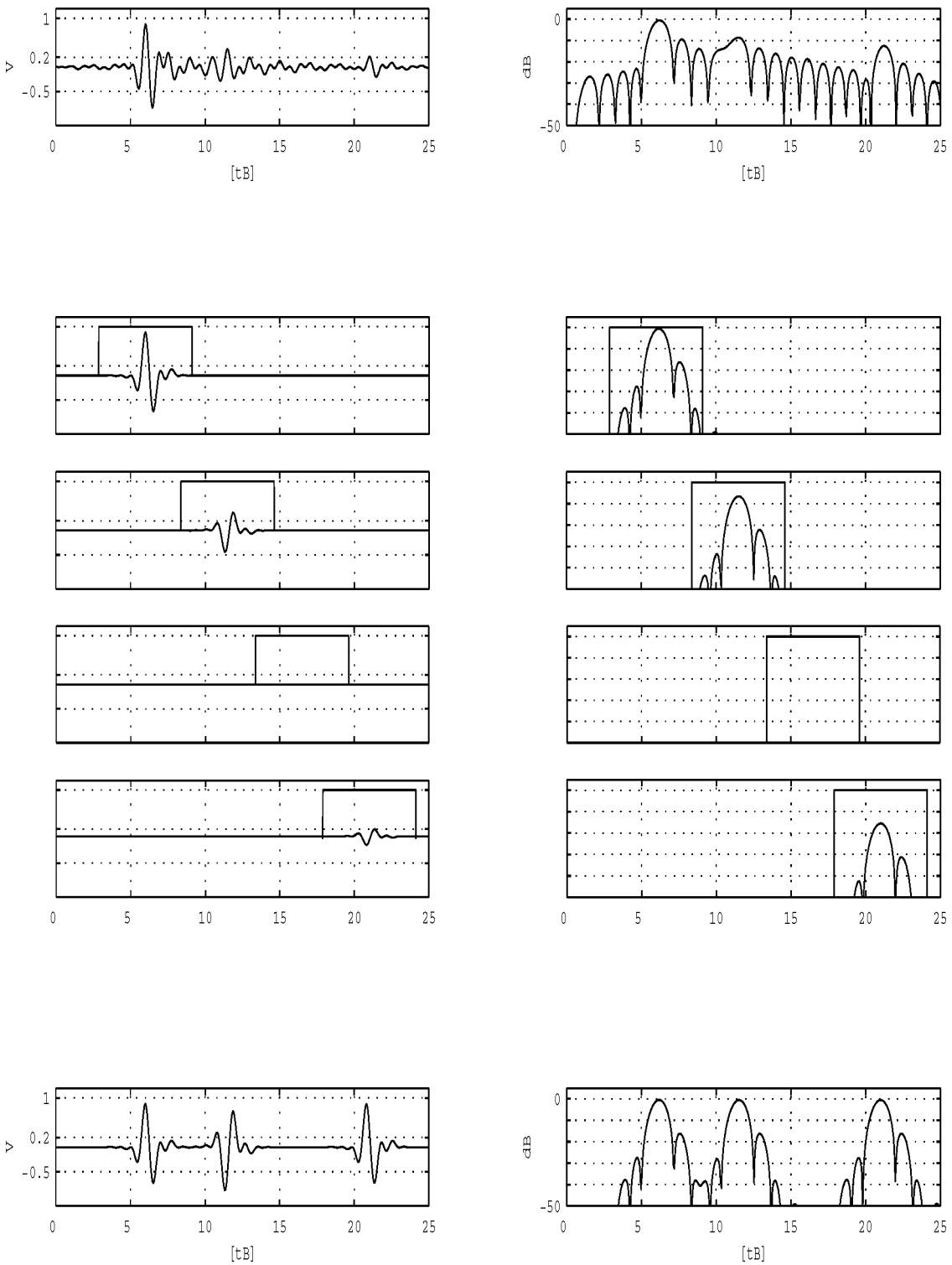

Figure E.3: Hardware range-gating and sensitivity range control of the simulation in Table 4.2. The left column is the real component of the synthesised profile and the right column is the envelope response plotted with a dB scale. The range-gates are shifted along the unambiguous range in four steps. The sensitivity of the each range-gate is increased as a function of range. The bottom row contains the synthesised profile as a result of combining the four range-gates.

Appendix F

Digital Quadrature Sampling

Direct Quadrature Sampling was proposed by *Grace & Pitt*, 1968 and involves the direct sampling of a band-limited signal at four times its centre frequency or twice the Nyquist rate (refer also *Brown*, 1979). For high frequency RF signals, a heterodyne mixer can be used to down-convert the RF signal to an IF, which is then sampled at four times the IF frequency [*Considine*, 1983; *Waters & Jarrett*, 1982]. *Liu, Ghafoor & Stockmann*, 1989 uses this technique for the direct quadrature sampling of both time and frequency signals for array signal processing. Several commercial receiver designs using the direct quadrature sampling technique have been reported [*GEC-Marconi*, 1989; *Pellon*, 1992].

(An alternative way to obtain the quadrature component of a signal is by using a digital Hilbert transform [*Rice & Wu*, 1982; *McCorkle*, 1993], or instead using two digital filters which filter the negative frequencies [*Rader*, 1984]. The sampling requirement for these techniques is the Nyquist rate. These techniques emulate an analogue quadrature mixer in the digital domain, with advantages in improved gain and phase matching. However, distortion is introduced due to the finite order of the transform or filter. The load on the digital processor is substantially increased with higher order filters, which is traded for minimum distortion.)

Figure F.1 is a block diagram (based on the example by *Liu, Ghafoor & Stockmann*, 1989) of a stepped-frequency, heterodyne receiver using digital quadrature sampling. The received RF signal at frequency f is represented by $A\cos[\omega_f(t-\Delta t)+\phi]$. This signal is down-converted to an intermediate frequency ($IF = A\cos[\omega_{IF}t - \omega_f\Delta t + \phi]$) using a heterodyne mixer and band-pass filter. A single channel analogue-to-digital converter (ADC) digitises the IF signal at a sampling rate of twice the Nyquist frequency (*i.e.* $\omega_s = 4\omega_{IF}$). The sampled output is split into two

paths representing the I and Q channels of the digital down-conversion. The I channel is multiplied by $\cos(\omega_{IF}t_n)$, where $\omega_{IF}t_n$ is equal to $n\pi/2$ $(n = 0, 1, 2, \ldots N)$. The Q channel is multiplied by $\sin(\omega_{IF}t_n)$ or $\sin(n\pi/2)$. These multiplications are equivalent to square-wave switching, where the I data sequence is multiplied by the sequence $[1\,0\,-1\,0\,1\,\ldots]$, and the Q data sequence by $[0\,1\,0\,-1\,0\,\ldots]$. An interpolator resamples these I and Q data sequences to select the non-zero samples. The outputs are $x_I[t_n]$ and $x_Q[t_n]$, which are the I and Q baseband components of the incoming RF signal.

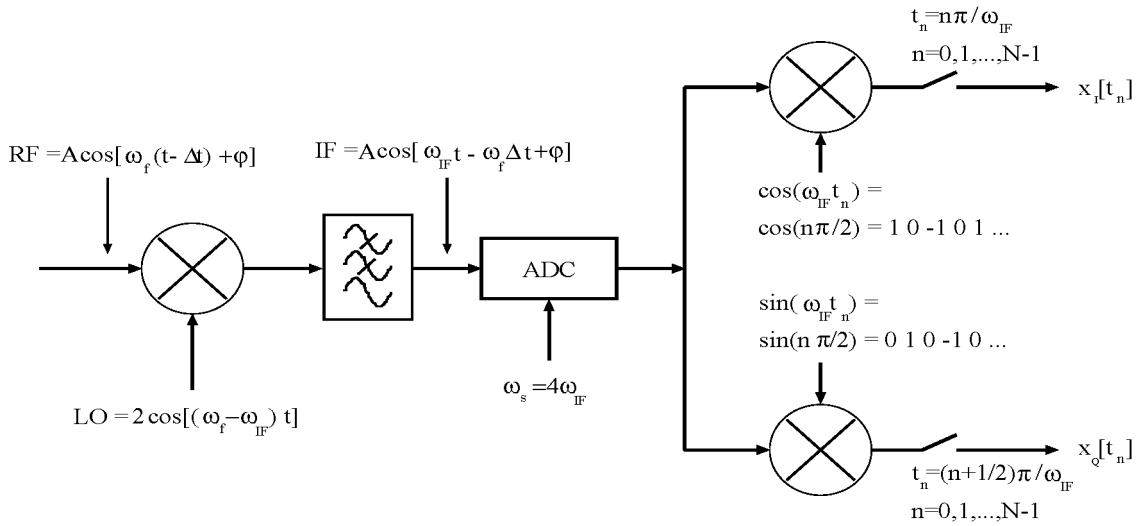

Figure F.1: Block diagram of heterodyne receiver with direct quadrature sampling

Bibliography

Agbinya, J. I., A Microwave FMCW Radar System for Sensing Small Subsurface Objects, *PhD Thesis*, La Trobe University, Vic., Australia, Feb. 1993.

Annan, A. P., Practical Processing of GPR Data, *Proc. of the Second Gov. Workshop on Ground Penetrating Radar: Technologies and Applications*, Columbus, Ohio, USA, 1–22, Oct. 26-28, 1993.

Annan, A. P. & S. W. Cosway, GPR Frequency Selection, *Proc. of the Fifth Int. Conf. on Ground Penetrating Radar (GPR '94)*, Kitchener, Ont., Canada, 747–760, June 12-16, 1994.

Annan, A. P. & J. L. Davis, Radar range analysis for geological materials, *Report of Activities, Paper 77-1B*, Geological Survey of Canada, 1977.

Arai, I. & T. Suzuki, Experimental Results on Subsurface Radar with Improved Resolution, *Journal of Electromagnetic Waves and Applications*, 7(11), 1479–1495, Nov. 1993.

Baker, P. L. & J. P. Cull, Ground Penetrating Radar and the Australian Mining Industry, *Radarcon 90*, Adelaide, SA, Australia, 263–266, Apr. 18-20, 1990.

Balanis, C. A., P. W. Shepard, F. T. Ting & W. F. Kardosh, Anisotropic Electrical Properties of Coal, *IEEE Trans. on Geoscience & Remote Sensing, GE&RS-18*(3), July 1980.

Barrett, C., M. Nicoloff, W. Steinway & J. Thomas, Earth Penetrating Radar Imaging System (EPRIS), *Proc. of the Second Gov. Workshop on Ground Penetrating Radar: Technologies and Applications*, Columbus, Ohio, USA, 175–192, Oct. 26-28, 1993.

Bashforth, M. & S. Koppenjan, Ground Penetrating Radar applications for hazardous waste detection, *SPIE Vol. 1942 Proc. of Underground and Obscured Object Imaging and Detection*, Orlando, Fl., USA, 56–64, Apr. 15-16, 1993.

Binder, B. T., M. F. Toups, S. Ayasli & E. M. Adams, SAR Foliage Penetration Phenomenology of Tropical Rain Forest and Northern U.S. Forest, *The Record of the IEEE 1995 International Radar Conference (RADAR '95)*, Alexandria, Virginia, USA, 158–163, May 8-11, 1995.

Blejer, D., C. Frost & S. Scarborough, UHF Ground Penetrating Measurements of Buried and Partially Buried Trihedrals, *SPIE Vol. 2217 Proc. of Aerial Surveillance Sensing Including Obscured and Underground Object Detection*, Orlando, Fl., USA, 50–62, Apr. 4-6, 1994.

Blom, R. G., R. E. Crippen & C. Elachi, Detection of subsurface features in SEASAT radar images of Means Valley, Mojave Desert, California, *Geology*, *12*, 346–349, 1984.

Botros, A. Z. & D. Olver, Analysis of Target Response of FM-CW Radar, *IEEE Trans. on Antennas and Propagation*, *AP-34*(4), 575–581, Apr. 1986.

Brown, G. H. & O. M. Woodward, Experimentally Determined Radiation Characteristics of Conical and Triangular Antennas, *RCA Review*, *13*, 425–452, 1952.

Brown, J. L., On Quadrature Sampling of Bandpass Signals, *IEEE Trans. on Aerospace and Electronic Systems*, *AES-15*(3), 366–371, May 1979.

Bungey, J. H., M. R. Shaw, S. G. Millard & C. Thomas, Radar Testing of Structural Concrete, *Proc. of the Fifth Int. Conf. on Ground Penetrating Radar (GPR '94)*, Kitchener, Ont., Canada, 305–318, June 12-16, 1994.

Buseck, D., J. Kositsky & R. Vickers, Ultra-Wideband Impulse SAR for Foliage and Ground Penetration, *Ultra-Wideband, Short-Pulse Electromagnetics 2*, New York, NY, USA, 125–131, 1995.

By, T. L., F-N. Kong & H. Westerdahl, Geo-Radar Development at the Norwegian Geotechnical Institute (NGI), *Proc. of the Fourth Int. Conf. on Ground Penetrating Radar*, Rovaniemi, Finland, 21–28, June 8-13, 1992.

Cafforio, C., C. Prati & F. Rocca, SAR Data Focusing Using Seismic Migration Techniques, *IEEE Trans. on Aerospace and Electronic Systems*, *AES-27*(2), 194–207, Mar. 1991.

Caldecott, R., M. Poirier, D. Scofea, D. E. Svoboda & A. J. Terzuoli, Underground mapping of utility lines using impulse radar, *IEE Proc. F, Commun., Radar & Signal Process.*, *135*(4), 342–354, Aug. 1988.

Cameron, R. M., R. Stryker, D. L. Mitchel & W. S. Halliday, Development and Application of Airborne Ground-Penetrating Radar for Environmental Disciplines, *SPIE Vol. 1942 Proc. of Underground and Obscured Object Imaging and Detection*, Orlando, Fl., USA, 21–33, Apr. 15-16, 1993.

Cariou, J., Performances of a Synthetic Pulse Ground Penetrating Radar in Relation to Impulse Radars, *54th EAEG Meeting*, Paris, France, 440–441, June 1-5, 1992.

Carlson, A. B., *Communication Systems - An Introduction to Signals and Noise in Electrical Communication*, McGraw-Hill, 1986.

Carr, A. E., L. G. Cuthbert & A. D. Olver, Digital signal processing for target detection in FMCW radar, *IEE Proc. F, Commun., Radar & Signal Proces.*, *128*(5), 331–336, Oct. 1981.

Chaudhuri, S. K. & J. L. Chow, A base-band radar with log-periodic antenna and post-reception processing scheme, *Arch. Elektron & Ubertr.*, *35*, 391–396, 1981.

Chew, W. C., W. H. Weedon & M. Moghaddam, Inverse Scattering and Imaging using Broadband Time-Domain Data, *Ultra-Wideband, Short-Pulse Electromagnetics 2*, New York, NY, USA, 549–562, 1995.

Chufo, R. L., Frequency Domain vs Time Domain Hardware Architecture for Underground Microwave Imaging, *Unpublished Abstract*, US Bureau of Mines, Pittsburgh, Pennsylvania, USA, 1995.

Chufo, R. L., An Electromagnetic Spatial Spectral Sensor for Geological Measurements in a Dispersive Media, *Proc. of the Second Gov. Workshop on Ground Penetrating Radar: Technologies and Applications*, Columbus, Ohio, USA, 223, Oct. 26-28, 1993.

Chufo, R. L. & W. J. Johnson, A Radar Coal Thickness Sensor, *IEEE Trans. on Industry Applications*, *29*(5), 834–840, Sept. 1993.

Church, R. H., W. E. Webb & J. R. Boyle, Ground-Penetrating Radar for Stata Control, *Report of Investigations 8954*, US Bureau of Mines, 1–16, 1985.

Church, R. H., W. E. Webb & J. B. Salsman, Dielectric Properties of Low-Loss Minerals, *Report of Investigations 9194*, US Bureau of Mines, 1988.

Churchill, F. E., G. W. Ogar & B. J. Thompson, Radar System Having Quadrature Phase Detector Compensator, *US Patent No 3,950,740*, Raytheon Company, Lexington, Mass., USA, Apr. 13, 1976.

Churchill, F. E., G. W. Ogar & B. J. Thompson, The Correction of I and Q Errors in a Coherent Processor, *IEEE Trans. on Aerospace & Electronic Systems*, *AES-17*(1), 131–137, Jan. 1981.

Collins, M. E., *Second International Symposium on Geotechnical Applications of Ground Penetrating Radar*, Soil Conservation Service, Gainesville, Fl., USA, Feb. 1988.

Considine, V., Digital Complex Sampling, *Electron. Lett.*, *19*(16), 608–609, Aug. 4, 1983.

Cook, J. C., RF Electrical Properties of Bituminous Coal Samples, *Geophysics*, *35*(6), 1079–1085, Dec. 1970.

Cook, J. C., Proposed monocycle-pulse VHF radar for airborne ice and snow measurement, *AIEE Comm. and Electronics*, *51*, 588–594, Nov. 1960.

Cook, J. C., Radar Transparencies of Mine and Tunnel Rocks, *Geophysics*, *40*(5), 865–885, Oct. 1975.

Coon, J. B., J. C. Fowler & C. J. Schafers, Experimental Uses of Short Pulse Radar in Coal Seams, *Geophysics*, *46*, 1163–1168, Dec. 1980.

Curlander, J. C. & R. N. McDonough, *Synthetic Aperture Radar - Systems and Signal Processing*, John Wiley & Sons, Inc., New York, NY, USA, 1991.

Daniels, D. J., Short pulse radar for stratified lossy dielectric layer measurement, *IEE Proc. F, Commun., Radar & Signal Proces.*, *127*(5), 384–388, Oct. 1980.

Daniels, D. J., D. J. Gunton & H. F. Scott, Introduction to Subsurface Radar , *IEE Proc. F, Commun., Radar & Signal Process.*, *135*(4), 277–320, Aug., 1988.

Daniels, J. J., R. Roberts, D. Grumman, K. Hayden & W. Ansari, *Proc. of the Second Gov. Workshop on Advanced Ground Penetrating Radar: Technologies and Applications*, The Ohio State University, Columbus, Ohio, USA, Oct. 26-28, 1993.

Darlington, S., US Patent No. 2,678,997, May 18, 1954.

Davis, J. L. & A. P. Annan, Ground-Penetrating Radar for High-Resolution Mapping of Soil and Rock Stratigraphy, *Geophysical Prospecting*, *37*, 531–551, 1989.

Davis, J. L., J. R. Rossiter, D. E. Mesher & C. B. Dawley, Quantitative Measurement of Pavement Structures Using Radar, *Proc. of the Fifth Int. Conf. on Ground Penetrating Radar (GPR '94)*, Kitchener, Ont., Canada, 319–334, June 12-16, 1994.

Dennen, R. S. & W. P. Stroud, Radar hazard detection in a coal structure, *Mining Engineering*, *43*(4), 413–418, Apr. 1991.

Dennis, P. & S. E. Gibbs, Solid-state linear FM/CW radar systems - their promise and their problems, *Proc. IEEE MTT Symp.*, 340–342, 1974.

Einstein, T. H., Generation of High Resolution Radar Range Profiles and Range Profile Auto-Correlation Functions Using Stepped-Frequency Pulse Trains, *Project Report TT-54*, MIT Licoln Laboratory, Lexington, Mass., USA, 18 Oct. 1984.

Elachi, C., L. E. Roth & G. G. Schaber, Spaceborne radar subsurface imaging in hyperarid regions, *IEEE Trans. on Geoscience Electronics*, *GE-22*(4), 383–388, July 1984.

Ellerbruch, D. A. & J. W. Adams, Microwave Measurement of Coal Layer Thickness, *NBSIR 74-387 Report*, Sept. 1974.

Ellerbruch, D. A. & D. R. Belsher, Electromagnetic Technique of Measuring Coal Layer Thickness, *IEEE Transactions on Geoscience Electronics*, *GE-16*(2), 126–133, Apr. 1978.

Etten, P. V. & R. D. Brown, System and Method for earth probing with deep subsurface penetration using low frequency electromagnetic signals, *US Patent No. 05357253*, Earth Sounding International, USA, Apr. 2, 1993.

Farmer, G. A., L. G. Cuthbert, A. D. Olver & A. Z. Botros, Distinguishing between types of hidden objects using an FMCW radar, *Electron. Lett.*, *20*(20), 824–825, Sept. 27, 1984.

Farr, T. G., C. Elachi, P. Hartl & K. Chowdhury, Microwave penetration and attenuation in desert soil: a field experiment with the shuttle imaging radar, *IEEE Trans. on Geoscience Electronics*, *GE-24*(4), 590–594, July 1986.

Fenner, T. J., A New Variable Frequency Antenna for an Impulse Ground Penetrating Radar System, *54th EAEG Meeting*, Paris, France, 432–433, June 1-5, 1992.

Foss, M. M. & R. J. Leckenby, Coal Mine Hazard Detection Using In-Seam Ground-Penetrating-Radar Transillumination, US Bureau of Mines, *Report of Investigations 9062*, 1987.

Fowler, J. C., Subsurface Reflection Profiling Using Ground-Probing Radar, *Mining Engineering*, *33*(8), 1266–1270, Aug. 1981.

Fowler, J. C., Coal Mine Hazard Detection using Synthetic Radar, *US Bureau of Mines OFR 134-84*, Dec. 1983.

Fowler, J. C., S. D. Hale & R. T. Houck, Coal Mine Hazard Detection Using Synthetic Pulse Radar, *US Bureau of Mines OFR 79-81*, Jan. 1981.

Fowler, J. C., L. A. Rubin & W. L. Still, Synthetic Pulse Radar including a Microprocessor Based Controller, *US Patent No. 4,218,678*, ENSCO Inc., Springfield, VA, USA, Aug. 19, 1980.

Fowler, J. C., H. S. Wheatley & J. L. Davis, Synthetic Pulse Radar System and Method, *US Patent No. 4,504,833*, XADAR Corp., Springfield, VA, USA, Mar. 12, 1985.

Freundorfer, A. P., Step Frequency Radar, *PhD Thesis*, University of Toronto, Ont., Canada, 1989.

Freundorfer, A. P., Underground Imaging Using the Step Frequency Radar, *M.A.Sc. Thesis*, University of Toronto, Ont., Canada, July 1983.

Freundorfer, A. P. & K. Iizuka, A Study on the Scattering of Radio Waves from Buried Spherical Targets Using the Step Frequency Radar, *IEEE Trans. on Geoscience & Remote Sensing*, *GS&RS-31*(6), 1253–1255, Nov. 1993.

Freundorfer, A. P., K. Iizuka & R. Ramseier, A method of determining electrical properties of geophysical media, *J. Appl. Phys.*, *55*(1), 218–222, Jan. 1, 1984.

GEC-Marconi, Research Centre Report, Chelmsford, Essex, UK, 1989.

Garvin, A. D. M., Range, resolution and imaging applications of a stepped-frequency continuous wave radar, *Trans. Sth. Afr. Instit. Elect. Eng.*, *82*(3), 206–216, Sept. 1991.

Garvin, A. D. M. & M. R. Inggs, Use of Synthetic Aperture and Stepped-Frequency Continuous Wave processing to obtain radar images, *IEEE Symp. on Comm. and Sig. Proc. (COMSIG 1991)*, South Africa, 32–35, 1991.

Giglio, D., J. Ralston & M. Braunstein, Perspective on underground and obscured target detection and imaging, *SPIE Vol. 1942 Proc. of Underground and Obscured Object Imaging and Detection*, Orlando, Fl., USA, 2–11, Apr. 15-16, 1993.

Gill, G. S., Waveform Generation and Signal Processing in Ultra Wideband Radar, *SPIE Vol. 2235 Proc. of Signal and Data Processing of Small Targets*, Orlando, Fl., USA, 118–128, Apr. 4-8, 1994.

Goldstone, B. J., Method of Compensating for Imbalances in a Quadrature Demodulator, *US Patent No. 4,003,054*, Raytheon Company, Lexington, Mass., USA, Jan. 11, 1977.

Goodman, R., S. Tummala & W. Carrara, Issues in Ultra-Wideband, Widebeam SAR Image Formation, *The Record of the IEEE 1995 International Radar Conference (RADAR '95)*, Alexandria, Virginia, USA, 479–485, May 8-11, 1995.

Grace, O. D. & S. P. Pitt, Quadrature sampling of high-frequency waveforms, *J. Acoust. Soc. Amer.*, *44*, 1453–1454, 1968.

Gunawardena, A. & D. Longstaff, Wave Equation Formulation of Synthetic Aperture Radar (SAR) Algorithms in Time-Space Domain, *Submitted to IEEE Trans. of Geoscience & Remote Sensing*, 1996.

Gunawardena, A. & D. Longstaff, Synthetic Aperture Radar Processing for Ground Penetrating Radar, *1995 Workshop on Applications of Radio Science (WARS '95)*, Canberra, ACT, Australia, June 25-27, 1995a.

Gunawardena, A. & D. Longstaff, A Matched Filter based Synthetic Aperture (SAR) Algorithm for Stepped Frequency Ground Penetrating Radar, *The Record of the IEEE 1995 International Radar Conference (RADAR '95)*, Alexandria, Virginia, USA, 239–243 , May 8-11, 1995b.

Gustavsson, A., P. O. Frölind, H. Hellsten, T. Jonsson, B. Larsson & G. Stenström, The Airborne VHF SAR System CARABAS, *Proc. of the 1993 IEEE Int. Geoscience & Remote Sensing Symposium (IGARSS '93)*, Tokyo, Japan, 558–563, Aug. 18-21, 1993.

Hamran, S-E., Radar Mapping of Physical Properties of Glaciers using Wavenumber Domain Inversion Techniques, *54th EAEG Meeting*, Paris, France, 454–455, June 1-5, 1992.

Hamran, S-E. & E. Aarholt, Glacier study using wavenumber domain synthetic aperture radar, *Radio Science*, *28*(4), 559–570, July 1993.

Hamran, S-E., D. T. Gjessing, J. Hjelmstad & E. Aarholt, Ground Pentrating Synthetic Pulse Radar : Dynamic Range and Modes of Operation, *Journal Applied Geophysics*, *33*(1-3), 7–14, Jan. 1995.

Hamran, S-E. & I. LeComte, Local Plane-Wavenumber Diffraction Tomography in Heterogeneous Backgrounds - Part I: Theory, *Journal of Seismic Exploration*, *2*, 133–146, 1993.

Hänninen, P. & S. Autio, *Proc. of the Fourth International Conference on Ground Penetrating Radar*, Geological Survey of Finland, Special Paper 16, Rovaniemi, Finland, June 8-13, 1992.

Harris, F., On Measuring the Gain and Phase Unbalance and DC Offsets of Quadrature A-to-D Converters with an Adaptive Cancelling Filter, *Proc. of the 21st ASILOMAR Conference on Signals, Systems, and Computers*, Nov. 2-4, 1987.

Harris, F. J., On the Use of Windows for Harmonic Analysis with the Discrete Fourier Transform, *IEEE Proc.*, *66 (1)*, 51–83, Jan. 1978.

Haykin, S. & J. A. Cadzow, Special Issue on Spectral Estimation, *IEEE Proc.*, *70*(9), 883–1125, Sept. 1982.

Helava, H., M. Herman, C. Leung, J. Oicles, L. Ragle, S. Wessman, A. Falk, J. Adams & S. J. Davis, Bulk Avalanche Semiconductor Switches (BASS) for High Resolution Ultra-Wideband Radar (UWBR) applications, *SPIE Vol. 1875 Proc. of Ultrahigh Resolution Radar*, Los Angeles, Ca., USA, 14–22, Jan. 20, 1993.

Hellsten, H., P. O. Frölind, A. Gustavsson, T. Jonsson, B. Larsson & G. Stenström, Ultra-wideband VHF SAR - Design and Measurements, *SPIE Vol. 2217 Proc. of Aerial Surveillance Sensing Including Obscured and Underground Object Detection*, Orlando, Fl., USA, 16–25, Apr. 4-6, 1994.

Hipp, J. E., Soil Electromagnetic Parameters as Functions of Frequency, Soil Density, and Soil Moisture, *IEEE Proc.*, *62*(1), 98–103, Jan. 1974.

Hogan, B. J., Radar System Inspects Walls of Tunnels Under Hudson River, *Design News*, Cahners Publishing Company, Jan. 1986.

Houck, R. T., Measuring the Electrical Properties of Coal Using Ground-Penetrating Radar, *IEEE Trans. on Geoscience & Remote Sensing*, *GE&RS-23*(6), 851–854, Nov. 1985.

Iizuka, K., Step frequency radar for measuring thickness of sea ice, *Unsolicited Proposal*, University of Toronto, Ont., Canada, 1978.

Iizuka, K. & A. P. Freundorfer, Detection of Nonmetallic Buried Objects by a Step Frequency Radar, *IEEE Proc.*, *71(2)*, 276–279, Feb. 1983.

Iizuka, K., A. P. Freundorfer & T. Iwasaki, A Method of Surface Clutter Cancellation for an Underground CW Radar, *IEEE Trans. on Electromagnetic Compatibility*, *EMC-31*(3), 330–332, Aug. 1989.

Iizuka, K., A. P. Freundorfer, K. H. Wu, H. Mori, H. Ogura & V-K. Nguyen, Step-frequency radar, *J. Appl. Phys.*, *56*(9), 2572–2583, Nov. 1, 1984.

Iwasaki, T., A. P. Freundorfer & K. Iizuka, A Unidirectional Semi-Circle Spiral Antenna for Subsurface Radars, *IEEE Trans. on Electromagnetic Compatibility*, *EMC-36*(1), 1–6, Feb. 1994.

Jaggard, D. L. & R. J. King, Sensitivity and Dynamic Range Considerations for Homodyne Detection Systems, *IEEE. Trans. on Instrumentation and Measurements*, *IM-22*(4), 331–338, Dec. 1973.

Jol, H. M., Ground penetrating radar antennae frequencies and transmitter powers compared for penetration depth, resolution and reflection continuity, *Geophysical Prospecting*, *43*, 693–709, July 1995.

Jonscher, A. K., The 'universal' dielectric response, *Nature*, *267*, 673–679, 1977.

Kabutz, M., RF Hardware Design of a Stepped Frequency Continuous Wave Ground Penetrating Radar, *MSc(Eng) thesis*, University of Cape Town, South Africa, June 1995.

Kabutz, M. H., A. Langman & M. R. Inggs, Hardware Cancellation of the Direct Coupling in a Stepped CW Ground Penetrating Radar, *Proc. of the 1994 IEEE Int. Geoscience & Remote Sensing Symp. (IGARSS '94)*, Pasadena, Ca., USA , 2505–2508 , Aug. 8-12, 1994.

Kay, S. M., *Modern Spectral Estimation - Theory & Application*, Prentice-Hall, Englewood Cliffs, NJ, USA, 1988.

Kerr, J. L., Short Axial Length Broad-Band Horns, *IEEE Trans. on Antennas and Propagation, AP-21*, 710–714, 1973.

Khanifar, A., J. K. Ridley, J. L. Bamber & R. P. Card, Microwave scatterometry in support of space-borne scientific missions, *IEE Electronics & Communication Engineering Journal*, *6*(6), 281–288, Dec. 1994.

Kitchen, J., The Effect of Quadrature Hybrid Errors on a Phase Difference Frequency Estimator and Methods for Correction, *M.App.Sc. (Communications) Thesis*, University of Adelaide, SA, Australia, Nov. 1991.

Kjartansson, E., Constant Q-wave propagation and attenuation, *J. Geophys. Res.*, *84*, 4737–4748, 1979.

Klauder, J. R., A. C. Price, S. Darlington & W. J. Albersheim, The Theory and Design of Chirp Radars, *Bell System Tech. J.*, *39*(4), 745–808, July 1960.

Kong, F-N. & T. L. By, Theory and Performance of a GPR System which uses Step Frequency Signals, *Journal of Applied Geophysics*, *33*(1-3), 15–26 , Jan. 1995.

Kong, F-N. & T. L. By, Ground Penetrating Radar using a Frequency Sweeping Signal, *Third Int. Conf. on Ground Penetrating Radar*, Lakewood, Colorado, USA, 37, May 14-18, 1990.

Kong, F-N., J. Kristiansen & T. L. By, A Radar Investigation of Pyramids, *Proc. of the Fourth Int. Conf. on Ground Penetrating Radar*, Rovaniemi, Finland, 345–349, June 8-13, 1992.

Kong, F-N., H. Westerdahl, T. L. By & N-O. Kitterod, Radar Tomography for Environmental Geotechnology : Field and Simulation Tests, *Proc. of the Fifth Int. Conf. on Ground Penetrating Radar (GPR '94)*, Kitchener, Ont., Canada, 1249–1260, June 12-16, 1994.

Koppenjan, S. & M. Bashforth, Ground Penetrating Radar applications: Department of Energy case studies, *SPIE Vol. 1942 Proc. of Underground and Obscured Object Imaging and Detection*, Orlando, Fl., USA, 145–153, Apr. 15-16, 1993a.

Koppenjan, S. & M. Bashforth, The Department of Energy's Ground Penetrating Ground (GPR), an FM-CW system, *SPIE Vol. 1942 Proc. of Underground and Obscured Object Imaging and Detection*, Orlando, Fl., USA, 44–55, Apr. 15-16, 1993b.

Koppenjan, S. & M. Martinez, Site Characterization at the Rabbit Valley Geophysics Performance Evaluation Range, *Proc. on Symp. of App. Geophy. to Engin. & Envir. Problems (SAGEEP '94)*, Boston, USA, 55–79, 1994.

Kumaresan, R., Estimating the Parameters of Exponentially Damped or Undamped Sinusoidal Signals in Noise, *PhD Thesis* , University of Rhode Island, USA, 1982.

Kurtz, J. L., Pulse Compression Waveforms and Error Effects, *Chapter 10 - Coherent Radar Performance Estimation*, Artech House, Norwood, MA, USA, 1993.

Kurtz, J. L. & R. G. Pauley, Radar Component and Subsystem Tests, *Chapter 15 - Coherent Radar Performance Estimation*, Artech House, Norwood, MA, USA, 1993.

Lane, T. L., Stepped-Frequency and ISAR Imaging Systems, *Chapter 11 - Coherent Radar Performance Estimation*, Artech House, Norwood, MA, USA, 1993.

Langman, A. & M. R. Inggs, A SFCW Polarimetric Ground Penetrating Radar, *Proc. of the Fifth Int. Conf. on Ground Penetrating Radar (GPR '94)*, Kitchener, Ont., Canada, 63–77, June 12-16, 1994.

Langman, A., M. R. Inggs & B. Flores, Improving the resolution of a stepped frequency CW ground-penetrating radar, *SPIE Vol. 2275 Proc. of Advanced Microwave and Millimeter-Wave Detectors*, San Diego, Ca., USA, 146–155, July 25-26, 1994.

LeComte, I. & S-E. Hamran, Local Plane-Wavenumber Diffraction Tomography in Heterogeneous Backgrounds - Part II: Green's Functions and Finite-Difference Traveltimes, *Journal of Seismic Exploration*, *2*, 287–299, 1993.

Liau, T. F., A. G. Carr & L. G. Cuthbert, Using Non-Fourier Techniques in Signal Processing for an FMCW Hidden-Object Dectection Radar, *Electron. Lett.*, *22*(9), 466–467, Apr. 24, 1986.

Ling, H., J. Moore, H. Kim, L. C. Trintinalia, R. Bhalla & G. Xu, Time-Frequency Processing of Wideband Radar Echo: From Fixed Resolution to Multiresolution with Superresolution, *Ultra-Wideband, Short-Pulse Electromagnetics 2*, New York, NY, USA, 527–533, 1995.

Liu, H., A. Ghafoor & P. H. Stockmann, A New Quadrature Sampling and Processing Approach, *IEEE Trans. on Aerospace and Electronic Systems*, *AES-25*(5), 733–747, Sept. 1989.

Liu, H. -P., D. L. Anderson & H. Kanamori, Velocity dispersion due to anelasticity; Implications for seismology and mantle composition, *Geophys. J. Roy. Astron. Soc.*, *47*, 41–58, 1976.

Longstaff, I. D., D. A. Noon & G. F. Stickley, A System for Correcting Receiver Errors in Radar, *Patent PCT/AU96/00217*, The University of Queensland, Qld, Australia, Apr. 18, 1994.

Lord, A. E. & R. M. Koerner, *Detection of Subsurface Hazardous Waste Containers by Nondestructive Techniques*, Noyes Data Corporation, Park Ridge, NJ., USA, 1990.

Lucius, J. E., G. R. Olhoeft & S. K. Duke, Abstracts of the Third International Conference on Ground Penetrating Radar, *USGS Open-File Report 90-414*, Lakewood, Colorado, USA, May 14-18, 1990.

Lukashenko, Y. I., A. I. Maslov, N. A. Terletzkiy & L. A. Tsiurupa, Subsurface sounding in the UHF band of lenses of ground water and continental glaciers, *Telecomm. & Radio Eng. (English Translation)*, *34*(4), 94–95, Apr. 1979.

Marple, S. L., *Digital Spectral Analysis*, Prentice-Hall, Englewood Cliffs, NJ, USA, 1987.

McCauley, J. F., G. G. Schaber, C. S. Breed, M. J. Grolier, C. V. Haynes, B. Issawi, E. Charles & R. Blom, Subsurface valleys and geoarcheology of the eastern Sahara revealed by shuttle radar, *Science*, *218*, 1004–1020, 1982.

McCorkle, J. W., Early Results from the Army Research Laboratory Ultra-Wide-Bandwidth Foliage Penetrating SAR, *SPIE Vol. 1942 Proc. of Underground and Obscured Object Imaging and Detection*, Orlando, Fl., USA, 88–95, Apr. 15-16, 1993.

McHugh, W. P., J. F. McCauley, C. V. Haynes, C. S. Breed & G. G. Schaber, Paleorivers and Geoarcheology in the Southern Egyptian Sahara, *Geoarcheology*, *3*(1), 1988.

Metratek, Metratek's Ground Penetrating Radar System, *Demonstrators Information for the Advanced Technology Demonstration at Jefferson Proving Ground (Phase 1)*, PRC Inc., Maryland, USA, May 13, 1994.

Mirkin, M. I., T. O. Grosch, T. J. Murphy, S. Ayasli, H. Hellsten, R. Vickers & J. M. Ralston, Results of the June 1993 Yuma ground penetrating radar experiment, *SPIE Vol. 2217 Proc. of Aerial Surveillance Sensing Including Obscured and Underground Object Detection*, Orlando, Fl., USA, 4–15, Apr. 4-6, 1994.

Mirkin, M. I., C. F. Lee, T. O. Grosch, B. E. Hodges, S. Ayasli, K. Kappra & K. Sturgess, Results on Ground Penetration SAR Phenomenology from June 1993 Yuma Experiment, *The Record of the IEEE 1995 International Radar Conference (RADAR '95)*, Alexandria, Virginia, USA, 164–170, May 8-11, 1995.

Monzingo, R. A. & S. P. Au, Evaluation of Image Response Signal Power Resulting from I-Q Channel Imbalance, *IEEE Trans. on Aerospace & Electronic Systems*, *AES-23*(2), 285–287, Mar. 1987.

Nathanson, F. E., *Radar Design Principles - Signal Processing and the Environment (2nd Ed.)*, McGraw-Hill, 1991.

Nicollin, F., Y. Barbin, W. Kofman, D. Mattieu, S-E. Hamran, P. Bauer, J. Achache & J. Blamont, An HF Bi-Phase Shift Keying Radar: Applications to Ice Sounding in Western Alps and Spitsbergen Glaciers, *IEEE Trans. on Geoscience & Remote Sensing*, *GS&RS-30*(5), 1025–1033, Sept. 1992.

Noon, D., Report on Mt Thorley Trials, *Confidential Report to Mt Thorley Mine*, The University of Queensland, Qld, Australia, Nov. 30, 1994.

Noon, D. A. & M. E. Bialkowski, An Inexpensive Microwave Distance Measuring System, *Micro. & Opt. Tech. Lett.*, *6*(5), 287–292, Apr. 1993.

Noon, D. A. & I. D. Longstaff, Performances of GPR across a Broad Frequency Spectrum, *1995 Workshop on Applications of Radio Science (WARS '95)*, Canberra, ACT, Australia, June 25-27, 1995.

Noon, D. A. & I. D. Longstaff, A new ground penetration radar relevant to the Australian mining Industry, *Workshop in Pattern Analysis/Recognition*, Townsville, Qld, Australia, 11–13, Oct. 2, 1992.

Noon, D. A., I. D. Longstaff & G. F. Stickley, Correction of I/Q Errors in Homodyne Step Frequency Radar Refocuses Range Profiles, *1994 Proc. IEEE Int. Conf. on Acoustics, Speech & Sig. Proc. (ICASSP '94)*, Adelaide, SA, Australia, 369–372, Apr. 19-22, 1994.

Noon, D. A., I. D. Longstaff & R. J. Yelf, Advances in the Development of Step Frequency Ground Penetrating Radar, *Proc. of the Fifth Int. Conf. on Ground Penetrating Radar (GPR '94)*, Kitchener, Ont., Canada, 117–132, June 12-16, 1994.

Nothdurft, S. L. & I. D. Longstaff, Measuring the Radio Wave Propagation Characteristics of the Ground, *1995 Workshop on Applications of Radio Science (WARS '95)*, Canberra, ACT, Australia, June 25-27, 1995.

Ødegård, R. S., S-E. Hamran, P. H. BØ, B. Etzelmüller, G. Vatne & J. L. Sollid, Thermal regime of a valley glacier, Erikbreen, northern Spitsbergen, *Polar Research*, *11*(2), 69–79, 1992.

Oicles, J., M. Staskus & P. Brunemeier, High-Power Impulse Generators for UWB Applications, *Ultra-Wideband, Short-Pulse Electromagnetics 2*, New York, NY, USA, 59–66, 1995.

Olver, A. D. & L. G. Cuthbert, FMCW radar for hidden object detection, *IEE Proc. F, Commun., Radar & Signal Process.*, *135*(4), 354–361, Aug. 1988.

Oppenheim, A. V. & R. W. Schafer, *Discrete-Time Signal Processing*, Prentice-Hall, Englewood Cliffs, NJ, USA, 1989.

Ottolini, R., Synthetic Aperture Radar Data Processing, *Standford Exploration Project*, 1987.

PRC, Evaluation of Individual Demonstrator Performance at the Unexploded Ordnance Advanced Technology Demonstration Program at Jefferson Proving Ground (Phase I), *Report No. SFIM-AEC-ET-CR-95033*, PRC Inc., Maryland, USA, Mar. 1995.

Parry, N. S. & J. L. Davis, GPR Systems for Roads and Bridges, *Proc. of the Fourth Int. Conf. on Ground Penetrating Radar*, Rovaniemi, Finland, 247–257, June 8-13, 1992.

Pellon, L. E., A Double Nyquist Digital Product Detector for Quadrature Sampling, *IEEE Trans. on Signal Processing*, *40*(7), 1670–1681, July 1992.

Peters, L., J. J. Daniels & J. D. Young, Ground Penetrating Radar as a Subsurface Environmental Sensing Tool, *IEEE Proc.*, *82*(12), 1802–1822, Dec. 1994.

Piper, S. O., Frequency-Modulated Continuous Wave Systems, *Chapter 12 - Coherent Radar Performance Estimation*, Artech House, Norwood, MA, USA, 1993.

Piper, S. O., Homodyne FMCW Radar Range Resolution Effects with Sinusoidal Nonlinearities in the Frequency Sweep, *The Record of the IEEE 1995 International Radar Conference (RADAR '95)*, Alexandria, Virginia, USA, 563–567, May 8-11, 1995.

Pippert, R. C., R. G. Plumb & K. Soroushian, Development of a Ground-Penetrating Radar to Detect Excess Moisture in Pavement Subgrade, *RSL Technical Report 9352-1*, University of Kansas Center for Research, Inc., USA, Jan. 1994.

Pippert, R. C., K. Soroushian & R. G. Plumb, Development of a Ground Penetrating Radar to Detect Excess Moisture in Pavement Subgrade, *Proc. of the Second Gov. Workshop on Ground Penetrating Radar: Technologies and Applications*, Columbus, Ohio, USA, 283–297, Oct. 26-28, 1993.

Pittman, W. E., R. H. Church, W. E. Webb & J. T. McLendon, Ground Penetrating Radar - A Review of Its Application in the Mining Industry, *Information Circular 8964*, US Bureau of Mines, 22, 1984.

Plumb, R. G. & H. Ma, Swept Frequency Reflectometer Design for In-Situ Permittivity Measurements, *IEEE Trans. on Instrumentation and Measurement*, *IM-42*(3), 730–734, June 1993.

Poirier, M. A., Comparison of Base Band Pulsed and Stepped Frequency Pulsed Radar Concepts for GPR Applications, *Proc. of the Second Gov. Workshop on Ground Penetrating Radar: Technologies and Applications*, Columbus, Ohio, USA, 221–222, Oct. 26-28, 1993.

Pottecher, G., Synthetic Pulse Ground Penetrating Radar, *54th EAEG Meeting*, Paris, France, 442–443, June 1-5, 1992.

Pottecher, G., A Synthetic Pulse GPR based on a Network Analyser, *Third Int. Conf. on Ground Penetrating Radar*, Lakewood, Colorado, USA, 56, May 14-18, 1990.

Rabiner, L. R., R. W. Schafer & C. M. Rader, The Chirp $\mathcal{Z}$ -Transform Algorithm, *IEEE Trans. on Audio and Electroacoustics*, *AU-17*(2), 86–92, June 1969.

Rader, C. M., A Simple Method for Sampling In-Phase and Quadrature Components, *IEEE Trans. on Aerospace and Electronic Systems*, *AES-20*(6), 821–824, Nov. 1984.

Ralston, J. M., System Analysis of Ultra-Wideband Instrumentation Radars: Impulse vs Stepped-Chirp Approaches, *SPIE Vol. 1875 Proc. of Ultrahigh Resolution Radar*, Los Angeles, Ca., USA, 114–123, Jan. 20, 1993.

Redman, J. D., A. P. Annan, J. P. Greenhouse, T. Klym & J. R. Rossiter, *Proc. of the Fifth International Conference on Ground Penetrating Radar (GPR '94)*, Waterloo Centre for Groundwater Research, Kitchener, Ont., Canada, June 12-16, 1994.

Ressler, M., L. Happ, L. Nguyen, T. Ton & M. Bennett, The Army Research Laboratory Ultra-Wide Band Testbed Radars, *The Record of the IEEE 1995 International Radar Conference (RADAR '95)*, Alexandria, Virginia, USA, 686–691, May 8-11, 1995.

Ressler, M. A. & J. W. McCorkle, Evolution of the Army Research Laboratory Ultra-Wideband Test Bed, *Ultra-Wideband, Short-Pulse Electromagnetics 2*, New York, NY, USA, 109–123, 1995.

Rice, D. W. & K. H. Wu, Quadrature Sampling with High Dynamic Range, *IEEE Trans. on Aerospace and Electronic Systems*, *AES-18*(4), 736–739, Nov. 1982.

Robinson, E. A., A Historical Perspective of Spectrum Estimation, *IEEE Proc.*, *70*(9), 885–906, Sept. 1982.

Robinson, E. A. & T. S. Durrani, *Geophysical Signal Processing*, Prentice-Hall, Englewood Cliffs, NJ, USA, 1986.

Robinson, L. A., W. B. Weir & L. Young, An RF Time-Domain Reflectometer Not in Real Time, *IEEE Trans. on Microwave Theory and Techniques*, *MTT-20*(12), 855–857, Dec. 1972.

Robinson, L. A., W. B. Weir & L. Young, Location and Recognition of Discontinuities in Dielectric Media Using Synthetic RF Pulses, *IEEE Proc.*, *62*(1), 36–44, Jan. 1974.

Rocca, F., Synthetic Aperture Radar: A New Application for Wave Equation Techniques, *Standford Exploration Project*, 1987.

Roe, K. C. & R. C. Wittmann, Improved Coal Interface Detector, *Nat. Bur. Std. NBSIR 82-1663*, Boulder, CO, USA, May 1982.

Rutt, D. R., Use of an ultra-wideband synthetic aperture radar technique for buried mine detection, *SPIE Vol. 1875 Proc. of Ultrahigh Resolution Radar*, Los Angeles, Ca., USA, 68–76, Jan. 20, 1993.

Ruttenberg, K. & L. Chanzit, High Range Resolution by means of Pulse to Pulse Frequency Shifting, *IEEE EASCON Record*, 47–51, 1968.

Sargis, P. D., F. D. Lee, E. S. Fulkerson, B. J. McKinley & W. D. Aimonetti, Ground-penetrating radar for buried mine detection, *SPIE Vol. 2217 Proc. of Aerial Surveillance Sensing Including Obscured and Underground Object Detection*, Orlando, Fl., USA, 38–49, Apr. 4-6, 1994.

Sato, M., E. Satoshi & N. Hiroaki, Analysis of a Directional Borehole Radar Signal with a Time-Frequency Distribution, *Proc. of the Fifth Int. Conf. on Ground Penetrating Radar (GPR '94)*, Kitchener, Ont., Canada, 593–607, June 12-16, 1994.

Sato, M., M. Takashi & N. Hiroaki, Polarimetric Borehole Radar Measurements in Granite, *Proc. of the Fifth Int. Conf. on Ground Penetrating Radar (GPR '94)*, Kitchener, Ont., Canada, 609–623, June 12-16, 1994.

Saunders, W. K., Post-War Developments in Continuous-Wave and Frequency-Modulated Radar, *IRE Trans. on Aerospace and Navigational Electronics*, *ANE-8*, 7–19, Mar. 1961.

Schaber, G. G., J. F. McCauley, C. S. Breed & G. R. Oleheft, Shuttle imaging radar: physical controls on signal penetration and subsurface scattering in the Eastern Sahara, *IEEE Trans. on Geoscience Electronics*, *GE-24*(4), 603–623, July 1986.

Scott, W. R. & G. S. Smith, Measured Electrical Constitutive Parameters of Soil as Functions of Frequency and Moisture Content, *IEEE Trans. on Geoscience & Remote Sensing*, *GE&RS-30*(3), 621–623, May 1992.

Seear, P., A Time of Change - Are Mining Methods set to change in the 1990's, *IIR Conference on Automated Mining Technology for the Coal Industry*, Sydney, Australia, Apr. 27-28, 1995.

Sheen, D. R., T. B. Lewis, S. C. Wei & D. Kletzli,, Imaging of buried and foliage-obscured objects with an ultrawide bandwidth polarimetric SAR, *SPIE Vol. 1942 Proc. of Underground and Obscured Object Imaging and Detection*, Orlando, Fl., USA, 12–20, Apr. 15-16, 1993a.

Sheen, D. R., S. C. Wei, T. B. Lewis & S. R. D. Graff, Ultrawide bandwidth polarimetric SAR imagery of foliage-obscured objects, *SPIE Vol. 1875 Proc. of Ultrahigh Resolution Radar*, Los Angeles, Ca., USA, 106–113, Jan. 20, 1993b.

Siggins, A. & G. Turner, Pulse Broadening of Subsurface Radar Signals, *54th EAEG Meeting*, Paris, France, 662–663, June 1-5, 1992.

Sinsky, A. I. & P. C. P. Wang, Error Analysis of a Quadrature Coherent Detector Processor, *IEEE Trans. on Aerospace & Electronic Systems*, *AES-10*(6), 880–883, Nov. 1974.

Skolnik, M. I., *Introduction to Radar Systems*, McGraw-Hill, New York, USA, 1962.

Skolnik, M. I., *Radar Handbook*, McGraw-Hill, New York, NY, USA, 1990.

Stacey, F. D., M. T. Gladwin, B. McKavanagh, A. T. Linde & L. M. Hastie, Anelastic damping of acoustic and seismic pulses, *Geophysical Surveys*, *2*, 131–151, 1975.

Steinway, W. & C. Barrett, Development Status of a Stepped-Frequency Ground Penetrating Radar, *SPIE Vol. 1942 Proc. of Underground and Obscured Object Imaging and Detection*, Orlando, Fl., USA, 34–43, Apr. 15-16, 1993.

Steinway, W. J., C. R. Barrett, M. D. Patz, J. E. Thomas & M. J. Nicoloff, Earth Penetrating Radar Imaging System Field Measurements, *SPIE Vol. 2217 Proc. of Aerial Surveillance Sensing Including Obscured and Underground Object Detection*, Orlando, Fl., USA, 63–73, Apr. 4-6, 1994a.

Steinway, W. J., J. E. Thomas, C. R. Barrett & B. G. Beck, Earth-penetrating synthetic image radar, *US Patent No. 05339080*, Coleman Research Corporation, Orlando, Fl., USA, Aug. 16, 1994b.

Stolt, R. H. & A. K. Benson, Seismic Migration - Theory and Practice, *Volume 5 - Handbook of Geophysical Exploration*, Geophysical Press, London, UK, 1986.

Stolte, C. & N. Klaus-Peter, Eccentricity-Migration: A Method to improve the imaging of pipes in radar reflection data, *Proc. of the Fifth Int. Conf. on Ground Penetrating Radar (GPR '94)*, Kitchener, Ont., Canada, 723–733, June 12-16, 1994.

Stove, A. G., Linear FMCW radar techniques, *IEE Proc. F, Commun., Radar & Signal Process.*, *139*(5), 343–350, Oct. 1992.

Stratton, J. A., *Electromagnetic Theory*, McGraw-Hill Book Company, New York, NY, USA, 1941.

Strick, E., The determination of Q, dynamic viscosity and creep curves from wave propagation measurements, *J. Geophyical Research*, *13*, 197–218, 1975.

Stuhr, F., R. Jordan & M. Werner, SIR-C/X-SAR: A Multifaceted Radar, *The Record of the IEEE 1995 International Radar Conference (RADAR '95)*, Alexandria, Virginia, USA, 53–61, May 8-11, 1995.

SwRI, *Geophysical Electromagnetic Systems*, Southwest Research Institute, San Antonio, Texas, USA, 1978.

Taylor, J. W., System and Method of Compensating a Doppler Processor for Input Unbalance and an Unbalance Measuring Sensor for use therein, *US Patent No. 4,616,229*, Westinghouse Electric Corp., Pittsburgh, Pa., USA, Oct. 7, 1986.

Thierbach, R., Twenty Years of Ground-Probing Radar in Salt and Potash Mines, *Proc. of the Fifth Int. Conf. on Ground Penetrating Radar (GPR '94)*, Kitchener, Ont., Canada, 957–979, June 12-16, 1994.

Tirkel, A. Z., C. F. Osborne & P. J. Osborne, Active Sensing of Spatial Defects using a Microwave Imager, *Radarcon 90*, Adelaide, SA, Australia, 429–435, Apr. 18-20, 1990.

Turner, G., The Influence of Subsurface Properties on Ground Penetrating Radar Pulses, *PhD Thesis*, Macquarie University, NSW, Australia, Dec. 1993.

Turner, G., Propagation Deconvolution, *Proc. of the Fourth Int. Conf. on Ground Penetrating Radar*, Rovaniemi, Finland, 85–93, June 8-13, 1992.

Turner, G. & A. F. Siggins, Constant Q Attenuation of Subsurface Radar Pulses, *Geophysics*, *59*(8), 1192–1200, Aug. 1994.

Turner, G., A. F. Siggins & L. D. Hunt, Ground Penetrating Radar - Will it Clear the Haze at Your Site?, *Proc. ASEG 10th Geophysical Conf.*, *24*(3/4), 819–832, Sept./Oct. 1993.

Turner, G., R. J. Yelf & P. J. Hatherly, Coal Mining Applications of Ground Radar, *Exploration Geophysics*, *20*(1/2), 165–168, 1989.

Ulaby, F. T., R. K. Moore & A. K. Fung, Microwave Remote Sensors - Active and Passive, *Volume 1, Chapter 2 - Plane Waves*, Addison-Wesley, Reading, Mass., USA, 1981.

Ulrych, T. J. & T. N. Bishop, Maximum Entropy Spectral Analysis and Autoregressive Decomposition, *Rev. Geop. Space Phys.*, *13*, 183–200, Feb. 1975.

Uratsuka, S., K. Okamoto, H. Mineno, F. Nishio & S. Mae, Step Frequency Radar Experiments on the Antarctic Sea Ice, *Journal of the Communications Research Laboratory*, *35*(146), 251–258, Nov. 1988a.

Uratsuka, S., K. Okamoto, F. Nishio, H. Mineno & S. Mae, Step Frequency Radar Experiments on the Antarctic Sea Ice, *Proc. of the 1988 IEEE Int. Geoscience & Remote Sensing Symp. (IGARSS '88)*, Edinburgh, Scotland, 1703–1706, Sept. 13-16, 1988b.

Vadnais, K. G., M. B. Bashforth, T. S. Lewallen & S. R. Nammath, Stepped-frequency ground penetrating radar, *US Patent No. 05325095*, US Department of Energy, Washington, DC, USA, June 28, 1994.

Vickers, R. S., V. H. Gonzalez & R. W. Ficklin, Results from a VHF impulse synthetic aperture radar, *SPIE Vol. 1631 Proc. of Ultrawideband Radar*, Los Angeles, Ca., USA, 219–225, Jan. 22-23, 1992.

Walton, E. K., Chapter 5 - The Measurement of Radar Cross Section, *Radar Target Imaging*, Springer Series on Wave Phenomena, Vol. 13, USA, 1994.

Walton, E. K., Modern Radar Signal Processing Algorithms applied to Ground Penetrating Radar, *Proc. of the Second Gov. Workshop on Ground Penetrating Radar: Technologies and Applications*, Columbus, Ohio, USA, 71–81, Oct. 26-28, 1993a.

Walton, E. K., Ground Penetrating Radar using Ultra-Wideband Noise, *Proc. of the Second Gov. Workshop on Ground Penetrating Radar: Technologies and Applications*, Columbus, Ohio, USA, 121–131, Oct. 26-28, 1993b.

Walton, E. K. & M. J. Gerry, Analysis of Dispersive Radar Scattering Mechanisms from Measured Data, *Ultra-Wideband, Short-Pulse Electromagnetics 2*, New York, NY, USA, 543–547, 1995.

Walton, E. K. & J. D. Young, The Ohio State University Compact Radar Cross-Section Measurement Range, *IEEE Trans. on Antennas and Propagation*, *AP-32*(11), 1218–1223, Nov. 1984.

Waters, W. M. & B. R. Jarrett, Bandpass Signal Sampling and Coherent Detection, *IEEE Trans. on Aerospace and Electronic Systems*, *AES-18*(4), 731–736, Nov. 1982.

Weedon, W. H., W. C. Chew & C. A. Ruwe, Step-frequency radar imaging for NDE and GPR applications, *SPIE Vol. 2275 Proc. of Advanced Microwave and Millimeter-Wave Detectors*, San Diego, Ca., USA, 156–167, July 25-26, 1994.

Wehner, D. R., *High-Resolution Radar*, Artech House, Norwood, MA, USA, 1995.

Westerdahl, H., R. Austvik & F-N. Kong, Geo-Radar in Tunneling - The Tunnel Radar, *Proc. of the Fourth Int. Conf. on Ground Penetrating Radar*, Rovaniemi, Finland, 41–45, June 8-13, 1992.

Wright, D. L., J. A. Bradley & T. P. Grover, Data Acquisition Systems for Ground Penetrating Radar with Example Applications from the Air, the Surface, and Boreholes, *Proc. of the Fifth Int. Conf. on Ground Penetrating Radar (GPR '94)*, Kitchener, Ont., Canada, 1075–1089, June 12-16, 1994.

Wright, D. L., J. A. Bradley & S. M. Hodge, Use of a new high-speed digital data acquisition system in airborne ice-sounding, *IEEE Trans. on Geoscience & Remote Sensing*, *GE&RS-27*(5), 561–567, May 1989.

Wright, D. L., S. M. Hodge, J. A. Bradley, T. P. Grover & R. W. Jacobel, A digital low-frequency, surface-profiling ice-radar system, *Journal of Glaciology*, *36*(122), 112–121, 1990.

Wu, K. H., Step Frequency Radar, *M. A. Sc. Thesis*, University of Toronto, Ont., Canada, 1979.

Yelf, R., G. Turner, P. Hatherly & D. Hagen, Appraisal of Ground Penetrating Radar in Underground Coal Mines, *NERDDC Project No. 1210 Final Report*, Australia, June 1990.

Yelf, R. J., GPR Mapping of Overburden and Guidance on Continuous Surface Miners, *ACARP Quarterly Reports*, Australia, 1991-1995.

Yelf, R. J. & G. Turner, Applications of Ground Radar to Coal Mining, *Third Int. Conf. on Ground Penetrating Radar*, Lakewood, Co., USA, 80, May 14-18, 1990.